Leveraging Tumor-Associated Macrophages for Anti-Cancer Immunotherapy Using Injectable Biomaterials

By

Evan Bryce Glass

Dissertation

Submitted to the Faculty of the

Graduate School of Vanderbilt University

in partial fulfillment of the requirements

for the degree of

DOCTOR OF PHILOSOPHY

in

Biomedical Engineering

January 31, 2022

Nashville, Tennessee

Approved:

Todd D. Giorgio, PhD, Chair

Barbara Fingleton, PhD

Young J. Kim, MD, PhD

Marjan Rafat, PhD

John T. Wilson, PhD

Fiona E. Yull, D.Phil.

This work is dedicated to the friends and family who have supported me on this journey.

ACKNOWLEDGMENTS

The process of earning a PhD is never an individual effort, it takes an entire team to accomplish. First and foremost, I would like to thank my primary advisor and mentor, Dr. Todd Giorgio, for all his guidance over the past 5+ years. His support of my work has driven me to push through every adversity that I've faced. The relentless positivity and energy that he brought to every meeting inspired me and kept me from falling into the bottomless pit of despair often associated with PhDs. Thank you for always motivating me to keep learning. I would also like to thank Dr. Fiona Yull for her constant support and positivity in the face of many failed nanoparticles experiments and Dr. Young Kim for his guidance as we developed a brand-new project from the ground-up. I would also like to thank the other members of my committee, Dr. John Wilson, Dr. Barbara Fingleton, and Dr. Marjan Rafat for their recommendations and support as I continued to develop these projects. From my lab-mates, I would like to thank Sydney Henriques for her assistance with *in vivo* studies and former lab members Dr. Shirin Masjedi and Dr. Stephanie Dudzinski who both played pivotal roles in early biological experiments with the nanoparticle studies. I also want to recognize current members Dr. Charleson Bell, Marsalas Whitaker, Fan Xue, and Sevrina Tekle as well as former members Dr. Andrew Cook and Mary Dockery. I would especially like to recognize the contributions of former lab members Dr. Christopher Haycook and Abigail Manning. Chris started at the same time as me 5.5 years ago and we shared the trials of writing our first (and second and third) grant applications together, navigating graduate classes, earning our Master's degrees, and finally defending our PhDs in the midst of a pandemic. It's been an honor to know Chris and go through this struggle together. I also want to recognize all the work Abby contributed as an undergraduate researcher. Joining our lab as a sophomore, she had no prior lab experience but

spent 2.5 years patiently learning from and helping me as we started a brand-new project together. The cryogel project never would have progressed this far without her help. From the lab of Dr. Craig Duvall, I would like to thank former member Dr. Meredith Jackson for all her training early on, I learned so much about all the polymer chemistry from her. I would also like to recognize Isom Kelly, Dr. Bryan Dollinger, Dr. Sean Bedingfield, Dr. Mukesh Gupta, Dr. Fang Yu, Shrusti Patel, and Carli DeJulius whose friendship and camaraderie have made working in a shared lab space a great experience. I also want to recognize current and former members from the lab of Dr. Fiona Yull: Alyssa Hoover, Whitney Harris, Dominique Parker, and Dr. Andrew Wilson for their assistance and advice. From my cohort, I would especially like to recognize Ethan Joll who was the first friend I made when starting graduate school as we sat together on the first day of TA orientation. We struggled through one of the hardest classes together and although we didn't see much of each other when diving into our research, he has remained a steadfast friend and supporter. And finally, from my first-year TA office, I want to acknowledge the group of friends that have been there for me the whole time: John Mendoza, Sigi Schlunk, Kuniko Hunter, Dr. Chris Haycook, and Dr. Katie Ozgun. From sharing office space our first year to many board game nights (both in-person and virtual), this group helped me keep my sanity.

Most importantly, I want to thank all of my supporters from outside of the lab. First, I want to thank my parents, Dana Glass-Mattie and Rick Glass, for their constant love and support as I oscillated between stubbornly overworking myself and threatening to drop out. They both always knew what to say to lift my spirits and remind me that God's plan would be made clear for me, and they were of course right. I would also like to thank my stepdad, Brad Mattie, and my stepmom, Mona Glass, who also supported me and provided positive words whenever I

needed them. I especially want to thank my brother, Coby Glass, who is also my best friend. It's not often that siblings move farther away from each other physically only to become closer friends, but that's what happened with us. Over the years, from Coby's college graduation to visiting him in Alaska and then moving cross-country in 3 days, we've had many adventures that will be cherished memories forever. I also want to thank my oldest friend Greg Pawel who has supported me from afar as he also navigates the path to a PhD and has helped relieve stress with many nights of gaming. I thank all of my extended family for their support, but most importantly I thank my grandparents Ken and Flo Franz. Flo (Grams) was always my biggest cheerleader through everything I did, and she taught me the value of relentless positivity through everything. I miss you all the time Grams, and I know you're still supporting me from above as I finally finish this journey. And finally, last but absolutely not least, I want to recognize and thank my incredible partner, the other half of the dynamic duo, Kennady Bullock. Kennady and I met through the trials of grad school and have gone through incredibly difficult times together, from lab changes to navigating grad school in a pandemic, yet we've always had each other's back. Her constant support has provided me with so much motivation to keep going, and I can't imagine the last few years without her. You've been my partner in crime through so much and I can't wait to see what's next for us. To everyone else that I've met and connected with during grad school, thank you as well for making this a truly unforgettable experience.

TABLE OF CONTENTS

Page

LIST OF TABLES

Tables **Page**

LIST OF FIGURES

Figures **Page**

Chapter 1

Introduction

1.1 Prevalence of Breast and Ovarian Cancer

Breast cancer is the most diagnosed type of cancer in the United States and just last year became the most diagnosed type of cancer worldwide, passing lung cancer.[1,2] The standard treatment of surgery combined with chemotherapy or radiation has proven effective in removing primary tumors but is often associated with local or distant recurrences. While the overall mortality rate of breast cancer is low compared to other cancer types (90% 5-year survival rate), development of metastases drops the survival rate to 29% and local recurrence increases the mortality rate 2- to 3-fold.[2,3] Additionally, these numbers are worsened when considering triple negative breast cancer (TNBC), which has a higher incidence of relapse and death.[4] In comparison, although ovarian cancer is not as commonly diagnosed, it does represent one of the lowest survival rates in cancer patients with only 49.1% of patients surviving 5 years after diagnosis.[2] This low survival rate is predominantly due to the late stage at which ovarian cancer is diagnosed. For epithelial ovarian cancer (EOC), which accounts for 90% of all ovarian cancer cases, 60% of diagnoses are made at Stage III or IV, which reflects the aggressive nature of this disease.[5] Similar to breast cancer, the primary standard of care remains surgery followed by platinum- or taxane-based chemotherapies. This treatment is effective in over 70% of patients, but only half of these patients still exhibit non-detectable levels of cancer cells 5 months after treatment, and in many of those patients a small number of chemotherapy-resistant cells can remain dormant for months before proliferating exponentially.[6] To address the challenges associated with development of metastases and post-surgery recurrence, anti-tumor immunotherapies provide a hopeful avenue forward.

1.2 Low Response Rates in Current Immunotherapies

Immunotherapies for cancer treatment have seen tremendous progress over the last decade, culminating in the first FDA-approved immunotherapy for TNBC.[7] The rise of immunotherapies, which leverage the patient's own immune system to generate anti-tumor responses, provides new therapeutic approaches to treating primary tumors and metastatic lesions simultaneously while also preventing recurrence. By training the immune system to recognize the cancer cells as diseased cells, the development of a systemic immune response along with immunological memory can address these two overarching challenges associated with most cancer types. The two most common immunotherapies currently in development, immune checkpoint blockades (ICBs) and chimeric antigen receptor (CAR) T cells, both primarily target the tumor-infiltrating lymphocyte (TIL) populations and are becoming increasingly common therapies for treating cancer.[8–10] However, a large fraction of patients remain unresponsive to these treatments, especially in the context of solid tumors.[11–13] In particular, TNBC patients treated with ICB monotherapies of pembrolizumab (anti-PD-1) or atezolizumab (anti-PD-L1) only had overall response rates (ORRs) of 23% and 10%, respectively.[14] Similarly, clinical trials examining the treatment of EOC patients with nivolumab or pembrolizumab resulted in ORRs of 15% and 8%, respectively.[15] One of the primary challenges with effectively treating solid tumors is overcoming the immunosuppressive tumor microenvironment (TME) that hinders T cell infiltration.[16,17] By priming the TME for a pro-inflammatory, anti-tumor immune response, more effective immunotherapies can be developed and even used in combination with current ICBs to raise the efficacy of these treatments. To explore this paradigm, the next wave of immunotherapies should target the most abundant immune cell in most tumors: macrophages.[18–20]

1.3 The Role of Tumor-Associated Macrophages and Potential for Novel Immunotherapies

While adaptive immune cell populations in tumors, such as TILs, can vary significantly from patient to patient, innate immune cells, and particularly tumor-associated macrophages (TAMs), are far more prevalent in most types of cancer, including breast and ovarian.[21,22] Macrophages, in general, exist on a spectrum of phenotypes and exhibit a range of functions. The two extremes of this spectrum are often referred to as "M1" for the classically-activated pro-inflammatory phenotype and "M2" for the alternatively-activated immune regulating phenotype (**Figure 1.1**).[23] TAMs comprise both phenotypes but are primarily M2-like.[24] These TAMs are immunosuppressive and function to promote tumor progression while suppressing anti-tumor immune responses. High levels of TAMs lead to worse prognosis and reduced survival in patients.[22,25,26] Additionally, TAMs establish the immunosuppressive TME that prevents other therapies, like ICBs, from being effective.[27,28] The prominence of TAMs and their role in promoting tumor progression and severity makes them a key target for the development of novel immunotherapies.

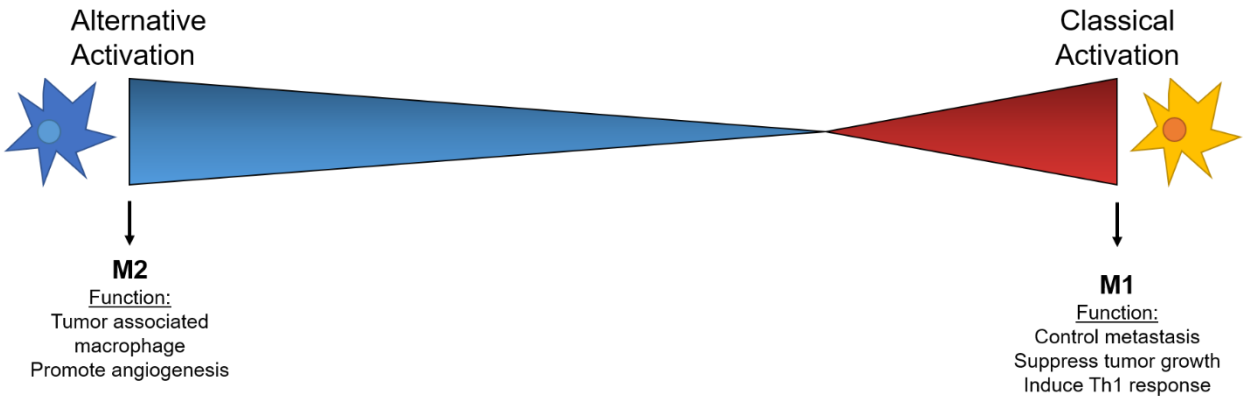

Figure 1.1: Diagram depicting spectrum of macrophage phenotypes with the two extremes (M1 and M2) shown. Figure adapted from ref. 23.

Early TAM-based therapies focused on preventing macrophage recruitment to the tumor.[29,30] Additionally, several groups have examined the effects of ablating tumor-resident macrophages to alleviate their immunosuppressive functions.[31–33] While both of these treatments led to reduction in tumor growth and, in the case of ablating TAMs, suppressed metastasis, a more robust treatment technique involves repolarizing the TAMs towards the M1 phenotype to induce an anti-tumor immune response. Abrogating TAMs functions to halt tumor progression, but also removes a potential key contributor to developing immunological memory to prevent recurrence. In this way, the macrophages can be leveraged to assist in the anti-tumor immune response as well as produce immunological memory. Macrophages are one of the drivers of immune memory development due to their function as antigen-presenting cells (APCs).[34] Along with dendritic cells, macrophages can endocytose foreign or diseased cells, process them to antigens, and then present those antigens to T cells to produce an adaptive immune response. Furthermore, recent work has also demonstrated the ability of macrophages to induce innate immune memory, a function previously thought to be exclusive to the adaptive immune system.[35,36] By reprogramming TAMs to take part in the anti-tumor immune response, more robust, long-term therapies may be developed.

Along with the benefits of developing immunological memory, M1 macrophages directly induce anti-tumor effects. Although previous research identified large TAM populations as being detrimental to patient outcomes, recent work has demonstrated that the ratio of M1/M2-like TAMs is an improved prognosticator of both tumor severity and potential for immunotherapy responsiveness.[37] In fact, evaluation of the M1/M2-like populations of TAMs in both breast and ovarian cancer revealed that patients with high M1/M2 ratios had more favorable tumor immune microenvironments and extended survival.[38,39] Increasing the M1-like TAM population also

increases the prevalence of inflammatory cues in the TME, which can subsequently induce tumor-mediated killing of cancer cells along with recruiting CD8+ T cells into the tumor. Increased inflammation in the TME has been shown to be a crucial factor for improving the therapeutic efficacy of anti-PD-L1 therapies, indicating that priming the TME by repolarizing TAMs also has the potential for use in combination therapies with ICB.[40] Therefore, there is substantial potential for immunotherapies that target and repolarize M2-like TAMs towards the M1 phenotype in the treatment of both breast and ovarian cancer.

1.4 Techniques for Repolarizing TAMs to a Pro-Inflammatory Phenotype

The unique trait of phenotypic plasticity displayed by macrophages is attributed to the various internal signaling pathways that change depending on which cell-signaling molecules (i.e. cytokines) are present. To effectively alter TAM function, therapies can be developed to target these pathways in multiple ways. One of the primary mechanisms driving macrophage phenotype is the nuclear factor-kappaB (NF-κB) pathway. Canonical NF-κB is activated by inflammatory cytokines or pattern recognition receptors (PRRs) and stimulates M1 polarization.[41] The activation of canonical NF-κB is key to pushing macrophages towards an inflammatory phenotype capable of producing inflammatory cytokines and driving a Th1 response.[42] To activate this pathway, two general techniques can be considered: knocking down the inhibitors of the pathway or delivering the signals which activate the pathway.

Inflammation is a controlled response primarily driven by the innate immune system and is the body's primary defense for fighting infections. However, this response must be tightly controlled to limit chronic inflammation, which overrides the homeostatic conditions of healthy tissue and can cause long-term damage and even development of other diseases.[43] Many biological safeguards are in place to prevent chronic inflammation and restore homeostasis, and

for macrophages in particular, the inflammatory response is resolved due to production of inhibitors to inflammatory signaling pathways that are produced in response to inflammatory cues. The NF-κB pathway has five inhibitors that comprise the IκB family with IκBα being the major regulator of canonical NF-κB.[41,44] Previous work by the Yull and Giorgio labs demonstrated that knockdown of IκBα expression results in activation of canonical NF-κB and M1 polarization.[45] To directly target and knockdown IκBα production, RNA interference (RNAi) was implemented.

RNAi is a widely studied technique that is useful for preventing mRNA translation into proteins, as reviewed by Sen and Blau.[46] Specifically, small interfering RNAs (siRNAs) are ideal for RNAi therapies due to their short length (20-25 base pairs) as well as their ability to be tailored for specific mRNA sequences.[47] The primary drawbacks with siRNA-based therapies include the limited ability of small oligonucleotides to cross cell membranes into the cytoplasm where they are functional and their rapid clearance from circulation when freely administered.[48] Furthermore, because widespread inflammation is a concern if the canonical NF-κB is systemically activated, there is a clear need for targeted delivery of siRNA against IκBα specifically to TAMs. For these reasons, a carrier designed to load and deliver siRNA to the cytoplasm of TAMs is crucial.

Alternative to knocking down inhibitors of NF-κB, M1 polarization can also be induced via direct stimulation with inflammatory cytokines. Inflammatory cytokines, such as interferons (IFNs) and tumor necrosis factors (TNFs), promote M1 polarization and lead to more inflammation.[49] However, systemic administration of free cytokines can cause off-target inflammation and widespread toxicity.[50] Similar to siRNA delivery, treatment with inflammatory cues relies on development of a delivery modality to localize treatment to the desired location.

1.5 Injectable Biomaterials for Localized Drug Delivery

To achieve localized macrophage activation and prevent widespread inflammation, targeted/localized therapeutics are needed. Drug delivery is an important area of research in the field of biomedical engineering, with applications in treating a variety of diseases including cancer[51], heart disease[52], autoimmune diseases[53], and others. To induce a specific therapeutic effect, the delivery vehicle can be as important as the therapeutic agent. In the context of cancer therapy, polymeric nanoparticles (NPs) provide a highly tailorable system and have been reviewed extensively for their ability to target and treat a variety of cancers.[54,55] The versatility of polymeric NPs allows for the design of "smart" materials to induce specific functions as well as decoration to create a targeted delivery system. Furthermore, polymeric nanocarriers can be derived from natural polymers such as chitosan, gelatin, alginate, or albumin to allow for lower immunogenicity.[56–58] Conversely, synthetic polymeric NPs allow for higher degrees of modification. For example, the copolymer poly(lactic-co-glycolic acid) (PLGA) is a well-studied, FDA-approved polymer that can be tailored for different rates of biodegradation (as determined by the ratio of lactic acid to glycolic acid) as well as decorated with targeting moieties by including different reactive groups on the end of the PLGA chain such as azides, maleimides, or sulfhydryls.[59] Similarly, poly(ethylene glycol) (PEG) is another commonly used polymer for nanocarrier delivery due to its ability to increase *in vivo* circulation time, reduce immunogenicity, and prevent protein adsorption.[60,61] The primary benefits of using a nanoscale system, especially in regards to macrophage delivery, is that spherical NPs with a diameter in the range of 100-150 nm have been shown to promote clathrin-mediated endocytosis in macrophages and are small enough to take advantage of exiting the bloodstream due to leaky, poorly assembled tumor vasculature associated with tumors.[62–65] However, further functionality in the

polymer design is needed since endocytosis typically leads to degradation of the particles when the late endosome binds with a lysosome to form an endolysosome.[66] Furthermore, siRNA functions in the cytoplasm so designing a polymer that can induce endosomal escape is crucial.

For our applications, we have developed a unique polymer specifically designed with the application of siRNA-loading and endosomal escape in mind. The Giorgio and Duvall labs have extensively studied a diblock copolymer system specifically designed to load small oligonucleotides and deliver them to the cytoplasm of cells.[67,68] Furthermore, prior research in the Giorgio lab has demonstrated the ability to label a triblock copolymer with a small molecule targeting moiety to target macrophages.[69,70] The combination of these systems has the potential for robust targeted siRNA delivery to TAMs.

In contrast to nanocarrier delivery systems, hydrogels are also a popular polymer-based delivery system used in many applications to allow for more localized, sustained release of bioactive cargo. Hydrogels consist of crosslinked polymers that form a hydrophilic scaffold able to absorb large volumes of water.[71] Hydrogels can also be designed for different applications, including creating cationic vs anionic gels to tailor sustained release of cargo and create temperature- or pH-responsive materials.[72] Recently, injectable hydrogels have gained traction to translate drug-loaded scaffolds to internal treatments as opposed to their previous use in surface-level, wound-healing applications. In particular, injectable hydrogels to treat cancer have become popular with scaffolds being loaded with immune checkpoint blockades to sustain anti-PD-1 release[73], proton scavengers to modulate acidity in the TME[74], neoantigens to stimulate an adaptive immune response[75], among others reviewed by Leach, et. al.[76] For macrophage-specific immune modulation, we identified a macroporous, “tough” alginate cryogel first developed by the Mooney lab at Harvard which could be modified for our applications.[77,78] The tough,

injectable cryogels allow for localized delivery of the drug-loaded scaffold which can have several benefits over the systemic administration of nanoparticles.

1.6 Polymeric Nanoparticles for Tailored Targeting

To deliver siRNA therapies to M2-like TAMs, this work has continued the development of prior polymeric NP systems to optimize both the reactive chemistry and the siRNA delivery to TAMs. This polymer system comprises a poly(ethylene glycol) (PEG) corona and a diblock copolymer core, which provides dual functionality to encapsulate siRNA and induce endosomal escape. The diblock core consists of equal numbers of repeating units of dimethylaminoethyl methacrylate (DMAEMA) and butyl methacrylate (BMA) to form PEG-b-(DMAEMA-co-BMA) (PEGDB) (**Figure 1.2**). The tertiary amine present on the DMAEMA block becomes protonated at low pH, forming a net positive charge that electrostatically interacts with the anionic phosphate groups on the oligonucleotide backbone. Once restored to physiologic pH (~7.4), the hydrophobic BMA group drives micellar assembly, forming a nanoscale polymeric complex (polyplex) with siRNA encapsulated in the core. The optimized molecular weight and balance of the number of repeating units for each monomer has been previously reported.[67,68]

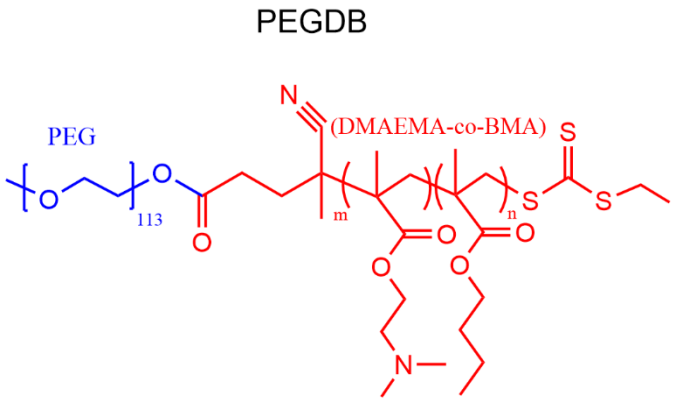

Figure 1.2: Schematic diagram of PEGDB polymer consisting of 5 kDa PEG chain with diblock copolymer core consisting of ~75 repeating units each of DMAEMA and BMA.

The second function of this NP system is the endosomal escape. Once endocytosed, the low pH induced by the endosome re-protonates the amines on the DMAEMA block, causing the

micelle to break apart. The hydrophobic BMA then inserts into and disrupts the endosomal membrane, subsequently releasing the siRNA cargo into the cytoplasm where it can bind the target mRNA. The endosomal escape mechanism of the PEGDB polymer has been previously characterized.[79] The final component of the polymeric NP system is corona decoration for macrophage targeting. Macrophage delivery, specifically M2-like TAMs, can be achieved by targeting the CD206 macrophage mannose receptor, which is upregulated on M2 macrophages and immunosuppressive TAMs.[25] Our lab has previously shown the ability to target unpolarized macrophages *in vitro* using a mannose-decorated triblock copolymer, demonstrating the feasibility of this approach.[69,70] However, the mannose decoration has not yet been translated to the diblock copolymer system, which simplifies the reaction conditions for fabrication and is more reproducibly synthesized than the triblock.

Mannose functionalization was achieved via the copper-catalyzed, azide-alkyne cycloaddition (CuAAC), or "click," reaction. CuAAC chemistry is a highly efficient reaction that occurs in simple reaction conditions (room temperature in water).[80,81] This reaction is achieved by using an azide-labelled PEGDB (AzPEGDB) in conjunction with an alkyne-functionalized mannose (Mn-alkyne) to form mannose-PEGDB (MnPEGDB). By using the efficient CuAAC reaction to functionalize AzPEGDB, this system allows for easy translatability for future applications. To target siRNA delivery to other cell types, the only change needed is to alter the small molecule functionalized with alkynes before "click" conjugation.

While the mannosylated-NP (MnNP) system is designed to function following intravenous (IV) administration, our specific applications involved treating ovarian tumors via intraperitoneal (IP) injections. By treating MnNPs via IP injections, the nanoparticles are localized near the tumor and in the ascites fluid, limiting the potential for off-target delivery

consequences that are common following IV administration of similar materials. Ascites is the fluid build-up in the peritoneal cavity associated with ovarian cancer development. Furthermore, IV delivery is often associated with increased dosing to achieve a therapeutic dose at the target site as well as susceptibility to rapid clearance through the spleen, liver, and kidneys.[82,83] The localized IP injection of MnNPs increases our therapeutic dosing and provides the highest probability for delivering siRNA payloads to TAMs and immunosuppressive macrophages in the ascites.

1.7 Macroporous Cryogels as Localized Repolarization Depots

While NPs allow for systemic delivery to treat diseases, alternative biomaterial approaches can be used for direct localized treatment. Hydrogels can be designed to withstand shear stresses and thus be injected through syringes. When covalently crosslinked at below freezing conditions in a process called cryogelation, "cryogels" maintain the same structure and characteristics of hydrogels with an added benefit of developing macropores (pores with diameters >75 μm) due to ice crystal formation during the gelation process. The alginate cryogels developed by the Mooney lab have the added benefit of undergoing secondary ionic crosslinking after the initial cryogelation, which creates a "tough" scaffold capable of withstanding injection through a syringe.[77] This combination creates a scaffold which can be directly injected to the desired site for treatment of disease.

Alginate is a naturally-occurring polysaccharide and is non-immunogenic, biocompatible, and biodegradable.[84] Furthermore, alginate can be modified to adjust properties such as stiffness, swelling, degradation rate, cell adhesion, and release of biomolecules.[84,85] For our applications, sodium alginate can be methacrylated which allows for subsequent covalent crosslinking at -20°C to form stable gels.[77] To form "tough" gels, the unreacted methacrylate groups can be

ionically crosslinking by adding divalent cations, in this case Ca^{2+}, to further crosslink the gels.[77] The hybrid combination of covalent and ionic crosslinking in hydrogels increases elasticity and stretchability due to the weaker ionic bonds "unzipping" while undergoing shear stresses.[86] The ionic crosslinks can then reform once the stress is removed, while the covalent bonds, which cannot reform after breaking, remain intact.[86] This interaction creates the "tough" cryogel that can be directly injected through a syringe for localized delivery. Here, we examine using this system for localized TAM repolarization via peritumoral injection in mammary tumors.

Another benefit of the cryogel system is the simple loading mechanism to deliver therapies. Biomolecules, especially cytokines and chemokines, can be loaded into the scaffold by mixing with the precursor alginate solution before the cryogelation step.[75,78] In particular, inflammatory cytokines, which can be toxic when delivered systemically, can be loaded into the cryogel and delivered directly to site of disease. When co-loaded with macrophage-specific chemokines, this system acts as a local depot for attracting and repolarizing TAMs. The macroporous structure created by the cryogelation process allows TAMs to infiltrate into the gel and the biodegradability allows for the macrophages to disperse after exposure to the inflammatory cues. To treat breast cancer, we chose the inflammatory cytokines interferon-gamma (IFN-γ) and interleukin-12 (IL-12) and combined them with the chemokine C-C motif ligand 2 (CCL2) which specifically attracts macrophages.[87] This cryogel loaded with IFN-γ, IL-12, and CCL2 (termed ILC) was compared with an empty gel (EG) treatment to evaluate effects on macrophage polarization *in vitro* as well as anti-tumor effects when injected into mice with polyoma (PyMT) mammary tumors.

Specific Aims

The concept of developing cancer immunotherapies using TAMs is not novel in itself, but most TAM-based therapies have focused on preventing macrophage recruitment to the tumor or ablating the TAM population in the TME.[31–33] Other therapies have been developed more recently, and are summarized in a review by Duan and Luo.[88] These therapies predominantly comprise ablation of TAMs, inhibiting recruitment, or preventing tumor-promoting functions such as blocking angiogenesis and immunosuppression.[88] However, a more promising and robust response is hypothesized if the TAMs are repolarized and leveraged as part of the anti-tumor immune response. While some groups have shown positive therapeutic outcomes by repolarizing TAMs for anti-tumor effects, there have been drawbacks with the current methods. Two recent examples involved the use of lipid nanoparticles (LNPs) to deliver siRNA to TAMs in a xenograft human tumor in mouse model and polymeric nanoparticles loaded with mRNA encoding Interferon Regulatory Factor 5 (IRF5) for ovarian cancer treatment in a mouse model.[82,89] Shobaki, et al. demonstrated tumor regression following siRNA delivery to knockdown signal transducer and activator of transcription 3 (STAT3) and hypoxia inducible factor 1 alpha (HIF-1α), but the IV injection led to significant off-target accumulation in the livers and spleens.[89] Zhang, et. al., attempted to limit the off-target delivery by delivering via intraperitoneal (IP) injection to treat ovarian cancer, but there was still significant IRF5 activation in the spleens.[82] Conversely, a recent study by Chen, et al. demonstrated tumor regression after post-operative treatment with a sprayable gel loaded with anti-CD47 antibodies to activate M1-like macrophages.[74] This technique, however, required surgical removal of the tumor to allow direct spray of the gel into the tumor resection site. To address the concerns associated with off-target delivery of nanoparticles and the invasiveness of current hydrogel-

based therapies, we developed two separate biomaterials systems to use in the treatment of ovarian cancer (nanoparticles) and breast cancer (cryogels) which can be locally injected. *These systems informed the overall goals for this dissertation, which are 1) to optimize the reactive chemistry to label diblock copolymer nanoparticles with mannose for targeted macrophage delivery of siRNA, 2) to evaluate the ability of siRNA-loaded MnNPs to alter immune cell composition in tumors and subsequently reduce tumor progression, and 3) to develop an injectable cryogel system to locally repolarize TAMs and induce an anti-tumor immune response. I therefore completed three independent aims to achieve these goals.*

Specific Aim 1: Optimize mannose decoration on polymeric nanoparticles to reduce toxicity and promote macrophage-specific delivery of siRNA payloads.

The experiments performed in this aim will test the hypothesis that *reducing the copper catalyst concentration for CuAAC chemistry can reduce the cell toxicity caused by residual copper while still efficiently labelling the nanoparticles with mannose to achieve macrophage-specific siRNA delivery*. To test this hypothesis, I will fabricate MnPEGDB polymers using a range of copper catalyst concentrations and evaluate mannose conjugation efficiency, residual copper content, and copper-induced cytotoxicity. Once I identify the optimal range of copper catalyst concentrations, I will evaluate macrophage targeting using immortalized human macrophages and primary murine bone marrow-derived macrophages (BMDMs). Finally, I will use the optimized MnPEGDB formulation to deliver IκBα siRNA to M2-polarized BMDMs and assess repolarization to an M1 phenotype.

Specific Aim 2: Translate IκBα-MnNP delivery to *in vivo* models of ovarian cancer to evaluate changes in immune cell composition and tumor development.

The experiment conducted in this aim will test the hypothesis that *mannosylated NPs can provide targeted delivery to TAMs in the ascites and solid tumor and that delivery of IκBα siRNA to the TAMs will drive an inflammatory M1 response to suppress tumor development.* To test this hypothesis, we will develop two separate models of ovarian cancer to evaluate a 3 consecutive-day treatment in late-stage disease (ID8 cells in C57Bl/6 mice) and a 2-3-week biweekly treatment in a more aggressive tumor model (TBR5 cells in FVB mice). In collaboration with the Yull and Rathmell labs, we will evaluate biodistribution of the MnNPs to different organs and different cell types within those organs. Furthermore, we will examine the toxicity potentially associated with repeated dose treatments of MnNPs. Finally, we will demonstrate the effects of IκBα-MnNP treatment on suppressing tumor development and altering the immune cell populations to promote an anti-tumor immune response.

Specific Aim 3: Develop a macroporous, injectable cryogel system capable of locally repolarizing TAMs and driving an anti-tumor immune response.

Experiments in this aim will test the hypothesis that *tough cryogels loaded with inflammatory cytokines and a macrophage-specific chemokine will repolarize TAMs in the tumor microenvironment and drive an anti-tumor response.* To evaluate this hypothesis, I will fabricate the macroporous cryogels and characterize the mechanical and structural properties to demonstrate the desired macroporosity and toughness needed for local injection in tumors. I will evaluate the ability of the loaded gels to drive an M1 macrophage phenotype in several *in vitro* models that recapitulate the TME. Finally, in collaboration with the Kim lab, we will examine the efficacy of direct peritumoral injection of ILC gels in primary mammary tumors (PyMT cells in FVB mice) to promote an inflammatory immune response and reduce tumor severity.

Chapter 2

Optimizing Mannose "Click" Conjugation to Polymeric Nanoparticles for Targeted siRNA Delivery to Human and Murine Macrophages

Adapted from

"Optimizing Mannose "Click" Conjugation to Polymeric Nanoparticles for Targeted siRNA Delivery to Human and Murine Macrophages,"

Published in *ACS Omega* October 2019

by

Evan B. Glass, Shirin Masjedi, Stephanie O. Dudzinski, Andrew J. Wilson, Craig L. Duvall, Fiona E. Yull, and Todd D. Giorgio.

https://doi.org/10.1021/acsomega.9b01465

Graphical Abstract:

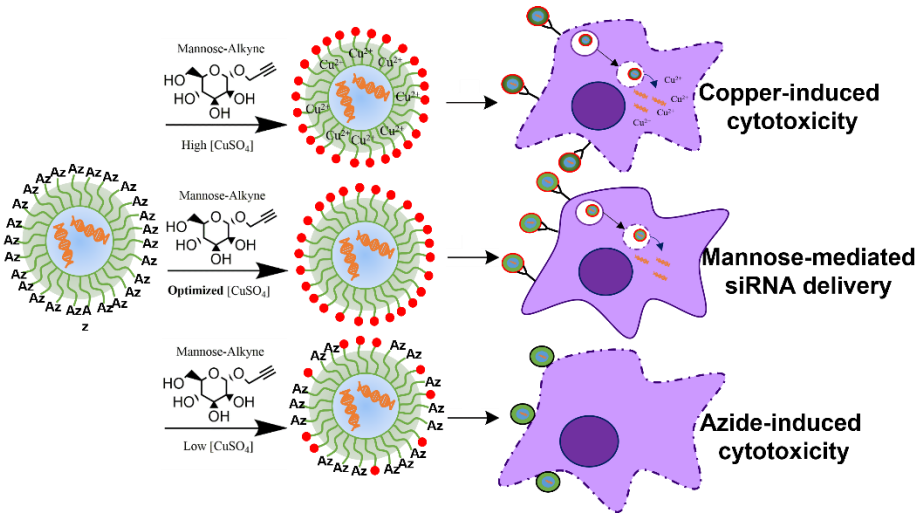

2.1 Abstract

"Smart", dual pH-responsive, and endosomolytic polymeric nanoparticles have demonstrated great potential for localized drug delivery, especially for siRNA delivery to the cytoplasm of cells. However, targeted delivery to a specific cell phenotype requires an additional level of functionality. Copper-catalyzed azide−alkyne cycloaddition (CuAAC) is a highly selective bioconjugation reaction that can be performed in conjunction with other polymerization techniques without adversely affecting reaction kinetics, but there exists some concern for residual copper causing cytotoxicity. To alleviate these concerns, we evaluated conjugation efficiency, residual copper content, and cell viability in relation to copper catalyst concentration. Our results demonstrated an optimal range for minimizing cytotoxicity while maintaining high levels of conjugation efficiency, and these conditions produced polymers with increased targeting to M2-polarized macrophages, as well as successful delivery of therapeutic siRNA that reprogrammed the macrophages to a proinflammatory phenotype.

2.2 Introduction

The development of bioorthogonal chemistry has allowed for transformative progress in using polymer chemistry in living systems. "Click" chemistry encompasses the most specific of these reactions and can be performed in aqueous conditions and in the presence of oxygen.[90] The discovery of copper-catalyzed azide-alkyne cycloaddition (CuAAC) in the early 2000s popularized the field since the addition of copper(I) salt significantly increased the reaction rate of 1,3-dipolar cycloaddition between azides and alkynes.[91,92] Further development of a Cu(II) "pre-catalyst" with a reducing agent, such as sodium ascorbate, enabled the use of solvents composed of water and an alcohol, which is necessary for reagents not soluble in water alone.[91,93] The non-harsh reaction conditions of CuAAC allow for direct *in vivo*

functionalization[90,94–96], and the high selectivity allows for the use of "click" chemistry in conjunction with other polymerization techniques.[97] However, one primary concern with this reaction is the potential for copper-associated toxicity that can result from residual copper catalyst.[98–100] Although copper-free "click" reactions, such as strain-promoted azide-alkyne cycloaddition (SPAAC), are available, the required cyclooctynes are difficult/expensive to synthesize, bulky and hydrophobic, and fail to produce regiospecificity associated with CuAAC.[101–103] Therefore, it is crucial to establish a method that ensures biological compatibility of CuAAC reaction products.

CuAAC is a powerful tool for functionalizing polymeric nanoparticles (PNPs) with a targeting moiety by conjugating each reagent with an azide or alkyne. Additionally, reverse addition-fragmentation chain-transfer (RAFT) polymerization can be combined with "click" chemistry to develop complex, "smart" PNPs that respond to physiological cues such as pH or temperature.[56,97,104–110] pH-responsive polymers can be used to induce endosomal escape and thus preserve the functionality of small interfering RNA (siRNA) for RNA interference (RNAi) therapies. These siRNA-condensing polymeric complexes (polyplexes) can then be decorated with small molecules using CuAAC. Our previous work has shown moderate success using a decorated triblock polymer[45,69], but here we describe "click" conjugation to an improved diblock copolymer. The triblock copolymer contained a 2-propylacrylic acid (PAA) block, but this reagent complicated the overall synthesis procedure, making the polymer less reproducible. For this reason, we developed a diblock copolymer, excluding PAA, which was simpler to fabricate, easier to reproduce, and maintained overall functionality.

The improved diblock copolymer comprises a poly(ethylene glycol) (PEG) corona and a diblock core consisting of dimethylaminoethyl methacrylate (DMAEMA) and butyl methacrylate

(BMA).[67,68,83] The polymer, termed PEGDB, can be fabricated with an azide group on the "outer" end of the PEG chain, which allows for "click" conjugation with an alkyne-functionalized targeting moiety. Here, we chose mannose to deliver RNAi therapies to M2-polarized macrophages, which overexpress the CD206 mannose receptor. Macrophages are the desired target since they are the most prevalent immune cell type in many tumors, and elevated levels of tumor-associated macrophages (TAMs) correlate with poor prognosis and reduced survival.[19–21,111,112] Recent studies have shown the therapeutic potential for targeting and "reprogramming" TAMs to function as M1 inflammatory macrophages, such as delivering siRNA against IκBα, an inhibitor of the classical Nuclear Factor-kappa B (NF-κB) pathway.[45,113–116] By conjugating a mannose-alkyne onto our azide-PEGDB polymer (MnPEGDB) via CuAAC, we develop a system capable of delivering therapeutic siRNA to the desired macrophage phenotype, while retaining the ability to induce endosomal escape. However, the residual copper in CuAAC reaction products and targeting efficacy of MnPEGDB has not been quantitatively characterized, creating uncertainties in the potential for toxicity or off-target effects of this polymer formulation.

When initially developing the diblock copolymer, we observed an unexpected toxicity in the MnPEGDB group compared to a PEGDB control polymer (**Supplemental Figure 2.S1**). The presence of copper ions in the synthesis procedure of MnPEGDB led us to examine residual copper content post-reaction. To this end, we evaluated conjugation efficiency and residual copper content using a range of copper catalyst concentrations. We also evaluated toxicity and uptake in several cell types. Once we determined the optimal reaction conditions, we used that polymer to deliver siRNA to polarized macrophages to quantify changes in gene and protein expression related to macrophage phenotype.

2.3 Materials and Methods

2.3.1 Materials

All materials were purchased from Sigma-Aldrich unless otherwise noted. Inhibitors were removed from dimethylaminoethyl methacrylate (DMAEMA) and butyl methacrylate (BMA) using an activated basic aluminum oxide column.[67,83] All DNA oligonucleotides were purchased from Integrated DNA Technologies (Coralville, IA). dsDNA was designed to be length-matched to the therapeutic IκBα siRNA and functionalized with a cyanine-5 (Cy5) fluorophore on the 5' end of the antisense strand. IκBα siRNA was designed based on previous studies done in our lab.[45]

2.3.2 Polymer Synthesis

Mannose-alkyne was fabricated as previously described.[69] All diblock copolymers were fabricated using 4-cyano-4-(ethylsulfanylthiocarbonyl)-sulfanylpentanoic acid (ECT) as a chain transfer agent (CTA) conjugated to either azide-PEG (AzPEG) or PEG. ECT was synthesized as previously described.[117,118] The AzPEG and PEG macro-CTAs were then RAFT polymerized with DMAEMA and BMA at a 50:50 molar ratio as previously described.[45,67,69] AzPEGDB was then conjugated with mannose-alkyne via CuAAC chemistry to produce MnPEGDB. All polymers were characterized using ^{1}H nuclear magnetic resonance (^{1}H-NMR) spectroscopy (Bruker, 400 MHz), Fourier transform infrared spectroscopy (FTIR, Bruker Tensor 27), and a Copper Assay Kit (Sigma-Aldrich). All NMR spectra are shown in **Supplemental Figures 2.S2-4**. Details for the polymer synthesis appear in **Supplemental Materials & Methods**.

2.3.3 Polyplex Formation

All polymeric complexes (polyplexes) were formed as previously described.[45,67,69,83] Initially, polymers were complexed with Cy5-labelled dsDNA, scrambled siRNA, or IκBα siRNA for 30 minutes in a 10 mM citrate buffer (pH=4). The solution was restored to pH=7.4 by adding a 10 mM phosphate buffer (pH=8) at 5x volume of the pH 4 solution. Polyplex N^+:P^- ratio was determined by mole ratio of protonated amines in DMAEMA polymer (assuming 50% protonation at physiological pH) to the number of phosphates on dsDNA/siRNA.[67,83] All polyplex treatments were performed at a dose of 50 nM dsDNA/siRNA with N^+:P^- 10:1. Particle size and zeta potential were characterized using a Malvern Zetasizer located in the Vanderbilt Institute of Nanoscale Science and Engineering (VINSE) core facility.

2.3.4 Cell Culture

ThP-1: Immortalized human macrophage cells (ThP-1) were chosen to evaluate toxicity in a human equivalent to inform potential future translatability of our polymer system. ThP-1 human monocytes were cultured in Roswell Park Memorial Institute (RPMI) 1640 medium (Thermo Fisher Scientific; 11879-020) supplemented with 10% fetal bovine serum (FBS), 25mM HEPES, 1% penicillin streptomycin (P/S), 1% Minimum Essential Medium (MEM) vitamins, and 4.4 μL β-mercaptoethanol at 37°C in a 5% CO_2 humidified atmosphere. To differentiate monocytes into mature macrophages, ThP-1 cells were plated in the aforementioned media supplemented with 0.1% (v/v) phorbol 12-myristate 13-acetate (PMA) (Thermo Fisher Scientific) and incubated for 4 days to allow for differentiation into mature macrophages.[119,120] These cells were primarily chosen as a human line to use for viability studies, but the expression of a mannose receptor also allows us to examine targeted uptake.[121] Cells were plated in 96-well plates at $1x10^5$ cells/well in 100 μL media. Polyplex or copper salt treatments were added on day 4.

L929: L929 murine fibroblasts were used to produce supplemental media for culturing bone marrow-derived macrophages (BMDMs) taken from mice. L929 cells were cultured in Dulbecco's Modified Eagle's Medium (DMEM) (Corning, Inc., Corning, NY; 15-013-CV) supplemented with 10% FBS, 1% L-glutamine, and 1% P/S. L929 cells were grown to confluency in T-175 flasks and 55 mL fresh media was added. On day 7, the media was collected, labeled L929 Week 1 media, and stored at -20°C. A fresh 55 mL media was added, cultured for an additional 7 days, collected, and labeled L929 Week 2 media before being stored at -20°C.

BMDM: All animal work was approved by the Vanderbilt University Institutional Animal Care and Use Committee. Healthy female FVB mice were sacrificed at 4-8 weeks of age and the femurs and tibias were extracted. The bone marrow was flushed out with DMEM using a 5 mL syringe and collected in DMEM (Corning; 15-018-CV). The cell suspension was centrifuged (Thermo Scientific, Sorvall ST 8 Centrifuge) at 1000xg for 5 minutes. Media was aspirated before resuspending the cell pellet in 2 mL ACK (Ammonium, Chloride, Potassium) Lysing Buffer (K•D Medical, Columbia, MD) and incubating on ice for 2 minutes to lyse red blood cells. The lysis solution was diluted in 20 mL DMEM and again centrifuged at 1000xg for 5 minutes. The media was aspirated and the resulting BMDMs were resuspended in 10 mL BMDM media: DMEM (15-018-CV) with 10% FBS, 1% P/S, 1% L-glutamine, and 14% 1:1 (v/v) L929 week 1 and week 2 media. The cells were counted by mixing 10 µL cell suspension with 10 µL Trypan Blue Stain (Thermo Fisher Scientific) and pipetting 10 µL of the resulting mixture into a cell counter slide (Bio-Rad) and running on an automated cell counter (Bio-Rad, TC20^{TM}). BMDMs were seeded in 12-well plates at $1x10^6$ cells/well in 1 mL media or in 96-well plates at $1x10^5$ cells/well in 100 µL media. To induce M1 and M2 polarization, BMDMs were

incubated with M1- or M2-inducing cytokines.[122] Briefly, all cells were plated on day 0. On day 2, cells were washed with sterile phosphate buffered saline (PBS) and then cultured with fresh media. On day 4, fresh media was added to M0 and M1 BMDMs while M2 macrophages were treated with media supplemented with 0.01 µg/mL IL-4 and 0.02 µg/mL IL-13. On day 7, M0 and M2 macrophages were not changed while M1 BMDMs received media supplemented with 0.1 µg/mL IFN-γ and 0.1 ng/mL LPS. On day 8, cells were treated for the appropriate experiment.

E0771: Murine breast cancer cells were used as a comparison to the BMDMs described previously. E0771 cells were cultured in RPMI 1640 (Thermo Fisher Scientific; 11875-093) supplemented with 10% FBS, 1% P/S, and 25 mM HEPES.

MDA-MB-231: Human breast cancer cells were used as a comparison to human ThP-1 macrophages. MDA-MB-231 cells were cultured in DMEM (Thermo Fisher Scientific; 11960-044) supplemented with 10% FBS, 1% L-glutamine, and 1% P/S.

MCF10a: Human epithelial cells were used as a healthy tissue control for all treatments. MCF10a cells were cultured in Bronchial Epithelial Cell Growth Medium (BEBM) supplemented with a BEBM Bulletkit (Lonza, Morristown, NJ).

2.3.5 Flow Cytometry

BMDMs were polarized, washed with 0.5 mL PBS, and then incubated with 0.5 ml 0.25% Trypsin-EDTA (Thermo Fisher Scientific) for 5 minutes. 1 mL of media was added to each well and cells were repeatedly aspirated with a disposable pipette to dislodge them from the surface and collected in 15 mL conical tubes. Tubes were centrifuged at 1500 rpm for 5 minutes and the supernatant was aspirated. The cell pellet was resuspended in 2 mL of fresh BMDM

media and the cells were counted as previously described. Cells were then placed in a 96-well round bottom weight flask at $1x10^6$ cells/well in 300 µL/well. The plate was spun down at 1500 rpm for 5 minutes and inverted and lightly tapped to remove supernatant without losing cell pellets. An Fc block consisting of 1 µL Fc block (Biolegend, San Diego, CA) and 50 µL of flow cytometry (FACS) staining buffer (PBS with 2% FBS) was added to each well. Plates were stored at 4°C for 10 minutes. A macrophage panel of antibodies consisting of the following was added: CD11b (1:400), F4/80 (1:200), CD86 (1:200), and CD206 (1:200) (Invitrogen, Carlsbad, CA). Each antibody was added in 50 µL of FACs buffer so the total volume when calculating the concentrations was in 100 µL per sample. Plates were stored at 4°C in the dark to allow for staining. Plates were spun down at 1500 rpm for 5 minutes and inverted and tapped to remove supernatant. Each well was resuspended in 200 µL FACS buffer and analyzed by flow cytometry.

2.3.6 Viability Assays

Polyplex Toxicity: Each cell type was cultured in 96-well plates for viability assays. BMDMs and ThP-1s were plated at $1x10^5$ cells/well while all other cells were plated at 25,000 cells/well. BMDMs and ThP-1s followed the plating protocols listed above. The other cell types were plated, incubated overnight to allow cells to adhere, and treated with polyplexes. All cells were treated with 50 nM of Cy5-dsDNA loaded into the various polymer formulations. The cells were incubated for 24 hours before conducting a CellTiter-Glo® Luminescence Assay (Promega, Madison, WI). All luminescent results were normalized to the average of the control well luminescence.

Copper Salt Toxicity: All cell types were plated as performed to assess polyplex toxicity. $CuCl_2$ was dissolved at 1 mg/ml in 10% (v/v) 200-proof ethanol and media (specific for cell type). This solution was then diluted to a range of 50-10000 μg/dL and 100 μL was added to each well. All cells were incubated for 24 hours before running the CellTiter-Glo® Luminescence Assay.

2.3.7 Polyplex Uptake

Cells were plated in 96-well plates and treated with 50 nM of Cy5-dsDNA-loaded polyplexes. The cells were incubated with the polyplexes for 2 hours and then washed 3x with 100 μL PBS. A final volume of 100 μL PBS was added and the fluorescence intensity was measured (Tecan Infinite M1000 Pro). All fluorescence results were normalized to the fluorescence of the PEGDB control polyplexes to determine mannose-associated uptake. To examine CD206-specific uptake of mannosylated polyplexes, we also performed a receptor-blocking experiment where polyplexes were added to media containing 100 mg/mL molecular grade D-mannose, as done previously.[69] The free mannose binds CD206 and prevents receptor-mediated uptake of fluorescent polyplexes. To evaluate decrease in uptake, the optimized copper catalyst concentration (0.25-0.75 mM) groups were averaged together since they demonstrated similar azide reduction.

2.3.8 Quantitative Reverse Transcriptase Polymerase Chain Reaction (RT-PCR)

BMDMs were plated in 12-well plates as described previously. After polarization to M1 and M2, the MnPEGDB fabricated with 0.75 mM copper catalyst was used to form polyplexes with either scrambled siRNA or IκBα siRNA. BMDMs were treated for 24 hours before mRNA was isolated from the cultured cells using RNeasy Mini kit (Qiagen, Valencia, CA). Residual

DNA was removed using RNase-Free DNase set (Qiagen). cDNA synthesis was performed using SuperScript IV reverse transcriptase kit (Invitrogen). The RT-PCR reaction was performed using a SYBR Green PCR super mix (Bio-Rad) and CFX Real time PCR instrument and software (Bio-Rad). Normalized levels of mRNA expression were calculated using the ΔΔCt method with GAPDH as an internal control. Each mRNA was normalized to an untreated control group of the corresponding polarization (M1 vs M2). All primer sequences used are summarized in the **Supplemental Table 2.S1**.

2.3.9 Luciferase Assays

Luciferase activity was measured in immortalized bone marrow-derived macrophages derived from transgenic mice which carry an NF-κB-dependent GFP/luciferase reporter (BMDM-NGL) on the FVB strain background. BMDM-NGL cells were polarized towards M2 by IL-4 treatment for 24 hours, followed by a further 24-hour treatment with PBS (control), IFN-γ and LPS (M1 polarized control), or mannosylated polyplexes loaded with either scrambled siRNA or IκBα-targeting siRNA. Cells were harvested in reporter lysis buffer and luminescence measured by the Promega Luciferase Assay system (Cat#4030) using a GloMax Luminometer (Promega, Madison, WI). Results were expressed as relative light units (RLU) normalized for protein content, as measured by the Bradford assay (Bio-Rad, Cat# 500-0002).

2.3.10 Western Blotting

BMDM-NGL cells were polarized towards M2 by IL-4 treatment for 24 hours, followed by a further 24-hour treatment with PBS (control), IFN-γ and LPS (M1 polarized control), or mannosylated polyplexes loaded with either scrambled siRNA or IκBα-targeting siRNA. Whole cell protein isolation, western blotting, and signal detection were performed as described (PMID:

26215403). Primary antibodies used were mouse monoclonal anti-IκBα (Cell Signaling Technology; Cat# 4814; 1:1000 dilution), rabbit polyclonal anti-arginase-1 (Gene Tex; Cat# GTX109242; 1:200 dilution) and mouse monoclonal anti-β-actin (Sigma Chemical Co., Cat# A5441 1:10000 dilution) as loading control.

2.3.11 Statistical Analysis

All data presented as mean ± standard error of the mean (SEM) except RT-PCR which is shown as mean ± upper/lower limit. For all FTIR, copper assay, and ThP-1 polyplex toxicity studies, a one-way ANOVA with Tukey's post-hoc test was used to compare all groups to all other groups. For copper salt viability assays, a two-way ANOVA with Dunnett's post-hoc test was used to compare all concentrations to the control within each cell type. For the BMDM polyplex toxicity studies and all polyplex uptake studies, a two-way ANOVA with Tukey's post-hoc test was used to compare all groups to all other groups. For all RT-PCR results, ΔΔCt values were compared using a one-ANOVA with Tukey's post-hoc test. Luciferase assay and western blotting signal detection were analyzed using a student's t-test. To establish statistical significance, we used the following: *$p<0.05$, **$p<0.01$, ***$p<0.001$, ****$p<0.0001$.

2.4 Results and Discussion

In this study, we directly examined the effects of altering the copper catalyst concentration for CuAAC reactions on both conjugation efficiency and residual copper content. Although CuAAC chemistry has been used previously to functionalize/decorate materials used in living systems[5–7], our polymers, functionalized using a 1 mM copper catalyst concentration, exhibited evident toxicity in contact with immortalized human macrophages (**Supplemental Figure 2.S1**); this toxicity was not observed in similar mannose-functionalized polymer

formulations used previously by our lab.[45,69] Additionally, we have previously used undecorated PEGDB polymers to deliver siRNA with limited toxic effects observed both *in vitro* and *in vivo*[67,83,123], so we hypothesized the resulting toxicity to stem from residual copper in this iteration of our polymer system. To our knowledge, no studies have been performed that directly quantify and compare CuAAC conjugation efficiency and residual copper content as a function of copper catalyst concentration. Moreover, the targeting specificity to M2 polarized macrophages for the resulting polyplexes has not been described in relation to mannose-decoration and residual copper. Here, we show that an optimal range for copper catalyst concentration can be achieved that improves M2 macrophage-specific targeting while also reducing copper-associated toxicity.

2.4.1 Synthesis and Characterization of Mannose-Functionalized Diblock Copolymers

The reaction scheme for functionalizing azide-PEGDB (AzPEGDB) with mannose-alkyne is shown in **Scheme 2.1**. To quantify conjugation of mannose onto the AzPEGDB polymers at each catalyst concentration, Fourier transform infrared (FTIR) spectroscopy was used to examine the change in height of the azide peak at 2100 cm^{-1}. By comparing peak height in the MnPEGDB polymers to that of the precursor AzPEGDB, we estimated conjugation efficiency as a function of copper catalyst concentration (**Figure 2.1A**). The lowest copper catalyst concentration (0.1 mM) resulted in an azide peak height which was not different than the

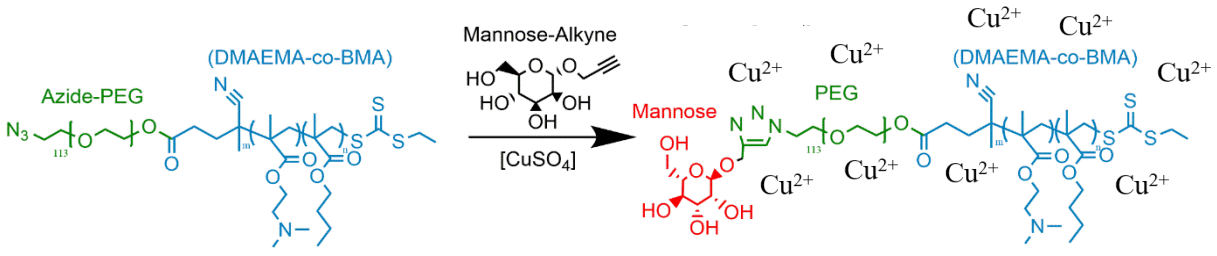

Scheme 2.1: Copper catalyst concentration controls the level of residual copper in the final polymer, even after optimal copper ion chelation with a Chelex resin.

height of the unreacted AzPEGDB. All other copper catalyst concentrations (0.25 mM and above) resulted in a significantly decreased peak height at 2100 cm^{-1}, suggesting conversion of the azide to a 1,2,3-triazole bond (**Figure 2.1B**).[124,125] The average reduction in azide peak for the higher catalyst concentrations (excluding 0.1 mM) was 64%, which is in the range of normal conjugation efficiency values for "click" reactions involving large molecules/polymers that cause steric hindrance.[126,127] This significant decrease in peak height suggests successful "click" conjugation of mannose onto the polymers when using a catalyst concentration of 0.25 mM and

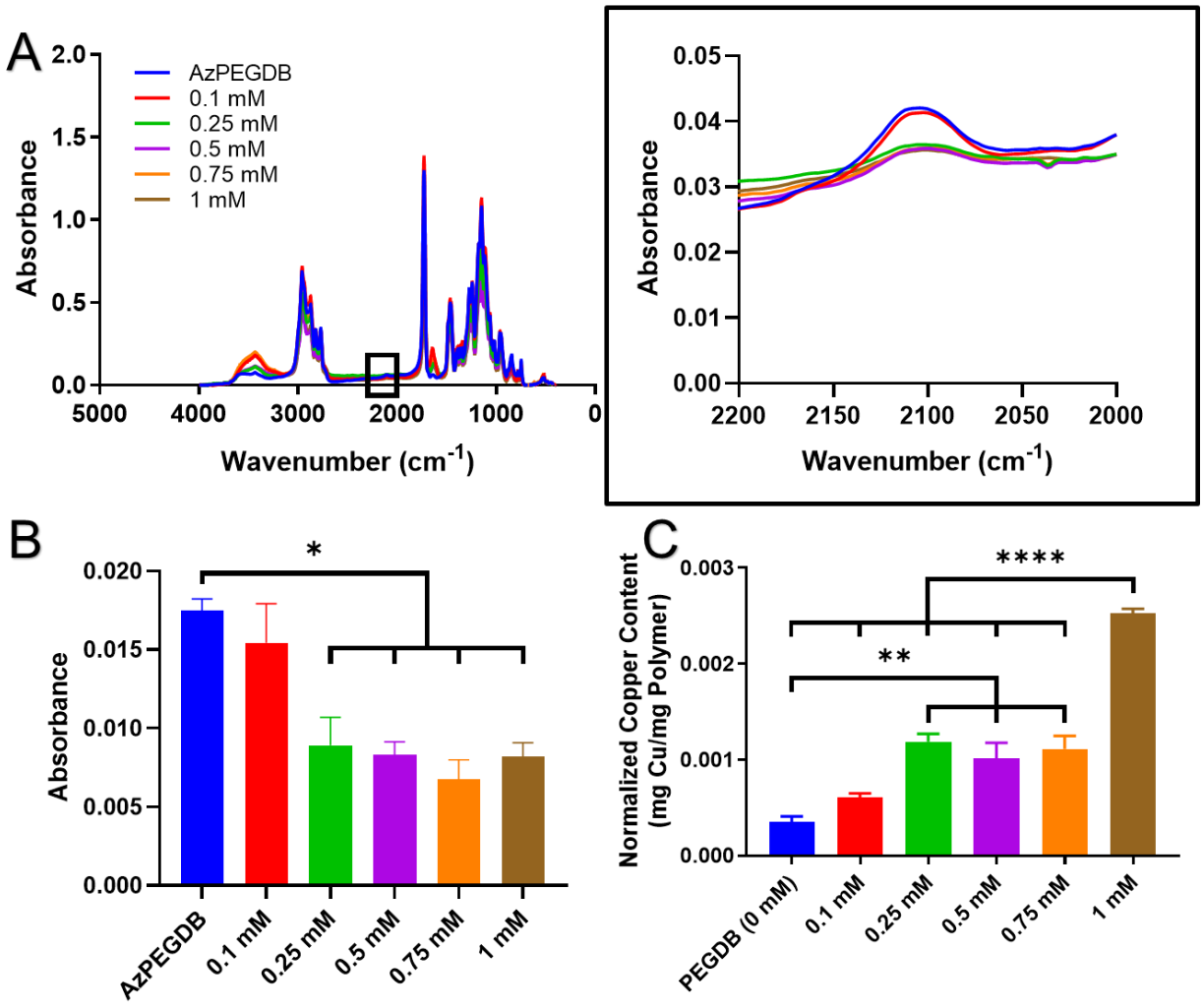

Figure 2.1: Characterization of CuAAC reaction products. (**A**) FTIR spectra of polymers, including detailed view of azide peaks. (**B**) Quantified height of the azide peaks confirms the CuAAC reaction depends on copper catalyst concentration. (**C**) Residual copper content, normalized to amount of polymer, reveals that altering the copper catalyst concentration does affect the amount of copper ions associated with the final polymer.

above. There was no significant improvement for conjugation efficiency when using catalyst concentrations above 0.25 mM, which is a four-fold reduction relative to commonly reported CuAAC catalyst concentration for polymer conjugation.[69,70]

After fabrication of the MnPEGDB and removal of residual copper using a Chelex resin following previously published methods[69,128], the polymers were dissolved in ethanol and molecular grade water. Residual copper was measured using a colorimetric assay that detects Cu^{2+} ions, and the assay results (copper ions in μg/dL) were normalized to provide mg of copper per mg of polymer. Residual copper in the final polymer product was significantly reduced for all catalyst concentrations below 1 mM (**Figure 2.1C**). Residual copper concentration for the lowest tested catalyst concentration (0.1 mM) was not significantly different from the PEGDB control polymer, which was not exposed to the CuAAC reaction conditions. Residual copper in the polymers produced using the three middle catalyst concentrations (0.25, 0.5, and 0.75 mM) were not significantly different from each other.

Other groups have previously reported the use of copper ligands as an alternative technique for employing CuAAC reactions to minimize the amount of residual copper.[129,130] However, this method is primarily employed for "click" conjugation performed in biological systems, such as directly functionalizing cell membranes, since post-reaction treatment is not feasible. For our applications, we can treat the resulting polymers with a chelating reagent that functions similar to the ligands by binding and removing excess copper ions. To minimize complexity of polymer fabrication, we chose to use a copper salt catalyst that could be removed post-treatment. This technique revealed that copper catalyst concentrations of 0.25, 0.5, and 0.75 mM supported robust "click" conjugation and resulted in significantly reduced residual copper

concentrations, suggesting that these were the optimal candidates for synthesis of MnPEGDB intended for future use in living systems.

2.4.2 Formation of Mannosylated Polyplexes

To assess the toxicity and delivery of the mannosylated carriers, we complexed the polymers with oligonucleotides to form polyplexes (**Scheme 2.2**). The MnPEGDB polymers, as well as a non-mannosylated PEGDB control polymer, were dissolved in a pH 4 buffer to protonate the amine groups on the DMAEMA monomers. Then, either Cy5-functionalized dsDNA (Cy5-dsDNA) or siRNA was added to the polymer solution and allowed to complex for 30 minutes. The solution was restored to physiological pH by adding 5x volume of a pH 8 buffer. Polyplex diameter (z-average) and surface charge were examined to ensure all polymer formulations were similar. The average diameter was approximately 150 nm with no differences among polymer groups (**Figure 2.2A-B**). The polymer synthesis conditions were selected to produce micelle diameters of approximately 150 nm for eventual efficiency in tumor accumulation after intravenous injection *in vivo*.[64,65,131] The polydispersity index for each polymer was less than 0.3 (**Supplemental Table 2.S2**), which is below the generally accepted value for drug delivery applications.[132] Zeta potentials for all polymers were not statistically different ($p>0.05$) and were near neutral, which is appropriate for intravascular administration

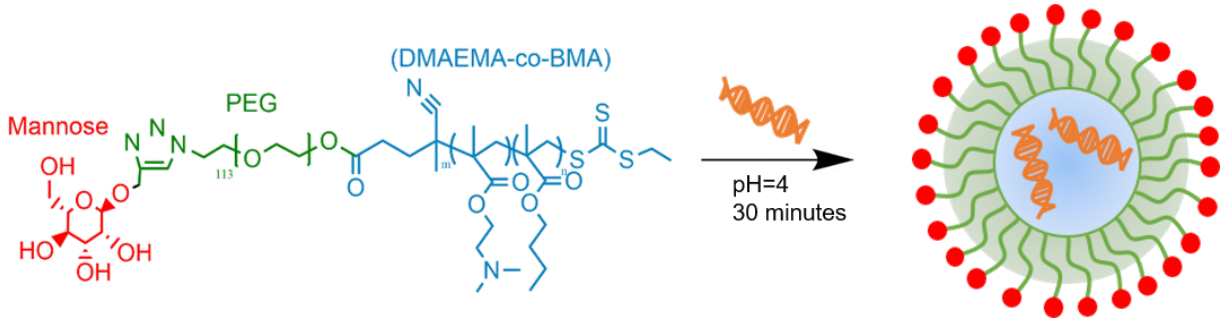

Scheme 2.2: MnPEGDB is complexed with small oligonucleotides (dsDNA or siRNA) for 30 minutes in a pH 4 buffer. The protonated amine group on the DMAEMA electrostatically interacts with the negative phosphates on the oligonucleotide, spontaneously forming a stable micelle with mannose presented on the corona of the polyplex.

(**Figure 2.2C-D**).[133] Overall, the size and surface charge characteristics of the polyplexes were appropriate for delivery to the tumor microenvironment after intravascular injection.

2.4.3 *In Vitro* Polyplex Toxicity Examination

The toxicity associated with residual copper in polyplexes was examined in multiple cell types. All cells were treated with a polyplex concentration corresponding to a 50 nM dose of siRNA, as done previously.[45,67,69] Cells were incubated with polyplexes for 24 hours before evaluating viability with a luminescent ATP-reporting assay. ThP-1 immortalized human macrophages demonstrated a significant decrease in viability when treated with polymers prepared with 0.1 mM or 1 mM copper catalyst compared to untreated controls (**Figure 2.3A**). The polymer fabricated with 1 mM catalyst had the highest amount of residual copper (**Figure 2.1C**), which is presumed to lead to the observed toxicity. Notably, the 0.1 mM catalyst group, which had the least amount of residual copper, also produced significant toxicity. The FTIR results (**Figure 2.1B**), however, suggest that this polymer had the largest residual azide peak, indicating the least amount of mannose conjugation and, presumably, the largest number of residual azides on the polymer. Azides are also known to be cytotoxic and we interpret the toxicity of the 0.1 mM polymer to be due to unreacted azides on the AzPEGDB.[134] This interesting observation of azide toxicity has been neglected in previous considerations of cytotoxicity from CuAAC reaction products, which have focused exclusively on the role of residual copper. Clearly, the optimal copper catalyst concentration is a balance between excess residual copper and relatively few unreacted azides and low residual copper but a greater concentration of remaining cytotoxic azides. Therefore, the optimal catalyst concentration range to limit cell toxicity in human macrophages for our polyplexes is between 0.25 and 0.75 mM, which corroborates the results of "click" conjugation and copper content.

To explore the impact of polyplexes on the viability of primary macrophages with varying levels of CD206 expression, bone marrow-derived macrophages (BMDMs) were cultured with cytokines to polarize them to either an M1 ($CD206_{low}$) or M2 ($CD206_{high}$) phenotype. Interferon-γ (IFN-γ) and lipopolysaccharide (LPS) were added to polarize BMDMs toward M1 and interleukin- (IL-) 4 and IL-13 were used to induce M2 polarization.[122] An additional group of unpolarized BMDMs (M0) were cultured in media with no cytokine treatment. BMDM skewing was characterized via flow cytometry by examining the expression of CD11b and F4/80 (general macrophage markers), CD86 (M1 marker), and CD206 (M2

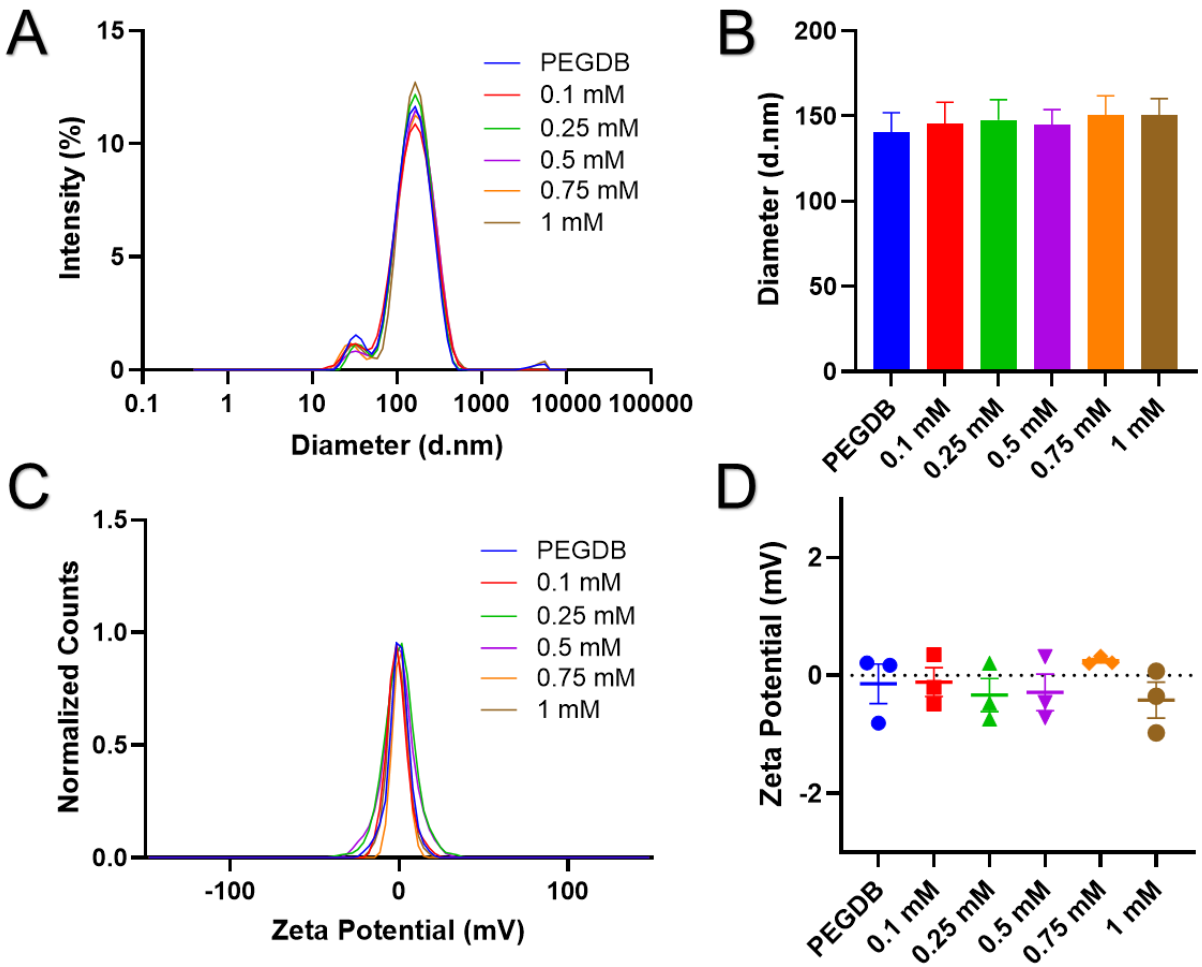

Figure 2.2: Polyplexes were suspended in DI water and Z-average diameter (**A**) distribution and (**B**) averages were measured with dynamic light scattering. Additionally, surface charge (**C**) distribution and (**D**) averages were measured by zeta potential measurement.

marker) (**Supplemental Figure 2.S5**). Following cytokine treatment, we observed significantly higher levels of CD86 expression in M1 macrophages compared to both M0 and M2 phenotypes. M2-polarized BMDMs had significantly higher expression of CD206 compared to both M1 and M0, and the M1 macrophages had a decreased level, though not statistically different, compared to unpolarized BMDMs. These results are consistent with the establishment of a $CD206_{low}$ population of M1s and a $CD206_{high}$ population of M2s. All three groups of BMDMs were treated with polyplexes as performed with ThP-1 cells. Unpolarized (M0) and $CD206_{high}$ (M2) BMDMs demonstrated no significant changes in viability with all treatments remaining above 90% viable compared to an untreated control (**Figure 2.3B**). Interestingly, viability of $CD206_{low}$ M1 macrophages, but not M0 or M2 macrophages, was significantly reduced following exposure to polyplexes prepared with 0.25-1 mM copper catalyst concentration (**Figure 2.3B**). This broad-ranging effect suggests a mechanism independent of the residual copper content. Classically activated macrophages initially respond to infection by producing inflammatory cytokines, chemokines, and reactive oxygen species (ROS) but resolution of the inflammatory reaction has been reported to involve mitochondrial-dependent macrophage cell death.[135,136] Therefore, we hypothesize that the loss of viability observed in the M1-polarized macrophages is induced by

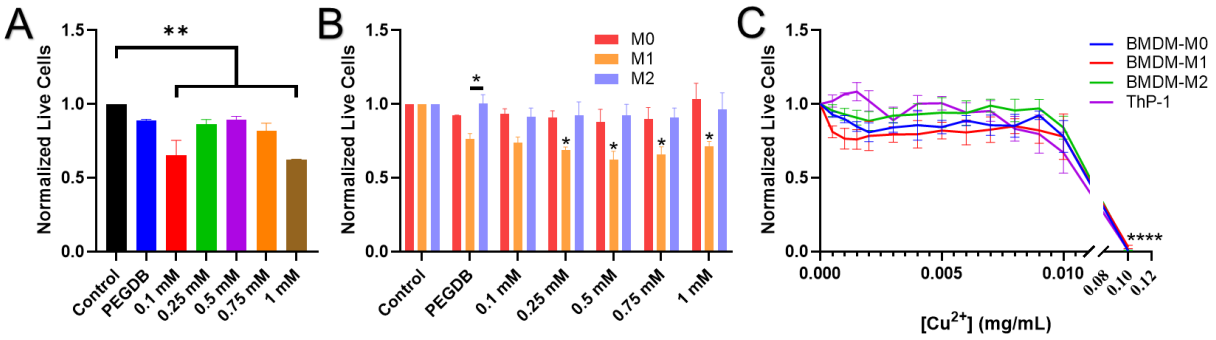

Figure 2.3: Macrophage viability assessed with polyplex treatment and Cu^{2+} treatment. (**A**) Viability of ThP-1 human macrophages was significantly decreased when treated with polyplexes fabricated with 0.1 and 1 mM copper catalyst. (**B**) M0 and M2 BMDMs displayed no toxicity in any treatment groups, but all M1 BMDMs had slight toxicity. (**C**) All macrophages displayed a trend of decreasing viability as concentration of copper salt treatment increased.

their additional activation in response to particle endocytosis. The lack of toxicity in M2 macrophages is encouraging for our applications. It is also important to note that although the same copper-associated toxicity found in ThP-1 macrophages was not observed in BMDMs, there is still concern for the toxic effects of copper in human macrophages for potential future applications. Additionally, we show that the polymer alone (PEGDB control) does not induce a significant change in macrophage viability. This diblock copolymer has been previously shown to be non-toxic to cells and we confirm those results here.[68,83,123]

All viability studies were repeated in human and murine TNBC cell lines and a non-tumorigenic human mammary epithelial cell line. MDA-MB-231 cells were chosen since they are well-established models with well-characterized properties and display a basal-like triple-negative phenotype.[137] E0771 cells were chosen as the murine equivalent since they are also basal-like triple-negative breast cancer cells, but are less aggressive than the often-used 4T1 model and therefore a better model for our applications.[138] MCF10a cells provide a non-tumorigenic, mammary epithelial control, but a murine analog could not be identified among many commercial sources, so only human mammary cells were included in this study. Treatment with polyplexes for 24 hours generated minimal toxicity in both TNBC cell lines. MDA-MB-231 cells treated with the 0.25, 0.5, and 0.75 mM copper catalyzed polymers maintained viability of over 90% but were still statistically decreased compared to the untreated control (**Supplemental Figure 2.S6A**). The E0771 cells exhibited a significant decrease in viability in all polyplex treatments, but none of the treated groups were different from each other (**Supplemental Figure 2.S6B**). Similarly, the MCF10a human mammary epithelial cells had baseline toxicity from the polyplex treatments compared to the untreated control (**Supplemental Figure 2.S6C**). Interestingly, when compared to the PEGDB control polymer, MCF10a cells only had

significantly decreased viability when treated with polymers made with 0.1 and 1 mM copper catalyst. These results are consistent with the ThP-1 human macrophages as these groups are presumed to have the highest number of azides (0.1 mM) and highest residual copper content (1 mM). In both E0771 and MCF10a cells, there does appear to be a slight decrease in viability in all polymer groups, indicating a potential cytotoxic effect from just the polymer system. The lack of toxicity in macrophages is encouraging for our applications, but we will take the off-target toxicity into consideration as we continue forward with our experiments. Overall, the range of 0.25 mM to 0.75 mM copper catalyst appears optimal for fabricating polyplexes that have minimal toxicity to both macrophages and mammary cells.

2.4.4 Effects of Copper Salt on Cell Viability

To assess the contributions of copper(II) alone to cell viability, each cell type was treated with a range of known $CuCl_2$ concentrations. In general, copper is known to be toxic to cells, but only above a threshold concentration.[99,139] This study allowed us to characterize the lower limits of copper cytotoxicity and inform the selection of CuAAC reaction conditions to enable use of the "click" reactions for biological applications. In human immortalized macrophages as well as primary BMDMs, we observed a trend of decreasing viability as Cu^{2+} concentration increased, but there was no significant change in viability up to 0.009 mg/mL, and only the ThP-1 cells had a significant decrease in viability at 0.01 mg/mL (**Figure 2.3C**). These findings are important for our applications since the highest amount of residual copper associated with the 1 mM MnPEGDB was approximately six-fold lower at 0.0015 mg/mL, as determined with the copper assay. Although these results indicate our CuAAC products are well below the cutoff for copper-induced cytotoxicity, our polymer system in particular appears to cause cell death at an elevated level when the residual copper concentration is above 0.0006 mg/mL. This relationship between

residual copper content and cell viability demonstrates that functionalization via CuAAC can produce biocompatible biomaterials by altering the amount of copper catalyst used.

Copper salt toxicity was also examined in TNBC and epithelial cell lines. MDA-MB-231 human TNBC cells and MCF10a human epithelial cells showed no significant change in viability at any Cu^{2+} concentration, although both did exhibit a trend in decreasing viability with increasing copper concentration. E0771 murine TNBC cells produced a trend of decreasing viability, though not statistically significant until the maximum dose (**Supplemental Figure 2.S6D**). Notably, the human cell lines (MDA-MB-231 and MCF10a) were not as susceptible to copper-associated toxicity at 0.1 mg/mL compared to all other examined cells. This result indicates that the concern for copper-associated toxicity in the human breast TME is minimal, providing support for the use of CuAAC in potential human therapeutics. Based on these results, the residual Cu^{2+} alone is not a predictor of cytotoxicity. Rather, the context of polymer, cargo, cell type, and the interaction with residual copper and azide control overall cytotoxicity.

2.4.5 Targeting Efficacy of Mannose-Functionalized Micelles

To evaluate the ability of mannose conjugation to increase uptake in $CD206_{high}$ cells, polyplexes were fabricated with Cy5-dsDNA and treated with cells at an optimized timepoint of two hours. Cell-associated fluorescence intensity was measured as an index of polyplex uptake and results were normalized to the PEGDB control polymer to demonstrate mannose-specific uptake of the decorated polyplexes. In ThP-1 human macrophages, the MnPEGDB produced with 0.75 mM copper catalyst significantly increased uptake efficiency compared to all other polymer groups (**Figure 2.4A**). The polymers catalyzed with 0.25 and 0.5 mM copper show slight, but non-significant, increases in uptake. Unchanged uptake in the 0.1 and 1 mM groups is presumed to be due to increased toxicity associated with those polymers. Our measure of

cytotoxicity was an ATP reporter, and since endocytosis is an ATP-dependent process, early disruption in ATP production may significantly suppress subsequent endocytosis of polyplexes. Polarized BMDMs were then used to examine the effects of CD206 expression on polyplex uptake. There was no significant difference in uptake regardless of mannose decoration for M0 or M1 BMDMs. In the M2-polarized macrophages, however, the polymer produced with 0.75 mM copper catalyst led to significantly increased uptake compared to the 0.1 and 1 mM groups, but not the 0.25 and 0.5 mM catalyst groups (**Figure 2.4B**). These results are consistent with our observations in human macrophages (**Figure 2.4A**) as well as the FTIR mannose conjugation results (**Figure 2.1B**), which indicated that CuAAC efficiency was not changed when increasing beyond a 0.25 mM copper catalyst concentration. Even more importantly, the 0.75 mM group was the only micelle treatment that produced significantly increased uptake in $CD206_{high}$ macrophages compared to both M0 and $CD206_{low}$, M1 macrophages. To verify uptake was due to CD206-specific uptake, we repeated uptake experiment in M2-polarized BMDMs using the optimized polymer groups (0.25-0.75 mM) and co-treated with free mannose sugar to block the CD206 receptor. By averaging across the three optimized groups, we determined mannosylated polyplex binding was decreased by almost 60% (**Supplemental Figure 2.S7**). These results indicate that polyplex uptake is CD206-dependent. Based on these results from both human and murine macrophages, using a copper catalyst concentration of 0.75 mM for the CuAAC led to significantly increased macrophage uptake and was shown to increase uptake in $CD206_{high}$ macrophages.

When examining uptake in mammary epithelial cells, both human cells lines (MDA-MB-231 and MCF10a) revealed no preferential uptake among the polymer groups (**Supplemental Figure 2.S8**). The E0771 murine TNBC cells demonstrated a significant increase in uptake for

the 0.75 mM group compared to the 1 mM group, but this change was not statistically different compared to all other polymer groups. Overall, our results indicate an optimal concentration of 0.75 mM copper catalyst for minimizing copper-induced toxicity as well as promoting mannose-associated targeting to CD206-expressing macrophages.

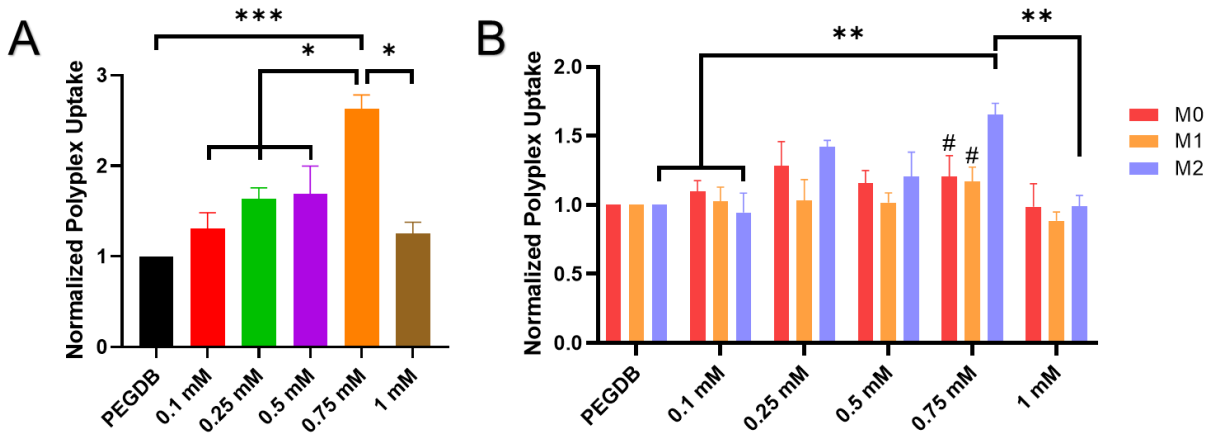

Figure 2.4: Polyplex uptake evaluated in human and murine macrophages. (**A**) ThP-1 human macrophages displayed preferential uptake of polyplexes formed with the 0.75 mM copper catalyst. (**B**) 0.75 mM catalyzed polymer targeted $CD206_{high}$ BMDMs over $CD206_{low}$ as well as unpolarized macrophages (#$p<0.05$), indicating mannose specificity. The 0.75 mM group also outperformed the PEGDB control, 0.1 mM, and 1 mM groups in just M2-polarized BMDMs (**$p<0.01$).

2.4.6 Evaluation of siRNA-Induced Macrophage Repolarization

We used the optimal MnPEGDB polymer prepared with 0.75 mM copper catalyst concentration to treat M1- and M2-polarized BMDMs with either scrambled or IκBα siRNA. We treated the macrophages with siRNA-loaded polyplexes for 24 hours before collecting the cells and isolating RNAs for use in RT-PCR. To examine a shift in phenotype, we examined mRNA expression of 6 genes: three M1 genes (CD86, TNF-α, iNOS), one M2 gene (CD206), and one general macrophage marker (F4/80).[45,140,141] The final mRNA we evaluated was IκBα, which we used to assess the ability of our siRNA sequence to knockdown the target gene. Relative gene expression was normalized to an untreated control group of the corresponding polarization.

Treatment with IκBα siRNA resulted in a significant increase in CD86 and TNF-α compared to untreated control and scrambled siRNA treatments in both M1 and M2 BMDMs, and we observed a significant increase in iNOS expression, but only in the M2-polarized macrophages (**Figure 2.5A-C**). Furthermore, CD206 significantly decreased after IκBα siRNA treatment compared to the untreated control in both phenotypes, but, interestingly, there was no significant change in CD206 expression between the scrambled siRNA control and the IκBα siRNA in M2 BMDMs. Most importantly, treatment with the therapeutic siRNA significantly decreased IκBα expression in both phenotypes, which is necessary for activating the classical

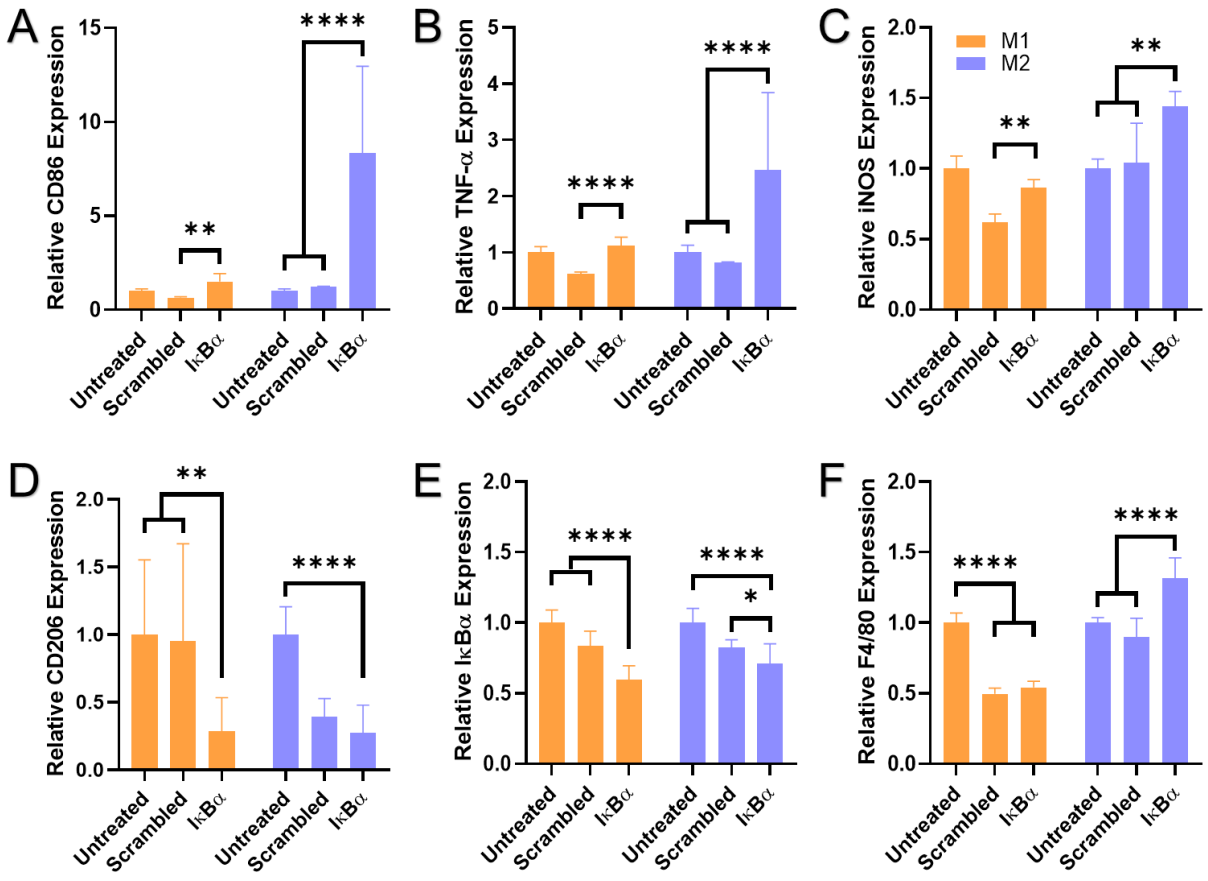

Figure 2.5: RT-PCR was used to examine relative mRNA expression after treatment with scrambled or IκBα siRNA. Expression was normalized to an untreated control group of the corresponding polarization (M1 vs M2). To assess a change in macrophage phenotype, we examined expression of the following: (**A**) CD86, a surface marker for inflammatory immune cells, (**B**) TNF-α, a pro-inflammatory cytokine, (**C**) iNOS, an IFN-γ induced isoform of nitric oxide synthase, (**D**) CD206, the macrophage mannose receptor overexpressed on M2 macrophages, (**E**) IκBα, an inhibitor of the classical NF-κB pathway, and (**F**) F4/80, a general macrophage marker.

pathway of NF-κB (**Figure 2.5D-E**). Taken together, these results indicate that not only is the IκBα siRNA pushing M2 macrophages toward an M1 phenotype, but the treatment does not significantly impact overall M1 macrophage gene expression. Finally, the expression of F4/80, which is known to be associated with macrophage activation[142,143], increases in M2 BMDMs treated with IκBα siRNA (**Figure 2.5F**). This result indicates that not only are the alternatively activated macrophages being skewed towards an M1 phenotype, they are also in a more activated state. The delivery of IκBα siRNA with our optimized polyplex system successfully skews M2 macrophages back to a classical phenotype, which is necessary for eventual application in inducing an inflammatory macrophage response in tumors.

To confirm macrophage repolarization after delivery of IκBα siRNA, we also evaluated protein expression. BMDMs expressing an NF-κB-dependent green fluorescent protein (GFP)/luciferase reporter (BMDM-NGL) were polarized to an M2 phenotype and then treated with either PBS (negative control), M1 cytokines (IFN-γ and LPS, positive control), mannosylated polyplexes loaded with scrambled or IκBα siRNA. After 24 hours of treatment, the cells were harvested in a reporter lysis buffer which allowed direct quantification of

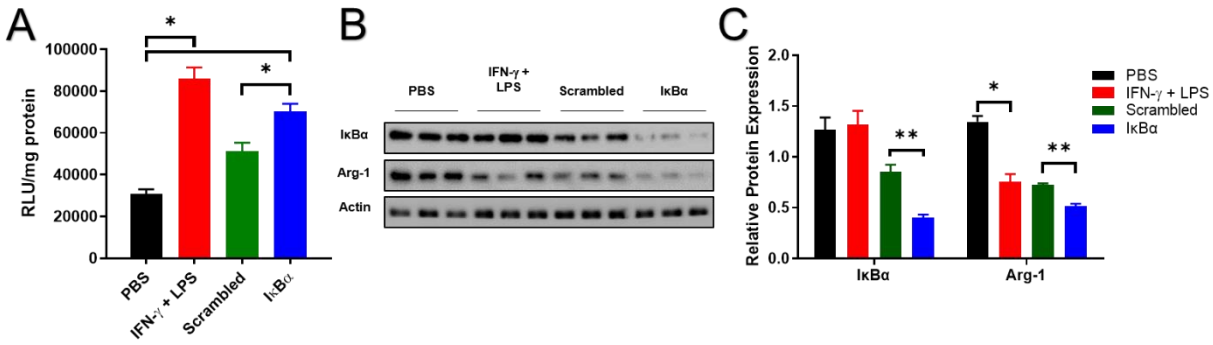

Figure 2.6: BMDM-NGL cells were polarized towards M2, followed by treatment with PBS, IFN-γ and LPS, or mannose-decorated polyplexes containing scrambled or IκBα-targeting siRNA. Effects on (**A**) luciferase activity of the NF-κB-dependent reporter and (**B**) protein levels of IκBα, and the M2 macrophage marker, arginase-1 (Arg-1). (**C**) Densitometry analysis of expression of IκBα and Arg-1 relative to β-actin loading control. Values are mean±SEM.

luminescence. The IκBα siRNA demonstrated elevated NF-κB activity as indicated by an increase in luminescence. This activation was on the level of M1 polarization, which provides evidence for successful phenotype repolarization (**Figure 2.6A**). In addition, the same treatments were repeated and the cells were collected for western blot to directly examine protein expression levels. By delivering the IκBα siRNA in our optimized MnPEGDB polymer, we demonstrate a significant knockdown in IκBα protein expression as well as a significant decrease in arginase-1 (Arg-1) expression, which is a protein overexpressed in M2 macrophages (**Figure 2.6B-C**). In conjunction with the results of RT-PCR, these results indicate that our polyplex system loaded with IκBα siRNA is able to repolarize macrophages from an M2 towards an M1 phenotype.

2.5 Conclusions

We have optimized the reaction conditions for functionalizing polymeric micelles with a targeting moiety using CuAAC. By altering the concentration of copper catalyst, we demonstrated an optimal range for efficient conjugation while minimizing residual copper and azide content. Our results indicated that cytotoxicity is a balance between excess Cu^{2+} versus residual azides. Our observation of azide toxicity due to incomplete CuAAC reaction is an underappreciated and avoidable potential cause of cell injury. Moreover, we showed that copper-associated toxicity can be eliminated from our polymer system, and that residual copper alone is not the main predictor of cytotoxicity. The toxicity observed in our polymer system appears to be synergistically associated with residual copper and the material system as a whole, both of which may exhibit exacerbated toxicity due to the intracellular delivery of the polyplexes. To our knowledge, this is the first study to examine cytotoxic effects of copper salt alone compared to copper ions associated with our polyplex system. These results indicate that concerns for

negative biological impacts of CuAAC reaction products can be mitigated by altering the reaction conditions. Overall, we show that CuAAC should not be discouraged for *in vivo* applications, but we recognize that some optimization of copper catalyst concentration and confirmation of low toxicity for each formulation/system may be necessary.

Mannosylated micelles prepared from our simplified polymer system enable increased delivery to human macrophages as well as $CD206_{high}$ primary murine macrophages, which is an improvement over the previous PEGDB polymer that can deliver siRNA but does not confer cell-specific delivery. This optimized polymer system also successfully delivered therapeutic siRNA and induced a shift in gene expression indicative of macrophage "repolarization" from an M2 phenotype towards an inflammatory M1 phenotype. We confirmed this repolarization by demonstrating a shift in mRNA expression for several M1/M2 markers as well as increased activation of NF-κB protein, indicative of classical macrophage activation. This improved polyplex formulation will be used in future studies to repolarize TAMs in co-cultures with tumor cells to quantify the cancer-killing properties of the macrophages.

2.6 Supplemental Materials & Methods

2.6.1 Mannose-Alkyne Synthesis

Briefly, D-mannose (Mn, 2g) was dissolved in dimethyl sulfoxide (DMSO) (20 mL, 10% w/v) in a 25 mL round bottom flask with a stir bar. The flask was sealed with a rubber top, placed on a stir plate, and purged with nitrogen (N_2 (g)) for 30 minutes while stirring. While purging, triethylamine (TEA, 1.082 mL) was added to activate the sugar into a nucleophile before propargyl bromide (0.547 mL) was added. Both TEA and propargyl bromide were added using a needle and syringe to prevent oxygen from leaking into the reaction vessel. The final molar ratio of mannose:TEA:propargyl bromide was 60:72:67 moles. After removing the nitrogen purge, the solution was heated to 40°C in an oil bath and stirred for 24 hours. The final solution was added to equal volume diethyl ether for extraction of excess reagents. The leftover ether was disposed and the resulting DMSO solution was collected. This extraction was repeated 5x. The final DMSO was mixed with equal volume nuclease-free water (Thermo Fisher Scientific, Waltham, MA) and extracted into equal volume dichloromethane to remove other byproducts as well as DMSO. Once again, this extraction was performed 5x. The final mannose-alkyne solution in nuclease-free water was collected, frozen at -80°C, and lyophilized. Synthesis of mannose-alkyne has been previously characterized and we confirm successful alkyne functionalization with 1H-NMR (**Supplemental Figure 2.S2**).[69] Although the reaction scheme depicts alkyne conjugation to a particular hydroxyl group, this reaction is not specific for only that hydroxyl. Near-random conjugation among hydroxyls is not anticipated to affect binding to CD206 since this receptor primarily binds mannose-like structures on bacterial cell walls.[69,144]

2.6.2 Fabrication of Macro-CTA for RAFT

All polymers were fabricated using 4-cyano-4-(ethylsulfanylthiocarbonyl)-sulfanylpentanoic acid (ECT) as a chain transfer agent (CTA). ECT was synthesized as previously described.[117,118] A 5 kDa hydroxyl PEG azide (500 mg, AzPEG, Polysciences, Inc., Warrington, PA) was reacted with ECT to form a macro-CTA suitable for RAFT polymerization. AzPEG was dissolved in dichloromethane (DCM) (5 mL) and mixed with 4-dimethylaminopyridine (DMAP) (30.2 mg, molar ratio 2.5:1 DMAP:AzPEG). Separately, ECT (130 mg) was dissolved in DCM (5 mL) at a 5:1 molar excess to AzPEG (accounting for total volume when combined). N,N'-dicyclohexylcarbodiimide (DCC, 102 mg) was added to the ECT solution at a 5:1 molar excess to the AzPEG. The ECT/DCC solution was added to a 25 mL round bottom flask with a N_2 balloon purge and stirred for 5 minutes to allow the DCC to activate the carboxylic acid group of the ECT. The AzPEG/DMAP solution was then added and the total solution (10 mL, 5% w/v AzPEG) was covered with aluminum foil and stirred for 48 hours at room temperature. After reacting, the solution was purified by dialyzing against methanol for 24 hours followed by dialyzing against deionized (DI) water for 24 hours using a 3.5 kDa-MWCO membrane.[67,83] The final solution was frozen at -80°C and lyophilized. Conjugation of ECT to the AzPEG was confirmed with 1H-NMR as previously described (**Supplemental Figure 2.S3**).[67]

2.6.3 RAFT Polymerization of Diblock Copolymers

The AzPEG and PEG macro-CTAs were then RAFT polymerized with DMAEMA and BMA at a 50:50 molar ratio as previously described.[45,67,69] The macro-CTA (150 mg) was dissolved in dioxane (8.39 mL, 14% w/v) with recrystallized 2,2′-azobis(2-methylpropionitrile) (AIBN) as the initiator (0.47 mg, 10:1 CTA:initiator molar ratio). Based on previous experience with the diblock copolymer, overall best performance was generally obtained from a polymer with approximately 120-140 monomers.[67] Previous syntheses with similar systems produced a

conversion rate of 60-65% so we designed the reaction at a degree of polymerization of 240. DMAEMA (576 µL) and BMA (543 µL) were added at 50:50 mol% and the entire solution was placed in a 50 mL round bottom flask and sealed with a rubber stopper. The solution was purged with N_2 for 30 minutes and then placed in an oil bath at 70°C for 24 hours. After completion of the reaction, the AzPEG(DMAEMA-co-BMA) (AzPEGDB) and PEGDB solutions were dialyzed for 24 hours in methanol and 24 hours in DI water using a 3.5 kDa-MWCO membrane. The solutions were then frozen and lyophilized for long-term storage. Fabrication of the PEG-ECT macro-CTA and subsequent RAFT polymerization of PEGDB has been previously well-characterized.[67,68,83,123,145]

2.6.4 Alkyne-Azide "Click" Functionalization

AzPEGDB (250 mg) was dissolved in 10% (v/v) 200-proof ethanol and 90% nuclease-free water (25 mL total, 10 mg/mL) in a 100 mL round bottom flask. Then, mannose-alkyne (5.93 mg, 1:3 azide:alkyne molar ratio) and sodium ascorbate (24.8 mg, 5 mM) were added to the reaction vessel. The copper catalyst (copper sulfate ($CuSO_4$)) was added at concentrations of 0.1, 0.25, 0.5, 0.75, or 1 mM (0.62 mg, 1.56 mg, 3.12 mg, 4.68 mg, 6.24 mg, respectively) to examine conjugation efficiency at different catalyst concentrations. The reaction vessel was sealed with a rubber stopper and placed on a stir plate for 48 hours at room temperature. Post-reaction, a Chelex resin (1.25 g, 5 g/100 mL, Bio-Rad, Hercules, CA) was added and stirred for 2 hours to remove residual Cu^{2+} ions. The solution was filtered through a 0.45 µm filter to remove the Chelex resin and dialyzed against DI water for 24 hours using a 3.5 kDa-MWCO membrane. The purified solution was frozen at -80°C and lyophilized.

2.7 Supplemental Figures

Figure 2.S1: Polyplex Toxicity in ThP-1 Human Macrophages

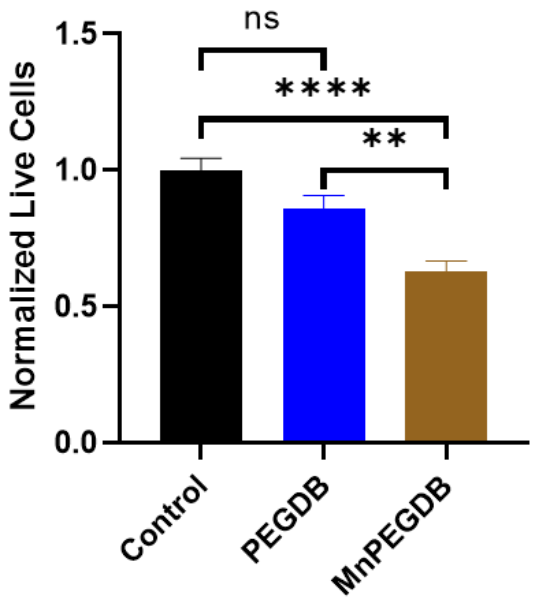

Supplemental Figure 2.S1: Viability studies with ThP-1 human macrophages treated with PEGDB and MnPEGDB (prepared with 1 mM copper catalyst) revealed a significant toxic effect in the MnPEGDB group, which we hypothesized to be caused by residual copper from CuAAC.

Figure 2.S2: Mannose-Alkyne Fabrication

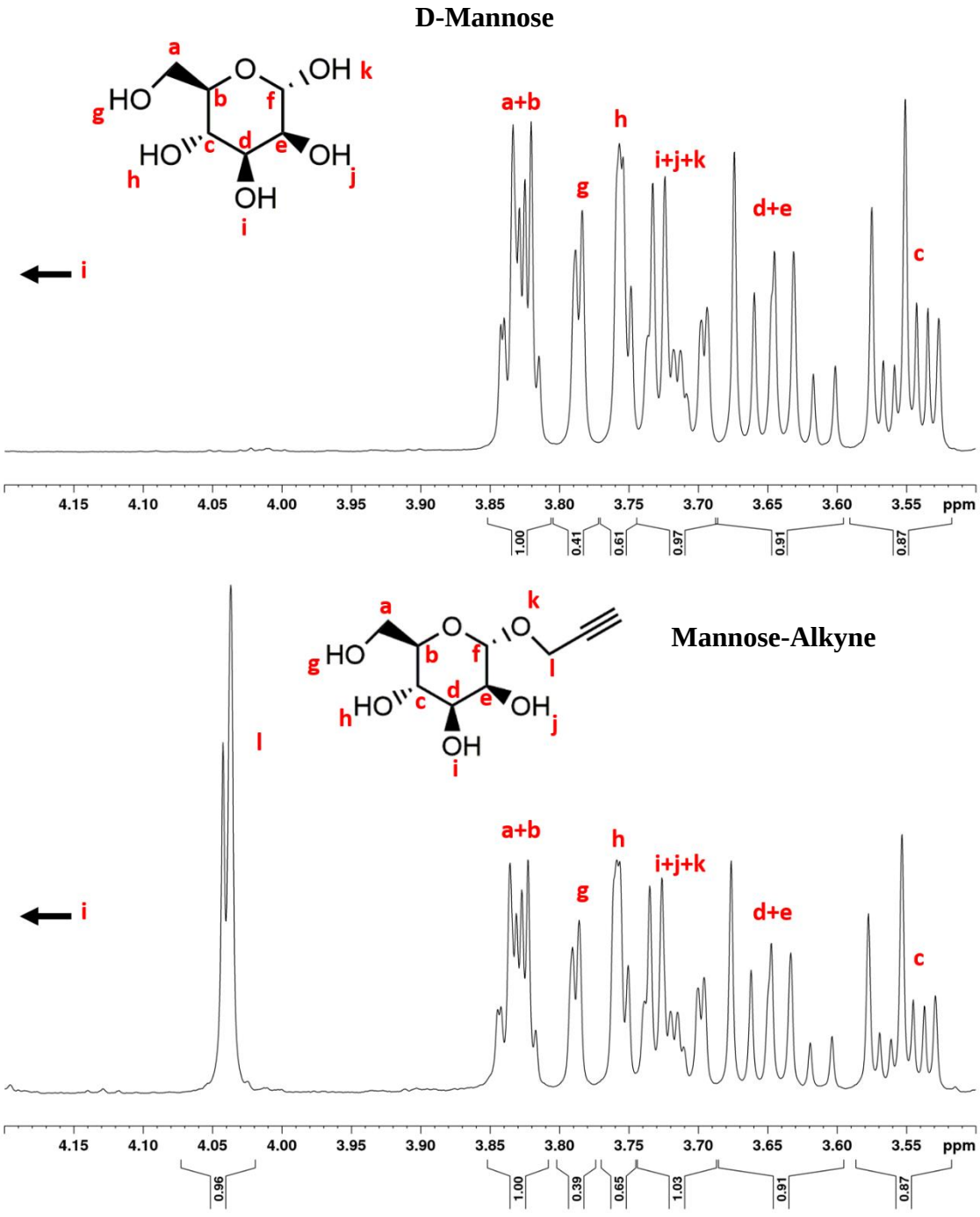

Supplemental Figure 2.S2: ^{1}H-NMR of mannose functionalization with propargyl bromide to form mannose-alkyne, performed in D_2O. Successful conjugation is confirmed by the appearance of the alkyne peak at δ 4.04s. Integration of peaks reveals a 1:1 conjugation efficiency. These results match previous data from our lab. Note that alkyne conjugation to mannose is not expected to be specific for a particular hydroxyl group.

Figure 2.S3: Azide-PEGDB Fabrication

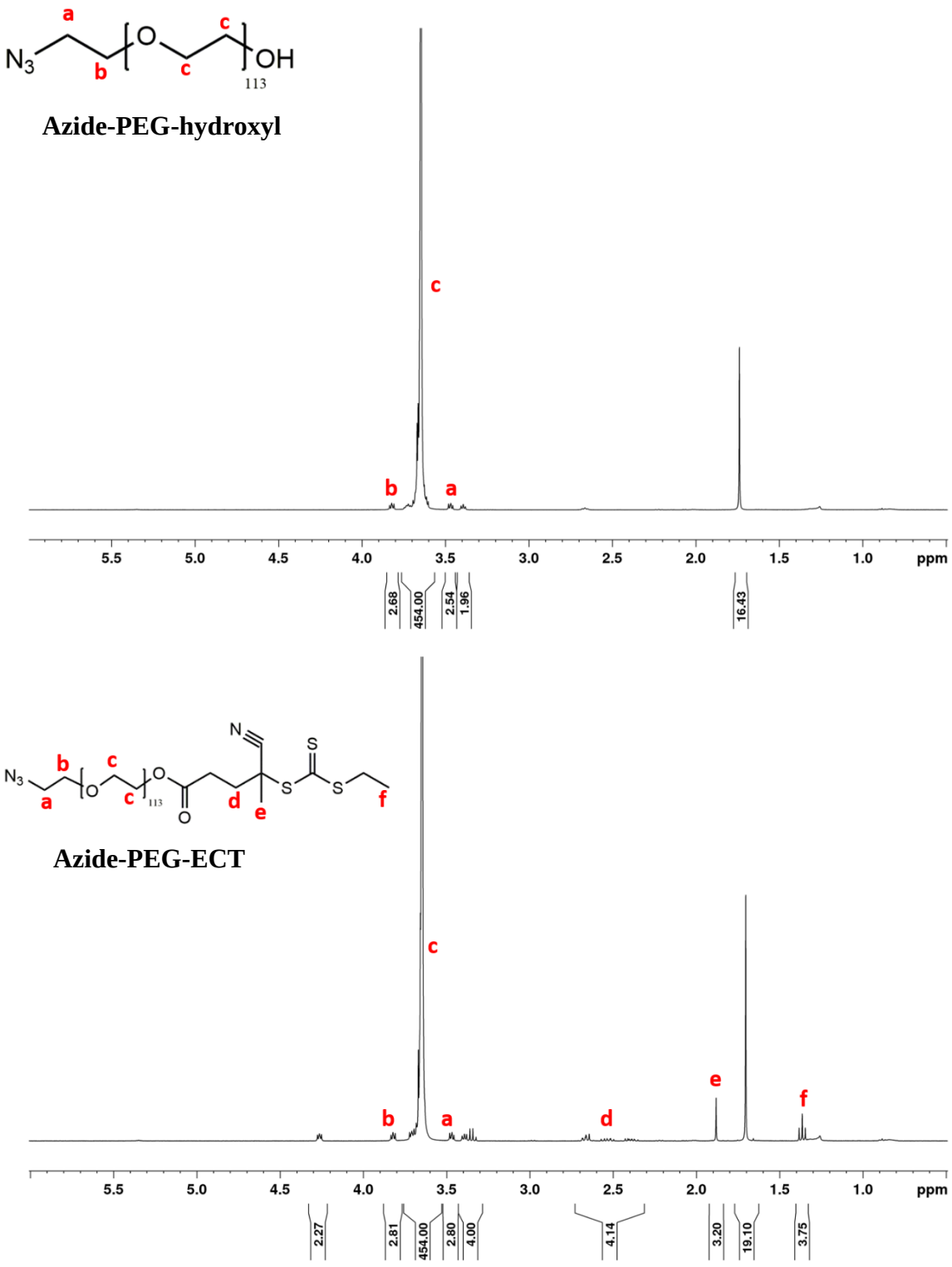

Supplemental Figure 2.S3: ^{1}H-NMR of Azide-PEG-DB reaction steps in CDCl3 – continued on next page.

Figure 2.S3: Azide-PEGDB Fabrication (Continued)

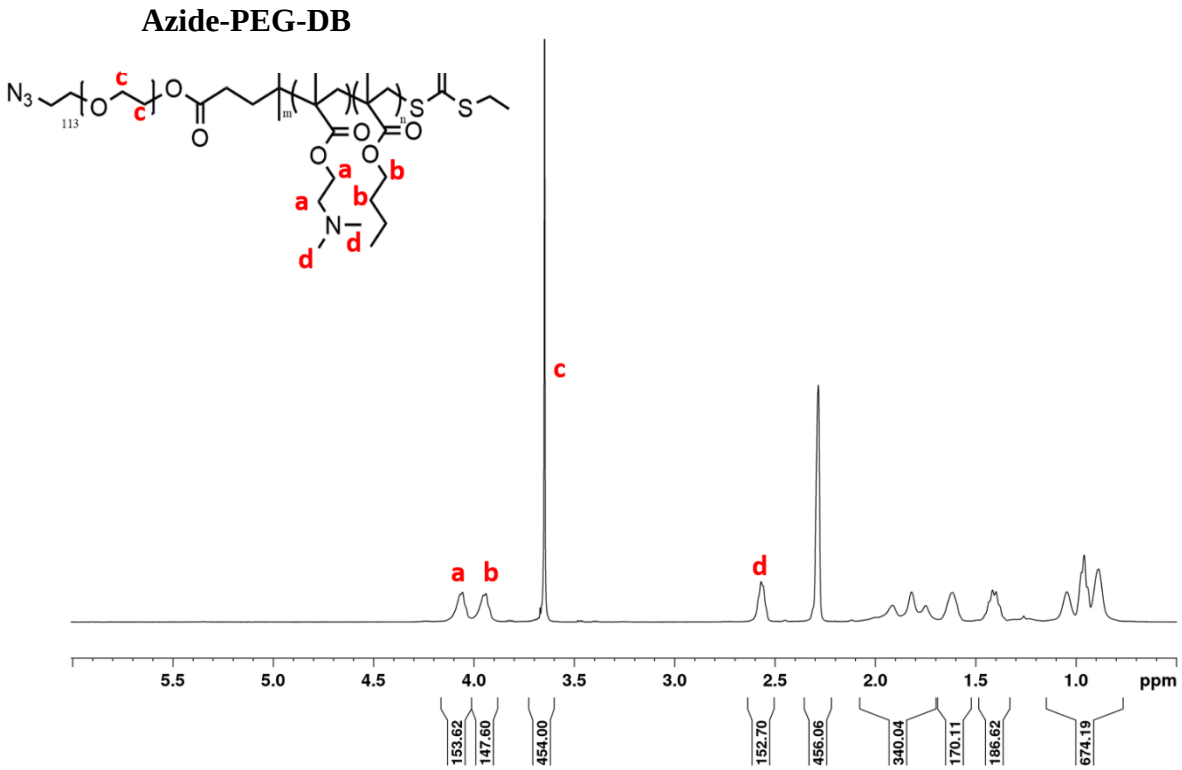

Supplemental Figure 2.S3: ^{1}H-NMR of each reaction step in CDCl3. Azide-PEG-hydroxyl is reacted with the ECT macro-CTA to create Azide-PEG-ECT. Azide-PEG-ECT maintains the characteristic PEG peak at δ 3.65s (-OC**H**$_2$C**H**$_2$-) and adds the ECT peak δ 1.88s (CCNC**H**$_3$). RAFT polymerization produces AzPEGDB, which is confirmed by the DMAEMA (δ 4.05s, -OC**H**$_2$CH$_2$-) and BMA (δ 3.95s, -OC**H**$_2$CH$_2$-) peaks. Polymer repeating units for AzPEGDB were calculated by calibrating the PEG peak to the number of hydrogens in the polymer and comparing to the DMAEMA and BMA peak integrals. Overall spectra of AzPEGECT and AzPEGDB match previously reported data using a similar polymer system.

Figure 2.S4: MnPEGDB Polymers Fabricated with Various Copper Catalyst Concentrations

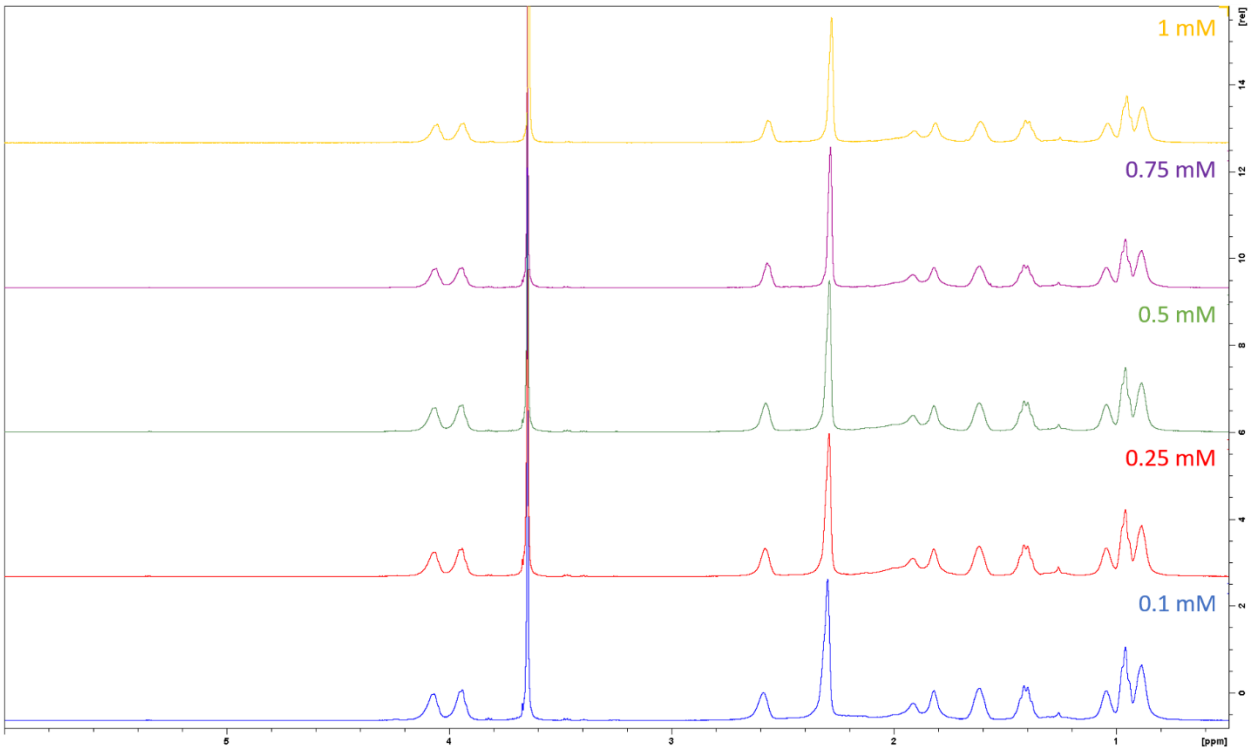

Supplemental Figure 2.S4: ^{1}H-NMR of MnPEGDB polymers in CDCl3. All spectra matched between groups, indicating no changes in overall polymer structure despite changing the copper catalyst concentration in the CuAAC reaction. Note that mannose is not detectable with NMR since the peaks (shown in Figure S2) overlap with the PEG peak, which has 113 repeating units per polymer compared to one for mannose.

Table 2.S1: RT-PCR Primer Sequences

Gene name	Forward sequence	Reverse sequence
CD86	TCTCCACGGAAACAGCATCT	CTTACGGAAGCACCCATGAT
TNF-α	CCCTCACACTCAGATCATCTTCT	GCTACGACGTGGGCTACAG
iNOS	TTCACCCAGTTGTGCATCGACCTA	TCCATGGTCACCTCCAACACAAGA
CD206	GCTCTTACTGACTGGCATGAG	CGCAGCTCTAGGAGCATGTG
IκBα	GAGCTCCGAGACTTTCGAGG	AGACACGTGTGGCCATTGTA
F4/80	CTTTGGCTATGGGCTTCCAGTC	GCAAGGAGGACAGAGTTTATCGTG
GAPDH	CCCTTAAGAGGGATGCTGCC	TACGGCCAAATCCGTTCACA
Actin-β	TATAAAACCCGGCGGCGCA	TCATCCATGGCGAACTGGTG

Table 2.S2: Characterization of Polyplex Diameter, Homogeneity, and Surface Charge

Polymer	Avg Diameter (d.nm)	PDI	Avg Zeta Potential (mV)
PEGDB	140 ± 16	0.287	-0.142 ± 0.471
0.1 mM MnPEGDB	146 ± 18	0.273	-0.111 ± 0.347
0.25 mM MnPEGDB	148 ± 17	0.254	-0.332 ± 0.398
0.5 mM MnPEGDB	145 ± 12	0.259	-0.286 ± 0.438
0.75 mM MnPEGDB	151 ± 16	0.262	0.249 ± 0.054
1 mM MnPEGDB	151 ± 14	0.300	-0.417 ± 0.430

Figure 2.S5: Flow Cytometry Gating Strategy and Polarized Macrophage Characterization

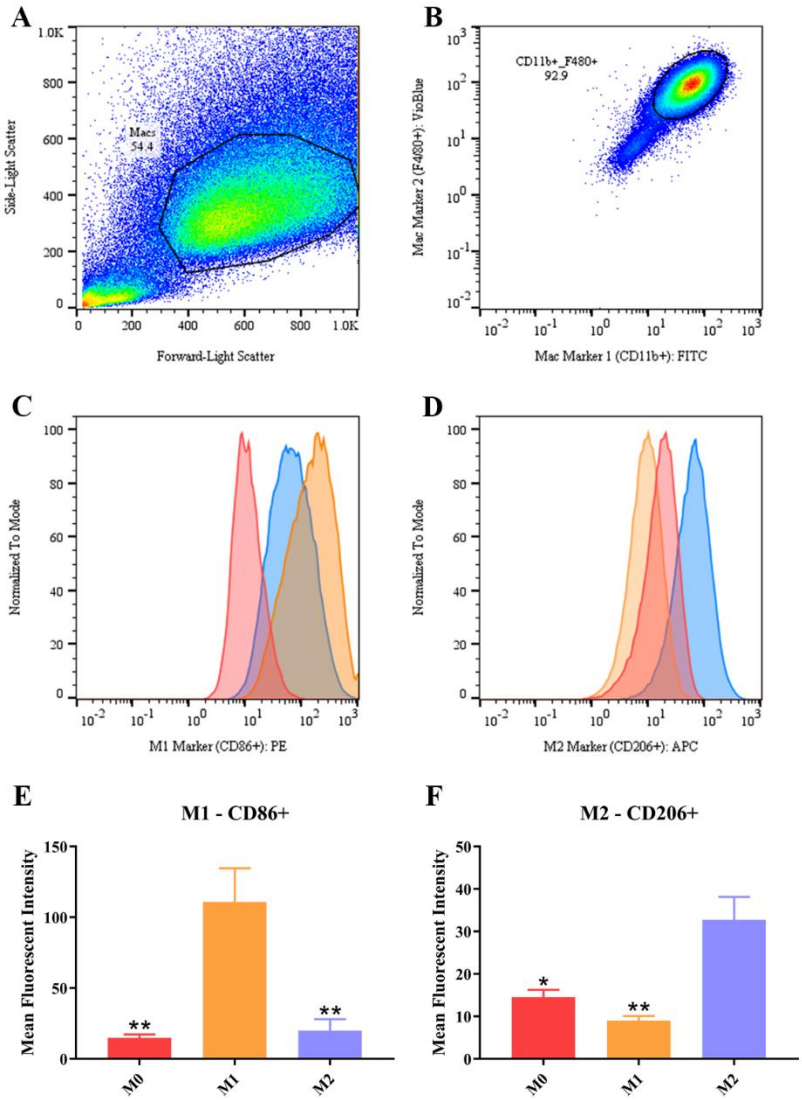

Supplemental Figure 2.S5: (**A**) Gating of overall cell population in flow cytometry based on side-light scatter intensity vs forward-light scatter intensity. (**B**) Gating of macrophages determined by a double-positive population expressing F4/80 and CD11b. (**C,D**) Histogram plots depicting expressions of M1 (CD86) and M2 (CD206) markers on the different macrophage phenotypes. (**E**) CD86 was significantly increased in the M1-polarized macrophages compared to both M0 and M2 (**F**) CD206 was significantly overexpressed in M2 BMDMs.

Figure 2.S6: Polyplex and Copper Toxicity in Human and Murine TNBC Cells and Human Mammary Epithelial Cells

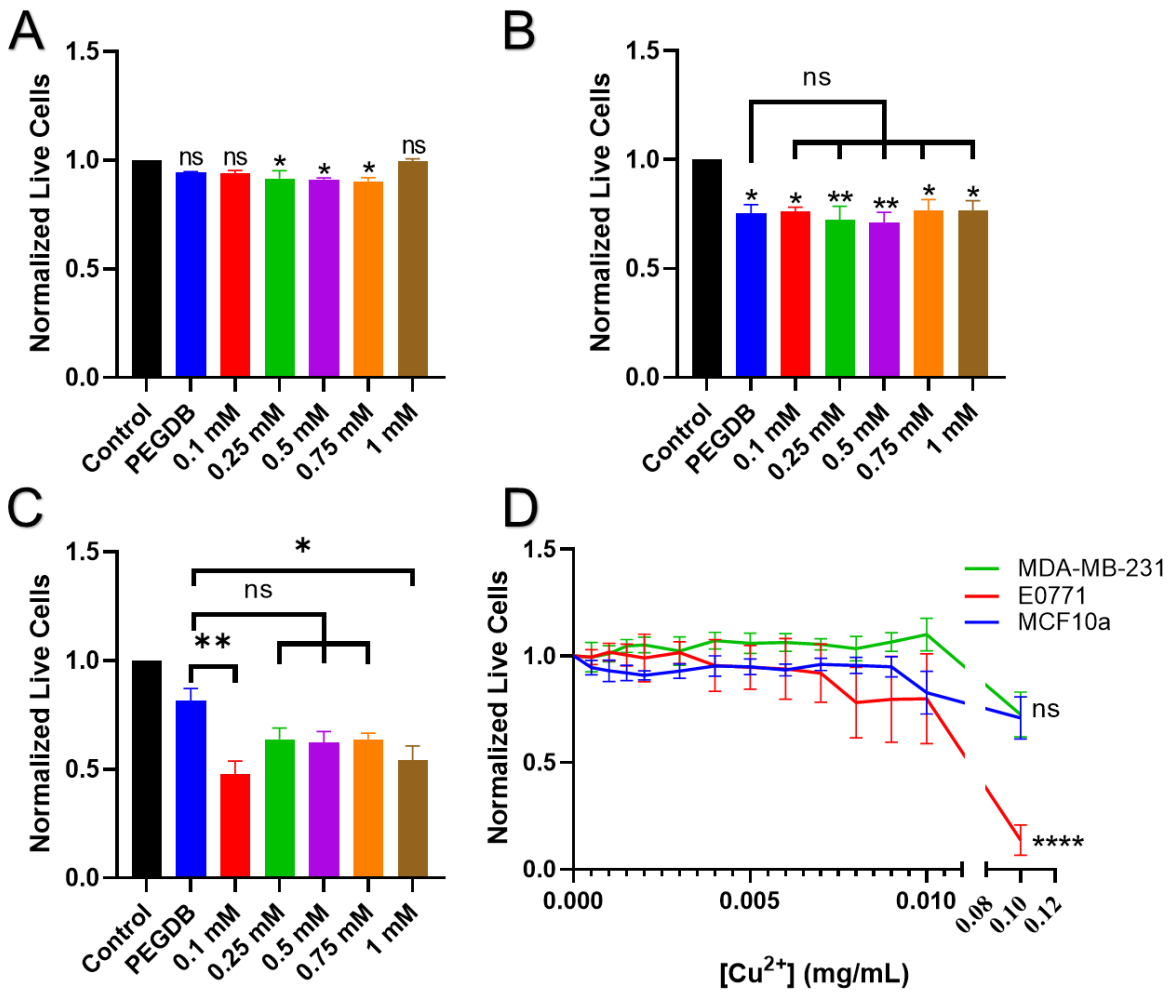

Supplemental Figure 2.S6: (**A**) MDA-MB-231 human TNBC cells significantly decreased in viability in the 0.25-0.75 mM-prepared MnPEGDB polyplexes compared to untreated control, but still had viability greater than 90%. (**B**) E0771 murine TNBC cells had significantly less viability in all treatments compared to untreated control, but none of the MnPEGDB groups were significantly different from the PEGDB control polymer. (**C**) MCF10a human epithelial cells treated with 0.1 and 1 mM MnPEGDB were significantly less viable than the PEGDB control polymer, but the 0.25-0.75 mM groups were not significantly different. (**D**) All three cell types exhibited a trend of decreasing viability with increasing copper salt concentration, but only the E0771 murine TNBC cells had a significant change in viability at the highest concentration.

Figure 2.S7: CD206-Specific Uptake of Polyplexes Confirmed via Co-Incubation with Free Mannose

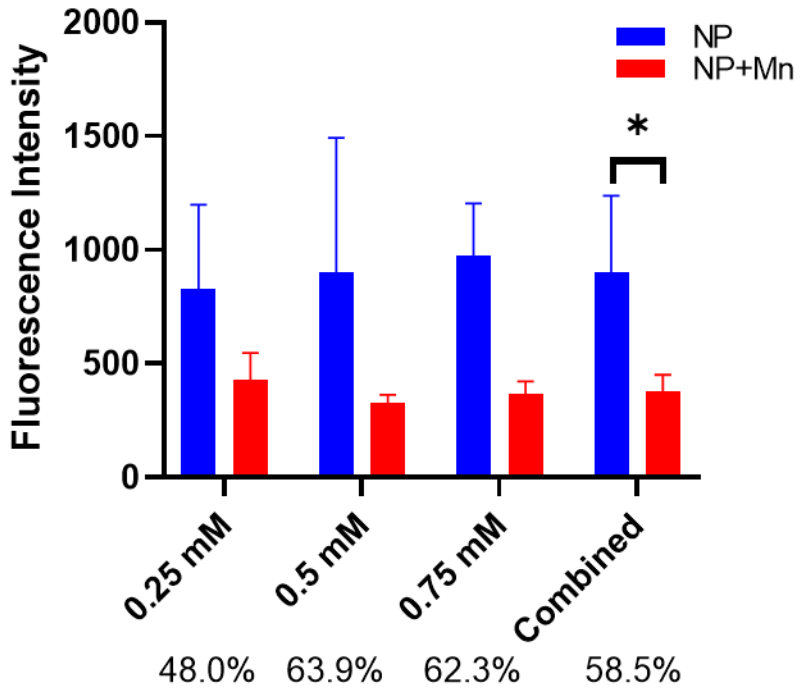

Supplemental Figure 2.S7: M2-polarized BMDMs were treated with either mannose-decorated nanoparticles (NP) or NPs plus free mannose (NP+Mn). Fluorescence intensity revealed that all three of the optimal polymer formulations resulted in decreased uptake after adding free mannose (n=2). An average of the three optimal groups (combined, n=6) revealed a significant decrease in uptake with about 59% decrease due to mannose blocking the CD206 receptor.

Figure 2.S8: Polyplex Uptake in TNBC Cells and Mammary Epithelial Cells

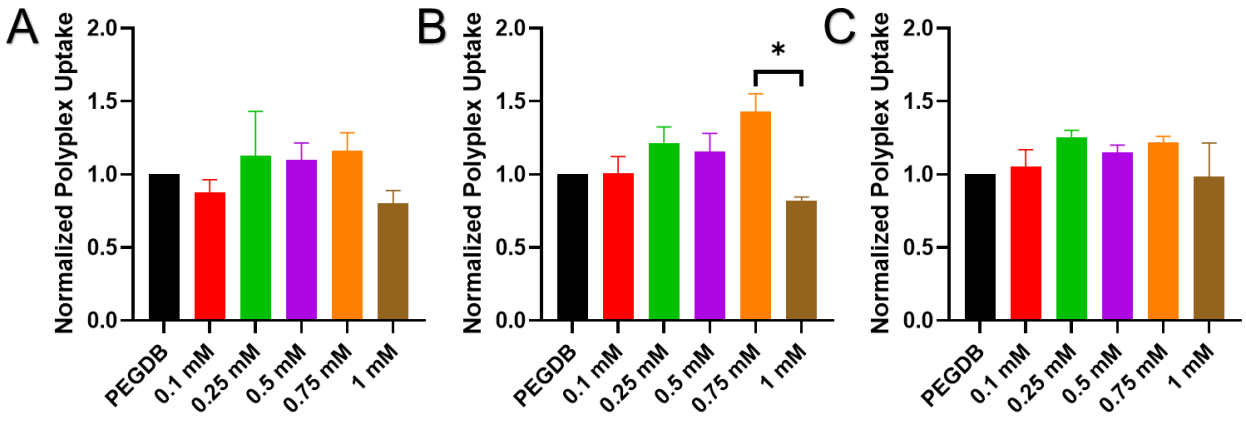

Supplemental Figure 2.S8: (**A**) MDA-MB-231 cells had no significant changes in uptake regardless of mannosylation or copper content, indicating non-specific uptake of particles. (**B**) E0771 cells only exhibited a significant change in uptake between the 0.75 and 1 mM groups, but no other groups were different from each other. (**C**) MCF10a cells also displayed non-specific uptake, with no polymer groups differing from each other.

Chapter 3

Stimulating TAM-Mediated Anti-Tumor Immunity with Mannose-Decorated Nanoparticles in Ovarian Cancer

Adapted from

"Stimulating TAM-Mediated Anti-Tumor Immunity with Mannose-Decorated Nanoparticles in Ovarian Cancer,"

Submitted to *BMC Cancer* November 2021

by

Evan B. Glass, Alyssa A. Hoover, Kennady K. Bullock, Matthew Z. Madden, Bradley I. Reinfeld, Whitney Harris, Dominique Parker, Demetra H. Hufnagel, Marta A. Crispens, Dineo Khabele, W. Kimryn Rathmell, Jeffrey C. Rathmell, Andrew J. Wilson, Todd D. Giorgio, and Fiona E. Yull

3.1 Abstract

Background: Current cancer immunotherapies have made tremendous impacts but generally lack high response rates, especially in ovarian cancer. New therapies are needed to provide increased benefits. One understudied approach is to target the large population of immunosuppressive tumor-associated macrophages (TAMs). Using inducible transgenic mice, we recently reported that upregulating nuclear factor-kappaB (NF-κB) signaling in TAMs promotes the M1, anti-tumor phenotype and limits ovarian cancer progression. We also developed a mannose-decorated polymeric nanoparticle system (MnNPs) to preferentially deliver siRNA payloads to M2, pro-tumor macrophages *in vitro*. In this study, we tested a translational strategy to repolarize ovarian TAMs via MnNPs loaded with siRNA targeting the inhibitor of NF-κB alpha (IκBα) using mouse models of ovarian cancer.

Methods: We evaluated treatment with MnNPs loaded with IκBα siRNA (IκBα-MnNPs) or scrambled siRNA in syngeneic ovarian cancer models. ID8 tumors in C57Bl/6 mice were used to evaluate consecutive-day treatment of late-stage disease while TBR5 tumors in FVB mice were used to evaluate repetitive treatments in a faster-developing disease model. MnNPs were evaluated for biodistribution and therapeutic efficacy in both models.

Results: Stimulation of NF-κB activity and repolarization to an M1 phenotype via IκBα-MnNP treatment was confirmed using cultured luciferase-reporter macrophages. Delivery of MnNPs with fluorescent payloads (Cy5-MnNPs) to macrophages in the solid tumors and ascites was confirmed in both tumor models. A three consecutive-day treatment of IκBα-MnNPs in the ID8 model validated a shift towards M1 macrophage polarization *in vivo*. A clear therapeutic effect was observed with biweekly treatments over 2-3 weeks in the TBR5 model where significantly reduced tumor burden was accompanied by changes in immune cell composition, indicative of

reduced immunosuppressive tumor microenvironment. No evidence of toxicity associated with MnNP treatment was observed in either model.

Conclusions: In mouse models of ovarian cancer, MnNPs were preferentially associated with macrophages in ascites fluid and solid tumors. Evidence of macrophage repolarization, increased inflammatory cues, and reduced tumor burden in IκBα-MnNP-treated mice indicate beneficial outcomes in models of established disease. We have provided evidence of a targeted, TAM-directed approach to increase anti-tumor immunity in ovarian cancer with strong translational potential for future clinical studies.

3.2 Background

The use of cancer immunotherapies, including immune checkpoint blockades (ICBs), is rapidly expanding as a result of early successes in clinical trials. Multiple clinical trials have resulted in FDA-approved treatments for a variety of cancers, including melanoma[146,147], non-small cell lung cancer[148], urothelial cancer[149,150], renal cell carcinoma[151], colorectal cancer[152], and triple-negative breast cancer (TNBC)[153], among others reviewed here.[154] While ICBs represent an important advancement in cancer therapy, disappointingly low overall response rates (ORRs) are commonly observed. In particular, clinical trials involving the treatment of epithelial ovarian cancer resulted in ORRs of 15% and 8% for monotherapies of nivolumab and pembrolizumab, respectively.[155–157] Epithelial ovarian cancer (EOC) is estimated to be the fifth leading cause of cancer-related deaths in females in the U.S. and is in desperate need of improved therapies.[158] The relatively late presentation of disease in most patients contributes to overall survival of 40% at diagnosis.[15] The primary standard of care (surgery followed by platinum- and taxane-based chemotherapy) is initially effective in over 70% of patients, but only half of these patients exhibit non-detectable levels of cancer cells 5 months after treatment.[6] Even in those patients, small

numbers of chemotherapy-resistant cells can remain dormant in the peritoneal cavity for several months before growing exponentially.[6] However, as with many other types of cancer, ovarian cancer is a prime candidate for macrophage-specific immunotherapy.

Tumor-associated macrophages (TAMs) are the most abundant immune cell in most types of cancer, including epithelial ovarian cancer.[159,160] TAMs are prevalent in both the solid tumor as well as the ascites fluid associated with ovarian cancer progression. Ascites development is correlated with severity of ovarian cancer (present in over one-third of patients) and is linked to poor disease prognosis as well as development of chemoresistance.[161–163] TAMs in both the tumor and ascites promote an immunosuppressive tumor microenvironment (TME), hinder the efficacy of ICB, and drive tumor progression and metastasis.[164,165] Several techniques to alter the TME, including TAM ablation or limiting TAM recruitment, have been attempted with moderate successes.[31,33] However, a potentially more robust method leverages macrophage plasticity. This phenomenon provides the opportunity to target M2-like immunosuppressive TAMs and "repolarize" them into an M1-like pro-inflammatory, anti-tumor phenotype. Repolarizing TAMs for cancer immunotherapy is a rapidly growing field of study with encouraging early results.[37,82]

Our lab has previously identified the nuclear factor-κB pathway (NF-κB) as a target for repolarizing macrophages both *in vitro* and *in vivo* since this pathway drives macrophage phenotype.[166,167] This work provides evidence that modulating macrophage phenotype in mouse cancer models induces beneficial therapeutic outcomes. Using transgenic mice, we have recently demonstrated M1 macrophage repolarization, increased cytotoxic T cell responses, and reduced tumor burden in syngeneic mouse models of ovarian cancer.[167] The goal of the present study is to

evaluate a new translational approach involving a targeted nanoparticle-based delivery of an siRNA cargo to specifically stimulate NF-κB activity in ovarian TAMs.

Our group has extensive experience designing nanoparticle formulations for delivering siRNA to cells *in vivo*.[45,83,168] We have previously used a small interfering RNA (siRNA) sequence specific for the inhibitor of NF-κB alpha (IκBα). Because IκBα functions to inhibit the canonical NF-κB pathway, our previous work confirmed that delivering siRNA against IκBα can increase activity of the canonical pathway and induce M1 polarization.[45,166]

Although siRNA-based therapies are promising, delivery platforms are crucial to their success because oligonucleotides are unable to cross cell membranes and are rapidly cleared from circulation when administered as unformulated macromolecules.[48] Targeted formulations can enhance delivery of functional siRNA to the appropriate cells while simultaneously minimizing activity in non-target cells and tissues.[169,170] By combining an siRNA against IκBα with a targeted delivery system, we aim to increase the specificity of M1 activation to the tumor microenvironment and limit off-target effects elsewhere. The phenotypic diversity of macrophages, often characterized by the differing expression levels of various surface receptors, allows for targeting via the CD206 macrophage mannose receptor, which is overexpressed on M2-polarized macrophages and TAMs.[171] The overexpression of CD206 on immunosuppressive TAMs allows for targeting with mannose-decorated delivery systems.[69,82,166] Specifically, polymers designed to form nanoscale micelles containing siRNA and decorated with mannose enable the targeted delivery of RNA interference (RNAi) therapies that modulates macrophage phenotype.[166] These micelles are spherical with diameters of 100-150 nm to promote clathrin-mediated endocytosis into the targeted macrophages, which has been extensively documented.[62,63,172] Our group has previously demonstrated MnNP targeting to macrophages

using a mannosylated triblock copolymer.[69,70] This system has since been improved via the development of a diblock copolymer that is more reproducible and simpler to fabricate.[67] The mannose-decorated diblock copolymer was shown to successfully target M2-polarized bone marrow-derived macrophages (BMDMs) and repolarize them to an M1 phenotype.[166]

Mannosylated nanoparticle (MnNP) delivery systems can be especially beneficial in the context of ovarian cancer. EOCs with high levels of immunosuppressive TAMs, in both the solid tumor and ascites, result in poor prognosis for patients while cases with elevated M1-polarized macrophages are correlated with increased overall survival and progression-free survival.[39,173] Furthermore, intraperitoneal (IP) injection of nanoparticles allows for localized delivery with limited risk for off-target accumulation or rapid clearance that is often associated with intravascular (IV) delivery.[83] The potential for targeted repolarization of TAMs in EOC led to the hypothesis that IP injection of MnNPs loaded with IκBα siRNA (IκBα-MnNP) will locally target and reprogram macrophages to induce anti-tumor immunity in mouse models of ovarian cancer.

This study follows-up on our previous work by utilizing the optimized MnNPs to deliver IκBα siRNA to TAMs in mouse models of ovarian cancer. Two models of ovarian cancer were used to evaluate the effects of IκBα-MnNPs on TAMs. The ID8 ovarian tumors on a C57Bl/6 background enabled examination of treating late-stage disease while the TBR5 ovarian tumors on an FVB background allowed for evaluation of early-stage treatment in an aggressive disease model. MnNP biodistribution was evaluated to confirm limited off-target delivery in both models. Tumor-bearing mice were treated with IκBα siRNA-loaded MnNPs, scrambled siRNA-loaded MnNPs, or PBS to evaluate changes in tumor burden in terms of tumor weight and ascites accumulation. The safety profile of two treatment regimens was also evaluated to characterize

any toxicities caused by MnNP administration. Immune cell composition, macrophage phenotypes, and cytokine signaling were evaluated to investigate the mechanisms leading to differential outcomes and, ultimately, to demonstrate the effects of TAM repolarization on tumor suppression.

3.3 Materials and Methods

3.3.1 Materials

All materials were purchased from Sigma-Aldrich unless otherwise noted. Monomethyl ether hydroquinone inhibitors were removed from dimethylaminoethyl methacrylate (DMAEMA) and butyl methacrylate (BMA) using an activated basic aluminum oxide column. All DNA and RNA oligonucleotides were purchased from Integrated DNA Technologies (Coralville, IA). For *in vivo* biodistribution studies, double stranded DNA (dsDNA) designed to be length-matched to therapeutic IκBα siRNA and conjugated with a cyanine-5 (Cy5) fluorophore was used. IκBα siRNA sequence was based on previous studies and the scrambled siRNA sequence was randomized from the IκBα sequence and analyzed via the Basic Local Alignment Search Tool (BLAST, NCBI) to ensure no off-target effects with our sequence.[45,166] Oligonucleotide sequences are listed in **Supplemental Table 3.S1**.

3.3.2 Polymer Synthesis

The mannose-poly(ethylene glycol)-(DMAEMA-co-BMA) (MnPEGDB) polymer was fabricated as previously described.[67,69,70,166] Nucleophilic substitution of propargyl bromide with D-mannose to form mannose-alkyne was performed and characterized previously.[166] The core of the micelle comprises a diblock copolymer fabricated using 4-cyano-4-(ethylsulfanylthiocarbonyl)-sulfanylpentanoic acid (ECT) as a chain transfer agent (CTA)

conjugated to an azide-functionalized PEG (Az-PEG). The Az-PEG-ECT was then RAFT polymerized to DMAEMA and BMA as previously described to create a "smart" polymer capable of encapsulating anionic siRNA and inducing endosomal escape upon uptake.[67,79,166] The AzPEGDB was then reacted with Mn-alkyne (1:3 azide:alkyne molar ratio) via copper-catalyzed azide-alkyne cycloaddition (CuAAC) using a previously optimized copper catalyst concentration of 0.75 mM with 5 mM of sodium ascorbate.[166] Chemical structures and ^{1}H-NMR for all reaction steps are shown in **Supplemental Figures 3.S1-4**, and mannose conjugation was verified with Fourier transform infrared (FTIR) spectroscopy as previously described (**Supplemental Figure 3.S5**).[166] All chemical structures were made using ChemDraw (PerkinElmer). FTIR spectroscopy was performed at the Vanderbilt Institute of Nanoscale Science and Engineering (VINSE) and all ^{1}H-NMR experiments were performed at the Vanderbilt Small Molecule NMR Facility on a 400 MHz spectrometer (Bruker).

3.3.3 Nanoparticle Preparation

Nanoscale polymeric complexes were fabricated as previously described.[67,83,166] To form mannosylated-nanoparticles (MnNPs) with oligonucleotides, MnPEGDB was dissolved in 90% (v/v) 10 mM citrate buffer (pH=4) with 200-proof ethanol (EtOH). MnNPs were complexed with either Cy5-dsDNA, IκBα siRNA, or scrambled siRNA for 30 minutes to form micelles before adding 5× volume 10 mM phosphate buffer (pH=8) for a final solution pH of 7.4. The micelle N^{+}/P^{-} ratio, determined by mole ratio of protonated amines on the DMAEMA polymer to the number of phosphates on the oligonucleotides, was chosen as 10:1 based on previous studies.[67,166] Nanoparticle size and zeta potential were evaluated using a Malvern Zetasizer located at VINSE, and the results are shown in **Supplemental Figure 3.S6**. All *in vitro* treatments were conducted with a final concentration of 50 nM oligonucleotides and all *in vivo*

treatments were performed using a dose of 1 mg/kg (1 mg of oligonucleotide/kg of mouse weight). For *in vivo* NP preparation, the pH=7.4 solution was diluted in sterile phosphate buffered saline (PBS) without magnesium and calcium and centrifuged in 5000 MWCO Amicon® Ultra-15 Centrifugal Filters (Millipore Sigma; UFC905024) at 2000xg for 30 minutes. The concentrated NPs were diluted in PBS (-/-) and centrifuged again before adding PBS to get to the appropriate volume for a 1 mg/kg concentration. The final preparation was filtered through a 0.45 µm syringe filter before being used for intraperitoneal injection.

3.3.4 Cell Culture and Tumor Induction

Unless otherwise noted, all cells were cultured in Dulbecco's Modified Eagle's Medium (DMEM, low glucose, pyruvate, Gibco; 11885084) supplemented with 10% fetal bovine serum (FBS, certified, Gibco; 16000044) and 1% penicillin/streptomycin (P/S) at 37°C in a 5% CO_2 humidified atmosphere. ID8 ovarian tumor cells and TBR5 genetically modified ovarian tumor cells were used as previously described.[174–177] ID8 cells were from Dr. Sandra Orsulic[178] and TBR5 cells were from Dr. Balkwill.[179] All animal work was reviewed and approved by the Vanderbilt University Institutional Animal Care and Use Committee (IACUC). The ID8 cells were used in syngeneic C57Bl/6 background mice while TBR5 cells were used in syngeneic FVB background mice. For tumor induction, cells were resuspended in sterile PBS at a concentration of $5x10^6$ cells/200 µL. A sterile 3 mL Luer-Lok™ syringe with an 18G needle was used to inject of $5x10^6$ cells tumor cells in 200 µL PBS intraperitoneally (IP) into each mouse. At endpoint, all mice were euthanized via carbon dioxide inhalation with secondary cervical dislocation as approved by IACUC protocols.

Primary bone marrow-derived macrophages (BMDMs) were isolated from healthy female wild-type FVB mice and immortalized NGL-BMDMs were previously derived from NF-

κB green fluorescent protein (GFP)-luciferase (NGL) reporter transgenic mice on an FVB background.[180–182]

3.3.5 Culturing and Treating Bone Marrow-Derived Macrophages

Immortalized NGL-BMDMs were used from frozen stocks for *in vitro* experiments.[182] NGL-BMDMs were plated in 6-well plates at $1x10^6$ cells/well in 2 mL of DMEM (ThermoFisher; 11995073) supplemented with 10% FBS and 1% P/S. The macrophages were polarized to M1 with 10 ng/mL each of IFN-γ and LPS for 24 hours and to M2 with 10 ng/mL of IL-4 for 48 hours. M2-polarized NGL-BMDMs were treated with Scr-MnNPs or IκBα-MnNPs for 24 hours before collecting cells for luminescent measurements. Samples were prepared for luminescence readings using a Luciferase Assay System (Promega; E4030) following the manufacturer's instructions.

3.3.6 *In Vivo* Biodistribution Studies in Ovarian Tumor-Bearing Mice

For the preliminary 24-hour delivery study, 6 female C57Bl/6 mice were injected IP with $5x10^6$ ID8 ovarian tumor cells in 200 µL PBS. Tumors developed for 8 weeks before treatment. Control mice were injected with 200 µL PBS and treatment mice received 200 µL PBS containing MnNPs loaded with Cy5-dsDNA at the previously listed dosage. After 24 hours, the mice were sacrificed and the ascites, tumors, and spleens were collected. The ascites was centrifuged at 1500 rpm for 5 minutes, supernatant collected, and red blood cells (RBCs) lysed with 5 mL Geyz lysing buffer (4.15 g NH_4Cl, 0.5 g $KHCO_3$ in 500 mL MilliQ water) for 5 minutes at 37°C. This step was repeated as needed until a clear pellet was obtained. The resulting cells were resuspended in PBS with 1% BSA and snap-frozen in liquid nitrogen for RNA isolation or protein analysis. The solid tumors were collected into 3 mL DMEM (MT-10-13-CV)

containing 10% FBS and 1% P/S for one hour on ice. The tissue was cut into small pieces and resuspended in 3 mL DMEM with 200 µL Collagenase A (Roche; 10103578001), 300 µL hyaluronidase (Sigma; H4272), 500 µL DNase I (Sigma; D5025), and 30 µL amphotericin B (ThermoFisher; 15290026) and placed at 37°C for 2 hours with frequent vortexing. The solution was filtered through a 70 µm strainer to form a single cell suspension used for flow cytometry. Tumors were then treated with the same RBC lysis buffer as the ascites. Similarly, spleens were collected in DMEM (10% FBS, 1% P/S) for one hour on ice, chopped into small pieces, and immediately filtered through a 70 µm strainer twice. The final single cell suspension was treated with RBC lysis buffer before flow analysis.

The long-term biodistribution study was performed in the TBR5 ovarian tumor model. 10 female FVB mice received IP injections of $5x10^6$ TBR5 cells in 200 µL PBS (day 0). Tumors developed for 7 days before starting treatment on day 7. Mice either received IP injections of 100 µL PBS or 100 µL Cy5-MnNPs. Treatments were performed on days 7, 10, 14, and 17 before takedown on day 18. Single cell suspensions were made from tumors, ascites, and spleen as previously described and used for flow cytometry analysis.

3.3.7 Flow Cytometry of *In Vivo* Biodistribution

Single cell suspensions were obtained from the tumors, ascites fluid, and spleens of either ID8 or TBR5 tumor-bearing mice. For ID8 24-hour biodistribution, the cells were resuspended in flow buffer (PBS with 2 mM EDTA and 0.5% (v/v) BSA) at $1x10^6$ cells/50 µL buffer. The following anti-mouse antibodies were used: CD45 PE-Cy7 (eBioscience; 25-0451-82), F4/80 PE (eBioscience; 12-4801-82), and Gr-1 Alexa Fluor 700 (eBioscience; 53-5931-82). After staining for 30 minutes, the cells were rinsed in PBS and resuspended in flow buffer before running flow

analysis at the Vanderbilt Flow Cytometry Shared Resource. All flow analysis was performed using FlowJo v10.7.1. Flow gating strategy is shown in **Supplemental Figure 3.S7**.

For the TBR5 biodistribution study, flow cytometry was performed as previously described.[183] The cells were incubated in an Fc block (BD Biosciences; 553142) for 10 minutes at RT, stained for surface markers for 15 minutes at RT, washed with a FACS buffer containing PBS with 2% (v/v) FBS, and resuspended in the FACS buffer for flow analysis on a Miltenyi MACSQuant Analyzer 10 or 16. The eBioscience™ Foxp3/transcription factor staining buffer kit (Fisher Scientific; 00-5523-00) was used for intracellular staining. After surface staining, the cells were fixed and permeabilized for 20 minutes at 4°C before staining for intracellular markers for 30 minutes at 4°C. To quantify cell viability, a Ghost Dye Red 780 viability marker (1:4000, Cell Signaling Technology; 18452S) was used. The following anti-mouse antibodies were used: CD45 BV510 (1:1600, BioLegend; 103138), CD3 FITC (1:200, BioLegend; 100204), CD4 PerCP-Cy5.5 (1:600, BioLegend; 100540), CD8a PE (1:800, eBioscience; 12-0081-82), B220 e450 (1:400, ThermoFisher; 48-0452-82), NKp46 PE-Cy7 (1:200, BioLegend; 137618), CD11c PE (1:1000, BioLegend; 117308), CD11b e450 (1:1600, ThermoFisher; 48-0112-82), F4/80 PE-Cy7 (1:800, BioLegend; 123114), Ly6C FITC (1:4000, BioLegend; 128006), and Ly6G PerCP-Cy5.5 (1:800, BioLegend 127616). Flow cytometry data were analyzed with FlowJo v10.7.1. Representative gating strategies of ascites, tumors, and spleens are shown in **Supplemental Figures 3.S8-10**.

3.3.8 *In Vivo* Tumor Studies

Treatment of the ID8 ovarian tumor model was formulated as a late-stage disease treatment. Similar to uptake studies, $5x10^6$ ID8 ovarian tumor cells in 200 µL PBS were IP injected into 15 female C57Bl/6 mice (day 0) and allowed to develop tumors for 7 weeks.

Starting on day 49, mice received IP injections of 100 µL PBS, Scr-MnNPs, or IκBα-MnNPs for 3 consecutive days. MnNPs were given at a dose of 1 mg/kg. The mice were euthanized one day after the final treatment. Blood samples were collected for liver (aspartate aminotransferase, AST, and alanine aminotransferase, ALT) and kidney (blood urea nitrogen, BUN) enzyme measurements and the ascites volume was measured and collected. Normal ranges for serum AST, ALT, and BUN levels were referenced from the Vanderbilt University Translational Pathology Shared Resource TPSR). Tumors and spleens were then harvested. The ascites fluid was collected, centrifuged, and the supernatant stored for protein serum concentration analysis as described above. The remaining ascites cell pellet was further processed with RBC lysis as described above until the cell pellet was clear. The cell pellet was frozen at -80°C for RNA isolation. Tumors were weighed, cut in half, and one half was snap frozen in liquid nitrogen for RNA isolation. The other tumor half and the entire spleens were fixed in 10% formalin for 48-72 hours for histology before being switched to 70% EtOH. Processing, embedding and sectioning, and hematoxylin and eosin (H&E) staining of tumor tissue, as well as blood chemistry analyses, were performed by the Vanderbilt University Medical Center (VUMC) Translational Pathology Shared Resource (TPSR) core. H&E-stained tissues were imaged using the EVOS XL Core microscope (ThermoFisher) on 4x and 10x brightfield magnification.

The faster developing TBR5 model was used to model a more aggressive, early-stage treatment strategy. $5x10^6$ TBR5 ovarian tumor cells in 200 µL PBS were IP injected into 15 female FVB mice (day 0) and allowed to develop tumors for 7 days. A biweekly treatment was adopted to combat the aggressive growth. Mice received IP injections of 100 µL PBS, Scr-MnNPs, or IκBα-MnNPs on days 7, 10, 14, 17, and 21 and the mice were sacrificed on day 22. For the extended study, additional MnNP treatments were administered on days 24 and 28 before

euthanizing mice on day 29. Similar to the ID8 model, blood samples and ascites were collected immediately after takedown before surgically removing the spleens and tumors. The ascites was centrifuged and supernatant collected. The tumors were weighed and then split into two samples: one for fixation and one for snap freezing for RNA isolation. Spleens were fixed as previously described. The same analyses performed on the ID8 ovarian tumors were repeated here. For flow cytometry analysis, CD3 APC (1:200, BioLegend; 100236) and CD8a AF488 (1:1600, BioLegend; 100723) were used in place of CD3 FITC and CD8a PE used for biodistribution. The rest of the panel was the same with the addition of the following anti-mouse antibodies: CD206 APC (1:500, BioLegend; 141708), FOXP3 PE (1:125, ThermoFisher; 12-5773-82), and PD-1 PE (1:100, BioLegend; 135206). Flow gating strategy was repeated as previously shown. To visualize tumor cells populations, cells were gated on forward scatter (FSC) vs side scatter (SSC), single cells (FSC-area vs FSC-height), live/dead, and CD45-. The CD45- cells were visualized again as FSC vs SSC where a clear population of "big" SSC-high (SSChi) cells were present only in cells from the solid tumors and ascites, but not the spleen. Representative tumor cells gating is shown in **Supplemental Figure 3.S11**.

3.3.9 Immunofluorescent Staining for Confocal Imaging of Tumor Sections

The protocol of immunofluorescent staining and analysis has been previously described.[167] To evaluate CD8 T cell infiltration, the primary antibody rat anti-mouse CD8 (Novus Biologicals; BP1-49045SS, 1:100) was used with a secondary goat anti-rat IgG Alexa Fluor 488 (Abcam; ab150157). Previously sectioned tumor samples were deparaffinized in Xylenes 2x for 10 minutes each. The samples were then rehydrated in 100% EtOH 2x for 2 minutes each, and then once each in 90%, 80%, and 70% EtOH (v/v in DI water) for 2 minutes. The slides were then incubated on a shaker in 0.1% Sudan Black Dye solution (diluted in 70%

EtOH) for 20 minutes before one more 2-minute wash in 50% EtOH. The sections were then permeabilized in 1X Tris-buffered saline (TBS) with 0.1% Tween 20 (TBST) for 20 minutes, rinsed in TBS for 5 minutes, and finally rinsed briefly with Milli-Q DI water. Antigen retrieval was performed by placing slides in a rice cooker with a 10mM sodium citrate solution (pH=6.0) with 0.1% Tween 20 and heated for 15-20 minutes before cooling at RT for 30 minutes. The slides were then washed 3x with TBS for 5 minutes each. Slides were treated with a blocking buffer comprised of 4 mL 0.5% TBST, 0.04 g bovine serum albumin, and 250 µL goat serum (Abcam; ab7481) for one hour in a humidified chamber at RT. The blocking buffer was aspirated and 100 µL of primary antibody was added and incubated at 4°C overnight. The primary antibody was aspirated and each slide washed 3x for 10 minutes each in TBST and then rinsed a final time with TBS for 5 minutes while shaking. The TBS was aspirated and 100 µL of secondary antibody was diluted in blocking buffer (1:1000) and incubated at RT in the dark for 2 hours. The slides were washed 3x for 10 minutes each in TBST followed by a single 5-minute wash in TBS on a shaker. DAPI (0.1 µ/mL) was added to each slide and incubated at RT for 5 minutes to stain cell nuclei. The slides were washed 2x for 3 minutes each in TBS and then 20 µL ProLong™ Gold Antifade Mountant (ThermoFisher; P36930) was added to preserve fluorescent signal. Slides were stored at 4°C until imaging was performed via fluorescent microscopy (Nikon C1si + confocal microscope system on Nikon Eclipse Ti-0E inverted microscope base, Plan APO VC 20× objective, 405/488 dichroic mirror). Images were analyzed using Fiji in ImageJ.[184]

3.3.10 RNA Extraction for Quantitative Reverse Transcription Polymerase Chain Reaction (qRT-PCR)

For *in vitro* BMDM experiments, RNA was isolated using the RNeasy Mini Kit (Qiagen; 74106) and residual DNA was removed using the RNase-Free DNase set (Qiagen; 79256). cDNA was synthesized with SuperScript IV reverse transcriptase kit (Invitrogen; 18090050). Quantitative reverse transcription polymerase chain reaction (qRT-PCR) was performed using SsoAdvanced Universal SYBR Green Supermix (Bio-Rad; 1725270) on a CFX96 real-time PCR instrument and software (Bio-Rad) through the VUMC Molecular Cell Biology Resource (MCBR) core.

For *in vivo* experiments, RNA was extracted from both the ascites cells and tumor cells using TRIzol™ (Invitrogen; 15596026) and a Direct-zol RNA Miniprep kit (Zymo Research; R2050). Snap frozen tumor samples were ground into small pieces with a mortar and pestle before suspending in 300 µL TRIzol solution. The ascites pellet was resuspended in 300 µL TRIzol solution. Both solutions were used with the Direct-zol RNA Miniprep kit following the manufacturer's instructions. Final RNA concentration was measured with a NanoDrop 200 spectrophotometer (Biotek). cDNA fabrication and qRT-PCR were performed as described above. All primer sequences are listed in **Supplemental Table 3.S2**. For all experiments, target genes were normalized to a housekeeping gene (B2M or GAPDH) to obtain the ΔCT value. All qRT-PCR data is shown as relative expression using the $2^{-\Delta\Delta CT}$ method.

3.3.11 Western Blot

Protein isolated from ascites cells in the TBR5 experimental model was used for western blot analysis of IκBα expression. Whole protein isolation, western blotting, and signal detection were performed as previously described.[185] Primary antibodies used were rabbit polyclonal anti-IκBα (1:100 dilution, Cell Signaling Technology; 9242). Equal loading was confirmed using

mouse monoclonal anti-histone H3 (1:1000 dilution, Cell Signaling Technology; 14269S) as a loading control. Uncropped blots are shown in **Supplemental Figure 3.S12.**

3.3.12 Statistical Analysis

All statistical analyses were performed using a one-way ANOVA with Tukey's multiple comparison test in the case of two or more groups, a two-way ANOVA with Tukey's multiple comparison test in the case of two or more groups in two or more sets, or a two-tailed student's t-test in the case of only two groups, all with $\alpha = 0.05$. Statistical analyses were performed using GraphPad Prism v8.4.3. All figures were made using Adobe Photoshop 2020 v21.2.2.

3.4 Results

3.4.1 Quantifying Changes in NF-κB Activation in MnNP-Treated Macrophages

Knockdown of IκBα by targeted siRNA results in activation of the canonical NF-κB pathway known to promote inflammation through the M1 polarization of macrophages.[41,42] To assess activation of canonical NF-κB following treatment with IκBα siRNA loaded into MnNPs, immortalized BMDMs derived from NF-κB green fluorescent protein (GFP)-luciferase (NGL) reporter transgenic mice (FVB background) were cultured.[45,180] The NGL-BMDMs express a GFP-luciferase fusion protein in response to NF-κB activation allowing for luminescence as a method to quantify M1 polarization. BMDMs were polarized to an M2 phenotype via interleukin-4 (IL-4) stimulation for 24 or 48 hours before treating with MnNPs for 24 hours. Control groups of M1-polarized or unpolarized (M0) BMDMs were also included. M1 polarization was induced via treatment with interferon-γ (IFN-γ) and lipopolysaccharide (LPS) for 24 hours. For the 48 hour-stimulated M2 BMDMs, the IκBα-MnNP treatment significantly increased luminescence compared to both the PBS control and the Scr-MnNP treatment,

indicating activation of canonical NF-κB (**Figure 3.1**). M2 macrophages treated with MnNPs loaded with IκBα siRNA activated NF-κB to levels equivalent to M1 macrophages treated with PBS as estimated by luminescence intensity, indicating a robust shift in macrophage phenotype induced by IκBα-MnNP treatment. Interestingly, for the 24 hour-stimulated M2 BMDMs, both Scr-MnNP and IκBα-MnNP treatments increased luminescence, indicating potential activation of canonical NF-κB due to the mannosylated carriers themselves. There was no significant change in luminescent intensity for Scr-MnNP treatments between 24- and 48-hour IL-4 stimulation, while the IκBα-MnNP treatment significantly increased luminescent intensity for the longer stimulated M2 macrophages.

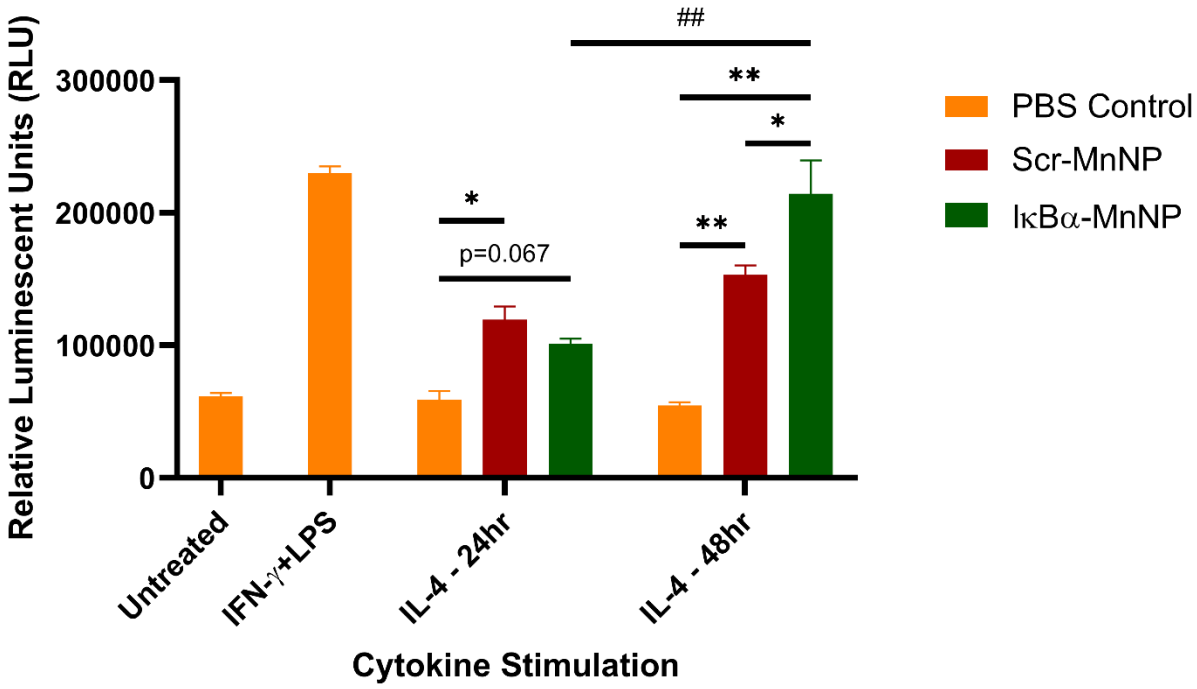

Figure 3.1: NF-κB Activation in MnNP-Treated Polarized NGL-BMDMs. BMDMs isolated from NGL reporter mice were polarized to M1 (IFN-γ+LPS) or M2 (IL-4, 24 or 48 hours) or left unpolarized (M0) and examined for luminescent readout. The M2-polarized BMDMs were also treated with MnNPs for 24 hours before measuring luminescence. For the 24 hour-polarized M2 BMDMs, the Scr- and IκBα-MnNP treatments both increased NF-κB activation, but this effect was more pronounced in the 48-hour IL-4-treated BMDMs, especially with the IκBα-MnNP (n=3, *p<0.05 **p<0.001 ##p<0.001).

3.4.2 Biodistribution Analysis of MnNPs in a Late-Stage ID8 Ovarian Tumor Model

Biodistribution studies were conducted to evaluate *in vivo* delivery of MnNPs to specific cell populations. Female C57Bl/6 mice received intraperitoneal (IP) injections of $5x10^6$ ID8 ovarian tumor cells and were monitored for tumor development for 8 weeks. The ID8 model is slow-developing (>7 weeks) and is often used for studying late-stage ovarian cancer.[176,186,187] These mice received a single IP injection of MnNPs loaded with Cy5-labeled double-stranded DNA (Cy5-MnNPs) 8 weeks after tumor induction. The ascites fluid, tumors, and spleens were collected from the mice 24 hours after MnNP administration and processed for flow cytometry. Cy5 fluorescence was used to estimate MnNP biodistribution. The general cell population was gated on forward-scatter (FSC) vs. side-scatter (SSC). Immune cells were gated on CD45 followed by F4/80 vs. Gr-1 to visualize immune cell subsets. The MnNPs were located almost exclusively in the tumor and ascites with 15.4% of cells in the tumor and 59.7% of cells in the ascites gating positive for Cy5 compared to <1% of cells in the spleens (**Figure 3.2A**). Additional gating on the general macrophage population (CD45+/F4/80+) revealed that 75.7% of TAMs and 61.3% of the macrophages in the ascites were associated with Cy5-MnNPs, consistent with the anticipated delivery of cargo to these cell types in the peritoneal cavity (**Figure 3.2B**). Gr-1 gating demonstrated the same trends in both mature macrophage (F4/80+/Gr-1-) and myeloid cell (F4/80-/Gr-1+) populations, with high percent uptake in the tumor and ascites and negligible delivery to the spleen (**Figure 3.2C,D**). These results suggest that even a single IP injection of MnNPs examined after 24 hours is able to deliver the payload to high percentages of macrophages in the tumors and ascites.

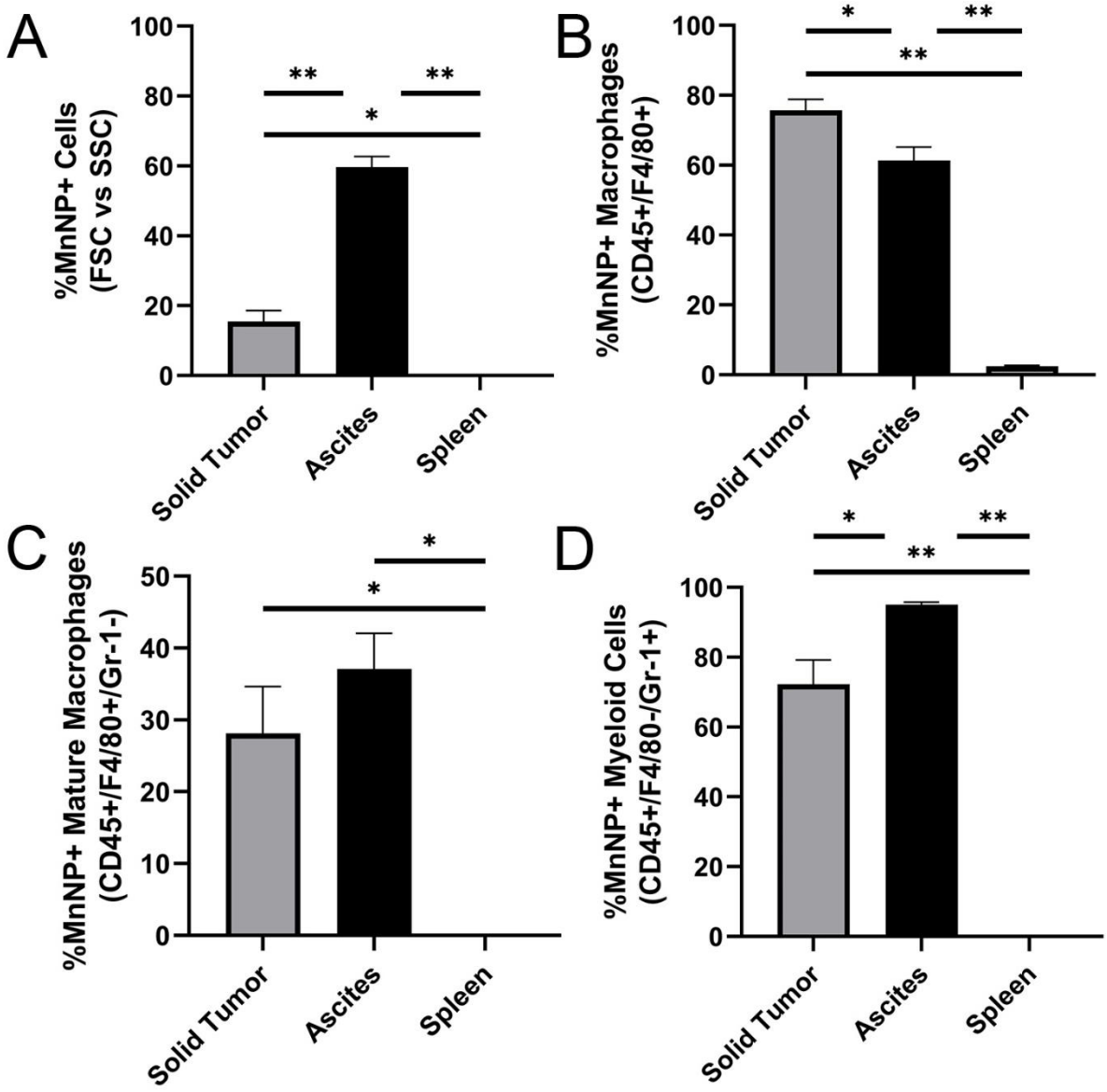

Figure 3.2: MnNP Biodistribution in ID8 Tumor Model. C57Bl/6 mice bearing ID8 ovarian tumors were treated IP with Cy5-MnNPs. After 24 hours, the ascites, tumors, and spleens were collected for flow cytometry analysis. (**A**) The general cell population gated on FSC vs. SSC revealed a high percentage of MnNP+ cells in the ascites and almost 20% of cells in the tumor, but negligible delivery to any cells in the spleen. (**B**) Gating on CD45+/F4/80+ macrophages revealed that about 60% of macrophages in the ascites and ~75% of TAMs were MnNP+. Additional gating for (**C**) Gr-1- mature macrophages and (**D**) Gr-1+ myeloid cells also revealed high percentages of MnNP uptake in the ascites and tumor (n=3, *$p<0.05$ **$p<0.001$).

3.4.3 Endpoint MnNP Treatment of Late-Stage Disease Reveals Encouraging Effects

To evaluate the anti-tumor efficacy of MnNP treatments in late-stage disease, ID8 ovarian tumor cells were injected into the peritoneal cavity of female C57Bl/6 mice and allowed to progress for 7 weeks. Once these mice approached humane endpoint, MnNP treatments were administered by IP injection daily for 3 consecutive days. The treatment groups included a PBS control or MnNPs containing the Scr siRNA (Scr-MnNPs) or the IκBα siRNA (IκBα-MnNPs). Mice were euthanized 24 hours after the final injection (**Figure 3.3A**). This model was chosen because ID8 ovarian tumors are known to produce high ascites volumes, which comprise large populations of immunosuppressive macrophages, and reflect a significant subpopulation of human ovarian cancers.[177] In this way, the ID8 model could be used to evaluate the effects of MnNP-mediated siRNA delivery to immunosuppressive macrophage populations in hopes of seeing changes in the immune cells. Additionally, a 3-consecutive day treatment at endpoint was used to evaluate toxicity of multi-day MnNP injections. Importantly, limited toxicity was observed in mice treated with MnNPs with serum levels of aspartate aminotransferase (AST), alanine aminotransferase (ALT), and blood urea nitrogen (BUN) all falling within normal ranges (indicated as horizontal dotted lines) despite slight elevation in AST levels in the IκBα-MnNP treatment (**Figure 3.3B-D**). While the 3-day MnNP treatment did not result in toxicity, there was also no significant change in tumor burden as evaluated by ascites volume and tumor weight at endpoint (**Figure 3.3E,F**). The trend of decreasing ascites volume from 5.1±1.4 mL in the control to 2.8±1.1 mL in the IκBα-MnNP treatment provided encouragement that beneficial changes were occurring, but this effect was minimal due to the late-stage treatment of advanced disease. However, hematoxylin and eosin (H&E) staining of tumor sections revealed visible differences in the treatment groups, most noticeably areas of decreased epithelial cellularity that

could result from an increase in cell death (**Supplemental Figure 3.S13**). For cells collected from the ascites, there was a significant increase in RNA expression of the M1 marker C-C motif chemokine ligand 3 (CCL3) and a trend of increased tumor necrosis factor-α (TNF-α) expression in the IκBα-MnNP treatment compared to control (**Figure 3.3G,H**). Finally, there was a significant decrease in immunosuppressive interleukin-6 (IL-6) expression in both MnNP treatments (**Figure 3.3I**). Expression of an additional M1 marker C-X-C motif ligand 9 (CXCL9), a chemokine responsible for attracting CD8 T cells, trended upward in the ascites, while CCL3 and TNF-α expression in cells from solid tumors also trended upward but not significantly (**Supplemental Figure 3.S14**).

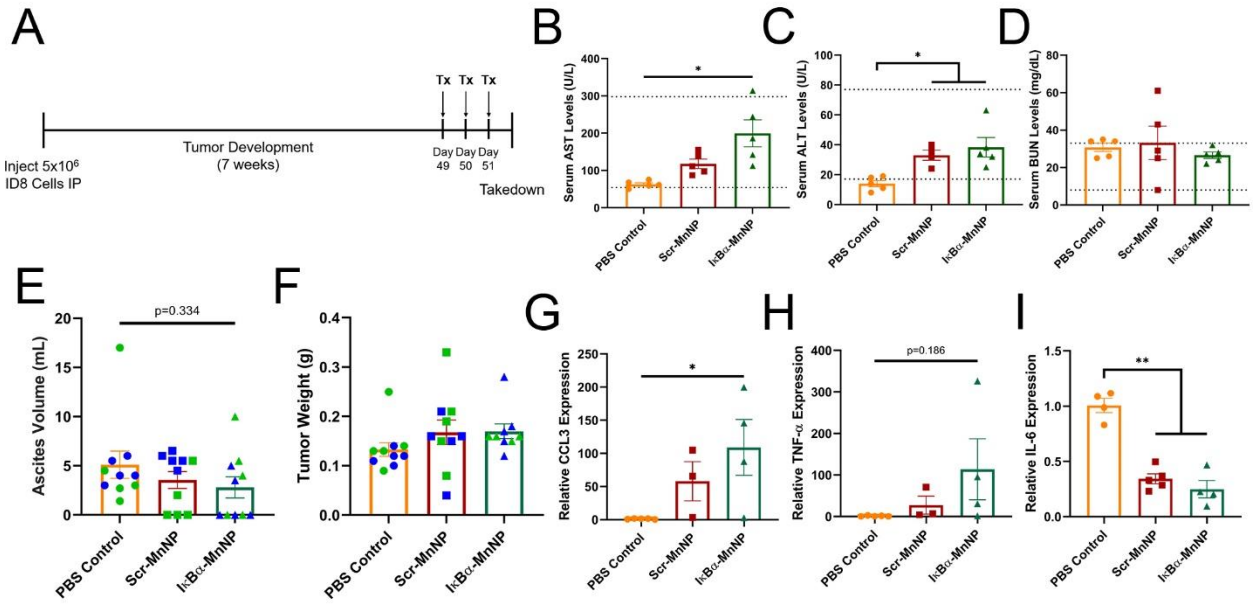

Figure 3.3: Endpoint Analysis of ID8 Tumors Treated with Therapeutic MnNPs. (**A**) Treatment schematic for development of ID8 ovarian tumor model and 3-day MnNP treatment. Serum levels of (**B**) AST, (**C**) ALT, and (**D**) BUN were evaluated at endpoint. AST and ALT were significantly elevated in IκBα-MnNP treatment, but still within normal ranges while BUN levels were unchanged (n=5, *p<0.05). Changes in (**D**) ascites volume and (**E**) tumor weight at takedown (n=10, color indicates experimental groupings). RNA isolated from the ascites cells revealed increases in the inflammatory cytokines (**G**) CCL3 and (**H**) TNF-α (PBS control n=5, Scr-MnNP n=3, IκBα-MnNP n=4, *p<0.05). (**I**) Cells in the ascites also significantly decreased in expression of IL-6 in both MnNP treatments (PBS control and IκBα-MnNP n=4, Scr-MnNP n=5, *p<0.05).

3.4.4 Biweekly Treatment of Ovarian Tumors Reveals Macrophage-Specific Delivery in Ascites and Solid Tumors

To evaluate the effects of repetitive IκBα-MnNP treatment on a more aggressive tumor model, the TBR5 ovarian model in FVB mice was adopted. Biodistribution was assessed to confirm preferential *in vivo* delivery of MnNPs to macrophage populations in the ascites and solid tumor. The TBR5 model exhibits rapid disease progression (over the course of 28 days) and provides a platform to characterize the impact of a feasible treatment schedule in an aggressive model. Due to rapid progression, a biweekly (twice per week) treatment regimen for 2 weeks (total of 4 treatments) was used. Cy5-MnNPs were delivered via IP injection to evaluate biodistribution. One day after the final treatment, the ascites, solid tumors, and spleens were collected and processed for flow cytometry analysis. Initial gating on the immune cell population (CD45) revealed that 89% of CD45+ immune cells in the ascites and 34.1% of CD45+ immune cells in the solid tumor were positive for Cy5-MnNPs compared to 11.4% and 2.6% uptake in the non-immune cell (CD45-) populations of the ascites and tumors, respectively (**Figure 3.4A**). Additionally, there was negligible uptake (<1%) in any cells in the spleen, supporting our hypothesis that IP delivery can abrogate the off-target delivery normally associated with IV treatment.

Additional gating on specific immune cell populations was performed to examine macrophage targeting. Lymphocyte gating included CD45+/CD3+/CD4+ and CD45+/CD3+/CD8a+ markers for CD4 and CD8 T cells, respectively. B cells were gated CD45+/CD3-/B220+ and natural killer (NK) cells were gated CD45+/CD3-/NKp46+. Myeloid populations were gated CD45+/CD11c+/CD11b- for dendritic cells (DCs) and CD45+/CD11c-/CD11b+ for macrophages (F4/80hi) and monocytes (F4/80lo). Macrophages and monocytes

were further gated Ly6C+/Ly6G- to remove neutrophils and eosinophils.[188] When examining delivery to the macrophage (CD11b+/F4/80hi), monocyte (CD11b+/F4/80lo), and other immune cell (CD11b-/F4/80-) populations in the different organs, the Cy5-MnNPs were almost exclusively localized to the macrophages and monocytes in the ascites and tumors with negligible uptake in the spleen (**Figure 3.4B**). In tumors, MnNP delivery was significantly greater in macrophages compared to all other immune cell populations (**Figure 3.4C**). Additionally, 85.7% of macrophages and 84.3% of monocytes in the ascites were Cy5-MnNP+, which was significantly elevated compared to all other immune cell populations (**Figure 3.4D**).

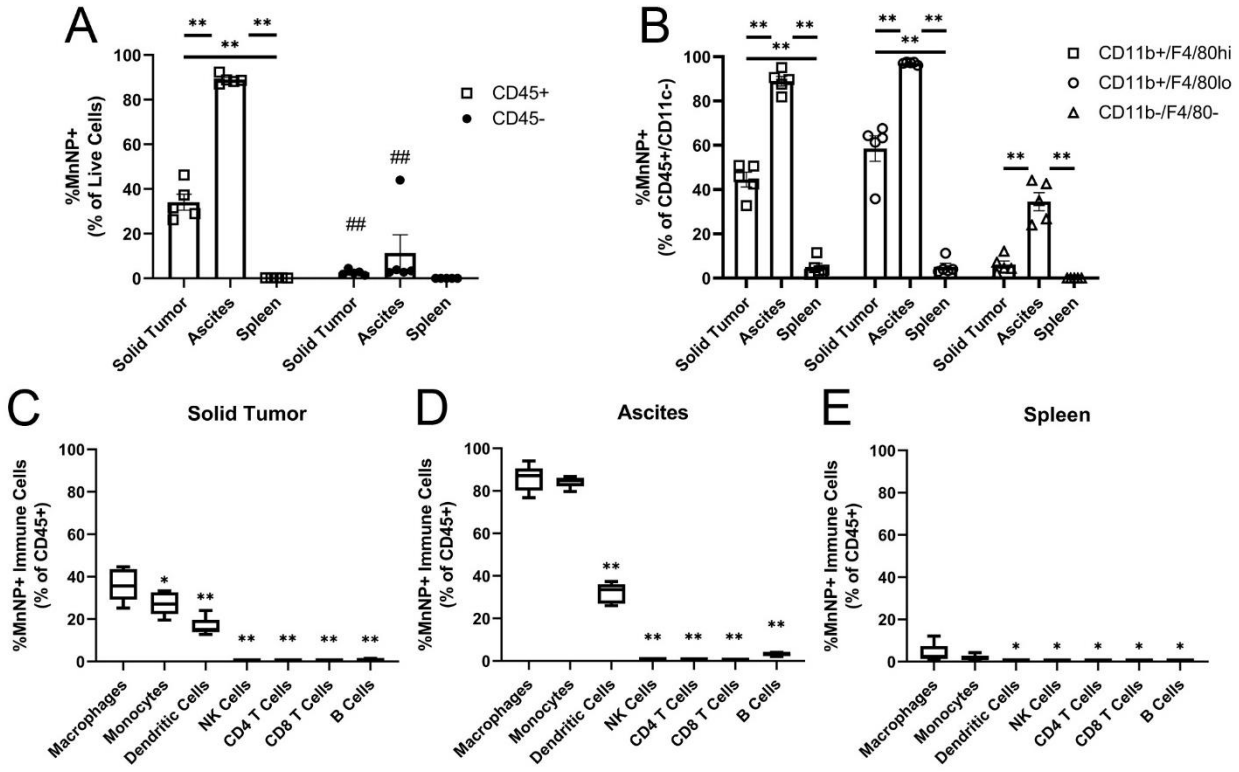

Figure 3.4: Biodistribution of Biweekly MnNP Treatment in TBR5 Model. MnNP biodistribution in the TBR5 ovarian tumor model was examined via flow cytometry. (**A**) Cy5-MnNPs demonstrated significant increase in uptake in CD45+ immune cells in both the ascites and solid tumor compared to the CD45- populations (n=5, ##p<0.001). MnNPs were also associated with over 89% of CD45+ cells in the ascites and 30% of CD45+ cells in the solid tumor (**p<0.001). (**B**) Direct comparison of the different organs for macrophages, monocytes, and other immune cells revealed targeted delivery to the tumors and ascites with minimal off-target delivery to the spleens (n=5, **p<0.001). Macrophages displayed significantly elevated %MnNP+ levels compared to most other immune cells in the (**C**) tumor, (**D**) ascites, and (**E**) spleen. The %MnNP+ macrophage population was significantly higher than all other immune cell subtypes in the tumor, and higher than all other subtypes except monocytes in the ascites and spleen (n=5, *p<0.05, **p<0.001).

Finally, only 3.9% of macrophages in the spleen exhibited uptake of Cy5-MnNPs, demonstrating limited off-target delivery (**Figure 3.4E**). These results demonstrate the intended targeting to TAMs as well as macrophages in the ascites with minimal off-target delivery to other immune cells or organs. Additionally, the biweekly treatment adopted for the aggressive tumor model exhibited greater MnNP uptake than observed in the previously used late-stage ID8 model.

3.4.5 Delivery of IκBα-MnNPs to TAMs Prevents Ascites Accumulation and Alters Immune Cell Phenotype

The TBR5 ovarian tumor model was used to elucidate the effects of IκBα-MnNP treatment on an aggressive ovarian tumor model. After tumor cell injection on day 0, MnNPs were injected on days 7, 10, 14, 17, and 21 before mice were humanely sacrificed on day 22 (**Figure 3.5A**). Serum was collected and evaluated for AST, ALT, and BUN levels as previously described and, similar to the ID8 model, there was no detectable toxicity as a result of MnNP treatment (**Figure 3.5B-D**). In contrast to the ID8 model, MnNP treatment in the TBR5 model significantly decreases ascites accumulation and slightly decreases tumor burden (**Figure 3.5E,F**). Additionally, the weight gain associated with ascites fluid buildup in the PBS control group was abrogated in the MnNP-treated mice (**Supplemental Figure 3.S15**).

Similar to the ID8 model, there were clear indications of changes in tumor tissue as evaluated by H&E staining of tumor sections. The PBS control tumor appeared to only contain healthy cells while the Scr-MnNP treatment revealed some indications of depleted tumor cell populations based on observations in decreased cellularity (**Supplemental Figure 3.S16**). Meanwhile, the IκBα-MnNP treatment appeared to result in immune cell infiltration as evidenced by the increase in darker stained areas in the tumor sections (**Supplemental Figure 3.S16**). In both the ascites and tumor cells, there was a trend of decreasing IκBα RNA expression

in mice treated with IκBα-MnNPs, but this change was not significant (**Supplemental Figure 3.S17**). Worthy of note was the observation of a relative increase in IκBα expression between the PBS control and the Scr-MnNP treatment in the ascites, which was abrogated by IκBα-MnNP treatment. However, there was a clear decrease in IκBα protein levels in the cells isolated from the ascites, indicating functionality of the IκBα siRNA *in vivo* (**Figure 3.5G**). Delivery of IκBα-MnNPs also significantly increased expression of CXCL9 (M1 marker) and decreased Arginase-1 expression (M2 marker), while both MnNP treatments significantly decreased IL-6 expression

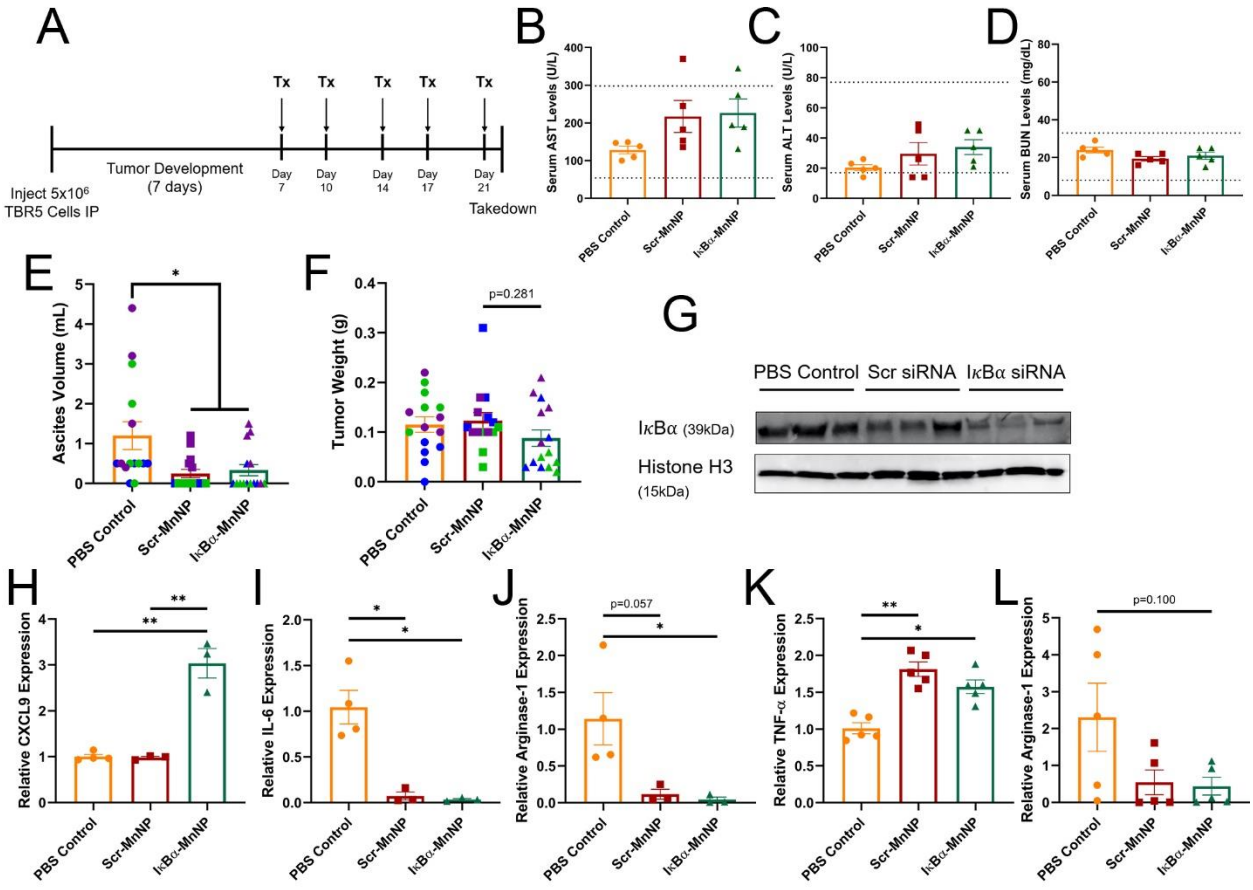

Figure 3.5: Endpoint Analysis of Biweekly MnNP Treatment in TBR5 Model. (**A**) Treatment schematic for development of TBR5 ovarian tumor model and biweekly MnNP treatment. Serum was collected at endpoint to evaluate circulating levels of (**B**) AST, (**C**) ALT, and (**D**) BUN (n=5). Changes in (**E**) ascites volume and (**F**) tumor weight at endpoint (n=15, *p<0.05). (**G**) Western blot analysis of cells in the ascites revealed changes in IκBα protein levels (cropped image of western bands). RNA was collected from ascites cells and examined for expression of (**H**) CXCL9, (**I**) IL-6, and (J) Arginase-1 (PBS Control n=4, Scr- and IκBα-MnNP n=3, *p<0.05, **p<0.001). RNA collected from tumor cells was examined for expression of (**K**) TNF-α and (**L**) Arginase-1 (n=5, *p<0.05, **p<0.001).

(**Figure 3.5H-J**). Importantly, MnNP treatment in TBR5 mice also significantly increased expression of the inflammatory cytokine TNF-α in the tumor, indicating a shift in the tumor microenvironment (**Figure 3.5K**). Finally, there was a 5.2-fold decrease in Arginase-1 expression in the IκBα-MnNP treatment compared to control (**Figure 3.5L**). Immunofluorescent (IF) staining of tumor sections for CD8 T cells was used to visualize T cell infiltration into treated tumors, which suggested an increase in CD8 T cells in tumors treated with IκBα-MnNPs (**Supplemental Figure 3.S18**).

3.4.6 Extended IκBα-MnNP Treatment Alters Immune Cell Populations and Provides Robust Anti-Tumor Immune Response

An extended MnNP treatment in the TBR5 model was used to further evaluate treatment effects on tumor progression and immune cell composition. TBR5 cells were injected IP and treatments started on day 7 and administered twice per week for 7 total treatments (**Figure 3.6A**). The extended treatment significantly reduced both ascites volume accumulation and final tumor weight in both MnNP treatments, with a slightly more pronounced effect in the IκBα-MnNP treatment (**Figure 3.6B,C**). The weight gain associated with ascites development was again abrogated similar to the previous study (**Supplemental Figure 3.S19**). Flow cytometry analysis was conducted to evaluate changes in immune cell populations after treatment. The percent of tumor cells (gated CD45-/SSChi) in the ascites and tumor was significantly decreased in the IκBα-MnNP treatment compared to the PBS control (**Figure 3.6D,E**). Similar to previous results, the Scr-MnNP treatment led to a non-significant decrease in the percent of tumor cells compared to the control, indicating a slight therapeutic effect of the MnNPs themselves. Furthermore, the immune cells in the tumor and ascites were altered due to MnNP treatments. The percent of M2-like TAMs (F4/80int/CD206+) was significantly decreased by IκBα-MnNP

treatment in both the tumor and ascites compared to both the PBS control and Scr-MnNP treatment (**Figure 3.6F**). The Scr-MnNP treatment significantly decreased the percent of M2-like TAMs compared to the control, but not to the level of IκBα-MnNPs. Similarly, the ratio of M2/M1-like TAMs was significantly decreased in both MnNP treatments, with the effect being more pronounced in the IκBα-MnNP treatment (**Figure 3.6G**). Additional analyses revealed that IκBα-MnNP treatment significantly increased the percent of classical (M1-like) monocytes (F4/80int/Ly6C+/Ly6G-) in the ascites and significantly increased the percent of NK cells (CD3-

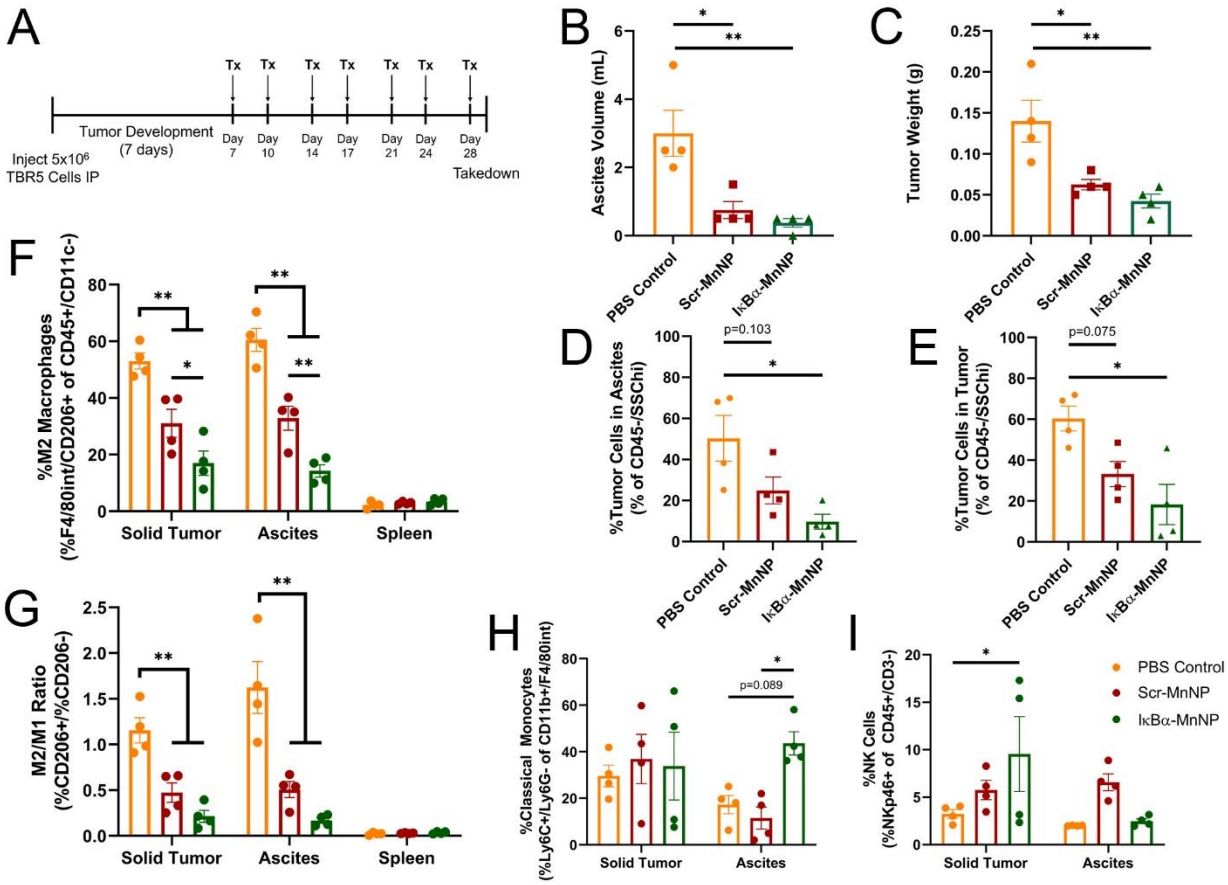

Figure 3.6: Increased Therapeutic Benefit in Extended MnNP Treatment Model. (**A**) Treatment schematic for extended MnNP treatment in the TBR5 tumor model. Changes in (**B**) ascites volume and (**C**) tumor weight at endpoint (n=4, *p<0.05, **p<0.001). Flow cytometry gating on CD45-/SSChi cells revealed significant changes in the percent of tumor cells in the (**D**) ascites and **(E**) tumors. Cells gated on F4/80int/CD206+ revealed significant decreases in (**F**) the percent of M2-like TAMs and (**G**) the ratio of M2 (CD206+):M1 (CD206-) TAMs. The cells also revealed significant increases in (**H**) classical monocytes (F4/80int/Ly6C+/Ly6G-) in the ascites and (**I**) NK cells (CD3-/B220-/NKp46+) in the tumor (n=4, *p<0.05, **p<0.001).

/B220-/NKp46+) in the tumor (**Figure 3.6H,I**). Quantification of all immune cell populations also revealed trends of increasing CD8 T cells and dendritic cells while the percent of CD4 T cells was decreased (**Supplemental Figure 3.S20**). Taken together these results demonstrate the robust anti-tumor effects of IκBα-MnNP treatment due to altering the tumor immune microenvironment.

3.5 Discussion

Repolarizing TAMs for cancer immunotherapy is a rapidly growing field of study with encouraging early results.[37,82] Our group has previously identified RNA interference (RNAi) as an ideal candidate for altering TAM phenotype.[45] We have also demonstrated the anti-tumor effects of repolarizing TAMs by activating canonical NF-κB specifically in macrophages.[167] One of the primary challenges associated with translating this successful approach to intact living systems is the need for strongly preferential delivery of the siRNA payload to TAMs *in vivo*. Our group has made tremendous progress in developing a polymeric nanoparticle system capable of targeting M2-like TAMs while simplifying and optimizing the fabrication process.[69,70,166] Additionally, our combined expertise in studying ovarian tumors along with the potential benefits of relatively localized delivery via IP injections led to our decision to evaluate MnNP treatment in models of ovarian cancer.[177] Additionally, Zhang, et. al., recently demonstrated ovarian tumor regression following IP administration of a different polymeric nanoparticle system loaded with mRNA encoding interferon regulatory factor 5 (IRF-5) to TAMs. However, this delivery system produced significant off-target IRF-5 activation in the spleens, causing M1 macrophage activation outside the TME.[82] In this study, we demonstrate the advantages of treating ovarian tumor-bearing mice with siRNA-loaded MnNPs to evaluate *in vivo* targeting to TAMs, changes in immune cell composition, and subsequent effects on tumor progression.

The initial *in vitro* study was designed to evaluate the ability of IκBα siRNA to activate the canonical NF-κB pathway in M2-polarized BMDMs. We had previously shown the knockdown of IκBα RNA expression and protein levels in M2 BMDMs treated with IκBα-MnNPs.[166] This study demonstrated that the knockdown of IκBα in BMDMs also corresponded with increased canonical NF-κB activation as evaluated by luminescent readout. This study was also the first to reveal the potential for the mannosylated carrier to stimulate pro-inflammatory effects in macrophages even with an inert siRNA payload. While the IκBα-MnNP increased luminescent readout to the level of the M1 control BMDMs, the Scr-MnNP also had an intermediate effect in increasing NF-κB activation. This result is consistent with other reports of inert particles decorated with mannose modulating macrophage phenotype and promoting inflammation with modest anti-tumor effects.[82,189] Jaynes, et al., have recently shown that even specific binding to the CD206 mannose receptor alters the receptor conformation and leads to subsequent changes in macrophage phenotype.[190] This phenomenon can provide extra benefit for our purposes as we consistently observed a synergistic effect of the MnNP loaded with IκBα siRNA producing a robust repolarization of macrophages to a pro-inflammatory phenotype.

After establishing NF-κB activation *in vitro*, the MnNPs were used to treat two separate models of ovarian cancer. These models were chosen to evaluate two forms of treatment: late-stage treatment of advanced disease (ID8) and early-stage, repetitive treatment of an aggressive disease model (TBR5). To examine biodistribution in the late-stage model, the mice developed tumors until close to humane endpoint (based on swelling due to ascites buildup) and then a single MnNP dose was administered 24 hours before collection. These results revealed that even 24 hours after a single treatment, MnNPs preferably associated with macrophages in the ascites and tumor with no targeting to the spleen. This experiment confirmed our hypothesis that an IP

injection for treating ovarian tumors could nullify the concerns often associated with IV injection of nanoparticles. Furthermore, the addition of the mannose moiety on the NPs prevented any off-target delivery to the spleen observed by other groups using non-decorated NP systems.[82] By injecting directly into the peritoneal cavity, the MnNPs were immediately exposed to the desired cell population in the target organ where they deliver a payload with improved specificity mediated via active endocytosis due to mannose conjugation. One of the major drawbacks with IV delivery of nanoparticles is the reliance on the enhanced permeability and retention (EPR) effect. While the EPR effect has been a cornerstone of developing nanomaterials therapies to target solid tumors, recent evidence shows the many challenges still hinder tumor targeting.[191–193] Furthermore, to ensure a therapeutic dose actually reaches the tumor, higher concentrations of nanoparticles are needed for IV delivery compared to IP, which is already localized to the tumor site. These biodistribution results validate our strategy for targeting TAMs in ovarian tumors via IP injections, and they demonstrate the reduced off-target delivery due to mannose conjugation which promotes active macrophage uptake in the ascites and tumor.

To evaluate therapeutic efficacy of MnNP treatment in ID8 tumors, we administered treatments on three consecutive days. One of the primary concerns with multi-day treatments was the toxicity potentially associated with nanoparticle injection. However, all treatments resulted in serum measurements within normal ranges indicating the safety of consecutive day treatments. This result is important as this regimen could be necessary for treating late-stage disease with a minimal timeframe available for treatment. These results from treating the late-stage model with therapeutic IκBα-MnNPs were encouraging because, although tumor burden was not significantly affected because of the late-stage treatment, the trend of decreased ascites volume provides positive signs of a therapeutic effect. The potential for reducing ascites

accumulation after only 3 days of treatment at late stages of disease progression is promising for the future of TAM-targeted immunotherapies, especially as a potential treatment for overcoming chemoresistance. Ascites development is commonly associated with ovarian cancer (present in over one-third of patients), is linked to worse disease prognosis, and contributes to the development of chemoresistance due to the large population of immunosuppressive cells.[161–163] These early indications reveal treatment with MnNPs can alter the tumor microenvironment in ways that may provide synergy with other approved therapies to produce more pronounced anti-tumor effects. Also, although tumor weight did not change, positive anti-tumor effects were observed in H&E staining of the solid tumor indicating the MnNPs could reach the tumor and cause some histological changes, even following only 3 days of treatment.

Furthermore, positive effects were seen in the changes of RNA expression in ascites cells, such as the significant increase in M1 marker CCL3 and the significant decrease in IL-6. The decrease in IL-6 expression is important since this cytokine is released by immunosuppressive TAMs and has a direct stimulatory effect on ovarian tumor cells.[194,195] Additionally, the observed increase in IκBα expression in the Scr-MnNP treatment compared to control indicates the effect of the negative feedback loop of IκBα production.[41] Consistent with our other findings, the Scr-MnNP treatment leading to an increased M1 response would subsequently cause an increase in IκBα production as the feedback loop in the macrophages is activated. The decrease in IκBα expression between the Scr-MnNP and IκBα-MnNP groups reveals the potential mechanism leading to a synergistic repolarization of TAMs. While both treatments potentially cause M1-induced inflammation, the IκBα-MnNP treatment prevents the feedback loop of producing more IκBα from occurring, allowing for a more robust macrophage repolarization. There were also trends of increasing CCL3 and TNF-α expression in the tumor

cells, indicating a slight pro-inflammatory effect in the solid tumors. These results suggest that the IκBα-MnNPs are altering the TME in the ascites, but at this timepoint in response to a short-term treatment, the solid tumor is not significantly altered. These results align with our observations of ascites volume decreasing after IκBα-MnNP treatment but not the tumor weight. Overall, treatment with IκBα-MnNPs provides benefits in the context of late-stage disease but will likely need to be used in combination with other therapies or started earlier in the disease development to produce robust anti-tumor effects. These encouraging results in a late-stage model indicate a potential future avenue for evaluating the synergistic effects of combining IκBα-MnNPs with chemotherapeutics to overcome the chemoresistance often associated with late-stage ovarian tumors. Combination therapies will be necessary for late-stage tumor treatment since single therapies are unable to fully overcome the immunosuppressive TME.

The encouraging results in late-stage treatment provided insight into the effects IκBα-MnNPs have on immune cells in the TME. A second model using TBR5 ovarian tumors was adopted to examine early-stage treatments in an aggressive model. To combat the more aggressive tumor model, a biweekly treatment regimen was implemented. This treatment was also possible since the mice were not close to humane endpoint at the start of the treatment. Biodistribution was again examined in the biweekly model with a comprehensive immune cell panel to determine the efficiency of specific targeting to macrophages. These results demonstrated the preferential delivery of MnNPs to the targeted cell populations (macrophages and monocytes) that express the CD206 mannose receptor. Significant MnNP delivery to the TAM populations (89% in the ascites and 34% in the tumors) is essential for altering macrophage phenotype to overcome the immunosuppressive TME. Furthermore, the low uptake in CD45- cells, which includes tumor cells, is important for preventing off-target delivery of

IκBα siRNA and therefore unwanted activation of NF-κB in cells besides macrophages. There was also minimal uptake in all other immune cells in the ascites and tumors, and less than 5% of any immune cell population in the spleen gated positive for MnNP delivery. These results indicate that the IP delivery is effectively localizing the MnNP delivery to the peritoneal cavity and increasing to the biweekly treatment does not increase the amount of nanoparticle dosage that escapes the peritoneum. Importantly, these results show improvements over previous studies using a similar NP system loaded with mRNA that did not include a targeting moiety, which resulted in significant off-target delivery to the spleens even after IP injections.[82] To achieve a macrophage-dependent anti-tumor immune response, it is important to repolarize a large enough population of the TAMs so that the M1 macrophages can overcome the immunosuppressive TME and increase inflammation and immune activation while also limiting potential systemic toxicity due to off-target delivery.

The therapeutic effect of IκBα-MnNP was prevalent in the TBR5 model. Importantly, increasing to a biweekly MnNP treatment did not increase toxicity based on AST, ALT, and BUN levels in the serum. These treatments also significantly decreased ascites volume, indicating an effect of the mannosylated carriers themselves, similar to the results seen in canonical NF-κB activation. The beneficial effect of mannosylated carriers alone on tumor suppression and polarizing macrophages toward the M1-like phenotype has been previously reported and is therefore not surprising in this context.[82,196] In fact, the potential combination of mannosylated carriers with IκBα siRNA could combine for a more robust anti-tumor effect. The tumor weights were not significantly altered in any of the treatment groups, likely due to low overall tumor burden as seen by the small tumor weights, but there was a clear trend in decreasing tumor mass in the IκBα-MnNP treatment. H&E staining of the tumor sections

revealed changes in tumor tissue histology and IF staining for CD8 T cells revealed a clear increase in T cell infiltration in the IκBα-MnNP treatment. This result is crucial to the future of developing macrophage-based immunotherapies as it supports the hypothesis that activating inflammatory macrophages can also "prime" solid tumors to be more responsive to T cell-based immunotherapies. This result is also supported by the significant increase in RNA expression of CXCL9 in the ascites, which is a chemokine produced by M1 macrophages to attract T cells and induce a Th1 response.[197] The evidence of increased T cell infiltration supports the potential future combination of MnNP treatment with immune checkpoint blockades which necessitate T cell infiltration for functionality. Increased tumor-infiltrating T cells and significant reduction in ascites volume associated with IκBα-MnNP treatment support the future directions of utilizing MnNPs for tumor treatments in combination therapies.

Western blot analysis of cells in the ascites revealed that the IκBα-MnNPs reduced IκBα protein levels, contributing to changes in immune cell composition. This change was also evidenced by the significant decreases in IL-6 and Arginase-1 which confirm a shift away from pro-tumor immune phenotypes. More importantly, there was a significant increase in TNF-α expression in the solid tumor. The biweekly treatment enabled MnNPs to successfully deliver to the TAMs in the solid tumor and alter immune cell phenotype. The trend in decreasing tumor weight, though not significant, demonstrated the effects of IκBα-MnNP delivery to TAMs, altering their phenotype, and inducing changes in other immune cells in the TME. The advantages of IP delivery of MnNPs to treat ovarian tumors are supported by the delivery studies and the therapeutic studies, both of which reveal nanoparticle penetration into the solid tumor as well as changes in immune cell phenotype in the tumor.

The addition of the extended treatment model was used to follow-up the original TBR5 experiment to further examine IκBα-MnNP therapeutic efficacy. The shorter treatment revealed positive signs of anti-tumor immunity, so the logical follow-up was to extend treatment by one week (two extra doses). These results immediately revealed the significant therapeutic benefits of MnNP delivery with the ascites volume and tumor weight being significantly reduced in the treatments. Similar to the previous cohorts, we once again saw therapeutic effects of the mannosylated carrier alone with a more pronounced effect in the IκBα-MnNP. Furthermore, this study examined in detail the immune cell populations comprising the ascites and tumor and revealed several significant findings. The significant shift in TAMs from an M2 to M1 phenotype *in vivo* indicates that the IκBα-MnNPs recapitulate the results seen *in vitro* and can produce the inflammatory microenvironment observed through PCR results in the previous studies. This effect was seen in both the ascites and the tumors which again validates the biweekly IP injection as a therapeutically effective treatment strategy. Furthermore, these results confirm the effects of Scr-MnNPs in shift TAMs away from an M2 phenotype, and the synergistic effect of loading with IκBα siRNA is evidenced by the significant decrease in the percent of CD206+ TAMs in the IκBα-MnNP treatment compared to the Scr-MnNP treatment. Also, in line with the previous observations of increased CD8 T cell infiltration, analysis of CD8 T cell populations revealed a trend of increased infiltration in IκBα-MnNP treated mice. Further increases in inflammatory monocyte and NK cell populations confirm the ability of macrophage repolarization to recruit and effect other immune cell populations to lead to anti-tumor immune responses.

Overall, these studies indicate a therapeutic benefit from IκBα-MnNP treatment in ovarian tumors. While the late-stage treatment of ID8 tumors did not significantly alter tumor

progression, there were signs of changes in the immune cell composition and a trend in decreasing ascites accumulation, indicating some positive responses. Future studies in this model may examine increasing the MnNP dosage or combining MnNP treatment with currently approved chemotherapies. Many patients develop chemoresistance in late-stage EOC and this phenomenon is often exacerbated by the buildup of ascites.[162,163] By implementing IκBα-MnNP treatment initially to reduce ascites accumulation, we could examine the potential effects of MnNPs to restore chemotherapy responsiveness in late-stage ovarian tumors. Similarly, the positive therapeutic effects seen in the early-stage treatment of the aggressive TBR5 model, in terms of tumor progression and immune cell composition, provide context for future directions in combining MnNP treatments with T cell-targeted immunotherapies. Many of the current T cell-based therapies are not as effective in treating solid tumors due to low T cell infiltration and high levels of immunosuppressive cytokines. Targeting TAMs to produce pro-inflammatory cytokines, such as IFN-γ and TNF-α, can promote an immune-favorable microenvironment while also producing T cell-specific chemokines, such as CXCL9, to recruit T cells to the tumor. The logical next step in this research will be to examine combination treatments with ICBs, such as anti-PD-1s, to potentially produce a more robust immune response and develop immunological memory to prevent subsequent recurrence. The results of this study demonstrated positive therapeutic results but have also informed our future directions for developing therapies to treat ovarian cancer in patients.

3.6 Conclusions

This work demonstrates the efficacy of MnNPs in inducing TAM-mediated anti-tumor immunity in mouse models of ovarian cancer. Delivery of IκBα siRNA to NGL-BMDMs activated canonical NF-κB, indicating repolarization of the macrophages toward an inflammatory M1-like

phenotype. Biodistribution studies in two different tumor models revealed preferential MnNP association with TAM and myeloid cell populations only in the ascites and solid tumors with minimal off-target delivery to other immune cells and negligible uptake in any cells in the spleens. These results supported the use of IP injections to provide localized delivery to the TME. The delivery of MnNPs to macrophages in the ascites led to a slight decrease in ascites buildup in the late-stage model, but a substantial decrease in the aggressive TBR5 model. The positive effect of mannosylated carriers on preventing ascites development in the aggressive TBR5 model indicates a potential for synergistic effects of IκBα siRNA with MnNPs. While the late-stage treatment of ID8 tumors did not significantly alter tumor progression, there were noticeable differences in RNA expression of various M1- and M2-associated markers, indicating beneficial immunostimulatory changes in the TME after MnNP treatment. In the more aggressive TBR5 model, the IκBα-MnNP treatment led to slight decreases in tumor weight, but also was associated with larger numbers of infiltrating CD8 T cells. The increase in tumor-associated T cells is highly encouraging for future studies involving combination treatments with immune checkpoint blockades which rely on the presence of T cells in the tumors for anti-cancer toxicity. Additionally, we demonstrated that an extended treatment of MnNPs in the TBR5 model significantly suppressed ascites accumulation and tumor development while also altering the immune cell composition in the TME. These results further support the hypothesis that activating macrophages can transform the TME into a pro-inflammatory niche which will support ICB therapies. Importantly, this study shines a light on the potential for IP administered therapies that can influence tumors in the peritoneal cavity through modulation of cells in the ascites. Overall, this work highlights the use of MnNPs in IP treatment of ovarian cancer and

provides a pathway forward for enhancing the current treatment paradigm in patients with a highly deadly disease.

3.7 Supplemental Figures

Supplemental Table 3.S1: Oligonucleotide sequences used for MnNP loading.

Oligonucleotide	**Sense Strand (5'→3')**	**Antisense Strand (5'→3')**
Cy5 dsDNA	dGdTdC dAdGdA dAdAdT dAdGdA dAdAdC dTdGdG dTdCdA dTdC	[Cy5]-dGdAdT dGdAdC dCdAdG dTdTdT dCdTdA dTdTdT dCdTdG dAdC
Scr siRNA	rArUrC rUrArG rGrCrC rGrCrU rArUrA rCrCrA rArGrU	rArCrU rUrGrG rUrArU rArGrC rGrGrC rCrUrA rGrArU
IκBα siRNA	rGrUrA rGrCrA rGrUrC rUrUrG rArCrG rCrArG rAdTdT	rUrCrU rGrCrG rUrCrA rArGrA rCrUrG rCrUrA rCdAdC
Key: d = DNA base, r = RNA base All oligonucleotides were purchased from Integrated DNA Technologies		

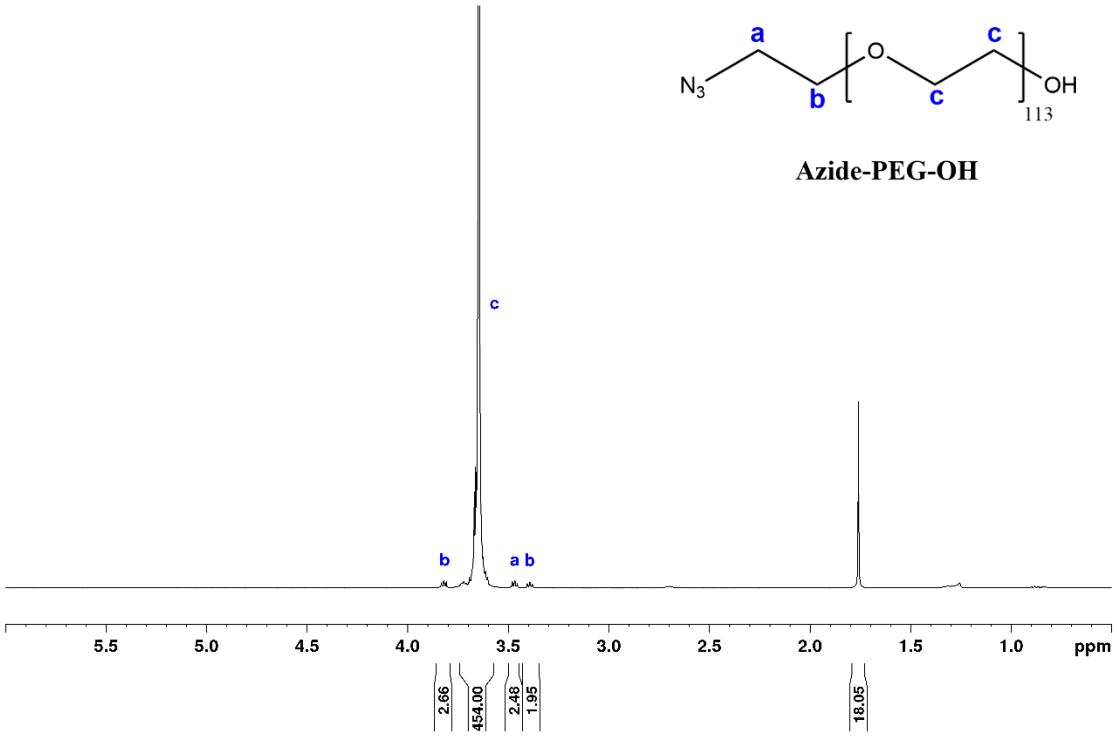

Supplemental Figure 3.S1: ^{1}H-NMR of azide-PEG-hydroxyl in $CDCl_3$. All peaks were normalized to the PEG (5 kDa) peak at δ 3.65 (-OC**H**$_2$C**H**$_2$-).

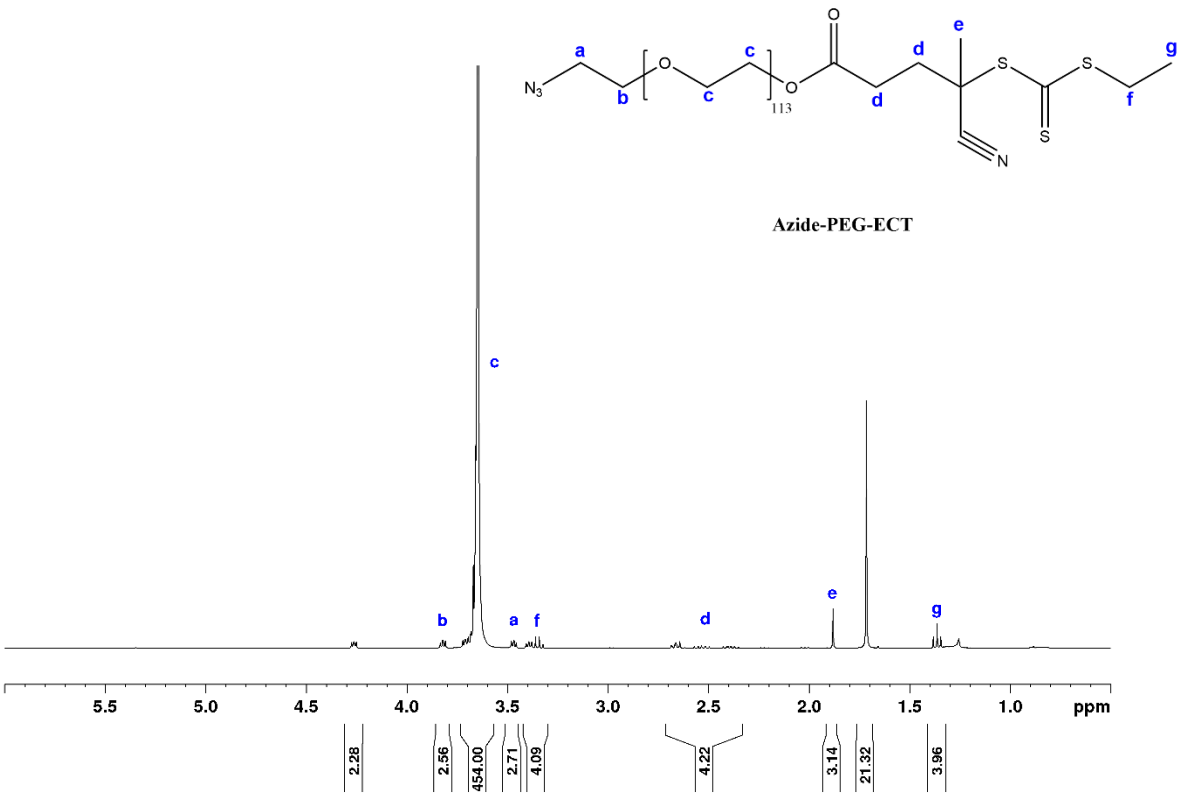

Supplemental Figure 3.S2: ^{1}H-NMR of azide-PEG-ECT in $CDCl_3$. Formation of the macro-CTA was confirmed by the characteristic ECT peak at δ 1.88 (CCNC**H**$_3$).

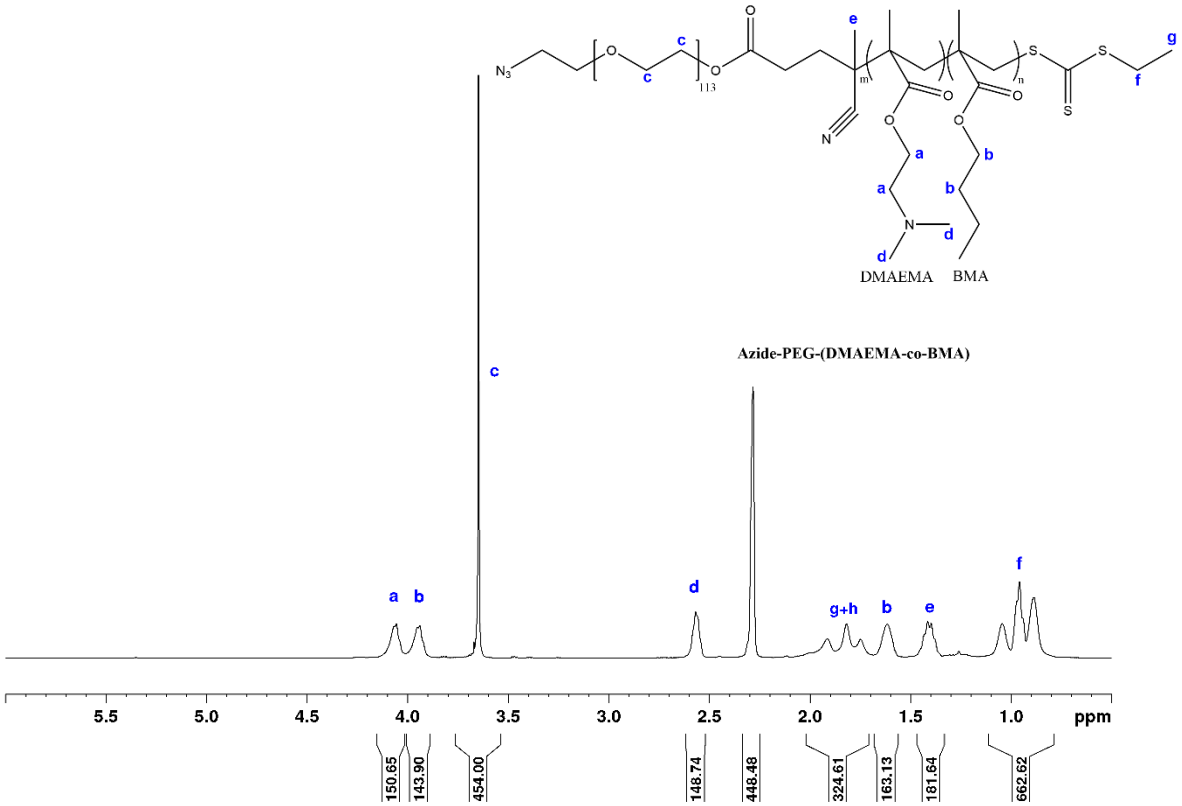

Supplemental Figure 3.S3: ^{1}H-NMR of azide-PEG-(DMAEMA-co-BMA) in $CDCl_3$. RAFT polymerization of the diblock copolymer was confirmed by the formation of the DMAEMA peak at δ 4.05 (-OC**H**$_2$C**H**$_2$-) and the BMA peak at δ 3.95 (-OC**H**$_2$C**H**$_2$-). Number of repeating units for DMAEMA and BMA were calculated by calibrating to the PEG peak of a known length.

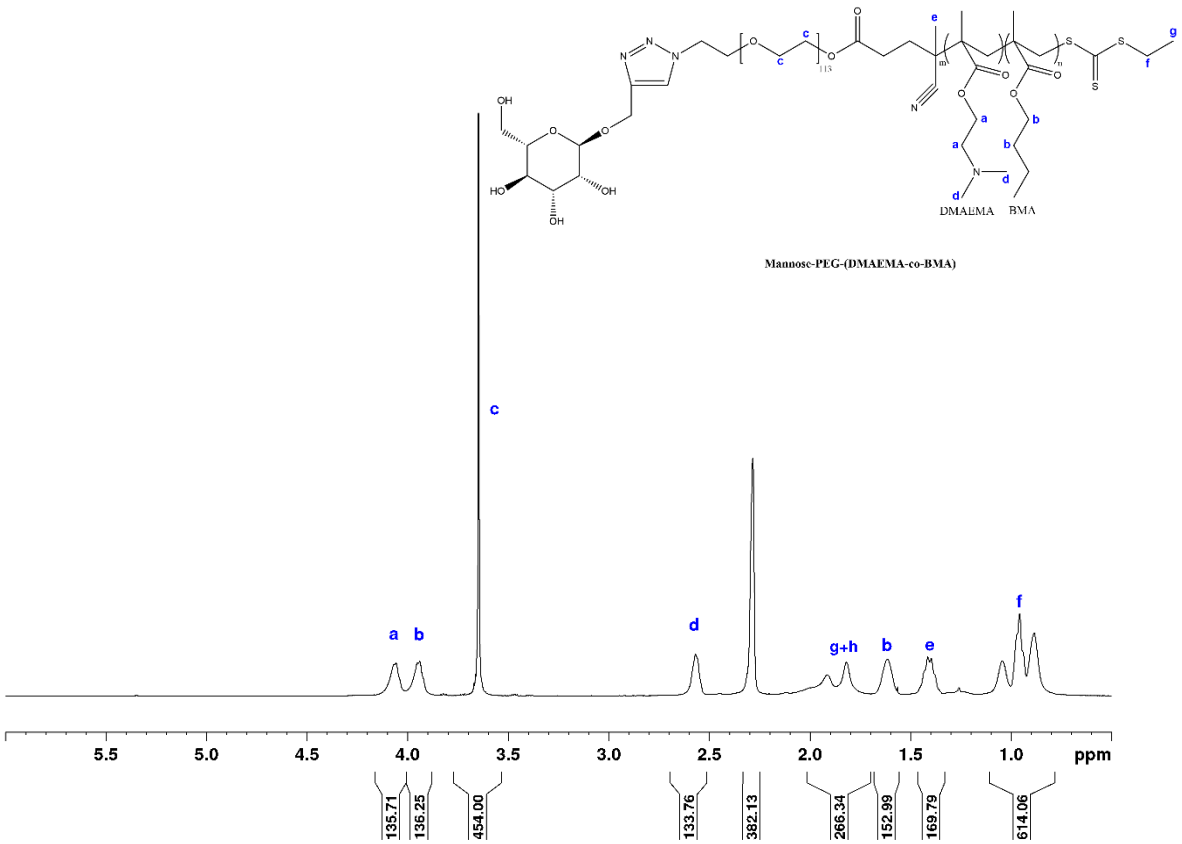

Supplemental Figure 3.S4: ^{1}H-NMR of mannose-PEG-(DMAEMA-co-BMA) in $CDCl_3$. Mannose conjugation cannot be ascertained via NMR due to the overlap of the mannose ^{1}H-NMR spectra (3.5-4 ppm) with the PEG peak.

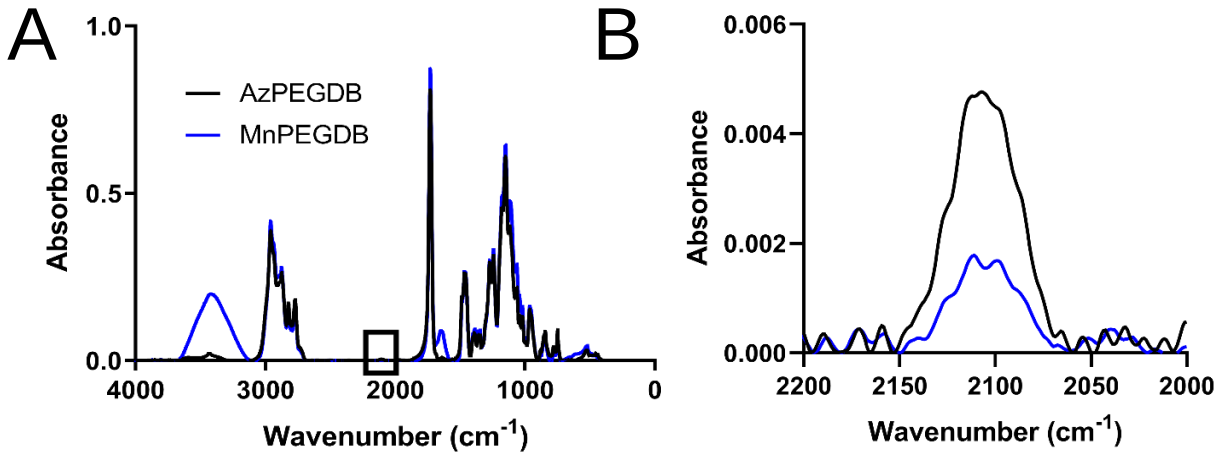

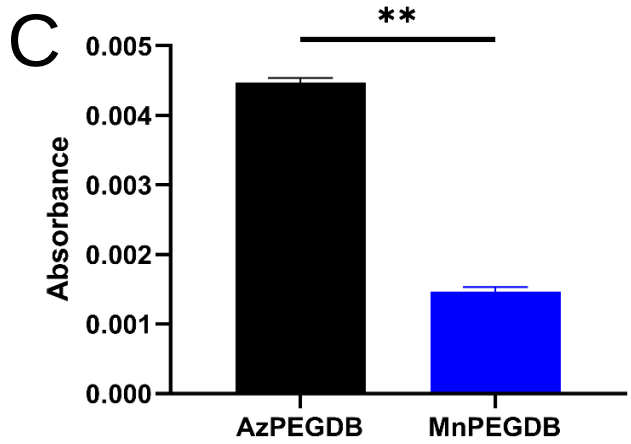

Supplemental Figure 3.S5: FTIR spectroscopy of AzPEGDB and MnPEGDB to quantify mannose conjugation. (**A**) Overall FTIR spectra reveals identical spectra with an increase in absorbance around 3300-3400 cm^{-1} consistent with the FTIR spectra of d-mannose. (**B**) Detailed view of the characteristic azide peak at 2100 cm^{-1} and (**C**) quantified azide peak height revealing a significant decrease in azide presence on the MnPEGDB (**p<0.001).

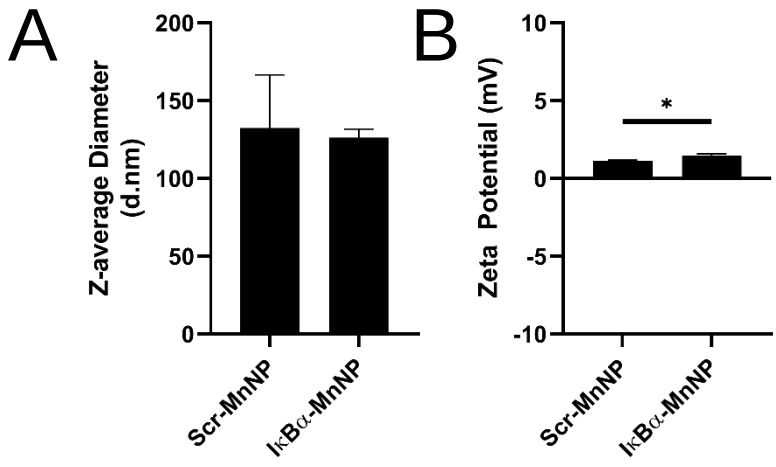

Supplemental Figure 3.S6: Polyplexes were formulated with either scrambled or IκBα siRNA and suspended in PBS (-/-, pH=7.4). (**A**) Z-average diameter averaged 130 nm for both formulations. (**B**) The zeta potentials for each were below 1.5 mV, indicating a near-neutral surface charge (*p<0.05).

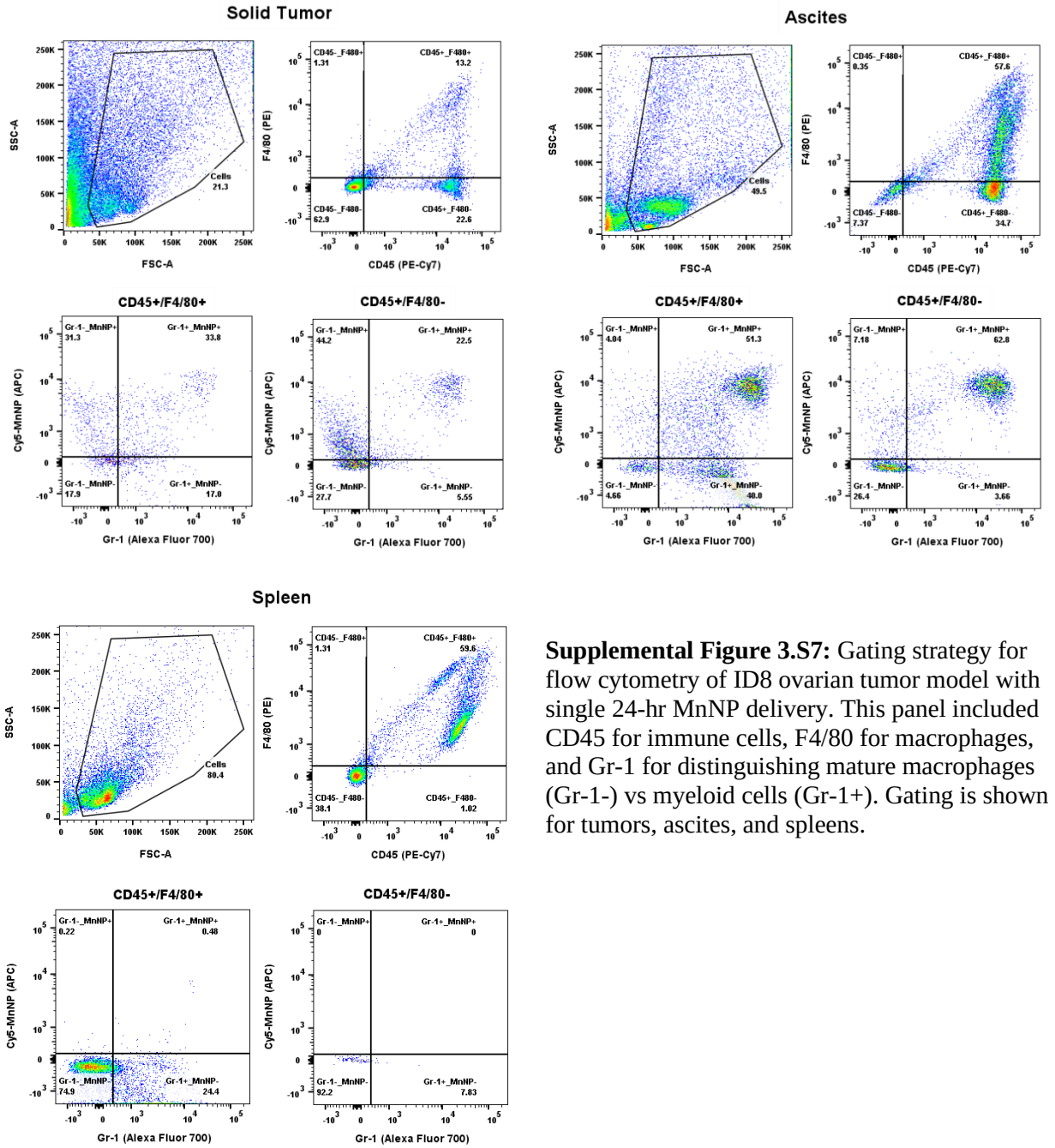

Supplemental Figure 3.S7: Gating strategy for flow cytometry of ID8 ovarian tumor model with single 24-hr MnNP delivery. This panel included CD45 for immune cells, F4/80 for macrophages, and Gr-1 for distinguishing mature macrophages (Gr-1-) vs myeloid cells (Gr-1+). Gating is shown for tumors, ascites, and spleens.

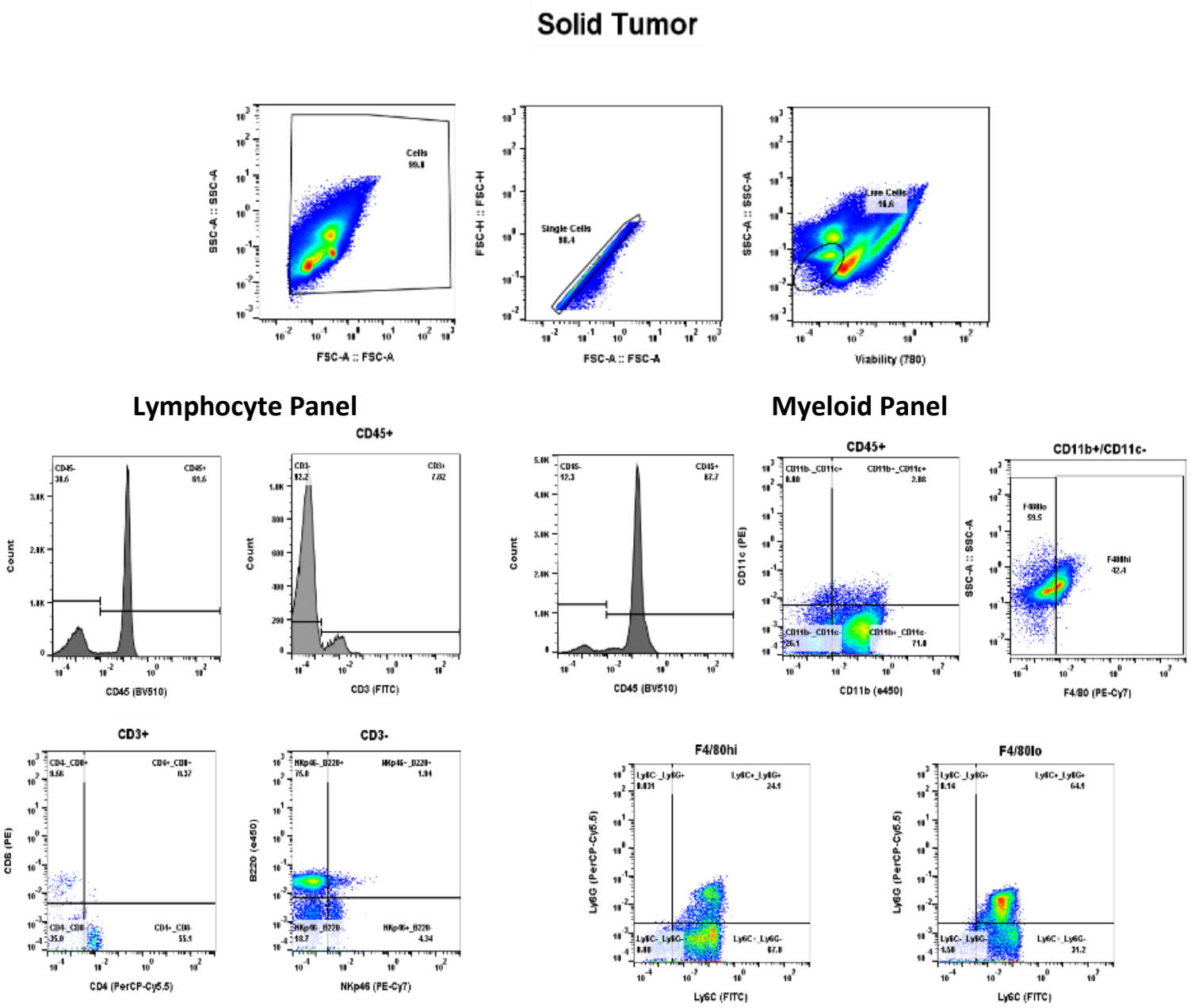

Supplemental Figure 3.S8: Gating strategy for flow cytometry of solid tumors in the TBR5 ovarian tumor model with biweekly MnNP delivery. The initial gating was performed using markers for live/dead (Ghost Dye Red) and pan-immune cells (CD45). The lymphocyte panel used markers for T cells (CD3, CD4, and CD8a), Natural Killer cells (NKp46), and B cells (B220). The myeloid panel used markers for dendritic cells (CD11c), macrophages (CD11b and F4/80), and myeloid cells (Ly6C and Ly6G).

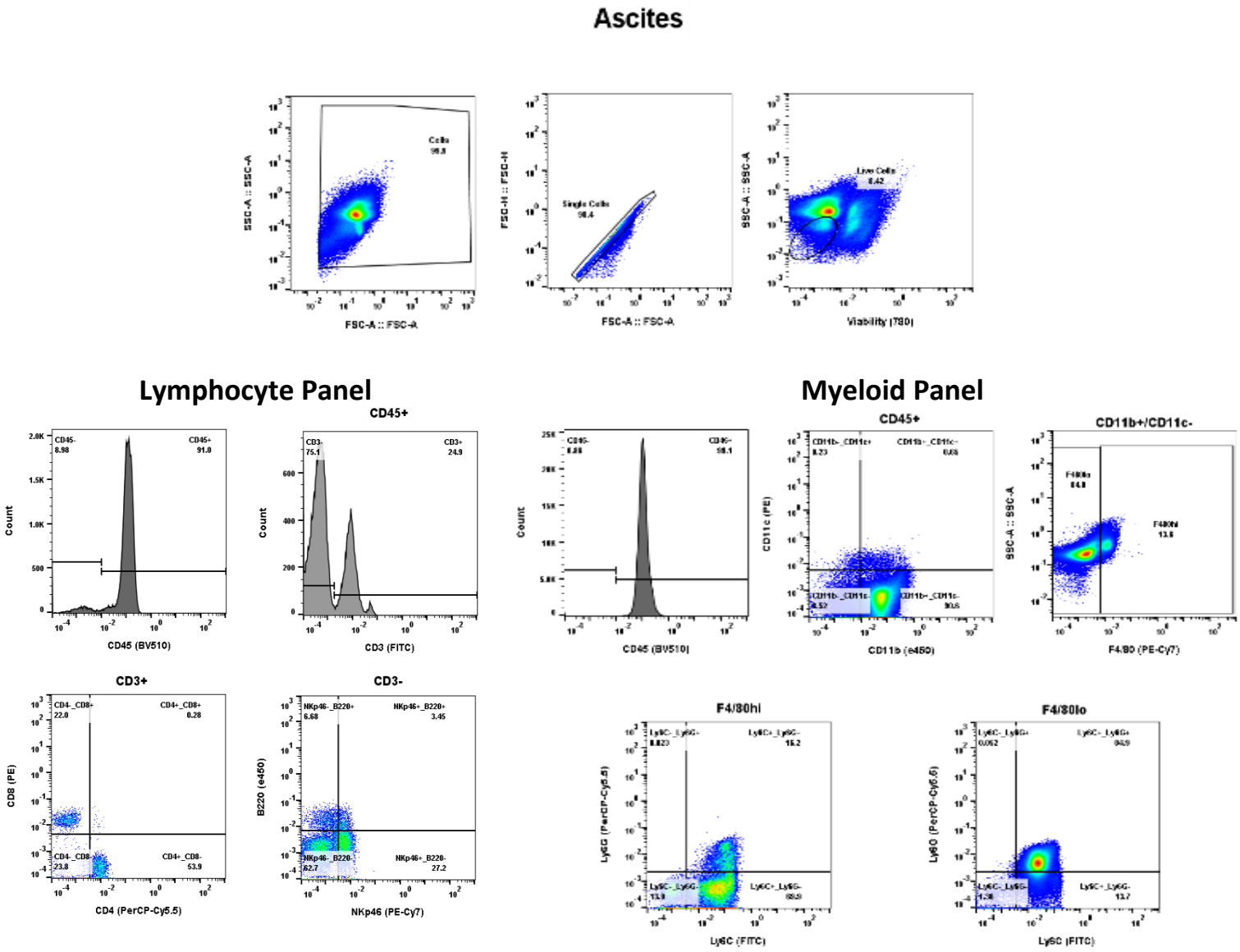

Supplemental Figure 3.S9: Gating strategy for flow cytometry of ascites cells in the TBR5 ovarian tumor model with biweekly MnNP delivery. The initial gating was performed using markers for live/dead (Ghost Dye Red) and pan-immune cells (CD45). The lymphocyte panel used markers for T cells (CD3, CD4, and CD8a), Natural Killer cells (NKp46), and B cells (B220). The myeloid panel used markers for dendritic cells (CD11c), macrophages (CD11b and F4/80), and myeloid cells (Ly6C and Ly6G).

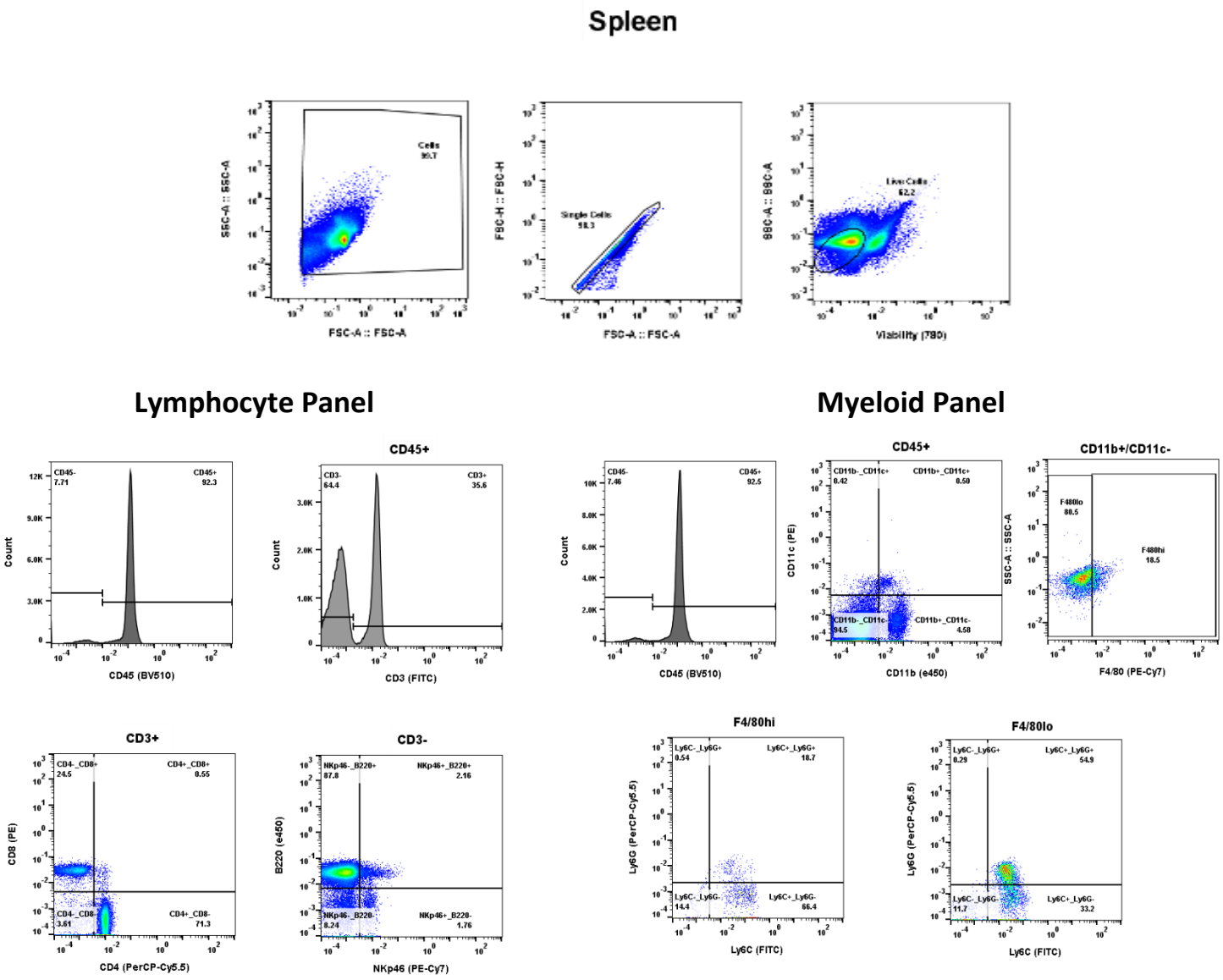

Supplemental Figure 3.S10: Gating strategy for flow cytometry of spleens in the TBR5 ovarian tumor model with biweekly MnNP delivery. The initial gating was performed using markers for live/dead (Ghost Dye Red) and pan-immune cells (CD45). The lymphocyte panel used markers for T cells (CD3, CD4, and CD8a), Natural Killer cells (NKp46), and B cells (B220). The myeloid panel used markers for dendritic cells (CD11c), macrophages (CD11b and F4/80), and myeloid cells (Ly6C and Ly6G).

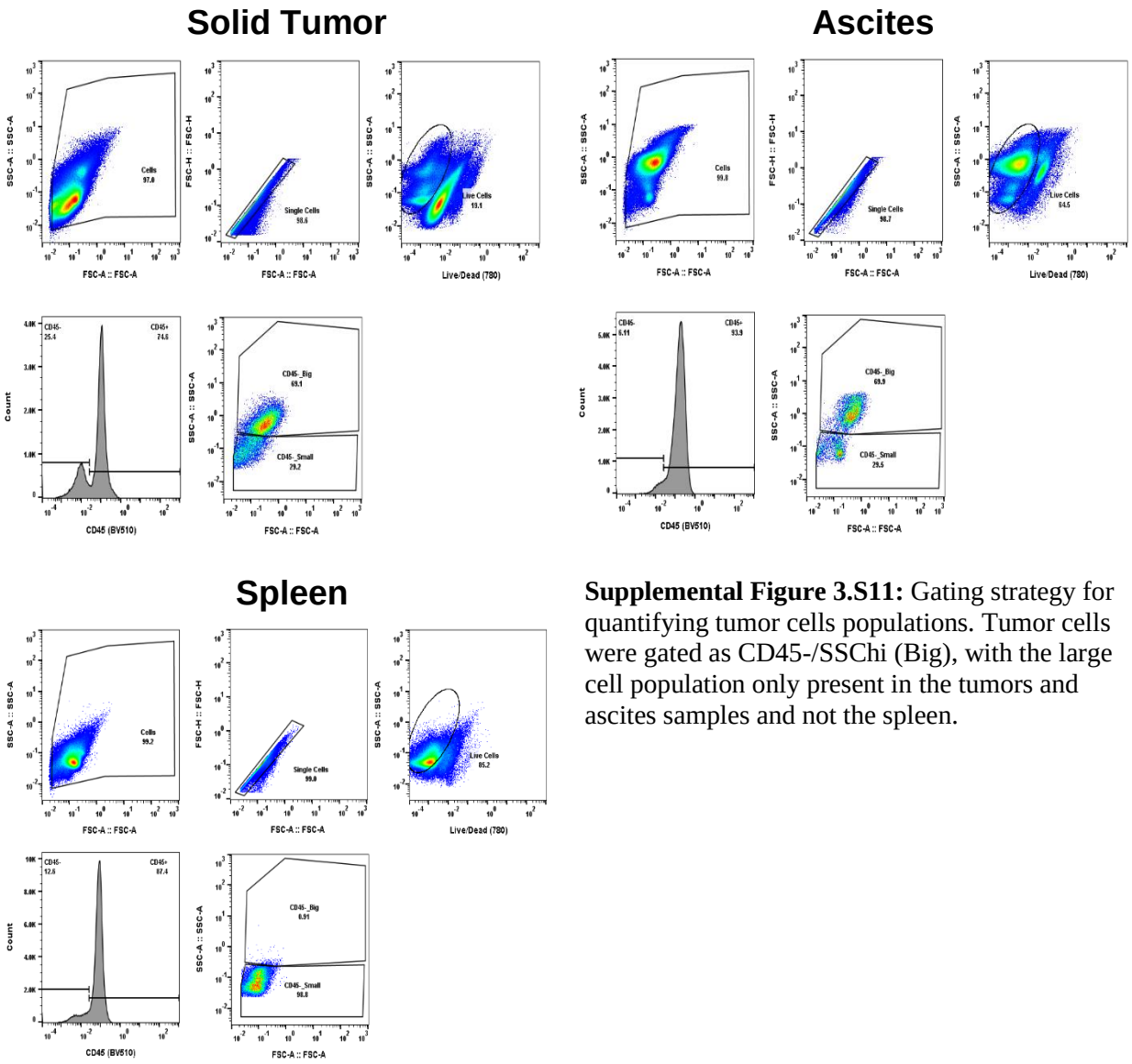

Supplemental Figure 3.S11: Gating strategy for quantifying tumor cells populations. Tumor cells were gated as CD45-/SSChi (Big), with the large cell population only present in the tumors and ascites samples and not the spleen.

Supplemental Table 3.S2: qRT-PCR primer sequences. IκBα, IL-6, CXCL9, CD206, B2M, and GAPDH were purchased from IDT. Arginase-1 and TNF-α were purchased from Sigma.

Target Gene	Forward Sequence (5'→3')	Reverse Sequence (5'→3')
IL-6	GATCCGGTGATAGTTCCTCTTCA	TCCAGAGTCAGCGCCTCATA
CD206	CAAGGAAGGTTGGCATTTGT	CCTTTCAGTCCTTTGCAAGC
IκBα	GAGCTCCGAGACTTTCGAGG	AGACACGTGTGGCCATTGTA
Arginase-1	CTCCAAGCCAAAGTCCTTAGAG	AGGAGCTGTCATTAGGGACATC
CXCL9	GTGGTGAAATGGAAAGATCAGGGC	AAGAGAGAAATGGGTTCCCTGGAG
TNF-α	CCCTCACACTCAGATCATCTTCT	GCTACGACGTGGGCTACAG
CCL3	TGCCCTTGCTGTTCTTCTCT	GATGAATTGGCGTGGAATCT
B2M	CTGCTACGTAACACAGTTCCACCC	CATGATGCTTGATCACATGTCTCG
GAPDH	CCCTTAAGAGGGATGCTGCC	TACGGCCAAATCCGTTCACA

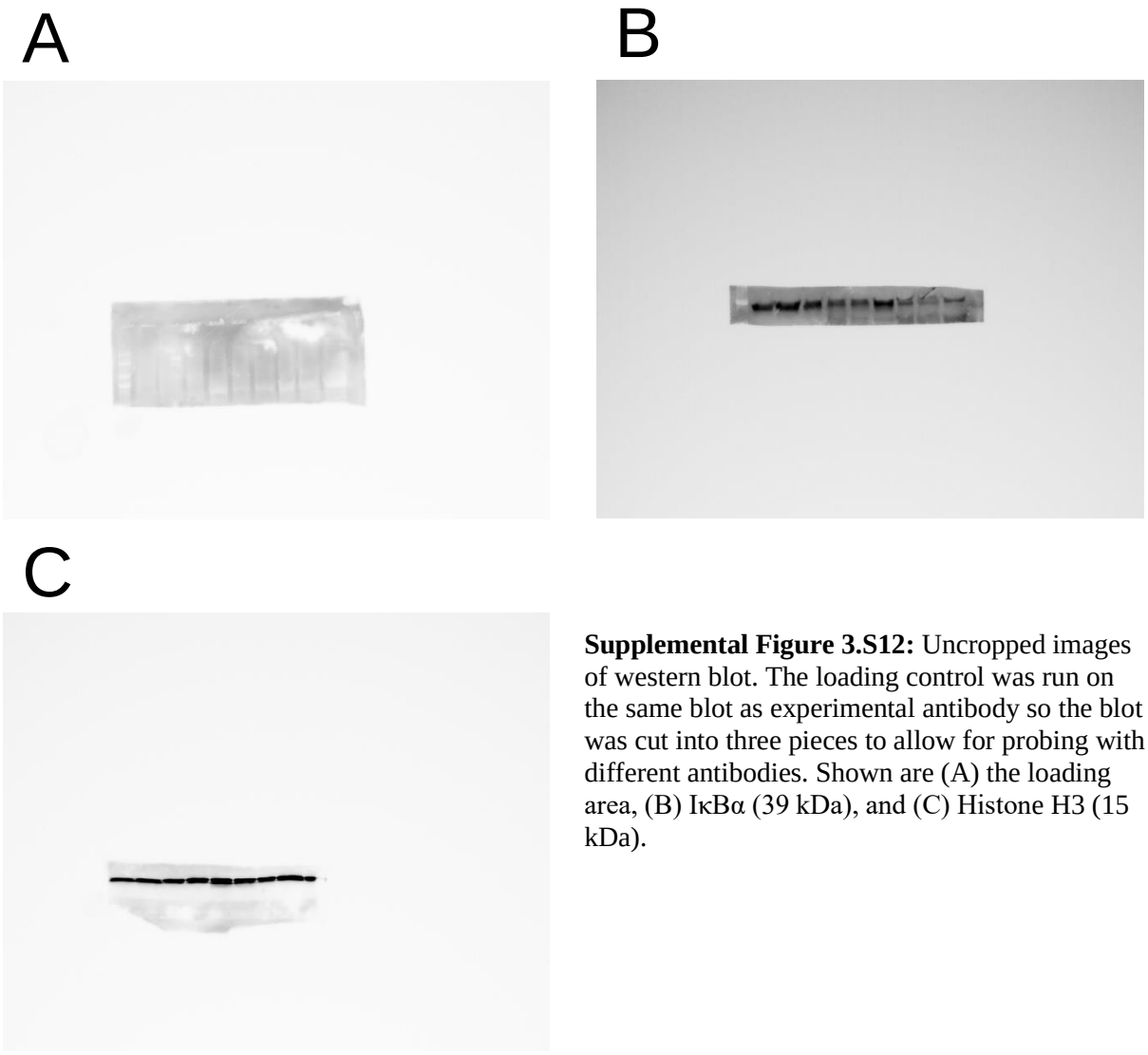

Supplemental Figure 3.S12: Uncropped images of western blot. The loading control was run on the same blot as experimental antibody so the blot was cut into three pieces to allow for probing with different antibodies. Shown are (A) the loading area, (B) IκBα (39 kDa), and (C) Histone H3 (15 kDa).

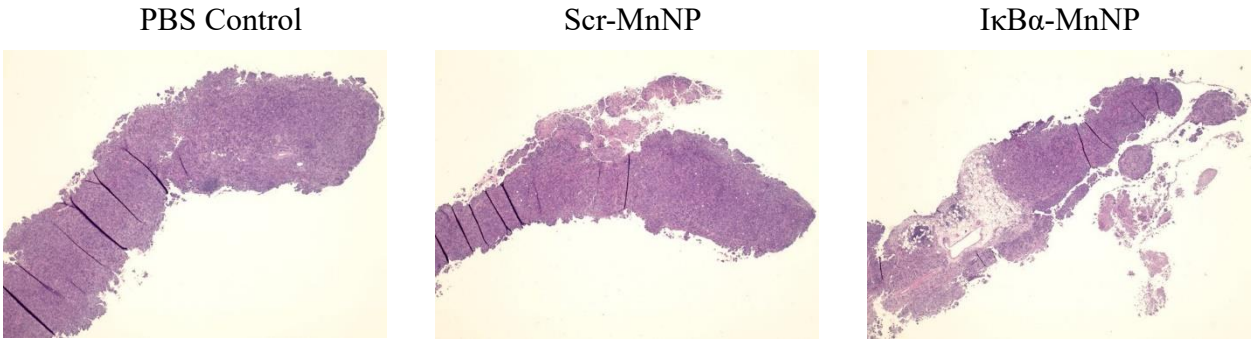

Supplemental Figure 3.S13: Solid tumors from the ID8 model were sectioned, stained with H&E, and imaged at 4X. The PBS control and Scr-MnNP tissue appeared to be all healthy tumor cells, while decreases in epithelial cellularity was evident in the IκBα-MnNP treatment, possibly indicating a decrease in tumor cells.

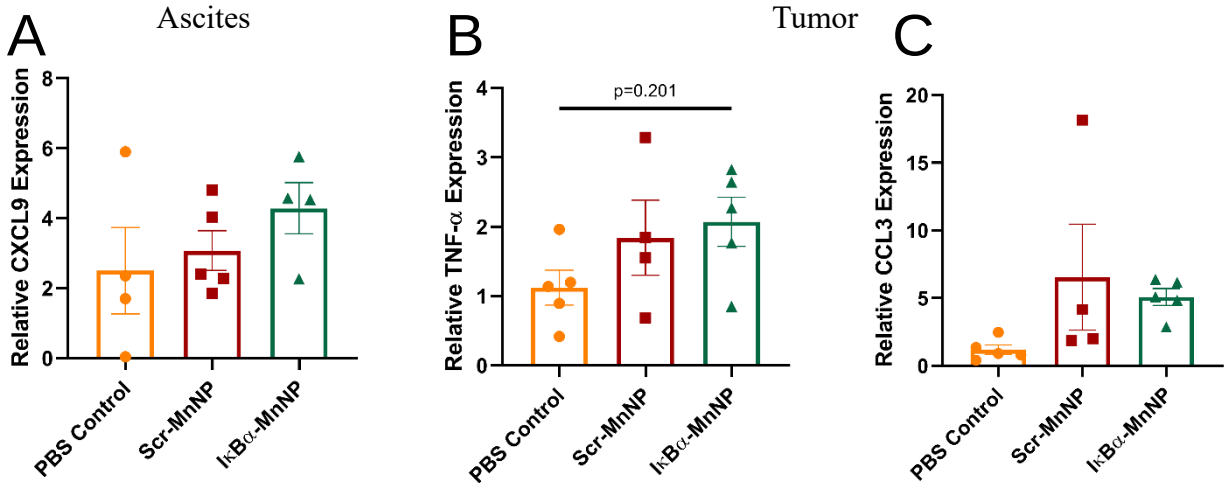

Supplemental Figure 3.S14: RNA isolated from ascites and tumor cells was used for qRT-PCR analysis. (**A**) CXCL9, a chemokine released by M1 macrophages that attracts Th1 cells, expression in the ascites increased in the IκBα-MnNP treatment. RNA from the tumor revealed slight increases in (**B**) TNF-α and (**C**) CCL3 expression, both inflammatory cytokines.

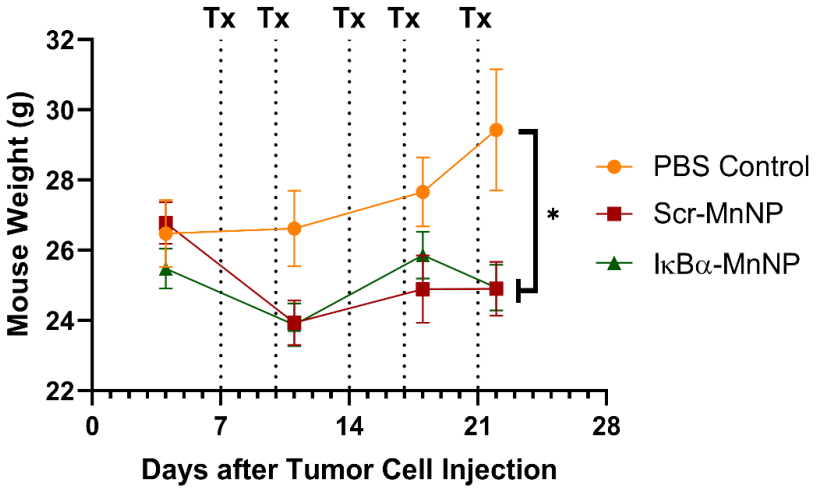

Supplemental Figure 3.S15: Change in overall mouse weight over the course of tumor development and MnNP treatment of TBR5-bearing mice. Scr-MnNP and IκBα-MnNP significantly reduced weight gain associated with ascites development compared to PBS control (n=5, *p<0.05).

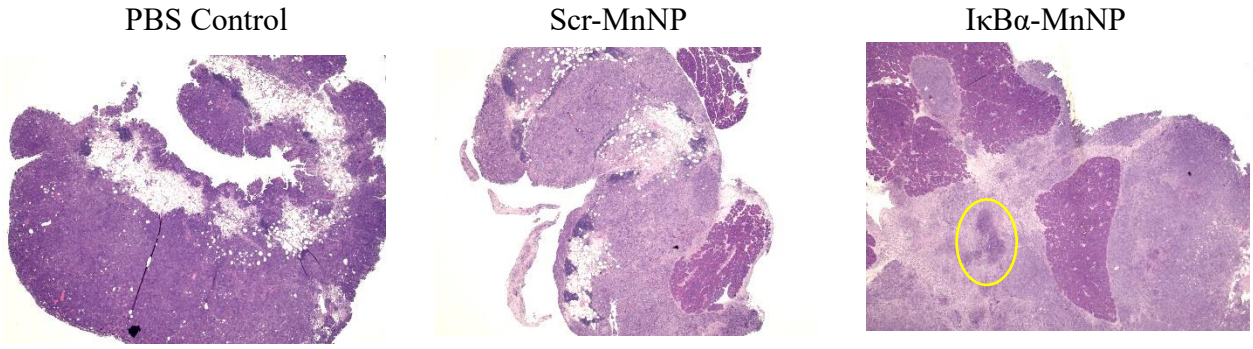

Supplemental Figure 3.S16: Solid tumors from the TBR5 model were sectioned, stained with H&E, and imaged at 4X. The PBS control tissue appeared to be all healthy epithelial cells, while loss of epithelial cellularity was evident in the Scr-MnNP treatment. The IκBα-MnNP treatment appeared to show signs of immune cell infiltration (yellow circles).

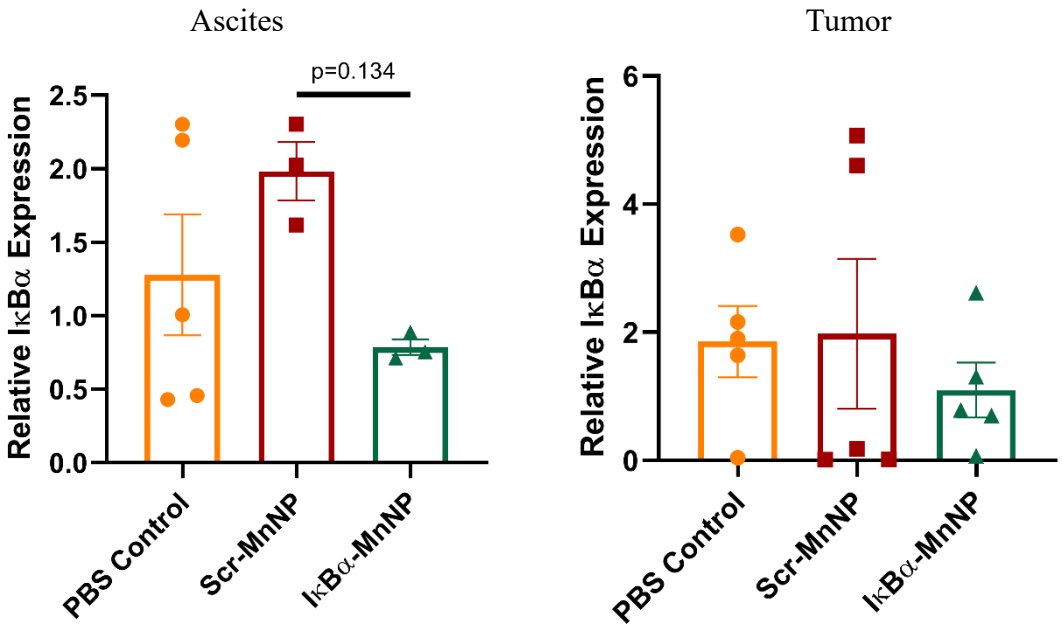

Supplemental Figure 3.S17: RNA isolated from the ascites and tumor cells was used for qRT-PCR analysis to evaluate expression of IκBα. IκBα expression increased in the ascites samples treated with Scr-MnNP, but this increase was offset in the IκBα-MnNP treatment. No significant changes were observed in the tumors, although there was a trend of decreasing IκBα expression in the IκBα-MnNP treatment.

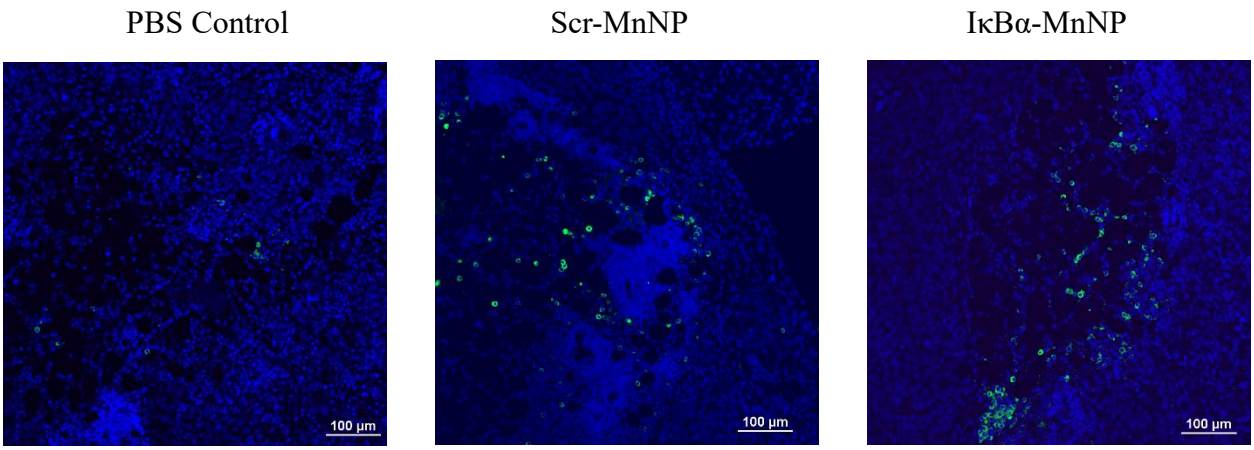

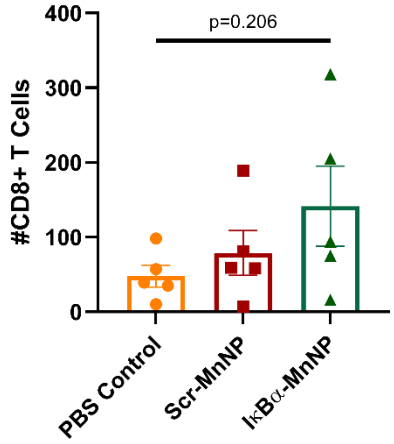

Supplemental Figure 3.S18: TBR5 tumors were sectioned and stained for cell nuclei (DAPI-blue) and CD8 (Alexa Fluor 488-green). Representative images revealed limited CD8 T cell presence in the control tumors, but both MnNP treatments induced CD8 T cell infiltration. Quantification of CD8+ T cells revealed a trend in increasing T cell infiltration in the IκBα-MnNP treatment compared to the PBS control and Scr-MnNP treatment.

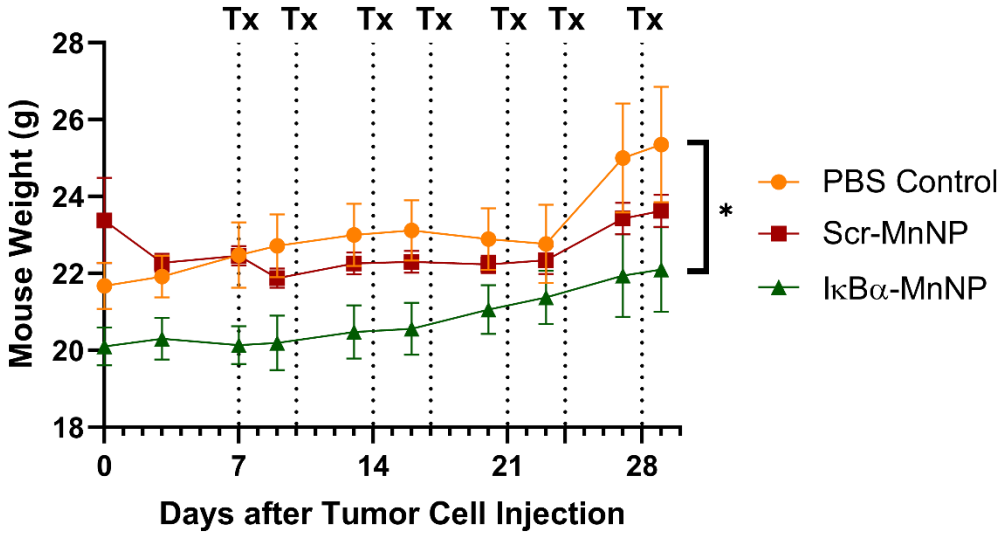

Supplemental Figure 3.S19: Mouse weights over the course of the extended biweekly treatment in the TBR5 model revealed a steady increase in the PBS control mice attributed to ascites accumulation which was not observed in the two treatments. These results match with the MnNP treatments preventing ascites accumulation observed when measuring ascites volume at endpoint.

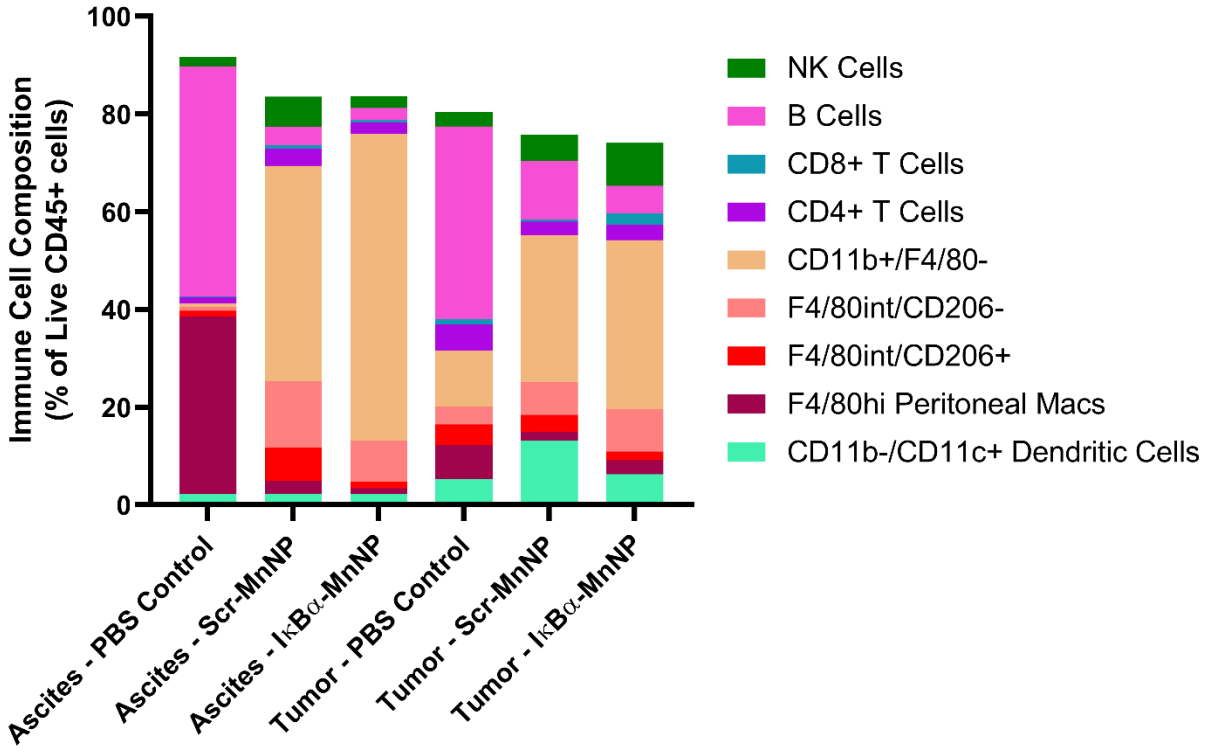

Supplemental Figure 3.S20: Quantification of immune cell composition in the ascites and tumors of TBR5 mice in the extended MnNP treatment revealed positive therapeutic trends in several subsets. These trends included an increase in NK cells, CD8+ T cells, dendritic cells, and M1 macrophages (F4/80int/CD206-) as well as a decrease in CD4+ T cells and M2 macrophages (F4/80int/CD206+).

Chapter 4

Injectable Alginate Cryogels as Localized Repolarization Depots for Tumor-Associated Macrophages

Adapted from

"Injectable Alginate Cryogels as Localized Repolarization Depots for Tumor-Associated Macrophages,"

In preparation for publication

by

Evan B. Glass, Sohini Roy, Abigail E. Manning, Benjamin C. Hacker, Sydney R. Henriques, Christopher P. Haycook, Marjan Rafat, Young J. Kim, and Todd D. Giorgio

4.1 Abstract

Current cancer immunotherapies have progressed in many clinical trials, but remain minimally effective in treating solid tumors. Targeting tumor-associated macrophages (TAMs) provides an opportunity for creating a pro-inflammatory tumor microenvironment capable of producing anti-tumor effects. Inflammatory cytokines are able to repolarize macrophages but can lead to widespread toxicity if delivered systemically and quickly dissipate when delivered locally. To this end, we have developed an injectable, macroporous cryogel capable of loading biomolecules and being locally delivered to the tumor site. This cryogel can be loaded with macrophage-specific chemokines to attract TAMs and co-loaded with inflammatory cytokines to create a localized inflammatory microenvironment. We evaluate the mechanical characteristics of fabricating and injecting tough alginate cryogels while also establishing CCL2 as a macrophage-specific chemokine and IFN-γ and IL-12 as inflammatory cytokines to repolarize macrophages. We also demonstrate the ability of the loaded cryogels to repolarize macrophages in three different *in vitro* models of immunosuppressive macrophages. Finally, we demonstrate significant changes in tumor progression in a mouse model of breast cancer when treated via peritumoral injection of loaded cryogels.

4.2 Introduction

Cancer immunotherapy, a strategy that leverages the immune system to generate an anti-tumor response, is a rapidly growing field with encouraging early clinical successes. Several reviews summarize the efficacy of these therapeutics, primarily immune checkpoint blockades (ICB) and chimeric antigen receptor (CAR) T cells, and inform the future directions of the field as a whole.[8–10] Despite the promising early returns of ICB and CAR T cell therapies, a significant fraction of patients are unresponsive to these treatments, especially in the context of solid

tumors.[8,11–13] One of the primary challenges with effectively administering these treatments in solid tumors is overcoming the immunosuppressive tumor microenvironment (TME) that prevents T cell infiltration and induces T cell exhaustion.[16,17] One technique to bypass the challenges associated with T cell-based immunotherapies involves targeting and activating the most prevalent immune cell in most tumors: macrophages.[18–20]

Macrophages display a spectrum of phenotypes, each with unique immune functions. The classically-activated (M1) macrophages are pro-inflammatory and generate a Th1, anti-microbial response. Alternatively-activated (M2) macrophages promote a Th2, wound healing response.[198] In the TME, tumor-associated macrophages (TAMs) display characteristics of both phenotypes, although the majority function as M2-like macrophages that promote tumor growth.[199–201] These TAMs release immunosuppressive signals, such as IL-10[202] and transforming growth factor beta (TGF-β)[203], which prevent other immune cells from recognizing and killing the cancer cells. However, by "repolarizing" the TAMs to be pro-inflammatory, the resulting TME will be "primed" for immune activation to induce anti-tumor effects. Additionally, recent work has shown that a higher ratio of M1/M2-like TAMs in breast cancer patients resulted in a favorable tumor immune microenvironment and an increase in immune checkpoint molecules.[38] Quantifying the M1/M2 ratio of TAMs, as opposed to whole macrophage number, has become a prominent prognostication tool as reviewed by Jayasingam, et. al.[37] In this way, a novel immunotherapy to increase the population of M1-like TAMs can be implemented to improve the response rates associated with currently FDA-approved immunotherapies.

Previous groups have demonstrated that simply ablating TAMs can reduce tumor growth and prevent metastasis.[31–33,204] However, rather than simply killing the macrophages, a more robust technique involves repolarizing the existing TAM population to drive an anti-tumor

response. Previous strategies have used toll-like receptor (TLR) agonists[205], small interfering RNA (siRNA)[45,166], bacterial cell mimics[206], and even cytokines[207] to repolarize macrophages. The systemic delivery of cytokines or other pro-inflammatory cues, either freely administered or loaded into nanoparticles/liposomes, are able to induce an M1-like response but can often be associated with widespread inflammation and off-target toxicity.[50] To alleviate these concerns, localized delivery of inflammatory cues is desirable as it limits the risk of affecting healthy tissue as well as minimizing the overall required dose to induce a positive effect. One technique for local release of inflammatory cytokines is via controlled delivery from an injectable scaffold.

Injectable biomaterials have shown great potential for a variety of applications, as detailed in several recent reviews.[76,208] Perhaps most intriguing is the ability to create an injectable hydrogel which contains pores large enough for cells to migrate inside the scaffold. By adding radical initiators to a methacrylated alginate solution and performing the gelation step at -20°C, ice crystals form between the crosslinking alginate backbone and cause large pores to form.[77] The resulting "cryogels" can then be further ionically crosslinked with divalent cations that electrostatically interact with the negatively-charged alginate polymer to form a tough cryogel, capable of being injected through a syringe while maintaining overall pore size and structure.[78] This scaffold can be loaded with different cell-signaling molecules to address a given application, including localized delivery into the TME. Mooney, et al, have shown the ability for this type of scaffold to function as a subcutaneous, "artificial" lymph node.[75,78] By loading the cryogels with chemokines specific for dendritic cells (DCs) and T cells, as well as irradiated tumors cells, the scaffold attracts DCs, which then endocytose the tumor cells and produce neoantigens that are presented to the colocalized T cells. In this way, the gel is producing tumor-specific, mature T cells that can recognize and kill the cancer cells. This strategy, however, is

limited by the ability of the T cells to infiltrate into the solid tumor, which is still restricted by the immunosuppressive TME. An alternative approach is to load the scaffold with macrophage-specific chemokines and inflammatory cytokines before directly injecting into or adjacent to the tumor. This cryogel system will allow for minimally invasive treatment of solid tumors by simply injecting the gel directly in or adjacent to the tumor site. Alternatively, this same system can be used in conjunction with the current standard of surgical removal, as Park, et al, have demonstrated with a different hydrogel system.[209] Finally, the alginate scaffold is small and tough enough to even be used in a biopsy punch, should the tumor not be easily accessible with a syringe for direct injection.

By developing a locally delivered macrophage repolarization depot, we aim to directly alter the immunosuppressive TME into a pro-inflammatory environment. By repolarizing the TAMs to a primarily M1 phenotype, the resulting production of inflammatory cytokines and T cell-specific chemokines will create an immunologically "hot" tumor that can induce robust anti-tumor immune responses. We propose a mechanism to alter the tumor microenvironment and promote T cell infiltration by repolarizing TAMs to the M1 phenotype. Macrophages, similar to DCs, function as antigen-presenting cells, so when stimulated they can endocytose diseased cells (i.e. tumor cells), process tumor-specific antigens, and present them to the infiltrating T cells. In this way, not only will the macrophages induce a localized anti-tumor response, but there is also the potential for development of immunological memory in the mature T cell population. The development of immunological memory is important for both treatment of distant metastases (via systemic circulation of tumor-specific T cells) and preventing recurrence, which is commonly associated with the current gold standard of surgery, chemotherapy, and radiation therapy.

We hypothesized that by finding the appropriate chemokines and cytokines, we could develop a novel scaffold system specific for macrophage recruitment and subsequent repolarization. First, to establish a macrophage-specific depot, we identified chemokine (C-C motif) ligand 2 (CCL2) as an M2-specific chemoattractant, as shown by Vogel, et al.[87] For macrophage repolarization, we chose to implement the cytokines interferon-γ (IFN-γ) and interleukin-12 (IL-12), both of which have been previously shown to induce an M1 macrophage phenotype.[166,210,211] To evaluate the efficacy of the chosen molecules, we performed preliminary experiments on cultured primary bone marrow-derived macrophages (BMDMs) using both free chemokine/cytokine as well as loaded cryogels. These cells have been previously used by our lab and are able to be polarized to an M1 or M2 phenotype via cytokine stimulation to allow for a more physiologically relevant *in vitro* model than immortalized cell lines.[166] Additionally, we repeated treatments on tumor-associated macrophages isolated from a spontaneous mammary tumor model in mice as well as cultured mouse tumor explants. These methods allowed us to directly quantify the effects of cryogel treatment on tumor-resident macrophages to observe migratory properties as well as changes in phenotype in a recapitulated TME. Finally, we translated the loaded cryogel for peritumoral injection into FVB mice bearing polyoma (PyMT) tumors to evaluate *in vivo* anti-tumor effects of stimulating M1 macrophage polarization.

4.3 Results and Discussion

4.3.1 Physical characterization of macroporous cryogels

Sodium alginate functionalization with aminoethyl methacrylate (AEMA) to form methacrylated alginate (MA-alginate) and subsequent crosslinking of methacrylate groups were confirmed with ^{1}H-nuclear magnetic resonance (NMR) spectroscopy (**Supplemental Figure 4.S1**). Covalent crosslinking of methacrylates was performed at -20°C to produce macroporous hydrogels (cryogels). Cryogelation occurred in Teflon molds to allow for tailoring of size and shape of cryogels (**Supplemental Figure 4.S2**). The overall physical structure of the cryogels was evaluated with scanning electron microscopy (SEM), including maintenance of macroporous structure after injection through a syringe (**Figure 4.1**). This retention of structure is crucial for eventual localized delivery of cryogels via peritumoral injection. Furthermore, cryogels were embedded in optimal cutting temperature (OCT) compound and cryosectioned to image internal

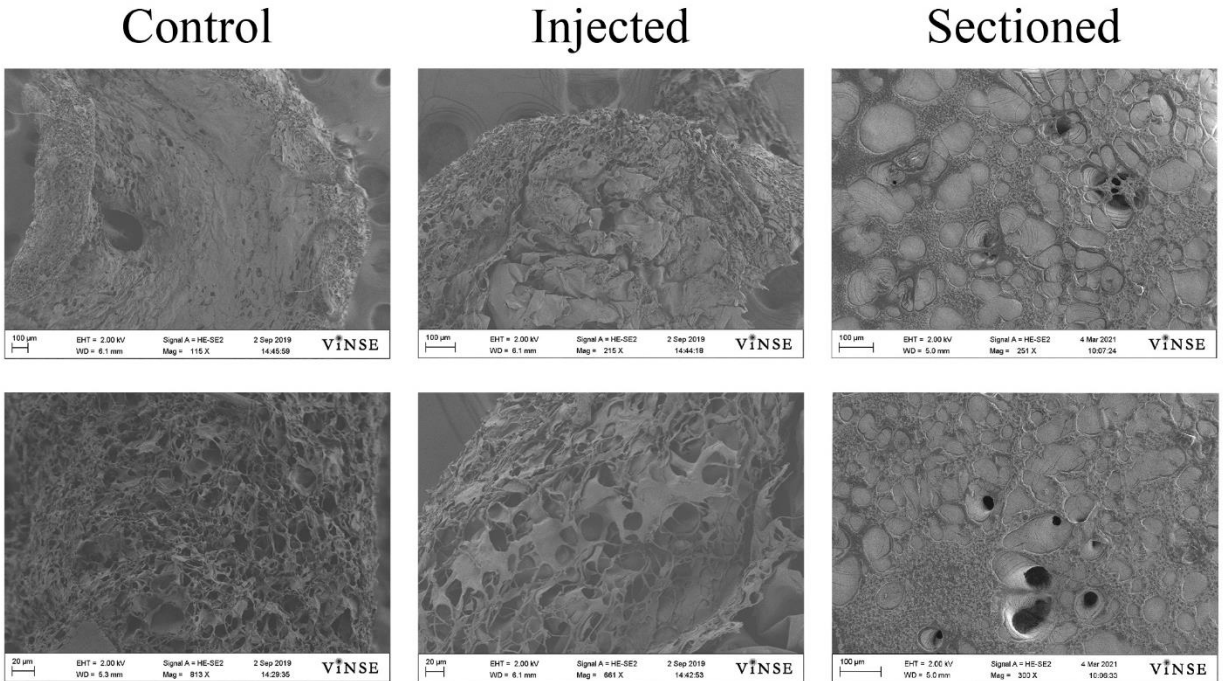

Figure 4.1: Maintenance of gel structure after injection. Cryogels were serially dried and imaged with SEM before and after injection through a 16G needle to evaluate changes in overall gel structure. Control gels were also fixed and cryosectioned to image the internal porosity of the gels, which displayed macroporosity throughout the gel.

porosity of the gels. SEM imaging of internal cryogel sections revealed the macroporous structure was present throughout the scaffold (**Figure 4.1**).

The mechanical properties of the cryogels, including stiffness, interconnected porosity, and swelling ratio, were also quantified and found to match previously published results (**Supplemental Figure 4.S3**).[78] Additional characterizations were performed to evaluate long-term storage of gels. Notably, the covalently crosslinked only gels (no ionic crosslinking) significantly increased in swelling ratio after more than one month of storage (**Supplemental Figure 4.S4**). However, the tough cryogels maintained interconnected porosity and swelling ratio up to 2 months after fabrication, indicating the ability to maintain mechanical characteristics long-term (**Supplemental Figure 4.S4**). These results are useful for future translatability of this system since long-term storage is an important consideration when scaling-up production.

To quantify the average pore size in hydrated cryogels, as opposed to the dehydrated samples imaged with SEM, the unreacted carboxyl groups on the alginate backbone were labelled with a Cy5-amine and imaged using a fluorescent confocal microscope in HBSS solution (**Figure 4.2**). ImageJ quantification confirmed the average pore size was large enough for cell infiltration into the gels with 73.4% pores in control gels being greater than 70 μm in diameter (**Figure 4.2A**). More importantly, pore diameter was maintained after injection through a 16G needle with 72.7% of pores in injected gels having a diameter larger than 70 μm (**Figure 4.2B**). Furthermore, there was no significant difference in average pore size before and after injection, with the average diameters measuring 86.0 and 87.1 μm for control and injected gels, respectively (**Supplemental Figure 4.S5**). The SEM and confocal microscopy combine to

illustrate the ability of the ionically crosslinked cryogels to withstand injection while maintaining overall structure and pore size.

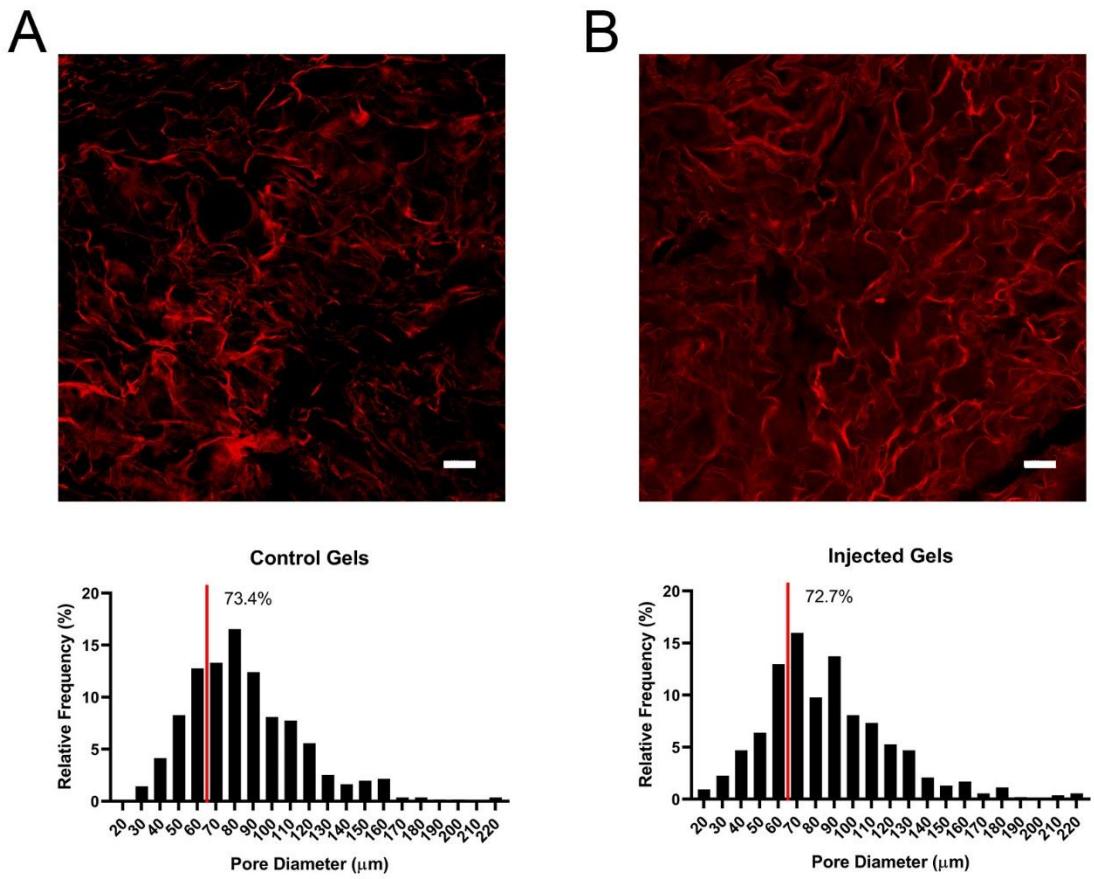

Figure 4.2: Measuring hydrated cryogel porosity. Cryogels were fabricated and then labelled with a Cy5-amine on the alginate backbone. Gels were then placed in HBSS solution and imaged while hydrated to evaluate pore size. (**A**) Control gels were imaged and pore size quantified in ImageJ revealing that 73.4% of the pores were larger than 70 μm in diameter. (**B**) Injected gels appeared similar in representative images and maintained a macroporous structure with 72.7% of pores having diameters larger than 70 μm.

4.3.2 Verification and loading of proteins for macrophage repolarization and chemoattraction

To evaluate the appropriate biomolecules for cryogel loading, preliminary *in vitro* studies were performed on cultured bone marrow-derived macrophages (BMDMs). BMDMs were isolated and polarized to classical (M1) or alternative (M2) phenotypes via cytokine stimulation as previously demonstrated.[166] Skewed macrophages were then treated with IFN-γ, IL-12, or a

co-treatment and examined for viability and phenotype change. While the IFN-γ treatment alone did result in significantly decreased viability in M0 and M2 BMDMs, both IL-12 and the co-treatment did not significantly affect macrophage viability (**Supplemental Figure 4.S6**). Based on the results from viability studies, a co-treatment of 100 ng/mL IFN-γ and 100 ng/mL IL-12 was chosen for repolarization studies. Treatment with IFN-γ alone significantly increased the expression of TNF-α and increased the M1 markers iNOS and CXLC9 147-fold and 40.5-fold, respectively, compared to the M2 control. However, IFN-γ treatment only decreased Arginase-1 expression 10-fold compared to a 74.8-fold decrease in the IL-12 treatment (**Supplemental Figure 4.S7**). While IL-12 did not increase expression of the M1 markers in single treatment, the co-treatment of IFN-γ and IL-12 increased M1 marker expression to the level of the IFN-γ single treatment and decreased Arginase-1 expression 2-fold more than IFN-γ alone (**Supplemental Figure 4.S7**). The results were further validated by evaluating inflammatory cytokines in the supernatant of cytokine-treated BMDMs. Analysis of inflammatory cytokines released by macrophages revealed an increase in inflammatory cytokines IL-1β and TNFα as well as the chemokines CXCL10 and CXCL9, which are essential chemokines in recruiting and activating T cells (**Supplemental Figure 4.S7**).[212] Based on these results, a cotreatment of 100 ng/mL each of IFN-γ and IL-12 was chosen for loading into the cryogels to induce macrophage repolarization.

To induce macrophage migration to the cryogels, the chemokine CCL2, also known as monocyte chemoattractant protein-1 (MCP-1), was examined for macrophage chemoattraction.[213] BMDMs were isolated and polarized to the M2 phenotype before replating in the cell channel of an Ibidi® chemotaxis assay. After the cells adhered, the reservoirs were filled with media containing 2% FBS with or without a range of CCL2 concentrations: 0.1, 0.5, 1 or 2 μg/mL. Cell tracking was performed in ImageJ and the data analyzed using Ibidi's Chemotaxis

and Migration Tool. Chemokine-induced migration was quantified by comparing the center of mass in the direction of the chemokine gradient (COMD), which resulted in a numerical value based on the distance in the x-axis cells migrated from their point of origin at time t=0 hours to their final location at time t=24 hours. All concentrations of CCL2 resulted in a large increase in COMD values compared to the negative control, but there were no differences between any of the concentrations evaluated (**Supplemental Figure 4.S8**). Based on these results, the same concentration as the cytokines (100 ng/mL) was chosen for gel loading.

Based on these results, IFN-γ, IL-12, and CCL2 were used for loading into the cryogels at a concentration of 100 ng/mL for each molecule for all subsequent experiments. Cryogels were fabricated with IFN-γ, IL-12, and CCL2 (ILC Gels) and incubated in 1 mL 0.1% (m/v) BSA in PBS at 37°C to evaluate cargo release. At certain timepoints, the gels were centrifuged, and the supernatant was collected and stored at -20°C. An enzyme-linked immunosorbent assay (ELISA) revealed that the three proteins exhibited similar release curves with about 90% of total cargo being released after 96 hours (**Figure 4.3**). However, one noticeable difference in the release profiles is the slower rate of release of IFN-γ during the first 48 hours. These slight differences could actually provide benefit when delivered *in vivo*. The rapid initial release of CCL2 functions to attract the TAMs immediately after injection and coupled with the rapid release of

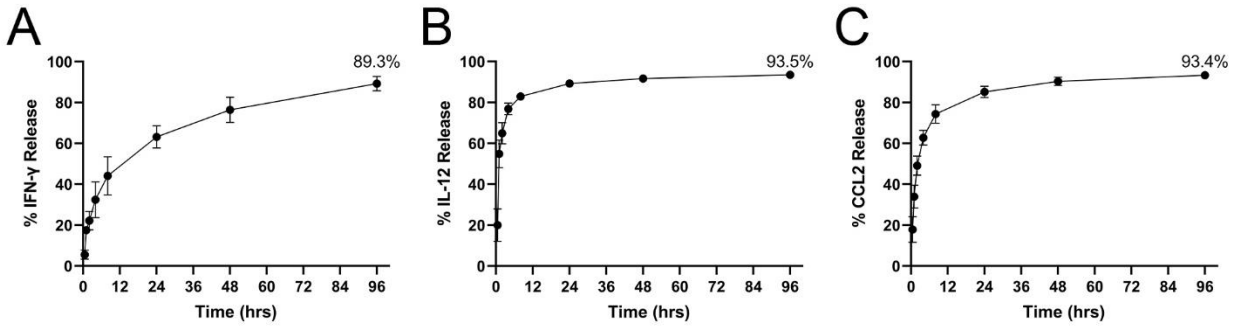

Figure 4.3: Release kinetics of loaded biomolecules. Evaluation of released proteins at various timepoints revealed similar burst release profiles for (**A**) IFN-γ, (**B**) IL-12, and (**C**) CCL2. All three molecules released greater than 89% of loaded cargo by 96 hours of incubation.

IL-12 over the first 12 hours creates an inflammatory microenvironment immediately surrounding the cryogel. The slower release of IFN-γ, which remains steady out to 48 hours, will prolong the exposure of inflammatory cues to the TAMs, helping to perpetuate the repolarization and reduce the chance of the immunosuppressive TME overpowering the pro-inflammatory microenvironment. Overall, this data confirms the ability to load the cell-signaling molecules for use in *in vitro* and *in vivo* experiments.

4.3.3 ILC-induced chemoattraction of M2 BMDMs

After establishing the release profiles, BMDMs were treated with either control cryogels (Empty Gels) or ILC Gels for 48 hours. Initial studies examined BMDM viability after cryogel treatment to ensure no toxicity. These studies demonstrated no significant changes in BMDM viability for any macrophage phenotype after a 48-hour treatment (**Supplemental Figure 4.S9**). To evaluate chemoattraction *in vitro*, the cryogels were labeled with a Cy5-amine and cultured with polarized BMDMs on coverslips. After 48 hours, the cells were fixed and permeabilized before labeling with AlexaFluor-488 (AF-488)-tagged anti-F4/80 and Hoechst. The cryogels were imaged twice in the same region, once on the surface of the coverslip where the cells were plated and again 100 μm higher on the z-axis to image the actual gel. The images were overlaid and a boundary drawn around the edge of the cryogel to visualize BMDM migration to the edge of the gels. Confocal imaging clearly visualizes the increased attraction of M2-polarized BMDMs to the edge of the ILC Gels when compared to both M0 (unpolarized) and M1-polarized macrophages (**Figure 4.4**). To quantify cell migration, a trans-well assay was performed with M2-polarized BMDMs plated on top of the trans-well membrane in media containing 2% serum, while below the membrane either 2% serum media (negative control), 100 ng/mL CCL2 (positive control), an empty gel, or an ILC gel were treated. The membranes were

removed after 6 hours of incubation, fixed, and stained with DAPI. The membranes were imaged using fluorescent confocal microscopy at the Cell Imaging Shared Resource (CISR) and the number of cells quantified using ImageJ. These results demonstrated a 1.7-fold increase in cell migration in the ILC gel treatment compared to the negative control, indicating successful chemoattraction via CCL2 loading into cryogels (**Supplemental Figure 4.S10**). This experiment also revealed an increase in cell migration from the empty gel alone, likely due to the innate response of macrophages to interact with foreign substances.[214] However, when combined with the visualization of M2 BMDMs preferentially migrating towards the loaded gels, the functionality of CCL2 is clearly not hindered by cryogel loading.

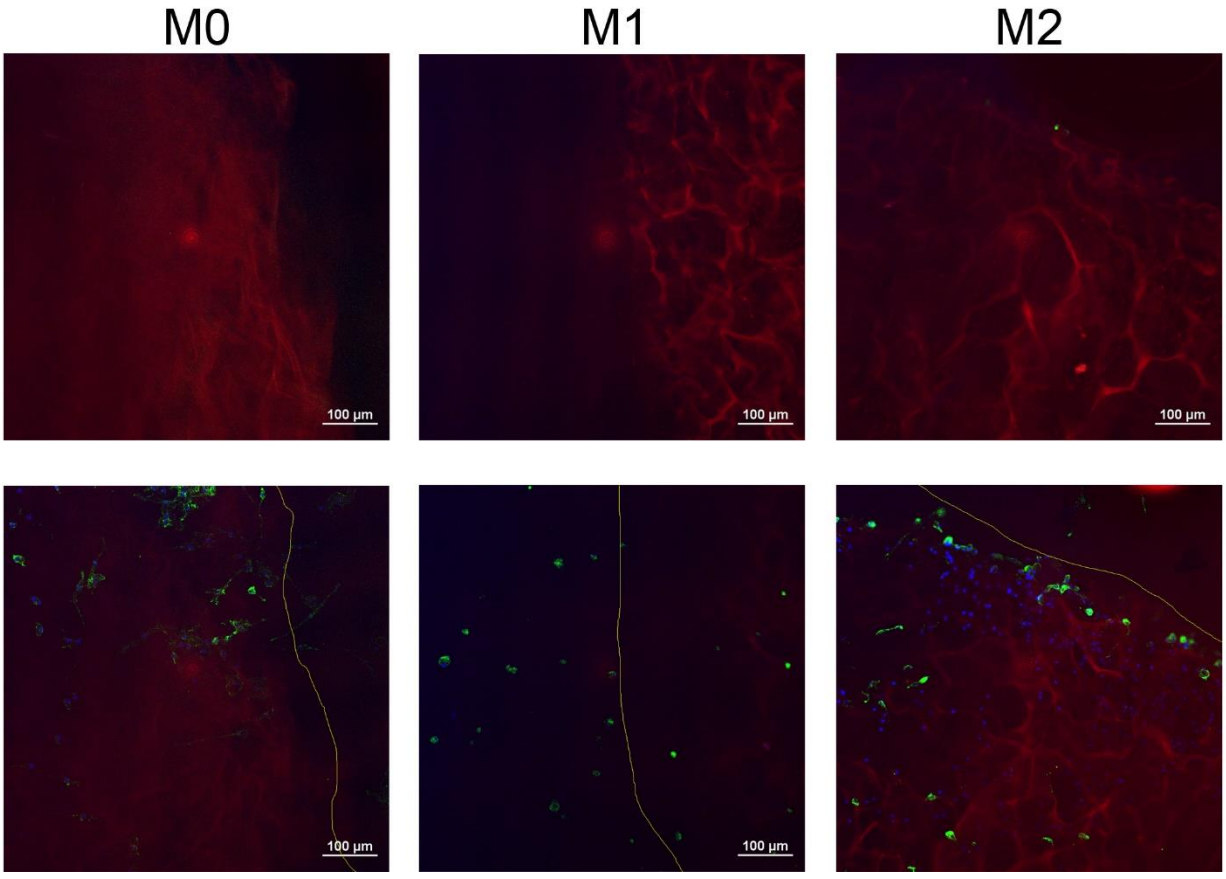

Figure 4.4: Fluorescent imaging of ILC-induced chemoattraction. Polarized BMDMs were cultured for 48 hours with ILC Gels before being fixed and stained with Hoechst (blue, nuclei) and anti-F4/80 (green) antibodies. Visually, there is clear evidence of preferential chemoattraction of M2-polarized BMDMs towards the cryogel compared to the unpolarized (M0) and M1-polarized BMDMs. Top images were taken 100 µm higher on the z-axis while bottom images were taken at the level of the coverslip where the cells were plated. Yellow line represents the outline of the gel from the 100 µm higher image.

4.3.4 BMDM repolarization from loaded cryogel treatment

Cryogel treatments were repeated and BMDMs were collected for analysis with qRT-PCR, flow cytometry, or a Luminex panel to evaluate changes in macrophage phenotype. Changes in RNA expression were consistent with treatments of the free cytokines and demonstrated robust activation of M1-associated markers. Noticeably, iNOS and IL-1β expression significantly increased in the ILC gel-treated group compared to both the control and EG treatment, while TNF-α and CXCL9 expression were also greatly elevated, though not statistically significant, indicating a shift towards a pro-inflammatory phenotype (**Figure 4.5A-D**). To further evaluate changes in protein expression, BMDM treatments were repeated for flow cytometry and Luminex analysis. Flow cytometry revealed a slight decrease in CD206 expression in the cryogel-treated BMDMs, though not significant (**Figure 4.5E**). However, the BMDMs treated with ILC Gels exhibited a significant increase in the receptor MHCII, to the level of the M1 controls (**Figure 4.5F**). This result is important as it demonstrates the treated macrophages are upregulating MHCII which is crucial to macrophages presenting antigens to T cells and subsequently activating T cells. Furthermore, a Luminex cytokine/chemokine assay was performed on the treated BMDMs to evaluate functional production of inflammatory markers. Several markers demonstrated significant upregulation in the ILC-treated BMDMs, including IL-1β, TNF-α, CXCL10, and CXCL9 (**Figure 4.5G-H**). This study provides strong evidence of the potential for ILC-treated tumors to repolarize TAMs and lead to a robust anti-tumor immune response since CXCL9 and CXCL10 are both crucial chemokines to stimulating a Th1 cytotoxic T cell response, necessary for stimulating an immune response.[212] Taken together, these results demonstrate effective repolarization of M2 BMDMs to a pro-inflammatory

phenotype capable of producing an inflammatory microenvironment and recruiting/activating T cells.

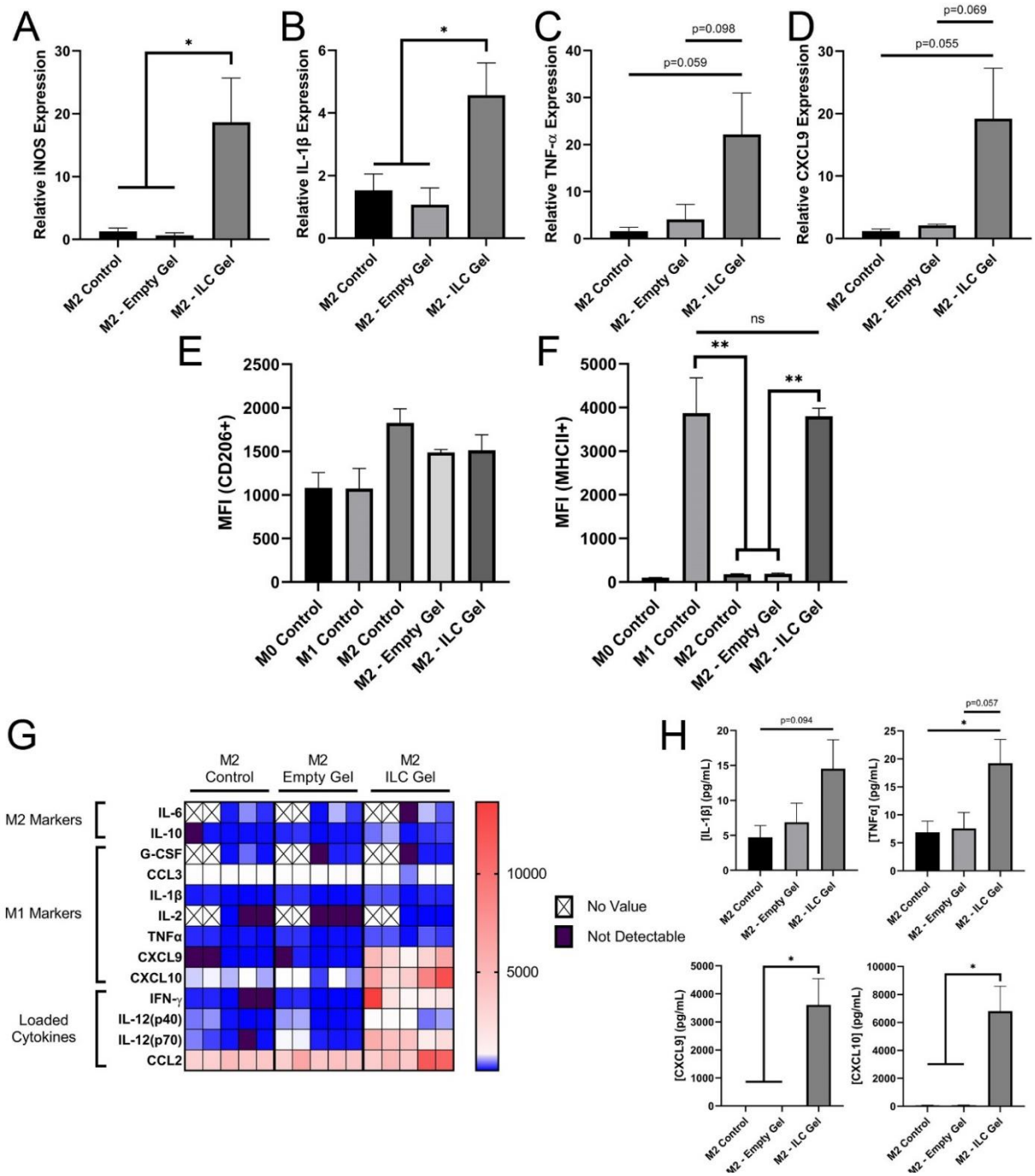

Figure 4.5: Evaluation of BMDM repolarization after treatment with ILC Gels. M2-polarized BMDMs were treated with Empty Gels or ILC Gels for 48 hours. qRT-PCR analysis of RNA expression revealed significant increases in (**A**) iNOS and (**B**) CD86 in ILC-treated cells compared to both control and Empty Gel treatment. ILC Gels also increased (**C**) TNF-α and (**D**) CXCL9 expression though not significantly. Flow cytometry analysis revealed (E) a decrease in CD206 and (F) a significant increase in MHCII. (G) Luminex analysis of released cytokines and chemokines revealed large shifts to a functional M1 phenotype, including (H) large increases in production of IL-1β, TNF-α, CXCL9, and CXCL10.

4.3.5 Examining cryogel-induced repolarization in disease-relevant *ex vivo* models

To evaluate a more relevant model of macrophage polarization, tumor-associated macrophages (TAMs) were isolated from primary mammary tumors. Transgenic mice expressing the polyoma middle T antigen (PyMT) spontaneously form mammary tumors and were used for isolating TAMs. The tumors were processed to a single-cell suspension and then the TAMs were isolated using CD11b magnetic bead purification. TAMs were then plated and treated with cryogels (Empty or ILC) for 48 hours. Similar to the results seen in treated BMDMs, the TAMs exhibited a robust change in phenotype when treated with the ILC Gels. RNA expression via qRT-PCR demonstrated significant increases in the M1 markers iNOS, CD86, and CXCL9 for the ILC-treated cells compared to both the control (untreated) group and the empty gel-treated group (**Figure 4.6A-C**). Furthermore, ILC Gel treatment also significantly decreased expression of Arginase-1, an enzyme overexpressed in M2-like macrophages (**Figure 4.6D**). In addition, flow cytometry analysis confirmed these results with a decrease in CD206 and TGF-β mean fluorescent intensity, and an increase in MHCII (**Figure 4.6E-G**). Luminex analysis of the released cytokines and chemokines also showed slight increases in inflammatory cytokines IL-1β and TNF-α along with substantial increases in CXCL9 and CXCL10, indicating a successful shift in the more clinically-relevant TAMs to a pro-inflammatory phenotype (**Figure 4.6H,I**). These results match the changes seen in BMDMs and also provide support for the ability of this treatment to effectively repolarize immunosuppressive TAMs into a potentially anti-tumor phenotype.

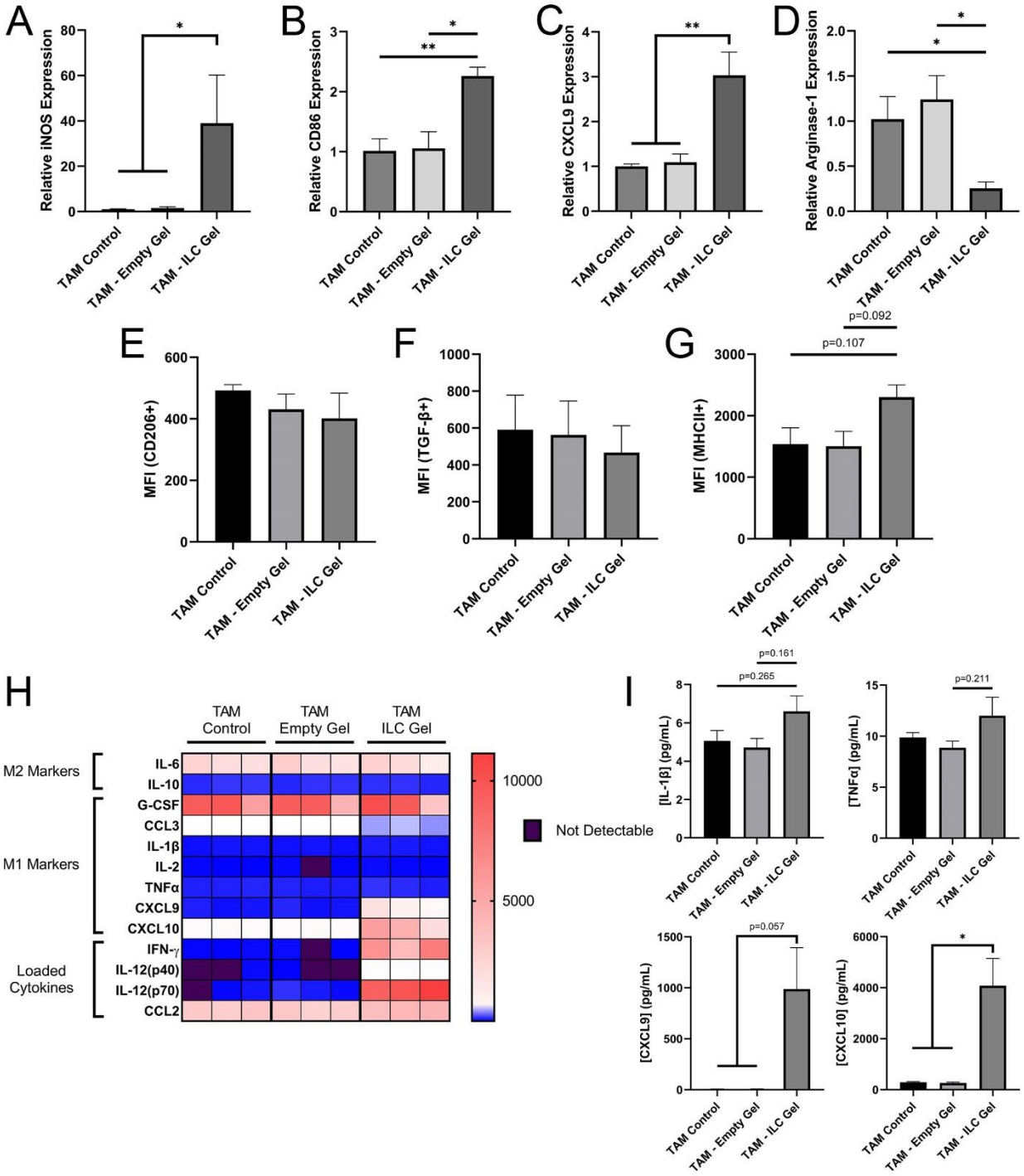

Figure 4.6: Repolarizing TAMs with loaded cryogels. TAMs isolated from spontaneous mammary tumors were treated for 48 hours with cryogels. The ILC-treated TAMs displayed significant increases in RNA expression of (**A**) iNOS, (**B**) CD86, and (**C**) CXLC9 and a significant decrease in (**D**) Arginase-1. Flow cytometry analysis revealed trends of (**E**) decreasing CD206 and (**F**) TGF-β and (**G**) a trend of increasing MHCII. (**H**) Luminex analysis once again revealed large shifts towards an M1 phenotype, including increased release of (**I**) IL-1β and TNF-α and significantly increased release of CXCL9 and CXCL10.

An additional *ex vivo* model was applied to further examine the ability of ILC Gels to repolarize TAMs in the context of the immunosuppressive tumor microenvironment. For this model, tumor explants around 2-3 mm in diameter were isolated from the PyMT mice and cultured *ex vivo*. These explants were examined for viability after 96 hours in culture to confirm the presence of live cells in *ex vivo* conditions (**Supplemental Figure 4.S11**). After verifying viability, the explants were cultured with Empty Gels or ILC Gels for 48 hours before collecting RNA for qRT-PCR or supernatant media for Luminex analysis. Expression of F4/80 was examined to verify the presence of live macrophages after 48 hours. The level of F4/80 expression in the explant control was less than the isolated TAM control, but both cryogel treatments resulted in no differences in F4/80 expression compared to TAMs alone, supporting the assumption that TAMs could be cultured in explants (**Figure 4.7A**). Expression of the PyMT gene to evaluate tumor cell population did not reveal any changes in any of the treatments, likely due to the short treatment timeframe of this study (**Figure 4.7B**). However, treatment with ILC Gels did significantly increase the expression of iNOS, TNF-α, and CXCL9 compared to the control and empty gel-treated explants, revealing a shift in macrophage phenotype in the context of an immunosuppressive TME (**Figure 4.7C-E**). Additionally, there was a trend in decreasing CD206 expression supporting the shift away from the immunosuppressive M2 phenotype (**Figure 4.7F**). These results correlate well to the measured cytokines and chemokines, which once again revealed large increases in IL-1β and TNF-α production, combined with significant increases in CXCL9 and CXCL10 release (**Figure 4.7G,H**). These results provide strong evidence that the loaded cryogel system can provide a robust macrophage repolarization depot to overcome the immunosuppressive microenvironment associated with culturing whole tumor

explants. These studies led to our subsequent *in vivo* evaluations of treating PyMT tumor-bearing mice with peritumoral injections of cryogels.

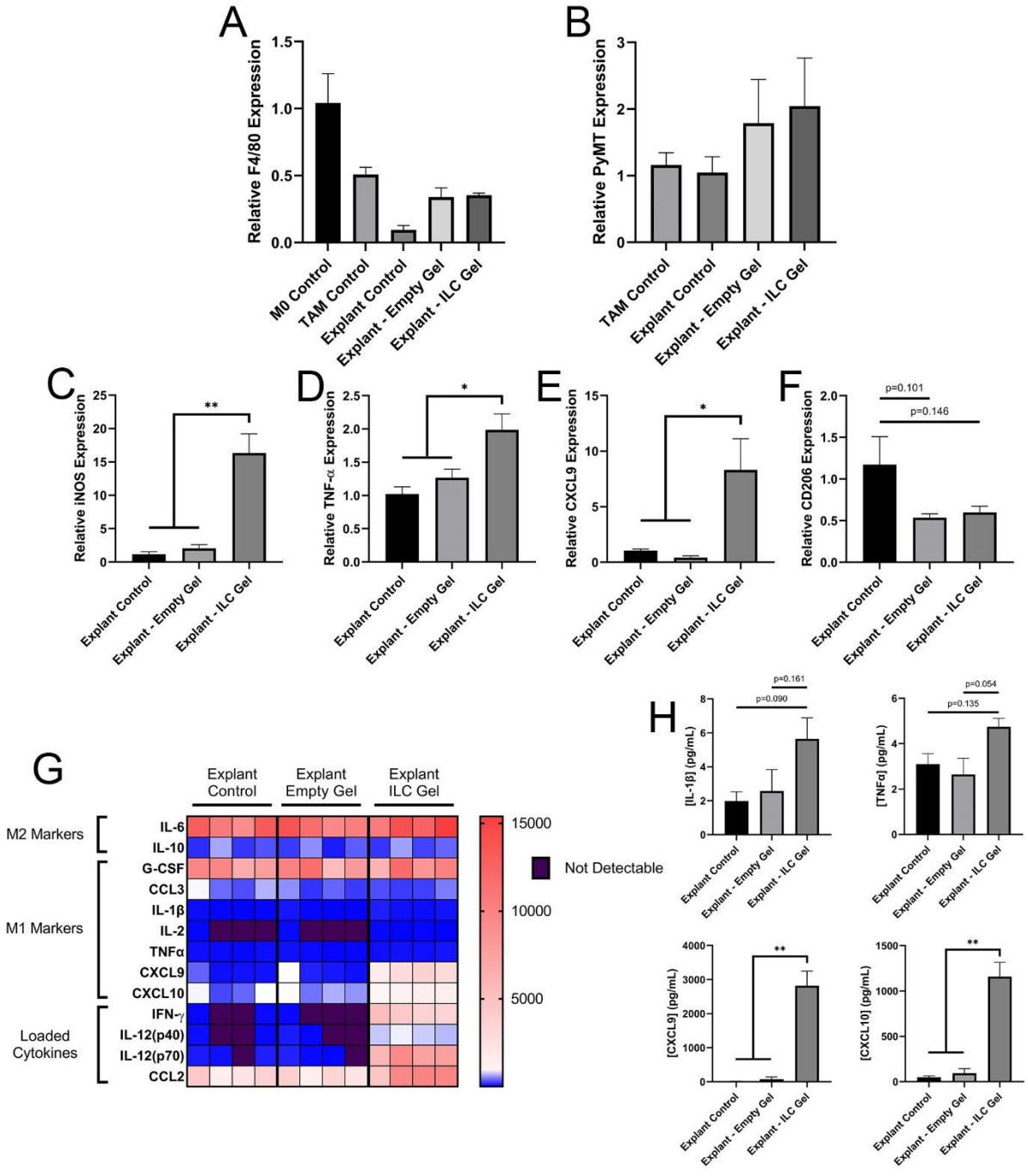

Figure 4.7: Stimulating inflammation in primary tumor explants. Tumor explants derived from spontaneous PyMT tumors were cultured *in vitro* with cryogels for 48 hours. qRT-PCR analysis revealed viable macrophages and tumor cells after 48 hours of cultured based on expression of (**A**) F4/80 and (**B**) PyMT, respectively. Additional qRT-PCR analysis showed significant increases in M1 markers (**C**) iNOS, (**D**) TNF-α, and (**E**) CXCL9 with a trend of decreasing M2 marker (**F**) CD206. (**G**) Luminex analysis revealed increased release of (**H**) IL-1β and TNF-α and significantly increased release of CXCL9 and CXCL10.

4.3.6 Evaluating Cryogel-Induced Changes in *In Vivo* Tumor-Immune Microenvironment

To evaluate the potential anti-tumor effects of peritumoral injection of ILC Gels, FVB mice were given orthotopic injections of $1x10^6$ PyMT cells directly into the #4 mammary fat pad. The tumors were allowed to develop until palpable (~4-5 weeks) and then injected peritumorally with 100 µL PBS loaded with nothing (saline control), one empty gel, or one loaded gel. The tumors were then measured 3x/week for 15 days before humanely sacrificing the mice to collect tissue for analysis. The relatively short timepoint of this study was chosen to effectively evaluate changes in the immune cell composition of the TME. Over the course of the entire study (tumor induction to endpoint), there were no changes in average weight of the mice, even after cryogel injection, providing evidence that there was no systemic toxicity associated with treatment (**Supplemental Figure 4.S12A**). After the 15-day treatment, ILC Gels significantly suppressed tumor growth compared to both the PBS control and the Empty Gel treatment (**Figure 4.8A,B**). Slowed tumor growth was observed as early as 11 days after cryogel injection, but the change was not significant until day 13. These results demonstrate that the gel treatment itself does not affect tumor development, but the loaded gel can significantly alter tumor development. Furthermore, tumor sections stained with H&E revealed some indications of decreased cellularity in the ILC Gel-treated mice which was not present in the PBS control or Empty Gel treatments (**Supplemental Figure 4.S12B-D**).

At endpoint, the tumors were surgically removed and weighed, but there was no significant difference in final tumor weight, although there was a trend of decreasing weight in the ILC Gel treatment (**Figure 4.8C**). The tumors were then processed to single-cell suspensions for flow cytometry analysis, and the initial gating on CD45 for whole immune cell population revealed a large increase in %CD45+ cells in the loaded cryogel treatment, indicating an increase

in immune cell infiltration in the tumors (**Figure 4.8D**). Next, TAM populations were examined by gating for CD45+/CD11b+/CD11c-/F4/80hi. Of these populations, there were no changes in the percent of M2-like TAMs (CD206+/MHCII-) or M1-like TAMs (CD206-/MHCII+) in any of the treatments (**Supplemental Figure 4.S13A,B**). However, when quantifying the ratio of M1:M2 TAMs, there was evidence of increasing the ratio of M1:M2-like TAMs in the ILC Gel treatment, indicating a shift towards an inflammatory phenotype (**Figure 4.8E**). While this result was not significant, the timing of this study could play a factor since the macrophages were likely repolarized early on as the inflammatory biomolecules were released from the gels, then normalized back to equal populations as the cytokines dissipated. However, the 15-day timepoint was primarily chosen to evaluate changes in lymphocyte populations. The general CD4+ and CD8+ T cell populations (gated CD45+/CD11b-) did not significantly change due to cryogel treatment (**Supplemental Figure 4.S13C,D**). However, when examining exhaustion marker lymphocyte activation gene 3 (LAG3) and immune checkpoint marker PD-1, there were significant changes in T cell composition. Both LAG3+/PD-1+ and LAG3+/PD-1- CD4 T cell populations significantly decreased in the ILC Gel treatment, indicating a significant decrease in the amount of exhausted CD4 T cells in the TME (**Figure 4.8F,G**). This coincided with an increase in the percent of non-exhausted CD4 T cells (**Figure 4.8H**). Furthermore, the same results were observed in a decrease in the percent of LAG3-/PD-1+ CD8 T cells and an increase in non-exhausted CD8 T cells (**Figure 4.8I,J**). Overall immune cell composition demonstrates the changes in the CD45+ immune cell population with trends of increasing M1/M2 ratio as well as increasing CD4 and CD8 T cells (**Supplemental Figure 4.S13E**). Taken together, these results demonstrate that localized delivery of inflammatory cytokines effectively slows tumors development and significantly alters the T cell populations in the TME. Furthermore, the

decreases in the exhausted T cell populations provide support for future studies examining combination treatments with other immunotherapies such as immune checkpoint blockades. In fact, other groups have shown that a combined strategy of decreasing both LAG3 and PD-1 expression on T cells can increase the ability of APCs, such as macrophages, to activate T cells.[215] Overall, the ILC Gels provide robust evidence for developing an anti-tumor immune response that warrants future consideration in combination studies to increase efficacy.

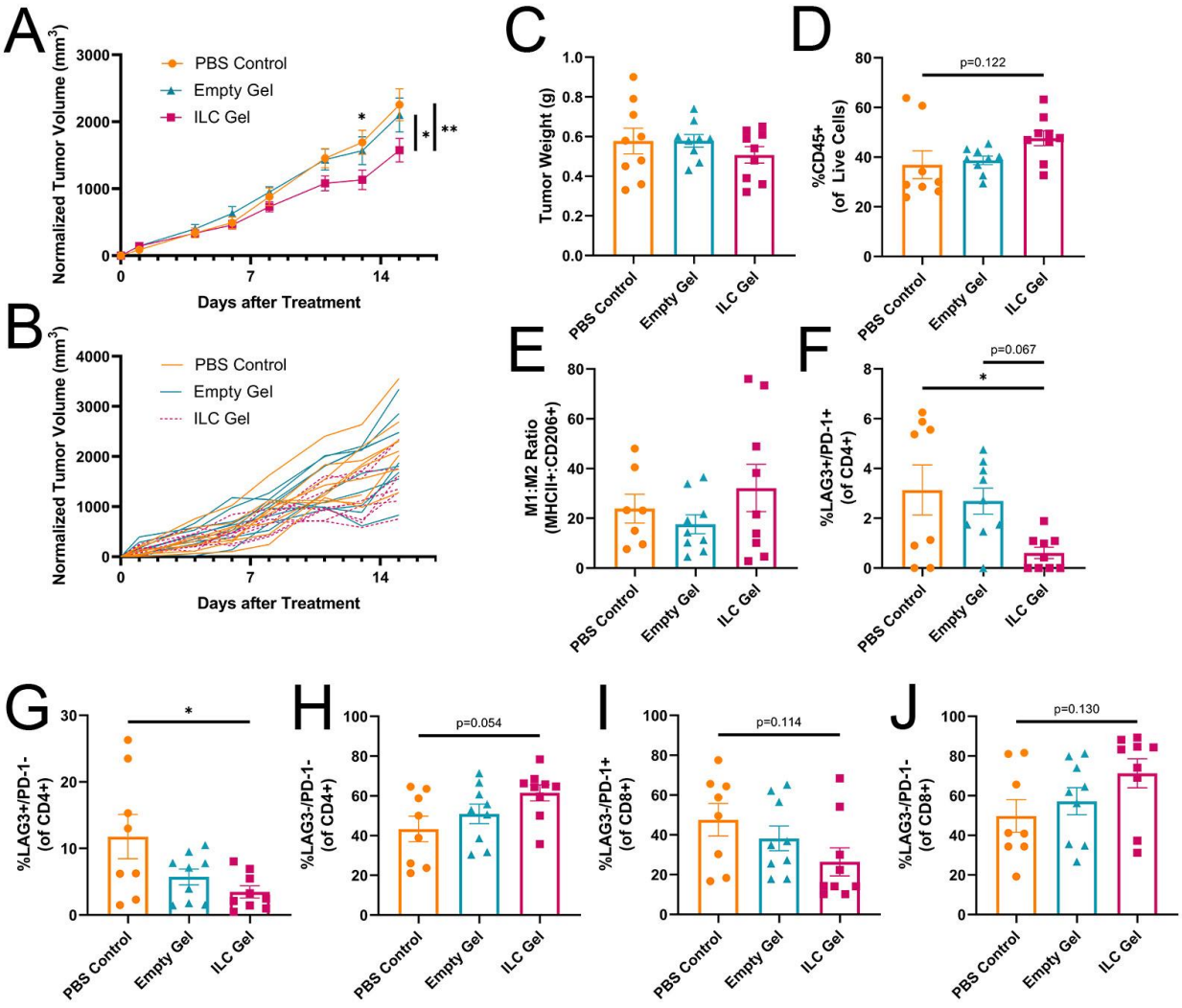

Figure 4.8: ILC Gel treatment significantly suppresses tumor progression and alters immune composition. FVB mice with PyMT tumors were treated with cryogels and allowed to develop for 15 days. The ILC Gel treatment significantly suppressed tumor volume growth over the 15 day treatment as shown by (**A**) the average tumor volumes (PBS n=8, EG and ILC n=9, *p<0.05, **p<0.001) and (**B**) the individual tumor volumes. (**C**) Final tumor weights were not significantly altered by cryogel treatment (PBS n=8, EG and ILC n=9). Flow cytometry analysis was used to evaluate (**D**) CD45+ immune cells and (**E**) the M1:M2 ratio of TAMs (PBS n=7, EG and ILC n=9,). T cell gating was used to evaluate CD4 populations based on (**F**) LAG3+/PD-1+, (**G**) LAG3+/PD-1-, and (**H**) LAG3-/PD-1- and CD8 populations based on (**I**) LAG3-/PD-1+ and (**J**) LAG3-/PD-1- (PBS n=8, EG and ILC n=9, *p<0.05).

4.4 Conclusions

The results of this study established a cryogel biomaterial system for localized TAM repolarization. The fabrication and characterization of the alginate cryogel demonstrated the macroporous structure due to cryogelation and the toughness provided by secondary ionic crosslinking enabling injection through a syringe without loss of structural properties. We also identified the appropriate biomolecules for chemoattracting and repolarizing M2 macrophages and demonstrated successful loading and subsequent release of these molecules from the cryogels. The loaded (ILC) cryogels were then used *in vitro* to evaluate changes in primary macrophage phenotype. These studies demonstrated the robust macrophage repolarization associated with ILC Gel treatment by evaluating changes in RNA expression (qRT-PCR), protein abundance (flow cytometry), and cytokine/chemokine release (Luminex) in three separate models. The primary BMDMs were polarized to M2 before treatment to demonstrate the plasticity of macrophages. The treatments were repeated with TAMs isolated from primary tumors and cultured tumor explants to evaluate changes in macrophages in the context of the TME, and both of these models exhibited significant increases in M1 macrophage phenotype. These results support the notion that localized treatment with ILC Gels can overcome the TME to repolarize TAMs. Finally, the cryogels were injected peritumorally in mice with primary mammary tumors. This study showed a significant suppression of tumor development due to ILC Gel treatment. Furthermore, although the myeloid cells changes were not significant, there was a large increase in the ratio of M1:M2-like TAMs. We also provided evidence that altering TAMs subsequently resulted in significant changes in the T cell populations as shown by the decrease in exhaustion marker LAG3 and checkpoint marker PD-1. Overall, we have developed a

translatable system that shows promise for future combination treatments with ICB therapies due to the priming of the TME shown in this study.

4.5 Materials and methods

4.5.1 Fabrication of Methacrylated-Alginate

MA-alginate was fabricated as previously described.[78] Briefly, 1.0 g UP MVG sodium alginate (NovaMatrix, Sandvika, Norway) was slowly added to a 0.1 M 2-(N-morpholino)ethanesulfonic acid (MES) buffer (pH=6.4) at 0.6% (w/v). The alginate was dissolved in a glass vial on a stir plate to generate a homogenous solution. To activate the carboxyl groups on the alginate backbone, NHS (1.3 g) and EDC (2.8 g) were added and allowed to stir for 5 minutes. AEMA (2.24 g) was added and the reaction vessel was covered and left to stir for 24 hours at room temperature. The alginate solution was then precipitated dropwise into excess acetone and filtered through a 0.45 μm filter to collect the solid MA-alginate. The resulting MA-alginate was dried in a vacuum oven overnight at RT. To purify the final product, the MA-alginate was dissolved at 1% (w/v) in deionized (DI) water and dialyzed against DI water for 3 days (MWCO = 3500 kDa). The final solution was collected, frozen at -80°C, and lyophilized. For NMR, MA-alginate was dissolved at 1% (w/v) in deuterium oxide (D_2O).

4.5.2 Cryogelation of MA-Alginate

To form cryogels, 10 mg MA-alginate was dissolved slowly at 1.5% (w/v) in DI water (667 μL) on a stir plate. The dissolved MA-alginate was then cooled for >1 hour at 4°C. Radical initiators N,N,N',N'-tetramethylethylenediamine (TEMED) (0.5% w/v) and ammonium persulfate (APS) (0.25% w/v) were added and the solution was immediately pipetted into a precooled (-20°C) PTFE mold and placed at -20°C. For all gel injection and cell culture

experiments, cryogels were designed to be circular with a 5 mm diameter and 1 mm thickness. For physical characteristic tests, including rheology measurements, square cryogels with 5x5x2 mm dimensions were used. For loaded cryogels, IFN-γ, IL-12, and CCL2 were added to the gelation solution at a final mass of 100 ng of each molecule per gel. The gels were crosslinked for 24 hours before thawing. The cryogels were rinsed with DI water to remove excess initiators and then ionically crosslinked in a 200 mM calcium chloride solution for 10 minutes to form "tough" cryogels. For NMR samples, the MA-alginate was dissolved in D_2O, mixed with radical initiators, and directly added to an NMR tube and left at -20°C overnight.

4.5.3 Physical Characterization of Cryogels

For SEM, cryogels (control or injected) were dehydrated in serial dilutions of ethanol in DI water. Gels were soaked in 30%, 50%, 70%, 90%, and 100% ethanol in DI water (v/v) for 20 minutes each. The fully dehydrated cryogels were then soaked in hexamethyldisilazane (HMDS) for 10 minutes and placed under vacuum for one hour. For cryosectioning, fully dried cryogels were placed in optimal cutting temperature (OCT) compound and frozen at -80°C. The frozen gels were then cryosectioned into 20 μm slices. Samples (whole gels or sections) were then placed on SEM specimen mounts with double-sided carbon tape. Sectioned gels were rinsed briefly with DI water to remove OCT and dried overnight in a vacuum oven. All samples were sputter-coated with Au and imaged on a Zeiss Merlin SEM in the Vanderbilt Institute for Nanoscale Science and Engineering (VINSE).

To quantify hydrated pore size, cryogels were labelled with Cy5-amine to create fluorescent gels. Briefly, cryogels were submerged in a 0.1 M 2-(N-morpholino)ethanesulfonic acid (MES) buffer (pH=6.5) at 1 mL/gel. NHS (7.8 mg) and EDC (16.8 mg) were added and mixed on a shaker for 10 minutes to activate the carboxyl groups on the alginate backbone. After

activation, Cy5-amine (6.9 µg, Cat. #130C0, Lumiprobe, Maryland, USA) was added and the solution was placed on a shaker for 2 hours in the dark. Excess Cy5-amine was washed off with DI water and gels were placed on a microscope slide and covered with a few drops of Hank's Balanced Salt Solution (HBSS) to prevent dehydration. Fluorescent imaging was conducted on a Nikon Czsi+ system with a Nikon Eclipse TioE inverted microscopy base, Plan ApoVC 20x differential interference contrast N2 objective, and a 505/565 dichroic mirror. All image acquisition was performed using Nikon NIS-Elements AR version 4.50.00. Image processing and analysis was done using Fiji in ImageJ version 1.53f51.[184]

All other physical characterizations were performed with square cryogels. To determine interconnected porosity and swelling ratio, we employed the wicking method.[77] Gels were hydrated in DI water for 2 minutes before measuring the hydrated mass (m_h). Excess water was wicked away with a kimwipe before weighing dehydrated gels (m_d). Interconnected porosity (P) was calculated as $(m_h - m_d)/m_h \times 100\%$. For swelling ratio, gels were serially dried in ethanol as done previously before placing under vacuum for 24 hours. The fully dried gels were weighed (m_{dry}) and swelling ratio calculated as m_h/m_{dry}. Rheology measurements were performed with a rheometer to determine Young's modulus (E) of the cryogels. Oscillation measurements were performed to determine storage modulus (G') and loss modulus (G"). These values were then used to calculate the shear modulus (G) using $G = \sqrt{(G'^2 + G"^2)}$. Young's modulus was then calculated as $E = 2 \times G(1+\nu)$ where Poisson's ratio (ν) was taken to be 0.5, which is common for hydrogel characterization.[216]

4.5.4 Culturing Bone Marrow-Derived Macrophages

BMDMs were isolated and cultured as previously described.[166] All animal work was approved by the Vanderbilt University Institutional Animal Care and Use Committee (IACUC). Bone marrow was flushed from the rear femurs and tibias of healthy female FVB mice. The collected cells were centrifuged (1000g, 5 minutes) and blood cells were lysed by resuspending in 2 mL ACK lysing buffer (KD Medical, Columbia, MD) and incubating on ice for 2 minutes. The lysis solution was diluted in 10x volume of DMEM and centrifuged. The resulting cells were resuspended in 10 mL L929-conditioned media: DMEM (15-018-CV) with 10% FBS, 1% P/S, 1% L-glutamine, and 14% 1:1 (v/v) L929 week 1 and week 2 media. L929 media was prepared as previously described.[166] BMDMs were counted and plated at $1x10^5$ cells/well in 96-well plates for cytokine viability studies and plated at $1x10^6$ cells/well in 12-well plates for all other studies. The cells were cultured for four days in L929-conditioned media to allow macrophages to mature. On day 4, M2-polarizing cytokines (10 ng/mL IL-4 and 20 ng/mL IL-13) were added and incubated for four days. On day 7, M1-polarizing reagents (100 ng/mL IFN-γ and 0.1 ng/mL lipopolysaccharide (LPS)) were added and incubated for 24 hours. All treatments were done on day 8 after macrophages were fully polarized.

4.5.5 Viability Assays on BMDMs

Free cytokine treatments were conducted at concentrations of 100 ng/mL or 500 ng/mL of IFN-γ (BioLegend; 575304) or IL-12 (R&D Systems; 419-ML-010/CF) for 48 hours, and the cotreatment was performed at 100 ng/mL each of IFN-γ and IL-12 for 48 hours. To assess viability, a CellTiter-Glo® Luminescent Cell Viability Assay (Promega; G7571) was used according to the manufacturer's instructions. For cryogel treatments, the fabricated cryogels were moved to a sterile 12-well plate and placed under ultraviolet (UV) light for 30 minutes to sterilize. The gels were then placed in PBS (-/-) to allow excess Ca^{2+} ions to leach out. The gels

were then briefly dipped in 70% ethanol (EtOH) before placing back in PBS (-/-) to rehydrate. The sterilized gels were then placed one gel per well in 12-well plates with polarized BMDMs for 48 hours. At endpoint, 500 µL of cell supernatant was moved to 5 wells of a 96-well plate (100 µL/well) and used for CellTiter-Glo® viability assay as described above.

4.5.6 CCL2-Induced Migration of BMDMs

CCL2-induced M2 BMDM migration was evaluated using a µ-Slide Chemotaxis plate (Ibidi®, Germany). After polarization, 6 µL of $2.5x10^6$ cells/mL M2 BMDMs were plated in the cell channel and incubated overnight to allow cells to adhere. The cell channel was washed twice with media containing 2% FBS and one chamber for each sample was filled with 60 µL 2% FBS media. The other chamber was filled with either 2% FBS (control) or varying concentrations of CCL2 in 2% FBS media. The chemotaxis plates were immediately placed in an incubation chamber under a Leica DMi8 microscope and imaged every 30 minutes for 24 hours. Cell migration was tracked via ImageJ Manual Tracking plugin by counting at least 20-30 cells/image with 3 sections per treatment condition. This data was then analyzed using the Chemotaxis and Migration Tool provided by Ibidi. To quantify chemokine-induced cell migration, the change in center of mass in the direction of the chemokine gradient (COMD) was reported.[217]

For all cryogel migration studies, empty and loaded cryogels were labelled with Cy5-amine and sterilized as previously described. To evaluate chemoattraction, Cy5-gels were placed on sterilized coverslips in 6-well plates. Macrophages were added dropwise onto the gels (500,000 cells/well in 2 mL media) and the cells were incubated for 48 hours. The coverslips were transferred to a new 6-well plate and washed with PBS (-/-). The cells were fixed with 5% formalin for 20 minutes at RT before washing 3x in a wash buffer (0.1% BSA w/v in PBS). The slides were then covered with a blocking buffer consisting of 5% goat serum (Abcam; ab7481)

v/v in PBS and incubated at RT for 45 minutes to prevent nonspecific antibody labelling. The blocking buffer was removed and 100 µL of 1:100 dilution of rat anti-mouse F4/80 (Bio-Rad; MCA497GA, Clone Cl:A3-1) was added and incubated at 4°C overnight. The cells were washed again before permeabilizing with 0.5% Triton X100 in PBS (-/-) for 5 minutes at RT. The cells were stained with Hoechst at 1µg/mL for 5 minutes at RT in the dark. ProLong Gold anti-fade mounting media (ThermoFisher; P10144) was added to the coverslip before placing on a microscope slide and imaging with a Nikon Czsi+ system with a Nikon Eclipse TioE inverted microscopy base, Plan ApoVC 20x differential interference contrast N2 objective, and a combination of 405/488 and 505/565 dichroic mirrors. Image analysis was performed using ImageJ.

4.5.7 Treating Isolated Tumor-Associated Macrophages and Whole Tumor Explants

For all TAM experiments, single transgenic mice with mouse mammary tumor virus promoter-polyoma middle T antigen (MMTV-PyMT, or PyMT) were bred on an FVB background. Female PyMT mice spontaneously develop tumors in mammary glands, which can be removed once palpable for single-cell isolation. Tumors were dissected before becoming necrotic (size <15 mm) and cut into small pieces. The tumor tissue was dissociated using a gentleMACS^{TM} Dissociator (130-093-235; Miltenyi Biotec) and the corresponding Tumor Dissociation Kit, mouse (Cat. #130-096-730, Miltenyi Biotec). After tissue dissociation, the samples were filtered through a 70 µm MACS® SmartStrainers (130-098-462; Miltenyi Biotec) and centrifuged at 300g for 7 minutes. Blood cells were lysed as described previously and the resulting solution recentrifuged. TAMs were isolated via CD11b magnetic bead separation by binding cells with CD11b magnetic beads (130-049-601; Miltenyi Biotec) and filtering through

LS columns (130-042-401; Miltenyi Biotec). Isolated TAMs were counted and plated at 500,000 cells/well in a 12-well plate and used for 48-hour cryogel treatments as previously described.

To establish a comprehensive *in vitro* model of the tumor microenvironment, PyMT tumor explants were cultured. Similar to isolated TAMs, primary PyMT tumors were surgically removed from PyMT mice and cut into small 2-3 mm pieces. These explants were then placed in a 12-well plate with 1 mL media consisting of DMEM (15-018-CV) supplemented with 1% L-glutamine, 1% P/S, 1% MEM vitamins, and 10% FBS. The explants were treated with cryogels as previously described for 48 hours.

4.5.8 Tumor Induction and *In Vivo* Experiments

Luciferase-expressing 17L3C polyoma (PyMT) cells were received from the lab of Barbara Fingleton and maintained as previously described.[218] PyMT cells were cultured in DMEM supplemented with 10% FBS, 1% P/S, and 1% L-glutamine as well as 10 µL 1 mg/mL Puromycin (Sigma; P8833) to maintain luciferase construct. For tumor induction, female FVB mice between 8-12 weeks of age were orthotopically injected with $1x10^6$ cells in 50 µL PBS (-/-) directly into the #4 mammary fat pad using Lo-Dose™ U100 Insulin Syringes (BD; 329461). The tumors developed until palpable (~250-500 mm^3) before treatment. Mice were treated by injecting 100 µL PBS (-/-) alone for saline control, or with 100 µL PBS (-/-) containing either a single empty gel or a single loaded gel, all injected adjacent to the palpable tumor (peritumorally). For PBS treatments, a sterile 1 mL Henke-Ject™ syringe was used with a 16G needle. For cryogel treatments, an autoclaved Gastight Microliter™ Syringe (Hamilton™; 763901) was used with a 16G needle. Mice were monitored by weighing 2x/week and measuring tumor volumes 3x/week over the course of the 15-day treatment. At endpoint, all mice were

euthanized following approved IACUC protocols using carbon dioxide inhalation followed by secondary cervical dislocation.

At endpoint, blood was collected via cardiac puncture and PyMT tumors were surgically removed and weighed. The blood was collected into BD Microtainer™ Capillary Blood Collector tubes (BD; 365967) and allowed to coagulate for 30 minutes at RT. The tubes were centrifuged at 1200xg for 10 minutes to separate serum from plasma, and the serum was collected and stored at -80°C. Tumors were separated into two pieces with the larger piece being used for single cell isolation for flow cytometry and the smaller piece either snap-frozen in a cryovial for RNA isolation or fixed in 10% formalin for tissue sectioning.

4.5.9 Cryogel Treatments for Quantitative Reverse Transcription Polymerase Chain Reaction (qRT-PCR)

RNA isolation, cDNA fabrication, and qRT-PCR analysis were performed as previously described.[166,167] For BMDMs and TAMs, RNA was isolated using the RNeasy Mini Kit (Qiagen; 74106). Residual DNA was removed using RNase-free DNase (Qiagen; 79256). cDNAs were synthesized using a SuperScript IV reverse transcriptase kit (Invitrogen; 18090050) and quantitative reverse transcription polymerase chain reaction (qRT-PCR) was performed using SsoAdvanced Universal SYBR Green Supermix (Bio-Rad; 1725270) on a CFX96 real-time PCR instrument and software (Bio-Rad) through the VUMC Molecular Cell Biology Resource (MCBR) core.

For tumor explants and *in vivo* tumor samples, tumor tissue was first placed in TRIzol™ (Invitrogen; 15596026) solution to lyse cells. For explants, the tissue was removed with tweezers from the 12-well plates and placed in 2 mL microcentrifuge tubes. The remaining media in the

wells was used to wash leftover cells off the plate and collect into tubes. The supernatant media was centrifuged at 1500 rpm for 5 minutes and the supernatant aspirated. The tumor explants were then added to the corresponding tube with leftover cells and 1 mL of TRIzol was added. The tubes were vortexed then stored at -80°C. The samples were thawed, vortexed, and refrozen each day for 2-3 days before collecting RNA using Direct-zol RNA kits per the manufacturer's instructions (R2050; Zymo Research).

For snap-frozen *in vivo* tumor samples, the frozen tumor pieces were placed in a mortar with liquid nitrogen and a pestle was used to break up the tumors into smaller pieces. The broken-up tumors were then resuspended in 600 µL TRIzol, vortexed, and frozen at -80°C until further use. Then, a Direct-zol RNA kit was used to isolate RNA as done with the explants. For both explants and *in vivo* tumors, cDNA fabrication and qRT-PCR analysis were performed as done with BMDMs and TAMs.

4.5.10 Flow Cytometry Analysis of Treated Cells

For BMDMs and TAMs, 1X Brefeldin and 1X Monensin were added to the cells about 12-14 hours before flow collection to preserve cytokines for flow staining. At endpoint, the cells were washed with PBS (-/-) and trypsinized using 0.25% trypsin for 5 minutes. Cells were collected, centrifuged at 1500 rpm for 5 minutes, and resuspended in 2 mL BMDM media for counting. The cells were then centrifuged again and resuspended in 500 µL PBS (-/-). For flow staining, the cells were centrifuged and moved to a 96-well plate. Cells were initially stained with surface markers before permeabilizing to stain with intracellular markers. For viability evaluation, a Live/Dead BV510 stain was used. The following anti-mouse antibodies were used: CD11b Alexa Fluor 700, MHCII PerCP-Cy5.5, CD206 PE, IL-10 FITC, IL-4 APC, TNF-α

BV650, iNOS PE, TGF-β APC, CD80 Texas Red, and IL-12 FITC. Flow gating strategy is shown in **Supplemental Figure 4.S14**.

For *in vivo* experiments, the tumors were rinsed in PBS before placing in 5 mL digestion buffer consisting of DMEM with enzymes from mouse tumor dissociation kit (Miltenyi Biotec; 130-096-730). The tumors were chopped up using scalpels and then transferred into gentleMACS^{TM} C tubes (Miltenyi Biotec; 130-093-237). The tubes were dissociated on a gentleMACS^{TM} Octo Dissociator (Miltenyi Biotec; 130-096-427) and then placed in an incubator at 37°C for 45 minutes. The dissociated tissue was then filtered through 70 μm SmartStrainers (Miltenyi Biotec; 130-098-462) before centrifuging and resuspending in PBS for cell counting. The cells were then stained for flow cytometry analysis as described previously. The anti-mouse antibodies used were: CD45 BV786, CD11b Alexa Fluor 700, CD11c PE-CF594, F4/80 APC, CD206 PE, MHCII PerCP-Cy5.5, CD4 BV605, CD8 BV786, NKG2A PE, NK1.1 APC, LAG3 PE-CF594, PD-1 BV421, and TIM3 PE-Cy7.

4.5.11 Statistical Analysis

All statistical analyses were performed using a one-way ANOVA with Tukey's multiple comparison test in the case of two or more groups, a two-way ANOVA with Tukey's multiple comparison test in the case of two or more groups across two or more sets, or a two-tailed student's t-test in the case of only two groups, all with $\alpha = 0.05$. Statistical analyses were performed using GraphPad Prism v9.3.0. All figures were made using Adobe Photoshop 2021 v22.5.1.

4.6 Supplemental Figures

Supplemental Figure 4.S1: NMR Characterization of Alginate Methacrylation and Cryogelation

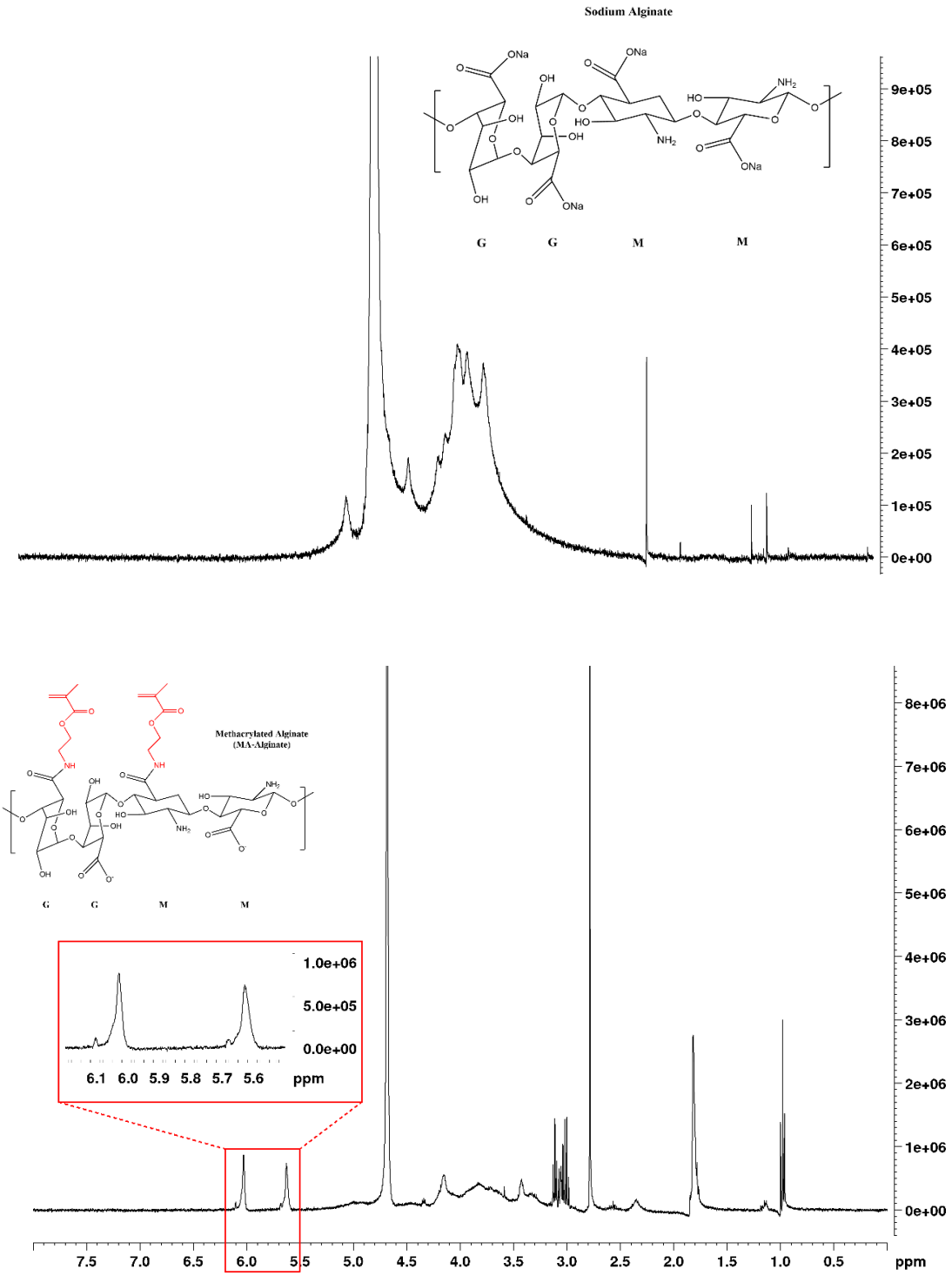

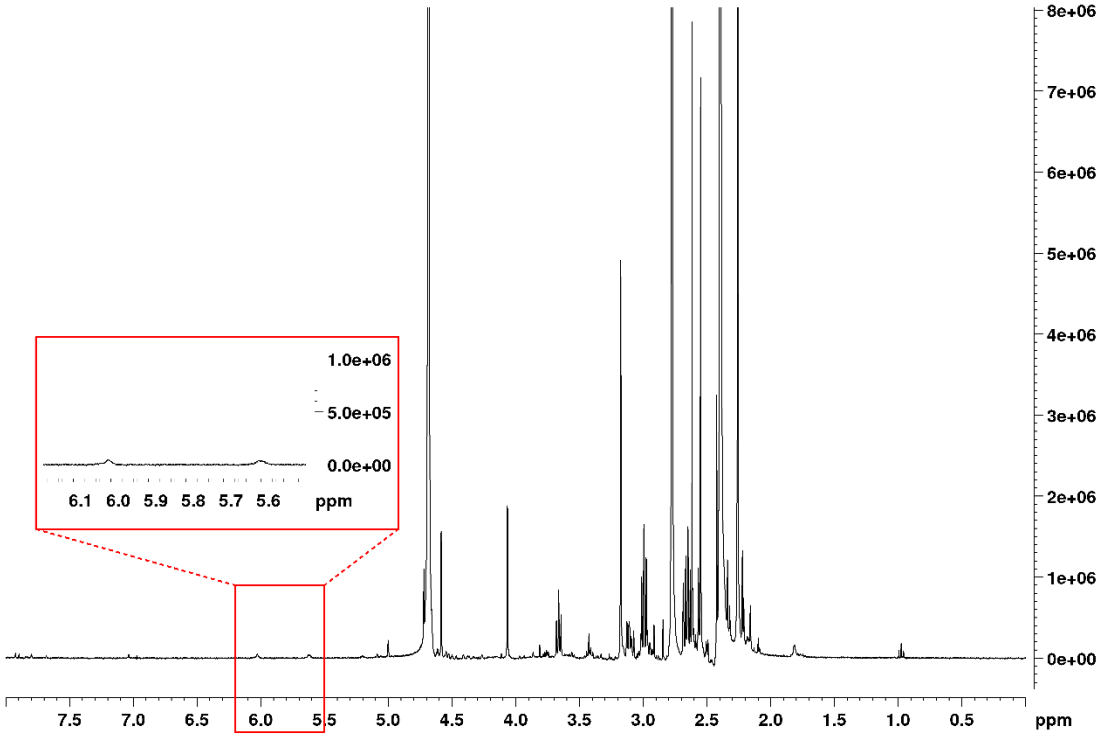

Supplemental Figure 4.S1: NMR analysis reveals appearance of methacrylate peaks after alginate methacrylation (red box, second figure) as well as disappearance of these peaks after crosslinking during cryogelation (red box, third figure).

Supplemental Figure 4.S2: Pictures of Cryogels

Covalently Crosslinked | Tough Cryogels | Injected Cryogels

Supplemental Figure 4.S2: Pictures of cryogels in DI water (Covalently Crosslinked), in $CaCl_2$ (Tough Cryogels), and after injection through a 16G syringe (Injected Cryogels).

Supplemental Figure 4.S3: Mechanical Characterization

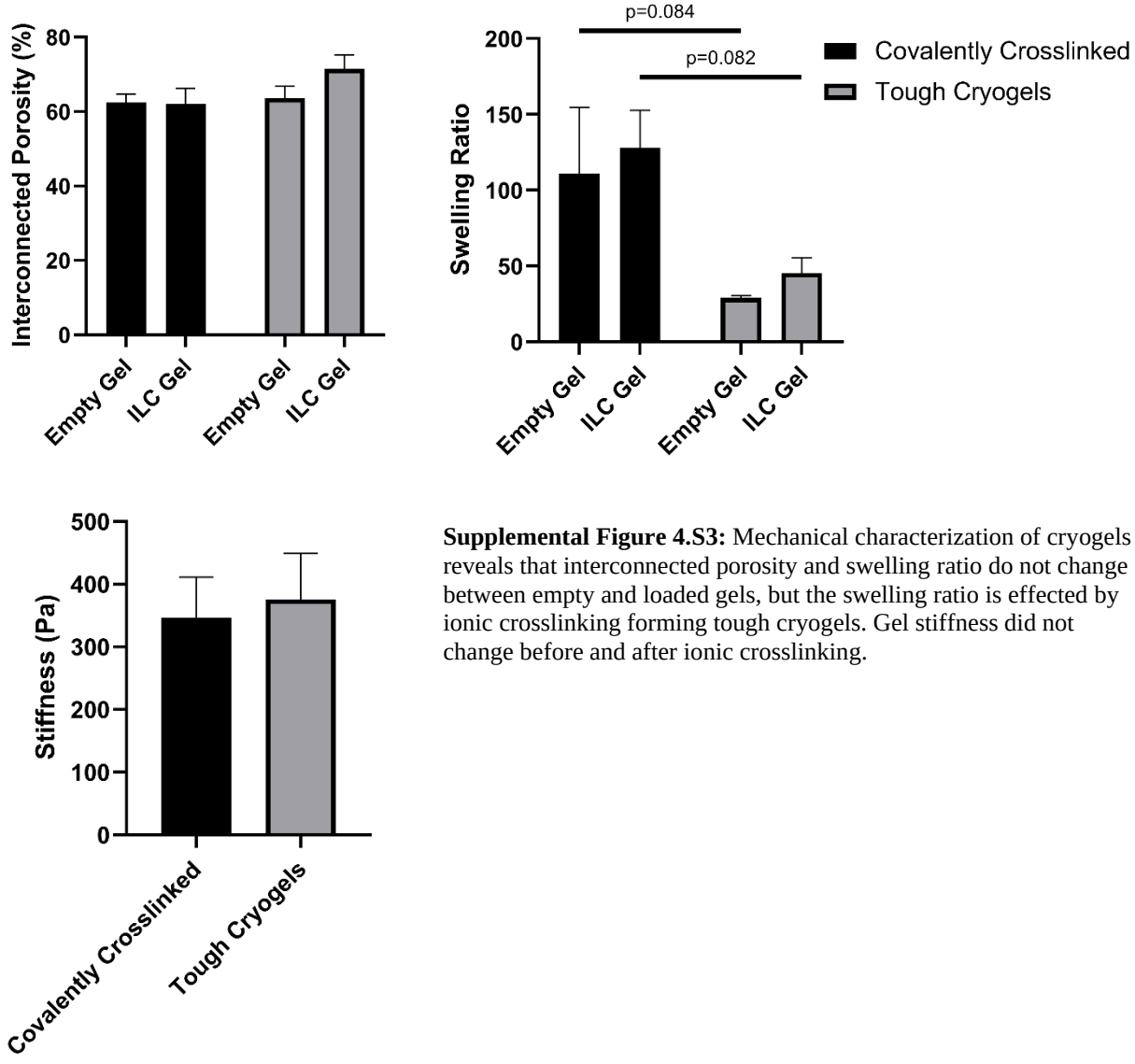

Supplemental Figure 4.S3: Mechanical characterization of cryogels reveals that interconnected porosity and swelling ratio do not change between empty and loaded gels, but the swelling ratio is effected by ionic crosslinking forming tough cryogels. Gel stiffness did not change before and after ionic crosslinking.

Supplemental Figure 4.S4: Mechanical Characterization (Storage)

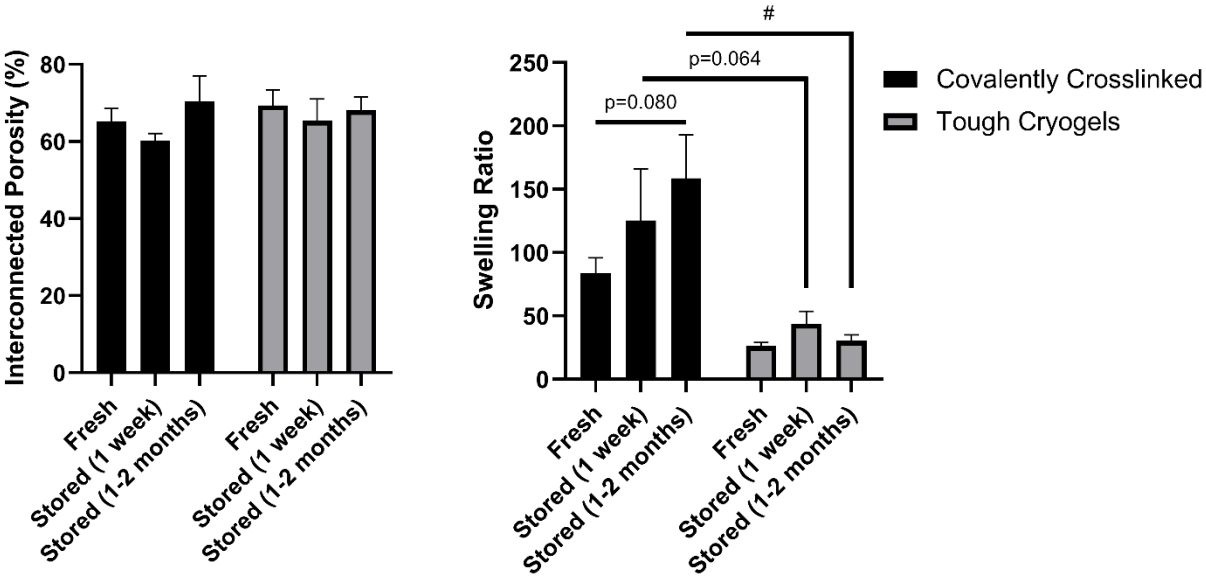

Supplemental Figure 4.S4: Characterization of cryogels stored long-term revealed that storage did not alter interconnected porosity, and only covalently crosslinked cryogels increased in swelling ratio after 1-2 months of storage while tough cryogels maintained a low swelling ratio for multiple months.

Supplemental Figure 4.S5: Average Pore Size - Control vs. Injected

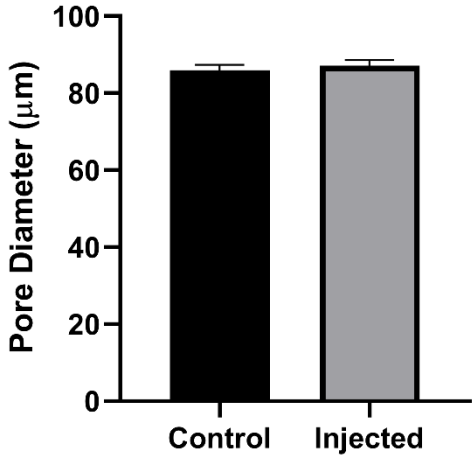

Supplemental Figure 4.S5: All measurements of pore size in control and injected gels were pooled together and compared and revealed no change in average pore diameter after injection through a 16G needle.

Supplemental Figure 4.S6: BMDM Cytokine Viability

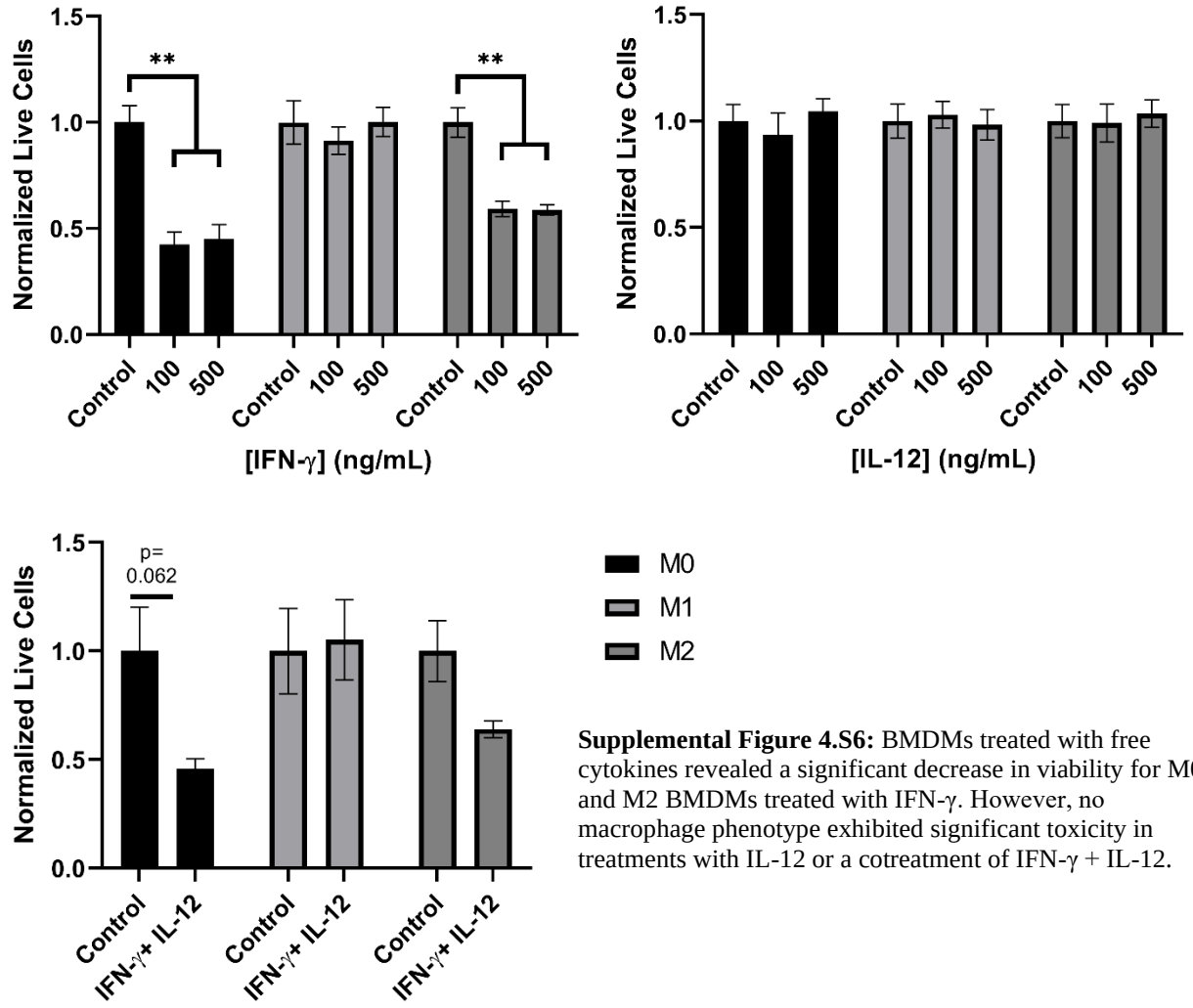

Supplemental Figure 4.S6: BMDMs treated with free cytokines revealed a significant decrease in viability for M0 and M2 BMDMs treated with IFN-γ. However, no macrophage phenotype exhibited significant toxicity in treatments with IL-12 or a cotreatment of IFN-γ + IL-12.

Supplemental Figure 4.S7: BMDM Repolarization with Free Cytokines

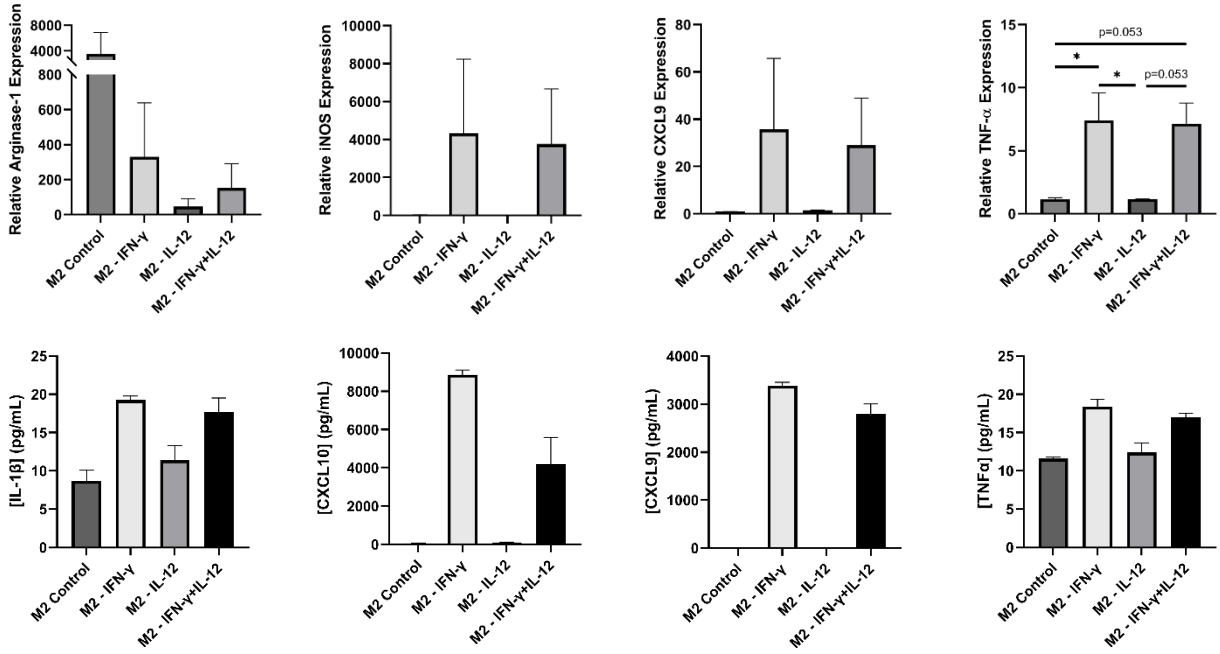

Supplemental Figure 4.S7: M2-polarized BMDMs treated with free cytokines exhibited large shifts to an M1 phenotype after treatment with IFN-γ and a more robust change in the cotreatment. These results were confirmed by measuring RNA expression with qRT-PCR (top row) and by analyzing released cytokines and chemokines via Luminex analysis (bottom row).

Supplemental Figure 4.S8: CCL2-Induced Chemoattraction of M2 BMDMs

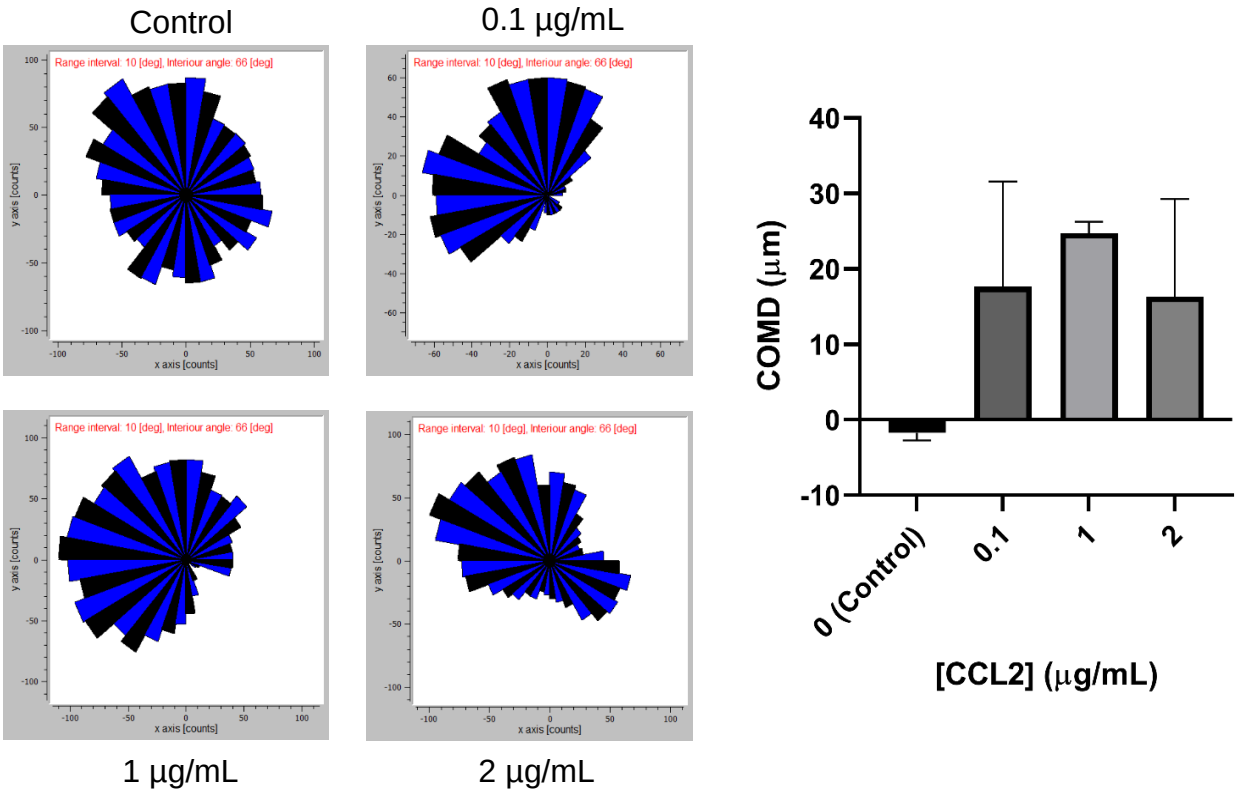

Supplemental Figure 4.S8: M2 BMDMs cultured in chemotaxis plates with a range of CCL2 concentrations revealed CCL2-induced migration which appeared maximal at 1 µg/mL.

Supplemental Figure 4.S9: Cryogel Viability in Polarized BMDMs

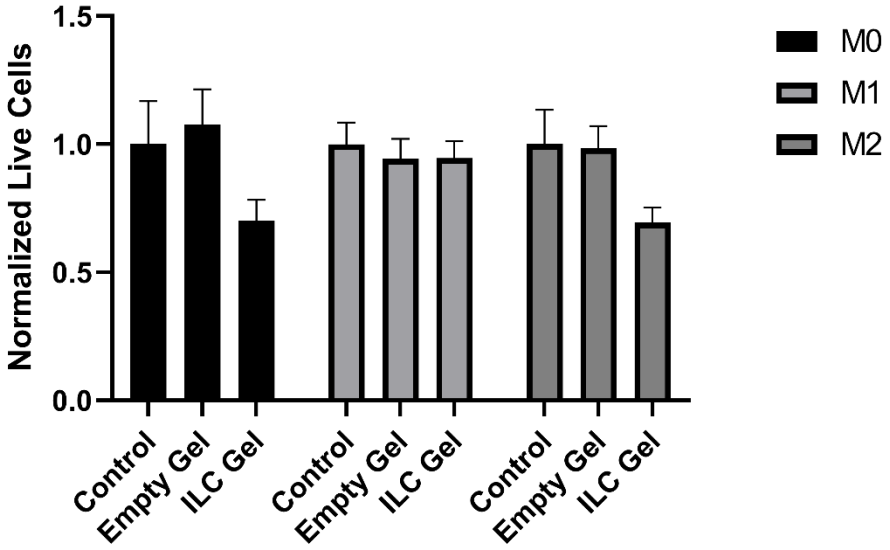

Supplemental Figure 4.S9: BMDMs treated with cryogels for 48 hours did not exhibit any significant decreases in viability.

Supplemental Figure 4.S10: Quantified ILC-Induced BMDM Migration in a Trans-well Assay

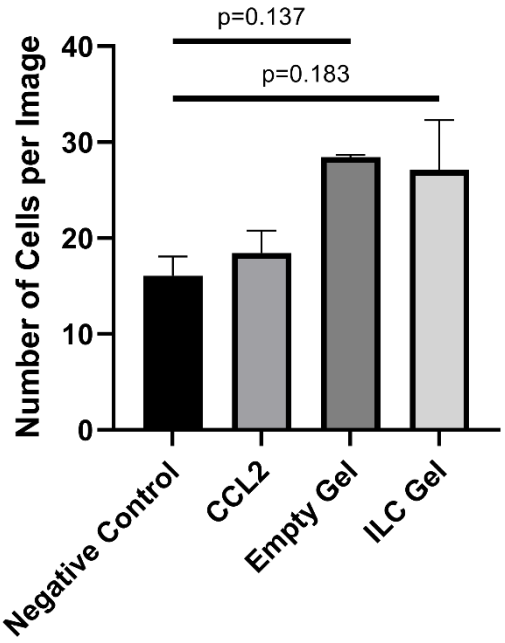

Supplemental Figure 4.S10: M2 BMDMs cultured in a trans-well plate with free chemokine (CCL2), empty gels, or loaded (ILC) gels exhibited increased migration across the membrane compared to the negative control (2% FBS media).

Supplemental Figure 4.S11: PyMT Explant *In Vitro* Viability

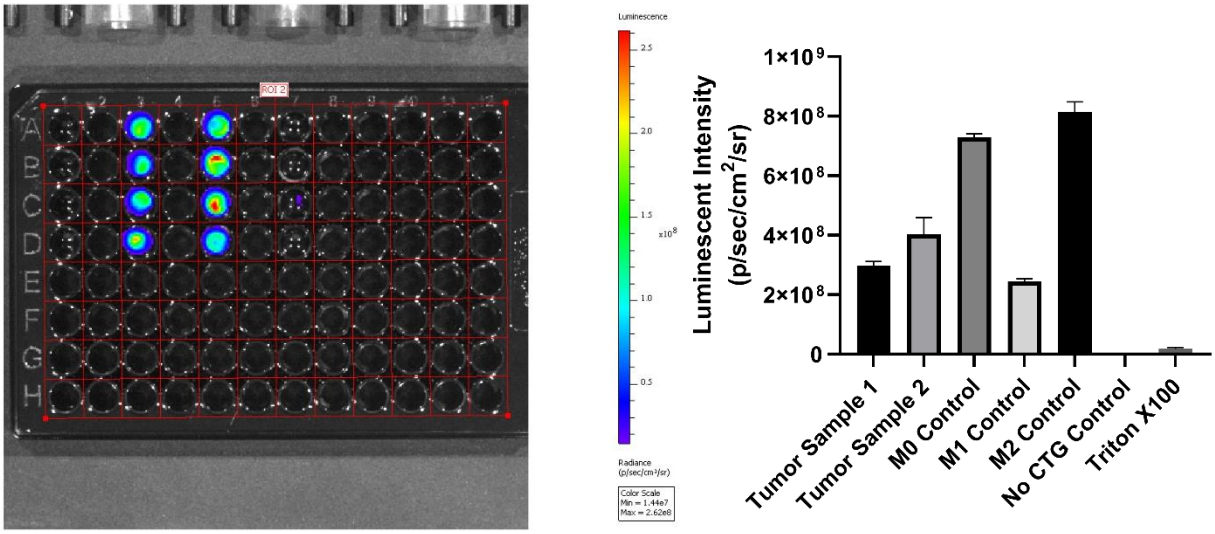

Supplemental Figure 4.S11: PyMT tumor explants were cultured for 96 hours *in vitro* and then evaluated with a CellTiter-Glo viability assay to ensure live cells were present after 4 days of culture.

Supplemental Figure 4.S12: Mouse Weights and Tumor Sections for *In Vivo* Cryogel Treatments

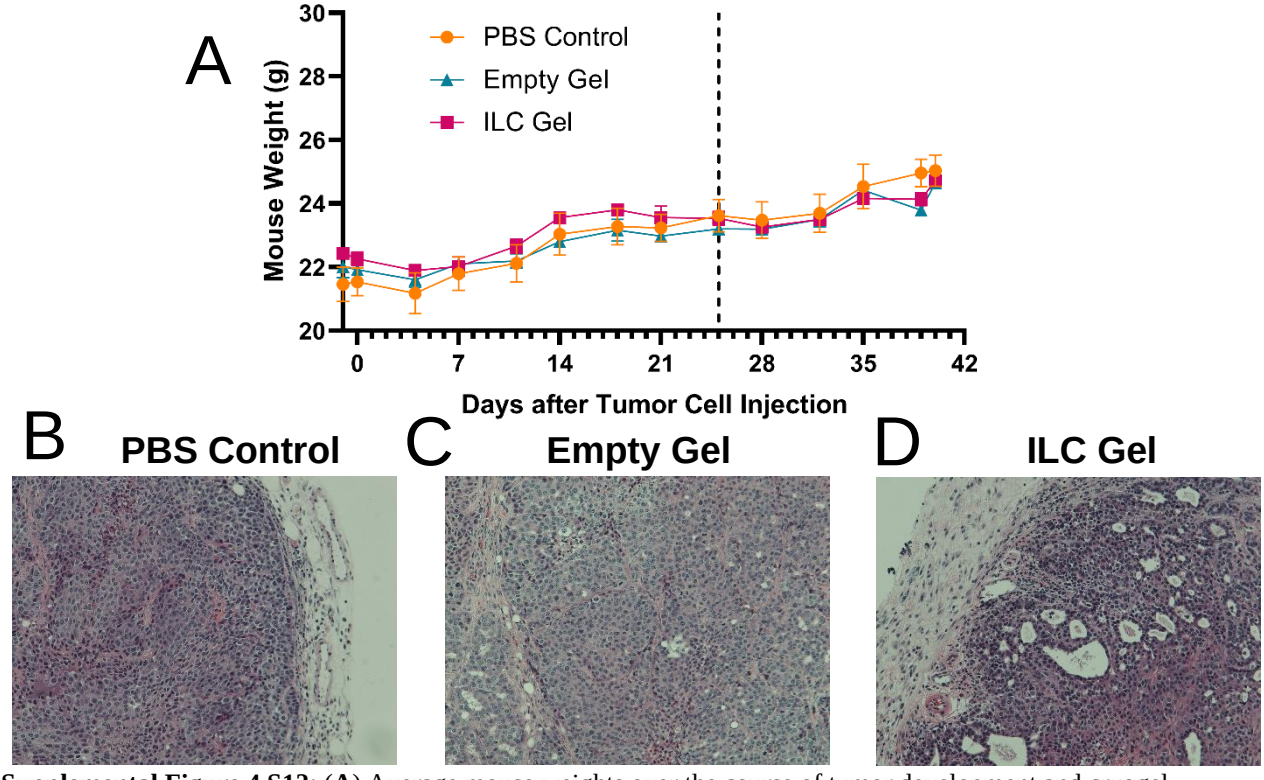

Supplemental Figure 4.S12: (**A**) Average mouse weights over the course of tumor development and cryogel treatment (n=5). Tumor sections were fixed and stained with H&E. (**B**) PBS control and (**C**) Empty Gel treatments appeared to have no effect on tumor cellularity while (**D**) ILC Gel treatment appeared to decrease cellularity.

Supplemental Figure 4.S13: Additional *In Vivo* Flow Cytometry Analysis

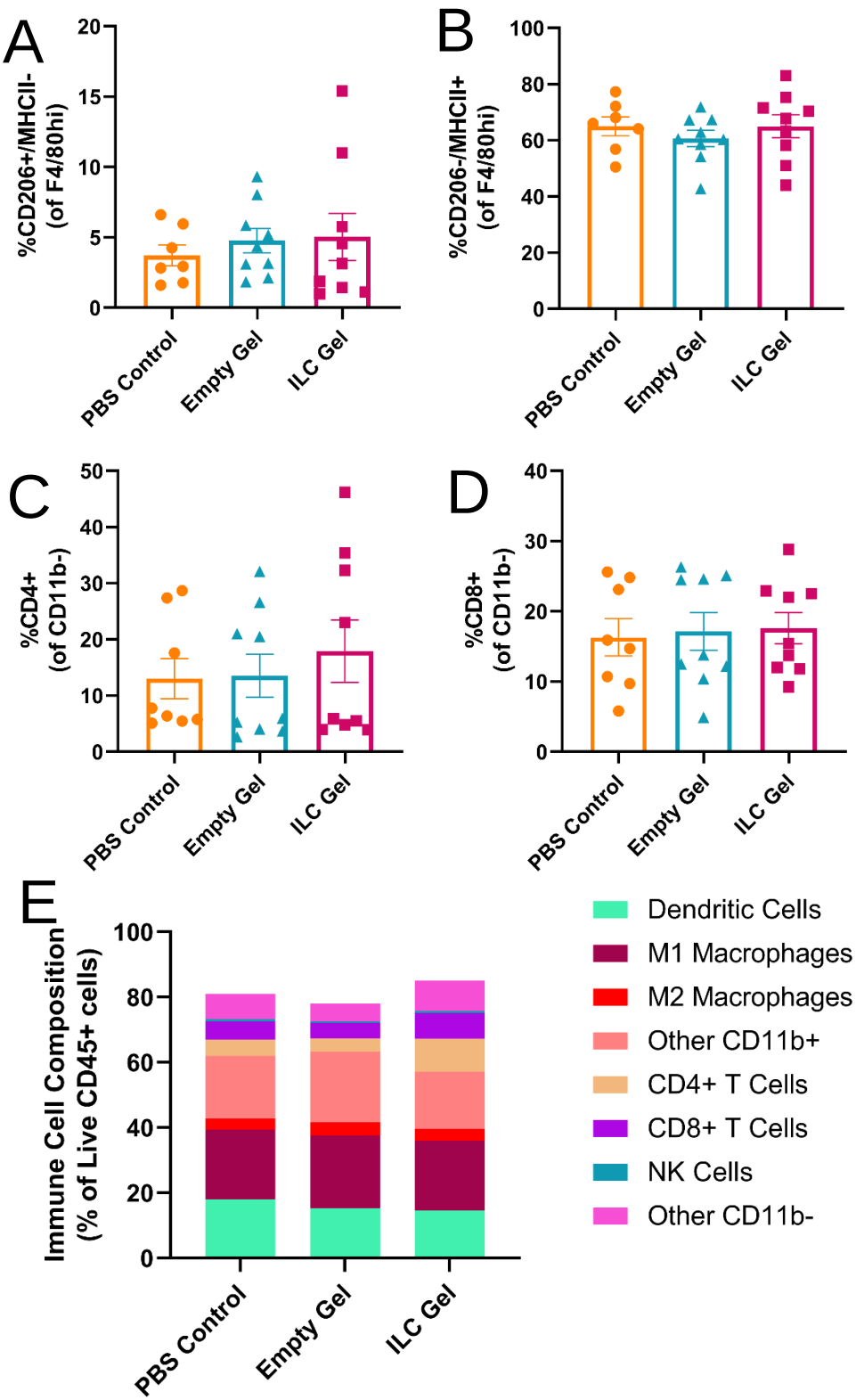

Supplemental Figure 4.S13: Flow cytometry gating for (**A**) M2 macrophages, (**B**) M1 macrophages, (**C**) CD4 T cells, and (**D**) CD8 T cells revealed no significant changes. (**E**) Overall immune cell composition revealed trends towards creating an anti-tumor immune environment.

Supplemental Figure 4.S14: Macrophage Flow Gating Strategy

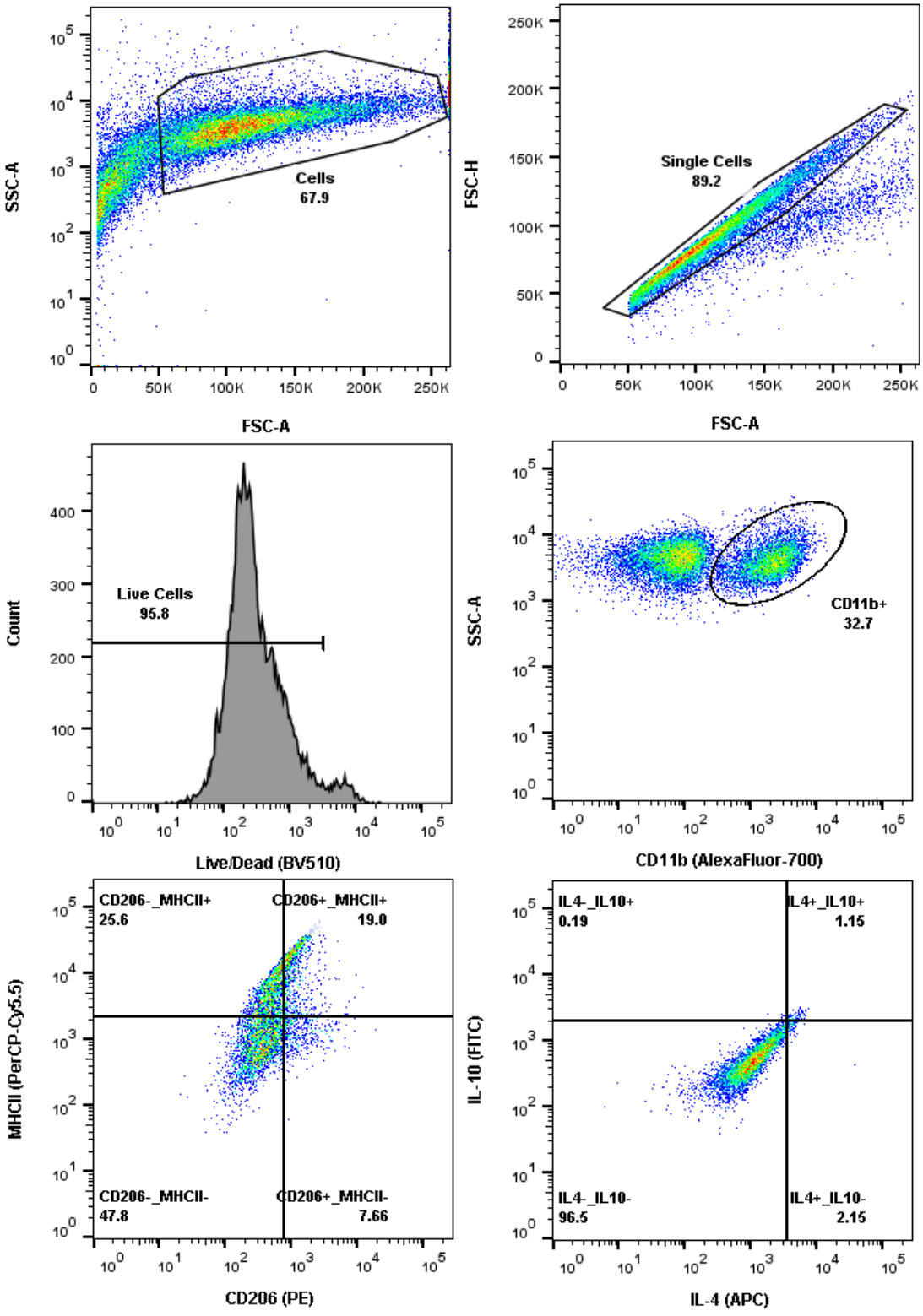

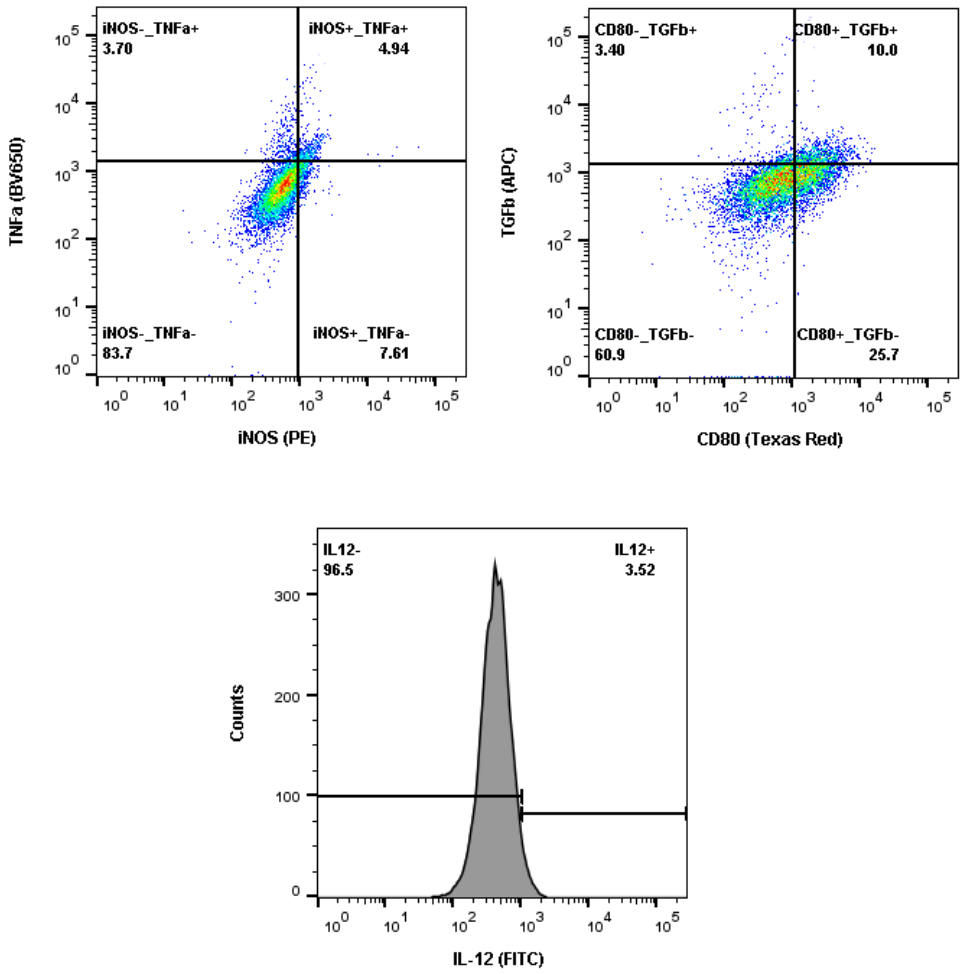

Supplemental Figure 4.S14: Flow gating for BMDMs illustrates gating for live cells, macrophages (CD11b+), and M1 (MHCII+/CD206+ or iNOS+/TNFa+) vs M2 (MHCII-/CD206+ or IL-4+/IL-10+).

Chapter 5

Summary, Impacts, and Outlook

5.1 Chapter Summaries and Impact

The research presented in this dissertation represents the development of two separate biomaterial drug delivery systems designed for localized delivery of macrophage repolarization treatments as novel forms of cancer immunotherapy. The overall goals of this work were two-fold. First, I aimed to develop the biomaterials systems using polymeric chemistry to fabricate siRNA-loaded, mannose-decorated nanoparticles and macroporous, injectable cryogels. Second, I applied the developed treatments to evaluate changes in macrophage phenotype *in vitro* followed by examining the effects of producing macrophage-induced anti-tumor immunity in multiple *in vivo* models. The work presented in this dissertation represents a major step in moving both of these biomaterials systems closer to translational use in treating cancer with novel immunotherapies.

5.1.1 Specific Aim 1

In chapter 2, I discovered cytotoxicity associated with nanoparticles made from the MnPEGDB attributed to residual copper content from the CuAAC reaction. I showed that mannose-alkyne conjugation efficiency was dependent on a minimum copper concentration and that reducing copper catalyst concentration lowered the residual copper content, so optimization was needed to balance these two factors. I examined the cytotoxicity of MnNPs fabricated with the different polymers and found that, in human macrophages, there was significant toxicity associated with residual copper at high copper catalyst concentrations and residual azides at low copper catalyst concentrations. This result indicated an optimal copper catalyst concentration in

the range of 0.25-0.75 mM Cu^{2+} that balanced conjugation efficiency and cell toxicity from copper and azide. While cytotoxicity from copper in CuAAC reactions is a well-established concern, my work was the first to identify the toxicity of excess azides when this reaction is carried out with reduced copper concentrations. I then demonstrated that the MnPEGDB fabricated with 0.75 mM copper catalyst significantly increased M2 macrophage targeting compared to the other polymers. This optimized polymer was used to deliver IκBα siRNA to M2 BMDMs. I showed that the new IκBα-MnNPs made with the diblock copolymer, as opposed to the previously used triblock copolymer, successfully repolarized macrophages to the M1, pro-inflammatory phenotype, indicating that the optimized polymer functioned to target M2 BMDMs and deliver therapeutic siRNA payloads.

The primary innovation of this work was the detailed analysis of the relationship between copper catalyst concentration in the CuAAC reaction and the resulting conjugation efficiency of mannose-alkyne with AzPEGDB and the subsequent cytotoxicity associated with copper content and free azides. Furthermore, the mannosylated diblock copolymer (MnPEGDB) was a novel iteration of previous polymers used in our lab but optimized with more reproducible fabrication (diblock copolymer) combined with "click" conjugation of a targeting moiety (mannose). Removing the third monomer (poly(acrylic acid), PAA) from our previous formulations significantly improved the predictability and reproducibility of polymer synthesis, but changed the resulting polymer properties and required this study to re-establish a functional, mannosylated delivery micelle. The improved polymer was used to make siRNA-loaded nanoparticles that repolarized M2 BMDMs to an M1 phenotype using IκBα siRNA.

5.1.2 Specific Aim 2

In chapter 3, I demonstrated the translatability of IκBα-MnNPs to repolarize TAMs *in vivo* for cancer immunotherapy. I initially validated the activation of NF-κB by treating BMDMs isolated from NGL-reporter mice to visualize NF-κB activity via luminescent readouts. Treatment with IκBα-MnNPs significantly increased NF-κB activation to the level of M1 controls. This experiment also revealed the unexpected phenomenon that MnNPs without functional payload (scrambled siRNA) also activated NF-κB, although not to the level of IκBα-MnNPs. Similar effects have been reported and provide an avenue for future experiments to elucidate the mechanisms of this result.

I also showed that MnNPs could target delivery to macrophages specifically in the solid tumors and ascites fluid of two different ovarian cancer models in mice, with negligible off-target delivery to the spleen. Furthermore, in the biweekly treatment of TBR5 tumors, we saw significant delivery to the macrophage population in the tumors and ascites compared to all other immune cell types, indicating the targeting ability of mannosylated NPs. After confirming targeted delivery, we showed beneficial therapeutic effects of IκBα-MnNPs in both models. For the ID8 tumor model, the 3-day treatment in late-stage disease decreased ascites accumulation slightly but did lead to significant, potentially beneficial, increases in some inflammatory markers, indicating shifts in the immune cell composition. Importantly, in the biweekly treatment of TBR5 tumors, we observed a significant decrease in ascites volume as well as significant increases in inflammatory markers, demonstrating a therapeutic effect caused by changes in the immune cell profile. Finally, the extended biweekly treatment of MnNPs significantly decreased ascites accumulation and solid tumor development as well as significantly changing the several immune cell populations, including decreasing M2-like TAMs and increasing classical monocytes and NK cells. Taken together, these results show the beneficial therapeutic effects of

IκBα-MnNPs in altering the immune cells in the TME to a pro-inflammatory, anti-tumor phenotype.

The major innovations demonstrated in this aim include the translation of the previously optimized MnPEGDB polymer to deliver therapeutic IκBα siRNA to ovarian TAMs *in vivo* as well as the increased delivery of RNAi therapeutics to the desired cell type with minimal off-target accumulation. This aim established the use of MnNPs to deliver siRNA therapeutics via localized IP injection to treat ovarian cancer while minimizing the risk of systemic toxicity or clearance through the liver and spleen associated with IV delivery to treat other types of cancer. Furthermore, we showed significant alteration of immune cell composition in the TME as well as signs of increased CD8 T cell infiltration, which is critical to improving the current low response rates associated with ICB therapies administered to ovarian cancer patients. These results provide direction for future studies evaluating combination therapies to increase the anti-tumor effects of immunotherapies with potentially substantial impact to improving the standard-of-care provided to ovarian cancer patients.

5.1.3 Specific Aim 3

In chapter 4, I introduced a novel biomaterial system for locally reprogramming TAMs. I initially demonstrated successful cryogel fabrication followed by extensive mechanical and physical characterization. I showed that the properties of this cryogel matched previously published results as well as showing the durability of these properties after 2+ months of storage, an important consideration for future translation and scale-up. Next, I performed preliminary *in vitro* studies using M2-polarized BMDMs to evaluate the ability of inflammatory cytokine treatment to reprogram macrophages to an M1 phenotype. I evaluated treatments of IFN-γ, IL-12, or a cotreatment and found the combination to provide the largest change in phenotype with

no significant changes in cell viability. I also used M2 BMDMs to evaluate chemoattraction due to CCL2 treatment. These studies provided evidence that loading the three biomolecules (IFN-γ, IL-12, and CCL2) could function to attract and repolarize macrophages. I then showed the release kinetics of the three molecules, which all exhibited similar release profiles although IFN-γ was slightly delayed compared to the other two molecules.

After establishing the background characterization of fabricating and loading the cryogels, I performed several *in vitro* studies to evaluate functionality in biological systems. I treated M2-polarized BMDMs and showed strong evidence of M1 polarization as evaluated by RNA expression (qRT-PCR), protein/receptor levels (flow cytometry), and cytokine/chemokine release (Luminex). I then repeated these studies in two biologically-relevant models that recapitulate the tumor microenvironment: TAMs isolated from spontaneous mammary tumors and whole tumor explants cultured *in vitro*. Both of these models mirrored the results observed when treating BMDMs, indicating the ILC Gels could repolarize macrophages even with other immunosuppressive cells present. Combined, these results supported our progress to inject cryogels peritumorally to evaluate *in vivo* anti-tumor effects of ILC Gels.

The final study of this chapter evaluated *in vivo* ILC Gel treatment of PyMT tumors. Here, I demonstrated that the ILC Gels significantly suppressed tumor development compared to both a saline control as well as an unloaded cryogel control. Furthermore, in collaboration with the Kim lab, we revealed changes in several immune cell populations driven by macrophage repolarization. While the final evaluation of these studies is still ongoing, the significant anti-tumor effects we have observed provide evidence than *in vivo* cryogel-induced macrophage repolarization is able to slow tumor progression and alter the tumor immune microenvironment in a therapeutically beneficial capacity.

The results of this chapter highlight the potential impact of locally injected biomaterials for repolarizing TAMs. Although injectable biomaterials have been used for cancer immunotherapies, the majority of these treatments have been used for subcutaneous injections or post-operative treatments and typically target the adaptive immune system.[74,75] Furthermore, cryogels have become a popular medium for drug delivery, 3D organoid modeling, and bioseparation as reviewed by Memic, et. al.[219] However, for targeting TAMs, most current treatment strategies revolve around small molecules, antibodies, or nanoparticles.[30,88,220–222] In this chapter, I developed a novel TAM-based immunotherapy via direct peritumoral injection of a macrophage repolarization depot. This strategy provides a distinct advantage over systemically administered therapies in that local treatment enables therapeutically significant drug dosing at the disease site in the absence of dose limiting off-target effects. Clearance of small molecules and nanoparticles by the reticuloendothelial system (RES) often requires administration of elevated systemic doses and/or the addition of complex, anti-translational chemical modifications to achieve useful delivery to the target tissues. The injectable drug-loaded cryogel removes these concerns by providing drug delivery adjacent to the tumor microenvironment. Furthermore, the changes in immune cell composition provide evidence for the potential future applications of this strategy in combination therapies to induce more robust anti-tumor immune responses. Creating an immunologically "hot" tumor can prime the TME for immune checkpoint blockade therapies to increase response rates in solid tumors.[223] While this approach has been postulated by many groups, we provide direct evidence in these studies that we can alter the tumor-immune microenvironment using relatively simple treatments. The reduced complexity of the cryogel system compared to some nanoformulations improves the translatability of this treatment since scale-up for clinical use will not involve an extensive amount of future

optimization. Overall, this chapter signifies a significant development in the field of biomaterials for repolarizing TAMs and will hopefully lead to clinically-relevant therapies in the future.

5.2 Shortcomings

5.2.1 Specific Aim 1

While we did comprehensively optimize the CuAAC reaction for conjugating mannose to AzPEGDB, we did not attempt other conjugation techniques as a comparison. Primarily, copper-free click chemistry, which uses diarylcyclooctyne (DBCO) in place of traditional alkynes for strain-promoted click chemistry, could be substituted for the azide-alkyne click reaction. We focused on optimizing the conditions for CuAAC chemistry due to the lower cost and increased availability of reagents relative to DBCO chemistry, which we anticipate would aid in future scale-up for clinical translation. Furthermore, the hydrophobicity of cyclooctynes as well as lack of regiospecificity associated with DBCO reactions were a concern when combining with our diblock copolymer system. However, evaluation of strain-promoted click conjugation of mannose-DBCO to AzPEGDB is an interesting avenue for consideration that was not included in our studies.

One experiment in particular, quantifying mannose conjugation to AzPEGDB, proved especially troublesome. Initially, we attempted to quantify mannose-alkyne binding to AzPEGDB via NMR spectroscopy, which was used for all other conjugation steps. However, the NMR spectra for mannose is between 3.5 and 4.05 ppm, which is the same range for both the PEG peak (~3.55 ppm) and the BMA peak (~3.95 ppm). Since NMR peak height is a product of the number of hydrogen atoms present in a particular molecular orientation, the number of repeating units (and thus molecular weight) of a polymer will affect the peak height. In the

MnPEGDB, we use a 5 kDa PEG chain (~113 repeating units) in conjunction with about 75 repeating units of BMA (142.2 g/mol * 75 repeating units = 10.7 kDa). When compared to the single mannose sugar (~180 g/mol) conjugated to the end of each polymer chain, the peak heights associated with the PEG and BMA mask the mannose peaks so that they are imperceptible using ^{1}H-NMR on a 400 MHz spectrometer. I followed up by working with Dr. Donald Stec at the Vanderbilt Small Molecule NMR Facility Core to attempt multidimensional analysis using ^{13}C-NMR on a 600 MHz spectrometer, which gave some indication of mannose, but was once again masked by the large PEG peak. Since we used FTIR spectroscopy to evaluate the decrease in the azide peak as an indicator of mannose conjugation, I tried measuring the mannose spectra using FTIR. Here, the mannose-alkyne peak resided around wavenumber 3500 cm^{-1} which once again appeared to give indications of mannose conjugation, but was interfered with by the larger PEG chain. Finally, I attempted an agglutination assay using Concanavalin A, a tetrameric lectin which binds mannose. In theory, this tetrameric molecule would move freely in solution until mixed with mannose-decorated nanoparticles, which would cause agglutination of the particles with the lectin and be measurable by absorbance readouts. However, once again this technique failed to demonstrate any conclusive evidence of mannose conjugation. I finally overcame this dilemma by conducting co-treatments of MnNPs and free mannose with BMDMs to evaluate interference in NP uptake due to free mannose competing for CD206 binding. This experiment finally provided support for mannose being present on the nanoparticles, but overall there is still the potential for future studies to better evaluate the amount of mannose present on the corona of these nanoparticles.

For targeting macrophages, we focused our efforts on mannose decoration to target the CD206 macrophage mannose receptor, but several other targeting moieties could have been

evaluated. For example, CD206 is known to bind a range of molecules, including additional sugars such as fucose and sialic acid as well as antibodies specific for CD206. Fucose and sialic acid provide an alternative approach to binding CD206 with the added benefit of being less recognized by the carbohydrate receptors found on cancer cells.[224,225] This increased specificity would remove the concerns associated with potential delivery of IκBα siRNA to cancer cells, since NF-κB activation in tumor cells promotes cell proliferation, suppresses apoptosis, and induces angiogenesis.[226] For antibody conjugation, the primary concern involves the size of whole antibodies creating a nanoparticle too large for *in vivo* delivery applications as well as creating steric hindrance to the number of antibodies that could be decorated onto the nanoparticles. However, recent work by another member of the Giorgio lab has demonstrated the ability to decorate F(ab') antibody fragments on a PLGA nanoparticle, which minimized the size of fabricated NPs and removed the Fc portion of antibodies often associated with clearance via Fc receptor-mediated recognition by the RES.[227] Finally, Ngambenjawong, et. al., have developed an M2-specific peptide (M2pep) which preferentially binds M2-like TAMs *in vivo*.[228] Along with these other options for targeting CD206, there are also other potential receptor targets such as CD163, an alternative scavenger receptor for hemoglobin/aptoglobin up-regulated on M2 macrophages.[229] This receptor has an affinity for apolipoprotein A1 (ApoA1) which is a high-density lipoprotein that could be used to create liposome-based macrophage targeting systems potentially useful for delivering hydrophobic cargos.[222] Despite optimizing mannose conjugation, more specific macrophage-targeting moieties were not included in these studies but do provide a basis for future work in examining TAM-targeting polymeric nanoparticles.

5.2.2 Specific Aim 2

The primary drawbacks from chapter 3 revolve around the initial results where we observed an increase in NF-κB activation in the MnNP treatment loaded with scrambled siRNA. While we did conduct follow-up experiments using non-mannosylated nanoparticles (PEG-NPs), there was still a slight increase in NF-κB activity with the Scr-PEG-NPs. Although it appears the mannose activation did lead to synergistic effect with the IκBα siRNA treatment, a potentially beneficial consequence for our application, the evidence of M1 polarization in the Scr-PEG-NP treatment indicates some potential activation potentially due to the siRNA treatment itself. It is well-known that the presence of RNAs in cellular cytoplasm leads to inflammasome activation via sensor proteins in the nucleotide-binding domain and leucine-rich-repeat-containing (NLR) family, especially NLRP3.[230] The activation of NLRP3 in response to various inflammatory signals coincides with NF-κB activation since these pathways contribute to one another.[42] So, the likely mechanism of increased luminescent readout in the treated NGL-BMDMs is siRNA-induced activation of NF-κB. While we conducted additional *in vitro* studies to evaluate this effect, there is still room for additional analyses. First, treatment with unloaded NPs would provide a control group with no siRNA. However, the challenges associated with this treatment require additional consideration. First, formulating unloaded nanoparticles using our diblock copolymer system results in micelles with an average diameter around 25 nm, which is significantly smaller than the ~140 nm diameter of the loaded MnNPs.[67] This difference is due, in part, to the micelle self-assembly component that is driven by electrostatic interactions between polymer and polynucleotide. In the absence of polynucleotide, micelles self-assemble only through hydrophobic interactions and without the polynucleotides and increase the diameter of the micelle core. The drastic size difference alters the potential for macrophage uptake, either through passive uptake or clathrin-dependent endocytosis, since macrophages exhibit optimal

endocytosis with particles around 100 nm in diameter.[63] A different nanoparticle system might enable evaluation of NF-κB activation induced by mannosylated particles versus RNA-delivery. For example, commercially-available jetPEI® functions as a DNA transfection agent which is also available with a mannose-conjugated formulation. A screening study comparing the MnNPs, PEG-NPs, unlabeled jetPEI, and mannose-labeled jetPEI either empty or loaded with siRNA could be used to further elucidate the mechanism of NF-κB activation.

Additionally, while our results demonstrated an improvement in targeting macrophages and monocytes in the solid tumors and ascites fluid in a biweekly treatment model of ovarian cancer, we did not compare the targeting of MnNPs to PEG-NPs. Future *in vivo* studies could add PEG-NPs loaded with Cy5-dsDNA to observe any changes in delivery. I hypothesize that a large percentage of the macrophage population will still take up the PEG-NPs due to their natural endocytotic nature, but that there will also be higher uptake in the dendritic cell population as well as potentially higher biodistribution to organs outside the peritoneal cavity, such as the spleens. This treatment was not included in our studies due to reagent unavailability but would provide an interesting comparison for evaluating mannose-induced targeting to macrophages versus passive uptake of nontargeted nanoparticles.

Finally, the biweekly treatment of TBR5 tumors resulted in a robust anti-tumor immune response which was not observed in the 3-day treatment of late-stage ID8 tumors. While we conducted the 3-day treatment near humane endpoint to evaluate treatment in late-stage disease, we did not evaluate the biweekly treatment in the ID8 model. This tumor model is known to develop large volumes of ascites fluid and would therefore be interesting to see if the biweekly treatment regimen could reduce the ascites accumulation. As mentioned previously, ascites often contributes to the development of chemoresistance in patients, so if future studies show

significant reduction of ascites accumulation due to selective NF-κB activation in TAMs and macrophages in the ascites, subsequent studies could evaluate combination with chemotherapies to improve efficacy. The dilemma with using the biweekly treatment in the ID8 models is when to begin treatment, as we would likely have to start well before the tumors are at late-stage. However, by using ascites accumulation as a marker, mice could undergo treatments as the peritoneal cavity starts to distend to characterize any slowed accumulation or reduction in ascites volume. These experiments might have better explained the mechanisms of IκBα siRNA function versus MnNP stimulation, the effect of MnNPs on increased macrophage targeting, and the potential increased therapeutic benefit of increasing dosing to a biweekly schedule.

5.2.3 Specific Aim 3

For chapter 4, the shortcomings centered around optimization of the alginate cryogel fabrication. While alginate has been used for hydrogel fabrication for years and the cryogel system is gaining traction, we chose to stick with previously published fabrication techniques rather than optimize the system for our applications. Based on our results, this system works as intended and resulted in significant suppression of tumor development *in vivo*, but there is obvious potential for improvement. For example, to truly attract macrophages to the cryogel, adhesion molecules would provide support for macrophages to chemoattract in response to CCL2 and then remain nearby by adhering to the gel itself. In this way, the TAMs would receive an extended exposure time to the inflammatory cytokines to boost M1 polarization. Additionally, the ILC Gels exhibited rapid burst release of all three biomolecules with IL-12 lagging slightly behind the other two. Ideally, the CCL2 should release first to attract TAMs to the gel, while IFN-γ and IL-12 undergo more steady-state release afterwards to increase the exposure time to inflammatory signals. One technique for extending the release of the cytokines is to bind them to

heparin molecules, which release slower from cryogels.[231] Furthermore, forming nano-in-micro systems (i.e. loading nanoparticles into microscale gels) can provide an extended release by co-loading cryogels with free CCL2 and PLGA nanoparticles encapsulating IFN-γ and IL-12. In this way, the CCL2 will still undergo immediate burst release over the first 24-48 hours, while the PLGA nanoparticles can be tailored to slowly degrade over the course of 1-2 weeks to extend the release of the inflammatory cytokines.

Another challenge associated with the studies in this chapter involves the size of the needle used for injecting cryogels. The large 16G needle is extremely invasive and can lead to tissue damage when administered. Further optimization into the mechanical properties of the cryogels, such as increasing the ratio of ionic to covalent bonds, can alter the elasticity of the gels and improve the shear-thinning properties needed to inject through a smaller gauge needle. Alternatively, the current cryogel properties are strong enough to endure placement in a biopsy punch so for translational applications, these gels could be delivered via biopsy punch to remove the need for the large needle.

Finally, although we showed significant upregulation of several M1 markers in all three *in vitro* models studied, there was little to no change in many of the M2 markers measured. While increasing inflammation is our ultimate goal, we also want to ensure that the macrophage repolarization is robust enough to prevent the M1 macrophages from being pushed back to an M2-like phenotype by the immunosuppressive TME. To this end, a larger screen of biomolecules could have been evaluated to characterize the potential for this effect as a function of ILC Gel fabrication and treatment parameters. Other inflammatory cytokines, such as TNF-α, could be examined, or we could evaluate other cell-signaling molecules such as toll-like receptor (TLR) agonists, antibodies, or even STING agonists.[49] Further evaluation of potent macrophage

repolarizing molecules could produce an even stronger anti-tumor immune response driven by M1 macrophage polarization.

5.3 Future Work and Potential Applications

Future work from these projects could fast-track the next round of clinical anti-cancer immunotherapies as well as extend to treating a variety of other diseases. Oligonucleotide loading into polymeric nanoparticles is an incredibly important scientific advancement, as evidenced by the development of COVID-19 vaccines this past year. The AzPEGDB diblock copolymer is currently optimized for loading of smaller siRNA sequences (~20-25 base pairs), but further work could translate this system to load larger mRNAs. By extending the length of the diblock copolymer, which drives complexation with RNAs, the longer sequence mRNAs may be loaded and used for a whole new range of applications. Furthermore, the CuAAC reaction was chosen for polymer labelling because of the flexibility of this reaction. By labelling practically any small molecule with an alkyne group, the same reaction can be used to conjugate different targeting moieties to the AzPEGDB. The combination of different corona decorations combined with siRNA/mRNA cargoes opens the door for a plethora of applications to treat a wide range of diseases.

In the current applications, although the current MnNP formulation demonstrated high specificity for macrophage uptake in the tumors and ascites after IP injections, other targeting moieties could allow for specific tumor targeting after IV injections. The simplest improvement to be tested is changing from a single monosaccharide mannose to a small oligosaccharide of repeating mannose sugars. The reactive chemistry to functionalize mannose with an alkyne would remain the same, followed by “click” conjugation to the AzPEGDB. Furthermore, a

screen of different functionalized polymers, including fucose, sialic acid, M2pep, and anti-CD206 F(ab') fragments could all be used to find the ideal candidate for targeting macrophages.

Additionally, to increase NP accumulation in the tumor site after IV injection while avoiding macrophage uptake in other organs, this polymer system can be mixed with another polymer with an extended PEG chain (20 kDa) containing a matrix metalloproteinase (MMP)-cleavable peptide linker. With the extended PEG polymer combined with the MnPEGDB, the longer 20K PEG will "hide" the mannose (or other targeting moiety) from circulating macrophages until the NPs accumulate in the tumor. Then, by designing a peptide only cleaved by MMPs found in tumors, such as MMP-2, MMP-9, and MMP-13, the longer PEG will be removed, thus exposing the mannose to macrophages in the tumors.[232] There is also the potential for combining the mannose-labelling with other polymer systems developed by our lab in conjunction with the Duvall lab, which have developed more stable NPs that complex with hydrophobically-functionalized siRNA as well as zwitterionic coronas, instead of PEG, which extend *in vivo* circulation time, thus increasing the time for NPs to localize in tumors.[83,233] Furthermore, in a similar vein to IP injection of MnNPs to allow for localized delivery to the tumor site, futures studies can evaluate treatment of breast cancer metastases, which primarily develop in the lungs.

MnNPs can also be used for direct lung delivery via intubation. The particles are small enough to be aerosolized in PBS, which allows for localized delivery to the lungs to treat metastatic lesions. This direct delivery could be beneficial to treating metastatic lesions while simultaneously giving IV injections to target the primary tumor. This technique could also be used to evaluate treatment of primary lung cancer, which has the highest rate of death of any type of cancer. We have established the feasibility of this method of administration (not included in

this dissertation), enabling creative future problem-solvers to leverage this additional non-systemic delivery approach.

The initial next steps for the cryogel system are to evaluate ways to alter the release rates of the biomolecules while also optimizing the cargo for strong macrophage repolarization. As previously mentioned, the extended release could be tested by adding heparin to the cryogel mixture or by separately loading the inflammatory cues in PLGA nanoparticles. Alternatively, using a similar strategy from the MnNPs, inflammatory stimulators such as TLR agonists, cytokines, or RNAs (siRNA/mRNA) could be reacted to the backbone of the cryogel using an MMP-cleavable peptide linker. In this way, the free chemokine would release immediately, while the bound molecules would remain in the gel until the MMPs reach them and cleave the peptides. Since many MMPs, including MMP-2 and MMP-9, are specifically released by tumor-associated macrophages, these inflammatory molecules would not be released until TAMs reach the gel and secrete MMPs around the peptides.[234]

Another possible route forward is to combine these two biomaterial systems to create a localized depot to release MnNPs. The MnNPs can be loaded with siRNA cargo and lyophilized. Then, the loaded MnNPs can be mixed with the alginate solution prior to cryogelation. By including a chemokine, the TAMs can be attracted to the gel, which will release MnNPs as it degrades. This nano-in-micro system will allow for more specific cell activation rather than releasing a large amount of inflammatory cues into the TME. General inflammation can sometimes increase tumor growth and severity, so the more specific delivery of IκBα siRNA via MnNPs will only activate macrophages to stimulate the anti-tumor immune response.

The most obvious next step for both of these projects is to start using combination therapies. The primary reason for targeting and repolarizing TAMs is because they are so

prevalent in the TME. However, once the macrophages are repolarized, they not only secrete more inflammatory cytokines, but also T cell-specific chemokines such as CXCL9 and CXCL10. We have shown in both systems that our treatments increase CD8 T cell infiltration into the tumors, thus priming them for increased responsiveness to immune checkpoint blockade (ICB) therapies. In this way, both systems should be used for combination treatments with anti-PD-1 therapies to evaluate the potential strong anti-tumor immunity developed by both activating macrophages and T cells. Furthermore, we believe that the activation of macrophages combined with recruitment of T cells will create a systemic and memory immune response, necessary to produce the abscopal effect. Future studies should focus on treating primary tumors followed by development of recurring, distant metastases. In the PyMT mouse model, this can be achieved by treating the primary tumor in the left flank #4 mammary fat pad, followed by injection of tumor cells into the right flank #4 mammary fat pad after regression is seen in the first tumor. In this way, we hope to see a systemic, long-term anti-tumor response from treating only the primary tumor.

Finally, both of these systems have provided enough encouraging early results that long-term translation to the clinic could be a possibility. For the MnNPs, clinical translation seems even more feasible with the development of the nanoparticle-based mRNA COVID vaccines. Intraperitoneal injection of MnNPs could provide therapeutically beneficial effects in ovarian cancer patients, especially if the treatments can reduce ascites fluid accumulation. Ascites build-up is linked to development of chemoresistance, so a potential combination of MnNPs with chemotherapies could abrogate the development of chemoresistance. For the cryogels, while injection with a 16G syringe is not desirable for most patients, there are several other options for translation to the clinic. First, since most tumors are primarily treated through surgical resection,

the cryogels can be placed into the resected cavity. Michael Goldberg's group has shown that surgical resection can increase infiltration of wound healing macrophages that promote recurrence and metastasis, both of which can be reduced when activating inflammatory macrophages.[209] The sustained release of inflammatory cues via cryogel implantation after surgical resection could provide similar benefits. Furthermore, cryogels could also be used for topical treatment of melanomas and other skin cancers which primarily present on the surface of the skin. Both of these treatment strategies provide hope for the future of clinical cancer immunotherapies to provide increased benefit to patients.

5.4 Conclusions

In a time where novel treatments have never been more relevant, we have shown advancement of two separate biomaterials systems for targeting macrophages in tumors. Polymeric nanoparticles have been studied for decades but are currently at the forefront of the scientific community due to the development of mRNA-based vaccines for COVID-19 as well as recent advancement in vaccinating against malaria. Here, we demonstrated how a similar system can be used for treating ovarian cancer, a highly deadly disease with low response rates to current immunotherapies. While hydrogels have also been studied for decades, the rise of cryogels with altered mechanical and structural properties have opened the way for new applications. Injectable cryogels in particular have shown great promise for localized treatment of disease, and the localized repolarization of TAMs is a prime example of how this system can be applied.

While both of these systems could be tricky for future translation into human patients, I provide a basis here for creating similar-functioning systems to potentially creating robust anti-tumor responses in patients. In particular, the peritumoral injection of alginate cryogels shows

therapeutically beneficial effects in mice, but a peritumoral treatment model does not translate well to treating cancer in people. However, since the standard-of-care for treating primary tumors is surgical resection, the cryogels could be placed locally in the site of resection at completion of the procedure. In this way, larger cryogels with potentially more cargo could be placed in the resection site and thus function to prevent recurrences or formation of metastases.

Taken together, the work shown in this dissertation showed the development of two systems for treating cancer. We demonstrated the optimization of the CuAAC reaction to conjugate targeting moieties onto polymeric nanoparticles and then demonstrated the specific targeting of siRNA cargoes to macrophages using those particles. We then demonstrated the *in vivo* efficacy of targeting TAMs using MnNPs loaded with siRNA designed to activate the canonical NF-κB pathway. This treatment resulted in significant reduction of ovarian cancer development and altered the immune composition of these tumors. Finally, we developed a novel cryogel system for locally delivering inflammatory cues to TAMs in breast cancer. We demonstrated significant suppression of breast cancer development and paved the way for future macrophage-targeted immunotherapy development to treat a variety of cancers.

5.5 Research Contributions

5.3.1 First-Author Publications

- **Glass EB**, Masjedi S, Dudzinski SO, Wilson AJ, Duvall CL, Yull FE, and Giorgio TD. Optimizing Mannose "Click" Conjugation to Polymeric Nanoparticles for Targeted siRNA Delivery to Human and Murine Macrophages. *ACS Omega* **2019**, 4 (16), 16756-16767.
- **Glass EB**, Hoover AA, Bullock KK, Madden MZ, Reinfeld BI, Harris W, Parker D, Hufnagel DH, Crispens MA, Khabele D, Rathmell WK, Rathmell JC, Wilson AJ, Giorgio TD, and Yull FE. Stimulating TAM-Mediated Anti-Tumor Immunity with Mannose-Decorated Nanoparticles in Ovarian Cancer. *BMC Cancer* In Review.

- **Glass EB**, Roy S, Manning AE, Hacker BC, Haycook CP, Dollinger BR, Rafat M, Kim YJ, and Giorgio TD: Injectable Alginate Cryogels as Repolarization Depots for Tumor-Associated Macrophages. *In Preparation*

5.3.2 Co-Authored Publications

- Haycook CP, Balsamo JA, **Glass EB**, Williams CH, Hong CC, Major AS, and Giorgio TD. PEGylated PLGA Nanoparticle Delivery of Eggmanone for T Cell Modulation; Applications in Rheumatic Autoimmunity. *International Journal of Nanomedicine* **2020**, 15, 1215-1228.
- Hoover AA, Hufnagel DH, Harris W, Bullock K, **Glass EB**, Liu E, Barham W, Crispens MA, Khabele D, Giorgio TD, Wilson AJ, and Yull FE. Increased canonical NF-kappaB signaling specifically in macrophages is sufficient to limit tumor progression in syngeneic murine models of ovarian cancer. *BMC Cancer* **2020**, 20 (970).
- Carr MH, **Glass EB**, Masjedi S, and Giorgio TD: Analyzing the Effects of IFN-γ-Induced Repolarization on Bone Marrow Derived Macrophage Viability. *Young Scientist* **2020**, 10.
- Jackson MA, Patel SS, Yu F, Cottam MA, **Glass EB**, Hoogenboezem EN, Fletcher RB, Dollinger BD, Patil P, Liu DD, Kelly IB, Bedingfield SK, King AR, Miles RE, Hasty AH, Giorgio TD, Duvall CL. Kupffer Cell Release of Platelet Activating Factor Drives Dose Limiting Toxicities of Nucleic Acid Nanocarriers. *Biomaterials* **2021**, 268.

References

1. Sung, H. *et al.* Global Cancer Statistics 2020: GLOBOCAN Estimates of Incidence and Mortality Worldwide for 36 Cancers in 185 Countries. *CA. Cancer J. Clin.* **71**, 209–249 (2021).

2. NIH National Cancer Institute. Cancer Stat Facts: Common Cancer Sites. *Annual Report to the Nation on the Status of Cancer* (2021). Available at: https://seer.cancer.gov/statfacts/html/common.html.

3. Dent, R. *et al.* Factors associated with breast cancer mortality after local recurrence. *Curr. Oncol.* **21**, 418–425 (2014).

4. Biswas, T., Efird, J. T., Prasad, S., Jindal, C. & Walker, P. R. The survival benefit of neoadjuvant chemotherapy and pCR among patients with advanced stage triple negative breast cancer. *Oncotarget* **8**, 112712–112719 (2017).

5. Torre, L. A. *et al.* Ovarian cancer statistics, 2018. *CA. Cancer J. Clin.* **68**, 284–296 (2018).

6. Bast, R. C., Hennessy, B. & Mills, G. B. The biology of ovarian cancer: New opportunities for translation. *Nat. Rev. Cancer* **9**, 415–428 (2009).

7. Cortes, J. *et al.* Pembrolizumab plus chemotherapy versus placebo plus chemotherapy for previously untreated locally recurrent inoperable or metastatic triple-negative breast cancer (KEYNOTE-355): a randomised, placebo-controlled, double-blind, phase 3 clinical trial. *Lancet* **396**, 1817–1828 (2020).

8. Chowdhury, P. S., Chamoto, K. & Honjo, T. Combination therapy strategies for

improving PD-1 blockade efficacy: a new era in cancer immunotherapy. *J. Intern. Med.* **283**, 110–120 (2018).

9. Yang, Y. Cancer immunotherapy: harnessing the immune system to battle cancer. *J. Clin. Invest.* **125**, 3335–3337 (2015).

10. Farkona, S., Diamandis, E. P. & Blasutig, I. M. Cancer immunotherapy: The beginning of the end of cancer? *BMC Med.* **14**, 1–18 (2016).

11. Carretero-González, A. *et al.* Analysis of response rate with ANTI-PD1/PD-L1 monoclonal antibodies in advanced solid tumors: A meta-analysis of randomized clinical trials. *Oncotarget* **9**, 8706–8715 (2018).

12. Nishino, M., Ramaiya, N. H., Hatabu, H. & Hodi, F. S. Monitoring immune-checkpoint blockade: response evaluation and biomarker development. *Nat. Rev. Clin. Oncol.* **14**, 655–668 (2017).

13. Hou, B., Tang, Y., Li, W., Zeng, Q. & Chang, D. Efficiency of CAR-T Therapy for Treatment of Solid Tumor in Clinical Trials: A Meta-Analysis. *Dis. Markers* **2019**, (2019).

14. Solinas, C. *et al.* Targeting immune checkpoints in breast cancer: An update of early results. *ESMO Open* **2**, 1–14 (2017).

15. Jayson, G. C., Kohn, E. C., Kitchener, H. C. & Ledermann, J. A. Ovarian cancer. *Lancet* **384**, 1376–1388 (2014).

16. Rabinovich, G. A., Gabrilovich, D. & Sotomayor, E. M. Immunosuppressive Strategies that are Mediated by Tumor Cells. *Annu. Rev. Immunol.* **25**, 267–296 (2007).

17. Tormoen, G. W., Crittenden, M. R. & Gough, M. J. Role of the immunosuppressive microenvironment in immunotherapy. *Adv. Radiat. Oncol.* **3**, 520–526 (2018).

18. Condeelis, J. & Pollard, J. W. Macrophages: Obligate partners for tumor cell migration, invasion, and metastasis. *Cell* **124**, 263–266 (2006).

19. Qian, B. Z. & Pollard, J. W. Macrophage Diversity Enhances Tumor Progression and Metastasis. *Cell* **141**, 39–51 (2010).

20. Noy, R. & Pollard, J. W. Tumor-Associated Macrophages: From Mechanisms to Therapy. *Immunity* **41**, 49–61 (2014).

21. Williams, C. B., Yeh, E. S. & Soloff, A. C. Tumor-associated macrophages: unwitting accomplices in breast cancer malignancy. *npj Breast Cancer* **2**, 15025 (2016).

22. Yuan, X. *et al.* Prognostic significance of tumor-associated macrophages in ovarian cancer: A meta-analysis. *Gynecol. Oncol.* **147**, 181–187 (2017).

23. Weagel, E., Smith, C., Liu, P. G., Robison, R. & O'Neill, K. Macrophage Polarization and Its Role in Cancer. *J. Clin. Cell. Immunol.* **6**, 4–11 (2015).

24. Gupta, V., Yull, F. & Khabele, D. Bipolar tumor-associated macrophages in ovarian cancer as targets for therapy. *Cancers (Basel).* **10**, 1–13 (2018).

25. Zhao, X. *et al.* Prognostic significance of tumor-associated macrophages in breast cancer: a meta-analysis of the literature. *Oncotarget* **8**, 30576–30586 (2017).

26. Zhang, W. jie *et al.* Tumor-associated macrophages correlate with phenomenon of epithelial-mesenchymal transition and contribute to poor prognosis in triple-negative breast cancer patients. *J. Surg. Res.* **222**, 93–101 (2018).

27. Arlauckas, S. P. *et al.* In vivo imaging reveals a tumor-associated macrophage mediated resistance pathway in anti-PD-1 therapy. *Sci. Transl. Med.* **9**, 1–20 (2017).

28. Gordon, S. R. *et al.* PD-1 expression by tumor-associated macrophages inhibits phagocytosis and tumor immunity. *Nature* **545**, 495–499 (2017).

29. Yin, S. *et al.* SI-CLP inhibits the growth of mouse mammary adenocarcinoma by preventing recruitment of tumor-associated macrophages. *Int. J. Cancer* **146**, 1396–1408 (2020).

30. Cassetta, L. & Pollard, J. W. Targeting macrophages: Therapeutic approaches in cancer. *Nat. Rev. Drug Discov.* **17**, 887–904 (2018).

31. Piaggio, F. *et al.* A novel liposomal Clodronate depletes tumor-associated macrophages in primary and metastatic melanoma: Anti-angiogenic and anti-tumor effects. *J. Control. Release* **223**, 165–177 (2016).

32. Gabrusiewicz, K. *et al.* Macrophage Ablation Reduces M2-Like Populations and Jeopardizes Tumor Growth in a MAFIA-Based Glioma Model. *Neoplasia* **17**, 374–384 (2015).

33. Lin, Y. *et al.* Selective ablation of tumor-associated macrophages suppresses metastasis and angiogenesis. *Cancer Sci.* **104**, 1217–1225 (2013).

34. Guerriero, J. L. Macrophages: Their Untold Story in T Cell Activation and Function. in *International Review of Cell and Molecular Biology* **342**, 73–93 (Elsevier Ltd, 2019).

35. Netea, M. G., Quintin, J. & Van Der Meer, J. W. M. Trained immunity: A memory for innate host defense. *Cell Host Microbe* **9**, 355–361 (2011).

36. Levy, O. & Netea, M. G. Innate immune memory: Implications for development of pediatric immunomodulatory agents and adjuvanted vaccines. *Pediatr. Res.* **75**, 184–188 (2014).

37. Jayasingam, S. D. *et al.* Evaluating the Polarization of Tumor-Associated Macrophages Into M1 and M2 Phenotypes in Human Cancer Tissue: Technicalities and Challenges in Routine Clinical Practice. *Front. Oncol.* **9**, 1–9 (2020).

38. Oshi, M. *et al.* M1 Macrophage and M1/M2 ratio defined by transcriptomic signatures resemble only part of their conventional clinical characteristics in breast cancer. *Sci. Rep.* **10**, 1–12 (2020).

39. Zhang, M. *et al.* A high M1/M2 ratio of tumor-associated macrophages is associated with extended survival in ovarian cancer patients. *J. Ovarian Res.* **7**, 1–16 (2014).

40. Jiang, X. *et al.* Role of the tumor microenvironment in PD-L1/PD-1-mediated tumor immune escape. *Mol. Cancer* **18**, 1–17 (2019).

41. Dorrington, M. G. & Fraser, I. D. C. NF-κB signaling in macrophages: Dynamics, crosstalk, and signal integration. *Front. Immunol.* **10**, (2019).

42. Liu, T., Zhang, L., Joo, D. & Sun, S. C. NF-κB signaling in inflammation. *Signal Transduct. Target. Ther.* **2**, (2017).

43. Okin, D. & Medzhitov, R. Evolution of Inflammatory Diseases. *Curr. Biol.* **22**, R733–R740 (2012).

44. Zhang, H. & Sun, S. C. NF-KB in inflammation and renal diseases. *Cell Biosci.* **5**, 1–12 (2015).

45. Ortega, R. A. *et al.* Manipulating the NF-kB pathway in macrophages using mannosylated, siRNA-delivering nanoparticles can induce immunostimulatory and tumor cytotoxic functions. *Int. J. Nanomedicine* **11**, 2163–2177 (2016).

46. Sen, G. L. & Blau, H. M. A brief history of RNAi : the silence of the genes. *FASEB J.* **20**, 1293–1299 (2006).

47. Laganà, A. *et al.* Computational Design of Artificial RNA Molecules for Gene Regulation. in *RNA Bioinformatics* (ed. Picardi, E.) 393–412 (Springer New York, 2015). doi:10.1007/978-1-4939-2291-8_25

48. Kanasty, R. L., Whitehead, K. A., Vegas, A. J. & Anderson, D. G. Action and Reaction: The Biological Response to siRNA and Its Delivery Vehicles. *Mol. Ther.* **20**, 513–524 (2012).

49. Van Dalen, F. J., Van Stevendaal, M. H. M. E., Fennemann, F. L., Verdoes, M. & Ilina, O. Molecular Repolarisation of Tumour-Associated Macrophages. *Molecules* **24**, (2019).

50. Tang, L. *et al.* Enhancing T cell therapy through TCR-signaling-responsive nanoparticle drug delivery. *Nat. Biotechnol.* **36**, 707–716 (2018).

51. Dawidczyk, C. M. *et al.* State-of-the-art in design rules for drug delivery platforms: Lessons learned from FDA-approved nanomedicines. *J. Control. Release* **187**, 133–144 (2014).

52. Godin, B. *et al.* Emerging applications of nanomedicine for the diagnosis and treatment of cardiovascular diseases. *Trends Pharmacol. Sci.* **31**, 199–205 (2010).

53. Hunter, Z. *et al.* A biodegradable nanoparticle platform for the induction of antigen-

specific immune tolerance for treatment of autoimmune disease. *ACS Nano* **8**, 2148–2160 (2014).

54. Bregoli, L. *et al.* Nanomedicine applied to translational oncology: A future perspective on cancer treatment. *Nanomedicine Nanotechnology, Biol. Med.* **12**, 81–103 (2016).

55. Begines, B. *et al.* Polymeric nanoparticles for drug delivery: Recent developments and future prospects. *Nanomaterials* **10**, 1–41 (2020).

56. El-Say, K. M. & El-Sawy, H. S. Polymeric nanoparticles: Promising platform for drug delivery. *Int. J. Pharm.* **528**, 675–691 (2017).

57. Sailaja, A. K., Amareshwar, P. & Chakravarty, P. Different Techniques Used for the Preparation of Nanoparticles Using Natural Polymers and Their Application. *Int. J. Pharm. Pharm. Sci.* **3**, 45–50 (2011).

58. Yang, J., Han, S., Zheng, H., Dong, H. & Liu, J. Preparation and application of micro/nanoparticles based on natural polysaccharides. *Carbohydr. Polym.* **123**, 53–66 (2015).

59. Martins, C., Sousa, F., Araújo, F. & Sarmento, B. Functionalizing PLGA and PLGA Derivatives for Drug Delivery and Tissue Regeneration Applications. *Adv. Healthc. Mater.* **7**, (2018).

60. Veronese, F. M. & Pasut, G. PEGylation, successful approach to drug delivery REVIEWS. *Drug Discov. Today* **10**, 1451–1458 (2005).

61. Otsuka, H., Nagasaki, Y. & Kataoka, K. PEGylated nanoparticles for biological and pharmaceutical applications. *Adv. Drug Deliv. Rev.* **55**, 403–419 (2003).

62. Kanasty, R., Dorkin, J. R., Vegas, A. & Anderson, D. Delivery materials for siRNA therapeutics. *Nat. Mater.* **12**, 967–977 (2013).

63. Baranov, M. V., Kumar, M., Sacanna, S., Thutupalli, S. & van den Bogaart, G. Modulation of Immune Responses by Particle Size and Shape. *Front. Immunol.* **11**, 1–23 (2021).

64. Elsabahy, M. & Wooley, K. L. Design of polymeric nanoparticles for biomedical delivery applications. *Chem. Soc. Rev.* **41**, 2545–2561 (2012).

65. Wang, J. *et al.* The Role of Micelle Size in Tumor Accumulation, Penetration, and Treatment. *ACS Nano* **9**, 7195–7206 (2015).

66. Bright, N. A., Davis, L. J. & Luzio, J. P. Endolysosomes Are the Principal Intracellular Sites of Acid Hydrolase Activity. *Curr. Biol.* **26**, 2233–2245 (2016).

67. Nelson, C. E. *et al.* Balancing cationic and hydrophobic content of PEGylated siRNA polyplexes enhances endosome escape, stability, blood circulation time, and bioactivity in vivo. *ACS Nano* **7**, 8870–8880 (2013).

68. Werfel, T. A. *et al.* Combinatorial optimization of PEG architecture and hydrophobic content improves ternary siRNA polyplex stability, pharmacokinetics, and potency in vivo. *J. Control. Release* **255**, 12–26 (2017).

69. Yu, S. S. *et al.* Macrophage-specific RNA interference targeting via "click", mannosylated polymeric micelles. *Mol. Pharm.* **10**, 975–87 (2013).

70. Ortega, R. A. *et al.* Biocompatible mannosylated endosomal-escape nanoparticles enhance selective delivery of short nucleotide sequences to tumor associated macrophages.

Nanoscale **7**, 500–510 (2015).

71. Mishra, S. B. & Mishra, A. K. Polymeric Hydrogels: A Review of Recent Developments. in *Polymeric Hydrogels as Smart Biomaterials* (ed. Kalia, S.) (Springer, 2015).

72. Li, Y., Yang, H. Y. & Lee, D. S. Advances in biodegradable and injectable hydrogels for biomedical applications. *J. Control. Release* **330**, 151–160 (2021).

73. Ruan, H. *et al.* A Dual-Bioresponsive Drug-Delivery Depot for Combination of Epigenetic Modulation and Immune Checkpoint Blockade. *Adv. Mater.* **31**, 1–8 (2019).

74. Chen, Q. *et al.* In situ sprayed bioresponsive immunotherapeutic gel for post-surgical cancer treatment. *Nat. Nanotechnol.* **14**, 89–97 (2019).

75. Bencherif, S. A. *et al.* Injectable Cryogel-based Whole Cell Cancer Vaccines. *Nat. Commun.* **6**, 6072–6078 (2016).

76. Leach, D. G., Young, S. & Hartgerink, J. D. Advances in immunotherapy delivery from implantable and injectable biomaterials. *Acta Biomater.* **88**, 15–31 (2019).

77. Bencherif, S. A. *et al.* Injectable preformed scaffolds with shape-memory properties. *Proc. Natl. Acad. Sci.* **109**, 19590–19595 (2012).

78. Shih, T. Y. *et al.* Injectable, Tough Alginate Cryogels as Cancer Vaccines. *Adv. Healthc. Mater.* **1701469**, 1–13 (2017).

79. Kilchrist, K. V. *et al.* Gal8 Visualization of Endosome Disruption Predicts Carrier-Mediated Biologic Drug Intracellular Bioavailability. *ACS Nano* **13**, 1136–1152 (2019).

80. Astakova, K. *et al.* "Clicking" gene therapeutics: A successful union of chemistry and biomedicine for new solutions. *Mol. Pharm.* **15**, 2892–2899 (2018).

81. Nandivada, B. H., Jiang, X. & Lahann, J. Click Chemistry: Versatility and Control in the Hands of Materials Scientists. *Adv. Mater.* **19**, 2197–2208 (2007).

82. Zhang, F. *et al.* Genetic programming of macrophages to perform anti-tumor functions using targeted mRNA nanocarriers. *Nat. Commun.* **10**, (2019).

83. Jackson, M. A. *et al.* Zwitterionic Nanocarrier Surface Chemistry Improves siRNA Tumor Delivery and Silencing Activity Relative to Polyethylene Glycol . *ACS Nano* **11**, 5680–5696 (2017).

84. Lee, K. Y. & Mooney, D. J. Alginate : properties and biomedical applications. *Prog. Polym. Sci.* **37**, 106–126 (2012).

85. Wang, Y. Programmable hydrogels. *Biomaterials* **178**, 663–680 (2018).

86. Sun, J. Y. *et al.* Highly stretchable and tough hydrogels. *Nature* **489**, 133–136 (2012).

87. Vogel, D. Y. S. *et al.* Macrophages migrate in an activation-dependent manner to chemokines involved in neuroinflammation. *J. Neuroinflammation* **11**, 1–11 (2014).

88. Duan, Z. & Luo, Y. Targeting macrophages in cancer immunotherapy. *Signal Transduct. Target. Ther.* **6**, 1–21 (2021).

89. Shobaki, N., Sato, Y., Suzuki, Y., Okabe, N. & Harashima, H. Manipulating the function of tumor-associated macrophages by siRNA-loaded lipid nanoparticles for cancer immunotherapy. *J. Control. Release* **325**, 235–248 (2020).

90. McKay, C. S. & Finn, M. G. Click chemistry in complex mixtures: Bioorthogonal bioconjugation. *Chem. Biol.* **21**, 1075–1101 (2014).

91. Rostovtsev, V. V, Green, L. G., Fokin, V. V & Sharpless, K. B. A Stepwise Huisgen

Cycloaddition Process: Copper(I)-Catalyzed Regioselective ‘Ligation’ of Azides and Terminal Alkynes. *Angew. Chem., Int. Ed.* **41**, 2596–2599 (2002).

92. Tornøe, C. W., Christensen, C. & Meldal, M. Peptidotriazoles on solid phase: [1,2,3]-Triazoles by regiospecific copper(I)-catalyzed 1,3-dipolar cycloadditions of terminal alkynes to azides. *J. Org. Chem.* **67**, 3057–3064 (2002).

93. Liang, L. & Astruc, D. The copper(I)-catalyzed alkyne-azide cycloaddition (CuAAC) ‘click’ reaction and its applications. An overview. *Coord. Chem. Rev.* **255**, 2933–2945 (2011).

94. Patterson, D. M., Nazarova, L. A. & Prescher, J. A. Finding the Right (Bioorthogonal) Chemistry. *ACS Chem. Biol.* **9**, 592–605 (2014).

95. Luo, W. *et al.* A Dual Receptor and Reporter for Multi-Modal Cell Surface Engineering. *ACS Chem. Biol.* **10**, 2219–2226 (2015).

96. Rogozhnikov, D., Luo, W., Elahipanah, S., O’Brien, P. J. & Yousaf, M. N. Generation of a Scaffold-Free Three-Dimensional Liver Tissue via a Rapid Cell-to-Cell Click Assembly Process. *Bioconjug. Chem.* **27**, 1991–1998 (2016).

97. Ranjan, R. & Brittain, W. J. Combination of Living Radical Polymerization and Click Chemistry for Surface Modification. *Macromolecules* **40**, 6217–6223 (2007).

98. Sletten, E. M. & Bertozzi, C. R. Bioorthogonal Chemistry: Fishing for Selectivity in a Sea of Functionality. *Angew Chem Int Ed Engl.* **48**, 6974–6998 (2009).

99. Brewer, G. J. Risks of copper and iron toxicity during aging in humans. *Chem. Res. Toxicol.* **23**, 319–326 (2010).

100. Li, L. & Zhang, Z. Development and applications of the copper-catalyzed azide-alkyne cycloaddition (CuAAC) as a bioorthogonal reaction. *Molecules* **21**, 1–22 (2016).

101. Pickens, C. J., Johnson, S. N., Pressnall, M. M., Leon, M. A. & Berkland, C. J. Practical Considerations, Challenges, and Limitations of Bioconjugation via Azide-Alkyne Cycloaddition. *Bioconjug. Chem.* **29**, 686–701 (2018).

102. Kennedy, D. C. *et al.* Cellular consequences of copper complexes used to catalyze bioorthogonal click reactions. *J. Am. Chem. Soc.* **133**, 17993–18001 (2011).

103. Devaraj, N. K. The Future of Bioorthogonal Chemistry. *ACS Cent. Sci.* **4**, 952–959 (2018).

104. Harvison, M. A. & Lowe, A. B. Combining RAFT Radical Polymerization and Click/Highly Efficient Coupling Chemistries: A Powerful Strategy for the Preparation of Novel Materials. *Macromol. Rapid Commun.* **32**, 779–800 (2011).

105. Liu, D., Yang, F., Xiong, F. & Gu, N. The Smart Drug Delivery System and Its Clinical Potential. *Theranostics* **6**, 1306–1323 (2016).

106. Sanchez-Sanchez, A., Fulton, D. A. & Pomposo, J. A. PH-responsive single-chain polymer nanoparticles utilising dynamic covalent enamine bonds. *Chem. Commun.* **50**, 1871–1874 (2014).

107. Sharker, S. M. *et al.* pH triggered in vivo photothermal therapy and fluorescence nanoplatform of cancer based on responsive polymer-indocyanine green integrated reduced graphene oxide. *Biomaterials* **61**, 229–238 (2015).

108. Wilson, J. T. *et al.* Enhancement of MHC-I Antigen Presentation via Architectural Control

of pH-Responsive, Endosomolytic Polymer Nanoparticles. *AAPS J.* **17**, 358–369 (2015).

109. Zhou, J. *et al.* Characterization and optimization of pH-responsive polymer nanoparticles for drug delivery to oral biofilms. *J. Mater. Chem. B* **4**, 3075–3085 (2016).

110. Han, N. *et al.* Development of Surface-Variable Polymeric Nanoparticles for Drug Delivery to Tumors. *Mol. Pharm.* **14**, 1538–1547 (2017).

111. Ojalvo, L. S., King, W., Cox, D. & Pollard, J. W. High-density gene expression analysis of tumor-associated macrophages from mouse mammary tumors. *Am. J. Pathol.* **174**, 1048–1064 (2009).

112. Zabuawala, T. *et al.* An Ets2-Specific Transcriptional Program in Tumor Associated Macrophages Promotes Tumor Metastasis. *Cancer Res.* **70**, 1323–1333 (2010).

113. Georgoudaki, A. M. *et al.* Reprogramming Tumor-Associated Macrophages by Antibody Targeting Inhibits Cancer Progression and Metastasis. *Cell Rep.* **15**, 2000–2011 (2016).

114. Guerriero, J. L. *et al.* Class IIa HDAC inhibition reduces breast tumours and metastases through anti-tumour macrophages. *Nature* **543**, 428–432 (2017).

115. Yang, J. *et al.* Myeloid IKKβ Promotes Antitumor Immunity by Modulating CCL11 and the Innate Immune Response. *Cancer Res.* **74**, 7274–7284 (2014).

116. Connelly, L. *et al.* Inhibition of NF-kappaB activity in mammary epithelium increases tumor latency and decreases tumor burden. *Oncogene* **30**, 1402–1412 (2011).

117. Nelson, C. E. *et al.* Tunable Delivery of siRNA from a Biodegradable Scaffold to Promote Angiogenesis In Vivo. *Adv. Mater.* **26**, 607–506 (2014).

118. Convertine, A. J., Benoit, D. S. W., Duvall, C. L., Hoffman, A. S. & Stayton, P. S.

Development of a novel endosomolytic diblock copolymer for siRNA delivery. *J. Control. Release* **133**, 221–229 (2009).

119. Mittar, D., Paramban, R. & McIntyre, C. *Flow Cytometry and High Content Imaging to Identify Markers of Monocyte-Macrophage Differentiation. BD Biosciences* (2011). doi:papers3://publication/uuid/05466CA5-7EF6-409B-8CA3-30840B508BB3

120. Genin, M., Clement, F., Fattaccioli, A., Raes, M. & Michiels, C. M1 and M2 macrophages derived from THP-1 cells differentially modulate the response of cancer cells to etoposide. *BMC Cancer* **15**, 1–14 (2015).

121. Diaz-Silvestre, H. *et al.* The 19-kDa antigen of Mycobacterium tuberculosis is a major adhesin that binds the mannose receptor of THP-1 monocytic cells and promotes phagocytosis of mycobacteria. *Microb. Pathog.* **39**, 97–107 (2005).

122. Ying, W., Cheruku, P. S., Bazer, F. W., Safe, S. H. & Zhou, B. Investigation of Macrophage Polarization Using Bone Marrow Derived Macrophages. *J. Vis. Exp.* **76**, 1–8 (2013).

123. Werfel, T. A. *et al.* Hydrolytic charge-reversal of PEGylated polyplexes enhances intracellular un-packaging and activity of siRNA. *J. Biomed. Mater. Res. - Part A* **104**, 917–927 (2016).

124. Collman, J. P., Devaraj, N. K., Eberspacher, T. P. A. & Chidsey, C. E. D. Mixed azide-terminated monolayers: A platform for modifying electrode surfaces. *Langmuir* **22**, 2457–2464 (2006).

125. Thode, C. J. & Williams, M. E. Kinetics of 1,3-dipolar cycloaddition on the surfaces of

Au nanoparticles. *J. Colloid Interface Sci.* **320**, 346–352 (2008).

126. Ahmad Fuaad, A. A. H., Azmi, F., Skwarczynski, M. & Toth, I. Peptide Conjugation via CuAAC 'Click' Chemistry. *Molecules* **18**, 13148–13174 (2013).

127. Liu, T. Y. *et al.* Self-Adjuvanting Polymer-Peptide Conjugates As Therapeutic Vaccine Candidates Against Cervical Cancer. *Biomacromolecules* **14**, 2798–2806 (2013).

128. Vasilyeva, S. V., Filichev, V. V. & Boutorine, A. S. Application of Cu(I)-catalyzed azide-alkyne cycloaddition for the design and synthesis of sequence specific probes targeting double-stranded DNA. *Beilstein J. Org. Chem.* **12**, 1348–1360 (2016).

129. Paredes, E. & Das, S. R. Click chemistry for rapid labeling and ligation of RNA. *ChemBioChem* **12**, 125–131 (2011).

130. Haldón, E., Nicasio, M. C. & Pérez, P. J. Copper-catalysed azide-alkyne cycloadditions (CuAAC): An update. *Org. Biomol. Chem.* **13**, 9528–9550 (2015).

131. Weissleder, R., Nahrendorf, M. & Pittet, M. J. Imaging macrophages with nanoparticles. *Nat. Mater.* **13**, 125–138 (2014).

132. Danaei, M. *et al.* Impact of particle size and polydispersity index on the clinical applications of lipidic nanocarrier systems. *Pharmaceutics* **10**, 1–17 (2018).

133. Clogston, J. D. & Patri, A. K. Zeta Potential Measurement. in *Characterization of Nanoparticles Intended for Drug Delivery* (ed. McNeil, S. E.) 63–70 (2010).

134. Jones, J. A., Starkey, J. R. & Kleinhofs, A. Toxicity and mutagenicity of sodium azide in mammalian cell cultures. *Mutat. Res. Toxicol.* **77**, 293–299 (1980).

135. Bosca, L., Zeini, M., Traves, P. G. & Hortelano, S. Nitric oxide and cell viability in

inflammatory cells: a role for NO in macrophage function and fate. *Toxicology* **208**, 249–258 (2005).

136. Hirota, K. & Hiroshi, T. Endocytosis of Particle Formulations by Macrophages and Its Application to Clinical Treatment. in *Molecular Recognition of Endotytosis* (ed. Ceresa, B.) (IntechOpen, 2012).

137. Kathryn, J. C., Sireesha V, G. & Stanley, L. Triple Negative Breast Cancer Cell Lines: One Tool in the Search for Better Treatment of Triple Negative Breast Cancer. *Breast Dis* **32**, 35–48 (2012).

138. Johnstone, C. N. *et al.* Functional and molecular characterisation of EO771.LMB tumours, a new C57BL/6-mouse-derived model of spontaneously metastatic mammary cancer. *Dis. Model. Mech.* **8**, 237–251 (2015).

139. Gaetke, L. M., Chow-Johnson, H. S. & Chow, C. K. Copper: Toxicological relevance and mechanisms. *Arch. Toxicol.* **88**, 1929–1938 (2014).

140. Martinez, F. O., Gordon, S., Locati, M. & Mantovani, A. Transcriptional Profiling of the Human Monocyte-to-Macrophage Differentiation and Polarization: New Molecules and Patterns of Gene Expression. *J. Immunol.* **177**, 7303–7311 (2006).

141. Roszer, T. Understanding the mysterious M2 macrophage through activation markers and effector mechanisms. *Mediators Inflamm.* **2015**, 1–16 (2015).

142. dos Anjos Cassado, A. F4/80 as a Major Macrophage Marker: The Case of the Peritoneum and Spleen. in *Macrophages* (ed. Kloc, M.) 161–179 (Springer, 2017).

143. Lin, H.-H. *et al.* The macrophage F4/80 receptor is required for the induction of antigen-

specific efferent regulatory T cells in peripheral tolerance. *J. Exp. Med.* **201**, 1615–1625 (2005).

144. Azad, A. K., Rajaram, M. V. S. & Schlesinger, L. S. Exploitation of the Macrophage Mannose Receptor (CD206) in Infectious Disease Diagnostics and Therapeutics. *J Cytol Mol Biol* **1**, 1–10 (2014).

145. Miteva, M. *et al.* Tuning PEGylation of mixed micelles to overcome intracellular and systemic siRNA delivery barriers. *Biomaterials* **38**, 97–107 (2015).

146. Weber, J. S. *et al.* Nivolumab versus chemotherapy in patients with advanced melanoma who progressed after anti-CTLA-4 treatment (CheckMate 037): A randomised, controlled, open-label, phase 3 trial. *Lancet Oncol.* **16**, 375–384 (2015).

147. Robert, C. *et al.* Anti-programmed-death-receptor-1 treatment with pembrolizumab in ipilimumab-refractory advanced melanoma: A randomised dose-comparison cohort of a phase 1 trial. *Lancet* **384**, 1109–1117 (2014).

148. Sul, J. *et al.* FDA Approval Summary: Pembrolizumab for the Treatment of Patients With Metastatic Non-Small Cell Lung Cancer Whose Tumors Express Programmed Death-Ligand 1. *Oncologist* **21**, 643–650 (2016).

149. Balar, A. V. *et al.* First-line pembrolizumab in cisplatin-ineligible patients with locally advanced and unresectable or metastatic urothelial cancer (KEYNOTE-052): a multicentre, single-arm, phase 2 study. *Lancet Oncol.* **18**, 1483–1492 (2017).

150. Bellmunt, J. *et al.* Pembrolizumab as second-line therapy for advanced urothelial carcinoma. *N. Engl. J. Med.* **376**, 1015–1026 (2017).

151. Motzer, R. J. *et al.* Nivolumab versus everolimus in advanced renal-cell carcinoma. *N. Engl. J. Med.* **373**, 1803–1813 (2015).

152. Overman, M. J. *et al.* Nivolumab in patients with metastatic DNA mismatch repair-deficient or microsatellite instability-high colorectal cancer (CheckMate 142): an open-label, multicentre, phase 2 study. *Lancet Oncol.* **18**, 1182–1191 (2017).

153. Schmid, P. *et al.* Atezolizumab and nab-paclitaxel in advanced triple-negative breast cancer. *N. Engl. J. Med.* **379**, 2108–2121 (2018).

154. Gong, J., Chehrazi-Raffle, A., Reddi, S. & Salgia, R. Development of PD-1 and PD-L1 inhibitors as a form of cancer immunotherapy: A comprehensive review of registration trials and future considerations. *J. Immunother. Cancer* **6**, 1–18 (2018).

155. Hamanishi, J. *et al.* Safety and antitumor activity of Anti-PD-1 antibody, nivolumab, in patients with platinum-resistant ovarian cancer. *J. Clin. Oncol.* **33**, 4015–4022 (2015).

156. Matulonis, U. A. *et al.* Antitumor activity and safety of pembrolizumab in patients with advanced recurrent ovarian cancer: Interim results from the phase 2 KEYNOTE-100 study. *J. Clin. Oncol.* **36**, (2018).

157. Kandalaft, L. E., Odunsi, K. & Coukos, G. Immune Therapy Opportunities in Ovarian Cancer. *Am. Soc. Clin. Oncol. Educ. B.* **3**, e228–e240 (2020).

158. Siegel, R., Miller, K., Fuchs, H. & Jemal, A. Erratum to "Cancer statistics, 2021". *CA. Cancer J. Clin.* **71**, 359–359 (2021).

159. Drakes, M. L. & Stiff, P. J. Regulation of ovarian cancer prognosis by immune cells in the tumor microenvironment. *Cancers (Basel).* **10**, (2018).

160. Colvin, E. K. Tumor-associated macrophages contribute to tumor progression in ovarian cancer. *Front. Oncol.* **4**, 1–6 (2014).

161. Ahmed, N. & Stenvers, K. L. Getting to know ovarian cancer ascites: Opportunities for targeted therapy-based translational research. *Front. Oncol.* **3**, 1–12 (2013).

162. Kipps, E., Tan, D. S. P. & Kaye, S. B. Meeting the challenge of ascites in ovarian cancer: New avenues for therapy and research. *Nat. Rev. Cancer* **13**, 273–282 (2013).

163. Latifi, A. *et al.* Isolation and Characterization of Tumor Cells from the Ascites of Ovarian Cancer Patients: Molecular Phenotype of Chemoresistant Ovarian Tumors. *PLoS One* **7**, (2012).

164. Zhu, Q., Wu, X., Wu, Y. & Wang, X. Interaction between Treg cells and tumor-associated macrophages in the tumor microenvironment of epithelial ovarian cancer. *Oncol. Rep.* **36**, 3472–3478 (2016).

165. Steitz, A. M. *et al.* Tumor-associated macrophages promote ovarian cancer cell migration by secreting transforming growth factor beta induced (TGFBI) and tenascin C. *Cell Death Dis.* **11**, (2020).

166. Glass, E. B. *et al.* Optimizing Mannose 'Click' Conjugation to Polymeric Nanoparticles for Targeted siRNA Delivery to Human and Murine Macrophages. *ACS Omega* **4**, 16756–16767 (2019).

167. Hoover, A. A. *et al.* Increased canonical NF-kappaB signaling specifically in macrophages is sufficient to limit tumor progression in syngeneic murine models of ovarian cancer. *BMC Cancer* **20**, (2020).

168. Jackson, M. A. *et al.* Kupffer cell release of platelet activating factor drives dose limiting toxicities of nucleic acid nanocarriers. *Biomaterials* **268**, 1–12 (2021).

169. Nikam, R. R. & Gore, K. R. Journey of siRNA: Clinical Developments and Targeted Delivery. *Nucleic Acid Ther.* **28**, 209–224 (2018).

170. Shim, M. S. & Kwon, Y. J. Efficient and targeted delivery of siRNA in vivo. *FEBS J.* **277**, 4814–4827 (2010).

171. Debacker, J. M., Gondry, O., Lahoutte, T., Keyaerts, M. & Huvenne, W. The Prognostic Value of CD206 in Solid Malignancies: A Systematic Review and Meta-Analysis. *Cancers (Basel).* **13**, 1–16 (2021).

172. Oh, N. & Park, J.-H. Endocytosis and exocytosis of nanoparticles in mammalian cells. *Int. J. Nanomedicine* **9**, 51–63 (2014).

173. Macciò, A. *et al.* Role of M1-polarized tumor-associated macrophages in the prognosis of advanced ovarian cancer patients. *Sci. Rep.* **10**, 1–8 (2020).

174. Wilson, A. J. *et al.* Aberrant over-expression of COX-1 intersects multiple pro-tumorigenic pathways in high-grade serous ovarian cancer. *Oncotarget* **6**, 21353–21368 (2015).

175. Xing, D. & Orsulic, S. A genetically defined mouse ovarian carcinoma model for the molecular characterization of pathway-targeted therapy and tumor resistance. *Proc. Natl. Acad. Sci. U. S. A.* **102**, 6936–6941 (2005).

176. Liao, J. B. *et al.* Preservation of tumor-host immune interactions with luciferase-tagged imaging in a murine model of ovarian cancer. *J. Immunother. Cancer* **3**, 1–9 (2015).

177. Wilson, A. J. *et al.* Tracking NF- κB activity in tumor cells during ovarian cancer progression in a syngeneic mouse model. *J. Ovarian Res.* **6**, 1–11 (2013).

178. Xing, D. & Orsulic, S. A Mouse Model for the Molecular Characterization of Brca1-Associated Ovarian Carcinoma. *Cancer Res.* **66**, 8949–8953 (2006).

179. Hagemann, T. *et al.* 'Re-educating' tumor-associated macrophages by targeting NF-κB. *J. Exp. Med.* **205**, 1261–1268 (2008).

180. Everhart, M. B. *et al.* Duration and Intensity of NF-κB Activity Determine the Severity of Endotoxin-Induced Acute Lung Injury. *J. Immunol.* **176**, 4995–5005 (2006).

181. Stathopoulos, G. T. *et al.* Host nuclear factor-κB activation potentiates lung cancer metastasis. *Mol. Cancer Res.* **6**, 364–371 (2008).

182. Han, W. *et al.* NADPH Oxidase Limits Lipopolysaccharide-Induced Lung Inflammation and Injury in Mice through Reduction-Oxidation Regulation of NF-κB Activity. *J. Immunol.* **190**, 4786–4794 (2013).

183. Reinfeld, B. I. *et al.* Cell-programmed nutrient partitioning in the tumour microenvironment. *Nature* **593**, 282–288 (2021).

184. Schindelin, J. *et al.* Fiji: An open-source platform for biological-image analysis. *Nat. Methods* **9**, 676–682 (2012).

185. Wilson, A. J. *et al.* HDAC4 Promotes Growth of Colon Cancer Cells via Repression of p21. *Mol. Biol. Cell* **19**, 4062–4075 (2008).

186. Wilson, A. J., Saskowski, J., Barham, W., Yull, F. & Khabele, D. Thymoquinone enhances cisplatin-response through direct tumor effects in a syngeneic mouse model of

ovarian cancer. *J. Ovarian Res.* **8**, 1–10 (2015).

187. Wilkinson-ryan, I., Pham, M. M., Sergent, P., Tafe, L. J. & Berwin, B. L. A Syngeneic Mouse Model of Epithelial Ovarian Cancer Port Site Metastases. *Transl. Oncol.* **12**, 62–68 (2019).

188. Rose, S., Misharin, A. & Perlman, H. A novel Ly6C/Ly6G-based strategy to analyze the mouse splenic myeloid compartment. *Cytom. A* **81**, 343–350 (2012).

189. Ye, J. *et al.* Drug-free mannosylated liposomes inhibit tumor growth by promoting the polarization of tumor-associated macrophages. *Int. J. Nanomedicine* **14**, 3203–3220 (2019).

190. Jaynes, J. M. *et al.* Mannose receptor (CD206) activation in tumor-associated macrophages enhances adaptive and innate antitumor immune responses. *Sci. Transl. Med.* **12**, 1–20 (2020).

191. Huynh, E. & Zheng, G. Cancer nanomedicine: addressing the dark side of the enhanced permeability and retention effect. *Nanomedicine* **10**, 1993–1995 (2015).

192. Danhier, F. To exploit the tumor microenvironment: Since the EPR effect fails in the clinic, what is the future of nanomedicine? *J. Control. Release* **244**, 108–121 (2016).

193. Sindhwani, S. *et al.* The entry of nanoparticles into solid tumours. *Nat. Mater.* **19**, 566–575 (2020).

194. Macciò, A. & Madeddu, C. Inflammation and ovarian cancer. *Cytokine* **58**, 133–147 (2012).

195. Browning, L., Patel, M. R., Horvath, E. B., Tawara, K. & Jorcyk, C. L. IL-6 and ovarian

cancer: Inflammatory cytokines in promotion of metastasis. *Cancer Manag. Res.* **10**, 6685–6693 (2018).

196. Gonzalez, P. S. *et al.* Mannose impairs tumour growth and enhances chemotherapy. *Nature* **563**, 719–723 (2018).

197. Haabeth, O. A. W. *et al.* Inflammation driven by tumour-specific Th1 cells protects against B-cell cancer. *Nat. Commun.* **2**, (2011).

198. Ley, K. M1 Means Kill; M2 Means Heal. *J. Immunol.* **199**, 2191–2193 (2017).

199. Singhal, S. *et al.* Human tumor-associated monocytes/macrophages and their regulation of T cell responses in early-stage lung cancer. *Sci. Transl. Med.* **11**, (2019).

200. Cassetta, L. *et al.* Human Tumor-Associated Macrophage and Monocyte Transcriptional Landscapes Reveal Cancer-Specific Reprogramming, Biomarkers, and Therapeutic Targets. *Cancer Cell* **35**, 588–602 (2019).

201. Henze, A. & Mazzone, M. The impact of hypoxia on tumor-associated macrophages. *J. Clin. Invest.* **126**, 3672–3679 (2016).

202. Ruffell, B. *et al.* Macrophage IL-10 Blocks CD8+ T Cell-Dependent Responses to Chemotherapy by Suppressing IL-12 Expression in Intratumoral Dendritic Cells. *Cancer Cell* **26**, 623–637 (2014).

203. Mantovani, A., Marchesi, F., Malesci, A., Laghi, L. & Allavena, P. Tumour-associated macrophages as treatment targets in oncology. *Nat. Rev. Clin. Oncol.* **14**, 399–416 (2017).

204. Soki, F. N. *et al.* Bone marrow macrophages support prostate cancer growth in bone. *Oncotarget* **6**, 35782–35796 (2015).

205. Wang, C. *et al.* The MSHA strain of Pseudomonas aeruginosa (PA-MSHA) inhibits gastric carcinoma progression by inducing M1 macrophage polarization. *Tumor Biol.* **37**, 6913–6921 (2016).

206. Pahl, J. H. *et al.* Macrophages inhibit human osteosarcoma cell growth after activation with the bacterial cell wall derivative liposomal muramyl tripeptide in combination with interferon-γ. *J. Exp. Clin. Cancer Res.* **33**, 1–13 (2014).

207. Duluc, D. *et al.* Interferon-γ reverses the immunosuppressive and protumoral properties and prevents the generation of human tumor-associated macrophages. *Int. J. Cancer* **125**, 367–373 (2009).

208. Li, J. *et al.* Advances of injectable hydrogel-based scaffolds for cartilage regeneration. *Regen. Biomater.* **6**, 129–140 (2019).

209. Park, C. G. *et al.* Extended release of perioperative immunotherapy prevents tumor recurrence and eliminates metastases. *Sci. Transl. Med.* **10**, 1–14 (2018).

210. Luheshi, N. *et al.* Th1 cytokines are more effective than Th2 cytokines at licensing anti-tumour functions in CD40-activated human macrophages in vitro. *Eur. J. Immunol.* **44**, 162–172 (2014).

211. Watkins, S. K., Egilmez, N. K., Suttles, J. & Stout, R. D. IL-12 Rapidly Alters the Functional Profile of Tumor-Associated and Tumor-Infiltrating Macrophages In Vitro and In Vivo. *J. Immunol.* **178**, 1357–1362 (2007).

212. Tokunaga, R. *et al.* CXCL9, CXCL10, CXCL11/CXCR3 axis for immune activation - a target for novel cancer therapy. *Cancer Treat. Rev.* **63**, 40–47 (2018).

213. Ruytinx, P., Proost, P., Van Damme, J. & Struyf, S. Chemokine-Induced Macrophage Polarization in Inflammatory Conditions. *Front. Immunol.* **9**, 1–12 (2018).

214. Mariani, E., Lisignoli, G., Borzì, R. M. & Pulsatelli, L. Biomaterials: Foreign bodies or tuners for the immune response? *Int. J. Mol. Sci.* **20**, (2019).

215. Lichtenegger, F. S. *et al.* Targeting LAG-3 and PD-1 to enhance T cell activation by antigen-presenting cells. *Front. Immunol.* **9**, 1–12 (2018).

216. Ahearne, M., Yang, Y., El Haj, A. J., Then, K. Y. & Liu, K. K. Characterizing the viscoelastic properties of thin hydrogel-based constructs for tissue engineering applications. *J. R. Soc. Interface* **2**, 455–463 (2005).

217. Tomasova, L., Guttenberg, Z., Hoffmann, B. & Merkel, R. Advanced 2D/3D cell migration assay for faster evaluation of chemotaxis of slow-moving cells. *PLoS One* **14**, 1–23 (2019).

218. Martin, M. D. *et al.* Effect of ablation or inhibition of stromal matrix metalloproteinase-9 on lung metastasis in a breast cancer model is dependent on genetic background. *Cancer Res.* **68**, 6251–6259 (2008).

219. Memic, A. *et al.* Latest Advances in Cryogel Technology for Biomedical Applications. *Adv. Ther.* **2**, 1–45 (2019).

220. Beltraminelli, T. & De Palma, M. Biology and therapeutic targeting of tumour-associated macrophages. *J. Pathol.* **250**, 573–592 (2020).

221. Pathria, P., Louis, T. L. & Varner, J. A. Targeting Tumor-Associated Macrophages in Cancer. *Trends Immunol.* **40**, 310–327 (2019).

222. Yang, Y., Guo, J. & Huang, L. Tackling TAMs for Cancer Immunotherapy: It's Nano Time. *Trends Pharmacol. Sci.* **41**, 701–714 (2020).

223. Zemek, R. M. *et al.* Sensitizing the Tumor Microenvironment to Immune Checkpoint Therapy. *Front. Immunol.* **11**, 1–12 (2020).

224. Chen, W. C. *et al.* Antigen delivery to macrophages using liposomal nanoparticles targeting Sialoadhesin/CD169. *PLoS One* **7**, 1–9 (2012).

225. Singh, Y. *et al.* Targeting tumor associated macrophages (TAMs) via nanocarriers. *J. Control. Release* **254**, 92–106 (2017).

226. Xia, Y., Shen, S. & Verma, I. M. NF-κB, an active player in human cancers. *Cancer Immunol. Res.* **2**, 823–830 (2014).

227. Haycook, C. P. *et al.* PEGylated PLGA Nanoparticle Delivery of Eggmanone for T Cell Modulation: Applications in Rheumatic Autoimmunity. *Int. J. Nanomedicine* **15**, 1215–1228 (2020).

228. Ngambenjawong, C., Cieslewicz, M., Schellinger, J. G. & Pun, S. H. Synthesis and evaluation of multivalent M2pep peptides for targeting alternatively activated M2 macrophages. *J. Control. Release* **224**, 103–111 (2016).

229. De Palma, M. & Lewis, C. E. Macrophage regulation of tumor responses to anticancer therapies. *Cancer Cell* **23**, 277–286 (2013).

230. Vanaja, S., Rathinam, V. K. & Fitzgerald, K. A. Mechanisms of inflammasome activation: recent advances and novel insights. *Trends Cell Biol.* **25**, 308–315 (2015).

231. Schirmer, L. *et al.* Heparin-based, injectable microcarriers for controlled delivery of

interleukin-13 to the brain. *Biomater. Sci.* **8**, 4997–5004 (2020).

232. Li, H. *et al.* Matrix metalloproteinase responsive, proximity-activated polymeric nanoparticles for siRNA delivery. *Adv. Funct. Mater.* **23**, 3040–3052 (2013).

233. Jackson, M. A. *et al.* Dual carrier-cargo hydrophobization and charge ratio optimization improve the systemic circulation and safety of zwitterionic nano-polyplexes. *Biomaterials* **192**, 245–259 (2019).

234. Quintero-Fabián, S. *et al.* Role of Matrix Metalloproteinases in Angiogenesis and Cancer. *Front. Oncol.* **9**, 1–21 (2019).